NETHERLANDS GEODETIC COMMISSION
PUBLICATIONS ON GEODESY NEW SERIES
NUMBER 33

THE RÔLE OF ORBIT ERRORS IN PROCESSING OF SATELLITE ALTIMETER DATA

by

E. J. O. SCHRAMA

1989
RIJKSCOMMISSIE VOOR GEODESIE, THIJSSEWEG 11, DELFT, THE NETHERLANDS

PRINTED BY W. D. MEINEMA B.V., DELFT, THE NETHERLANDS

ISBN 90 6132 239

Abstract

Title: The role of orbit errors in processing of satellite altimeter data

The problem of radial orbit errors in processing of satellite altimeter data is largely due to the inaccuracy of the gravity model which is required for the computation of the trajectory of the spacecraft. A commonly used technique for removing these errors consists of minimizing the crossover differences of profiles measured by the altimeter radar.

Several versions of the technique of least squares crossover minimization have been investigated using either SEASAT observations or simulated data. In these adjustments coefficients of error functions are estimated which are either locally defined over short arc segments, globally over long arc segments, or continuously over an entire arc having a length of several days. The solution of the corresponding normal equations consists of a homogeneous and a particular part.

For each crossover minimization problem (CMP) the homogeneous solution is always given as an analytical expression describing the invariances of the altimetric sea surface with respect to the crossover differences. These invariances are described by a surface deformation function which is characteristic for the problem in question. The number of coefficients in this function equals to the rank defect of the normal matrix in the CMP.

For the particular solution of a local CMP (using "tilt and bias" functions) it was found that 2 non-intersecting and non-overlapping master arc segments have to be fixed. However for global chronological segmented CMP's (using 3 parameter sine-cosine functions) only 1 master arc segment needs to be fixed for a particular solution. For continuous CMP's a particular solution is found by including 9 constraint equations in the form of pseudo observation equations. In this case the error function consists of a Fourier series truncated at a cutoff frequency of 2.3 cycles per revolution including a 2 parameter function modeling a long periodic effect in the orbit.

The underlying problem of gravitational radial orbit errors is described by means of the linear perturbations theory, which is based on the Lagrange planetary equations. Additionally the problem is formulated by means of the Hill equations describing perturbed satellite motions in an idealized circular orbit. It is shown that the non-resonant particular radial solution of the Hill equations coincides with the first-order radial solution derived from the linear perturbations theory assuming a near circular orbit.

The first-order radial solution has been compared with a simulated signal derived by numerical integration of the equations of motion. The simulated signal consists of the radial differences between two trajectories (resembling the SEASAT 3 day repeat configuration) integrated with different gravity models. It was found that the analytical orbit error model resembles closely the simulated signal after removal of a long periodic effect.

The validity of the general solutions of two global CMP's has been investigated by means of a simulation experiment. In this experiment crossover differences are simulated by means of the radial orbit error signal described above. In a second step it is attempted to reconstruct this signal by minimizing the simulated differences.

This experiment revealed that the general solution of the segmented CMP appears to be hampered by unrealistic velocity discontinuity effects of successive arc segment error functions. In addition, it fails to describe the C_{11} and S_{11} and higher degree and order components of a geographically correlated radial orbit error. This is not surprising since one can prove that the homogeneous solution of the segmented CMP (without velocity discontinuities) corresponds to the C_{00} and C_{10} component of the geographically correlated radial orbit error. For this reason the global segmented CMP is reformulated in a continuous approach where it is shown that the homogeneous solution coincides with the geographically correlated radial orbit error. Computations showed that the simulated signal deviates to approximately 15 cm r.m.s. with respect to the general solution of the continuous CMP.

Employing the latter technique 5 independent particular solutions of a radial orbit error signal have been computed from SEASAT crossover data. These solutions appear to be highly correlated and suggest the presence of a disturbing effect likely to be caused by gravity modeling errors. Additionally it was found that the individual solutions resemble a concentration of signal near the once per revolution frequency in the radial orbit error spectrum. This solution could in principle be used to improve a part of the gravity model that is used in the trajectory computation of the satellite.

In the last part an integrated approach is described where the problem of modeling errors in the orbit, the geoid and the permanent part of the sea surface topography (PST) caused by ocean circulation are considered simultaneously. It is argued that an application of the integrated approach is justified if simultaneously gravity model improvement is performed employing tracking data of other satellites at different inclinations and eccentricities. Other aspects of the integrated approach concern the modeling problems of the PST field, an omission effect of the gravity field and the relation with the global continuous CMP.

Key words: satellite altimetry, gravity models, gravitational orbit errors, crossover difference minimization, integrated altimetric approach.

Acknowledgement

I wish to thank the many people whose comments about this work and discussions on satellite altimetry have been so helpful. Special thanks go to Reiner Rummel for the stimulating thoughts and reviewing of my earlier manuscripts, Karel Wakker, Boudewijn Ambrosius and René Zandbergen, from the department of aerospace engineering at the Delft University of Technology, Dinos Danas who unfortunately left the department of geodesy and Carl Wagner whom I met at the summer school in Assisi (Italy), May - June 1988. I am also grateful to Mr. Marsh, Goddard Space Flight Center, who supplied the SEASAT GDR tapes which have been used for various investigations. This research is supported financially in the form of a research fellowship by the Netherlands Organization for Scientific Research (NWO).

Abbreviations, symbols, and acronyms

AGC	Automatic Gain Control
c.p.r.	Cycles Per Revolution
DORIS	Doppler Orbitography and Radio positioning Integrated by Satellite
ESA	European Space Agency
ESOC	European Space Operations Center
FFT	Fast Fourier Transform
FNOC	Fleet Numerical Oceanographic Center
GDR	Geophysical Data Record
GEM	Goddard Earth Model
GPS	Global Positioning System
GRS	Geodetic Reference System
GSFC	Goddard Space Flight Center
HE	Hill Equations
$H\frac{1}{3}$	Significant Wave Height
JPL	Jet Propulsion Laboratory
LHS	Left Hand Side
LPE	Lagrange Planetary Equations
LPT	Linear Perturbations Theory
LSA	Least Squares Adjustment
NASA	National Aeronautics and Space Administration
NOAA	National Oceanic and Atmospheric Administration
NSWC	Naval Surface Weapons Center
OSU	Ohio State University
PGS-S	Preliminary Gravity Solution-SEASAT
PRARE	Precise Range And Range-rate Equipment
PST	Permanent part of the Sea surface Topography
RHS	Right Hand Side
r.m.s.	Root Mean Square
SAR	Synthetic Aperture Radar
SMMR	Scanning Multichannel Microwave Radiometer
SST	Satellite to Satellite Tracking
SWH	Significant Wave Height
TOIL	Time-tagged Ocean, Ice, Land (GDR editing information)
USB	Unified S-Band (a radar tracking system)

Contents

Chapter 1

Introduction

Since the mission of Skylab in 1973 three satellites have been equipped with a radar altimeter. Two more missions are planned in the near future. The projects since the experimental mission of Skylab are those of GEOS-3 (operational from 1975 till 1978), SEASAT (in the summer of 1978) and GEOSAT (from 1985 up till now). For the next decade ERS-1 is expected to be launched in 1990 and TOPEX/POSEIDON will be realized in 1991.

The principles of satellite altimetry shall be introduced in chapter 2. Observations derived from the altimeter radar consist of distance measurements from the satellite to the closest point at the sea surface in the nadir. The purpose of these measurements is to determine the permanent (or mean) shape of the sea surface and its variations in time.

The uncorrected distance measurements of the altimeter radar are a result of a number of effects acting simultaneously. First of all there are several instrumental effects which affect the magnitude of the distance observations. Secondly the radar signal is influenced by the ionosphere and troposphere of the Earth. Thirdly the shape of the sea surface itself is determined by a number of time variable and permanent phenomena. Moreover the height of the altimeter above this surface is subject to the motions of the spacecraft orbiting around the Earth.

In chapter 2 it is explained that a successful application of satellite altimetry is only possible after removing a number of the mentioned effects. Some of the phenomena which determine the distance measurements can be derived with sufficient accuracy from in situ observations performed by other instruments on board the spacecraft such as microwave radiometers for correcting the wet tropospheric delay of the travel time of the radar pulse. Other effects, such as those caused by the position determination of the spacecraft, require an independent treatment. Eventually there remain a number of effects which are not corrected at all since it is the intention to observe them with the altimeter.

A fundamental problem of satellite altimetry is to *distinguish* between the mixture of phenomena in the eventual sea surface profiles 'delivered' by the altimeter. (In the sequel these profiles are simply called 'altimeter profiles') Essentially this topic is the main motivation for the study presented here where the role of a radial position uncertainty in satellite altimetry is discussed.

In chapter 2 it is shown that radial orbit errors and geoid undulation errors are dominating in altimetry. The main cause of a radial orbit error is still, even after 15 years of altimeter data, the uncertainty in modeling the a-priori gravitational field which is required for the computation of the position of the spacecraft. Another result of inaccurate gravitational models is the a-priori error of the geoid. This equipotential surface determines to great extent the geometrical shape of the sea surface.

In first instance research is focussed on an empirical removal of a radial orbit error from altimetric data in a local region. A straightforward approach described in chapter 3 employs so-called crossover differences consisting of the sea surface height discrepancies at intersecting profiles measured by the altimeter radar. Ideally these discrepancies should be small since it is expected that sea surface heights change no more than some 20 cm due to turbulences induced by currents, eddies and other phenomena, compare (Wunsch and Gaposchkin,1980). Yet the actual crossover differences of e.g. SEASAT and GEOSAT have a standard deviation of some 1.5 to 2 m. This cannot be caused by the inaccuracy of the geoid since the geoid represents a stationary surface cancelling in the crossover height difference. Crossover differences are primarily caused by orbit errors of the spacecraft and secondarily by the height variations of the sea surface.

Empirical modeling of radial errors is feasible due to the known long wavelength behavior of this effect. Accordingly the problem of local crossover minimization is to estimate linear functions which purpose it is to correct the sea surface heights along independent altimeter profiles, compare (Rummel & Rapp,1977). The properties of this estimation procedure formulated as a least squares minimization problem is described in chapter 3.

In chapter 4 the nature of gravitational orbit perturbations is worked out in detail for typical altimetric orbits which are usually 3 or 6 days long, nearly circular (an instrumental requirement of the altimeter) and only perturbed by the Earth's gravitational field. The author's main motivation for studying radial orbit perturbations due to gravitational effects is to obtain a better insight in the nature of the problem. Accordingly the linear perturbation theory, originating from Kaula (1966), is evaluated for radial variations in near circular trajectories. Additionally, an alternative technique, based on the Hill equations described by Kaplan (1976) and Colombo (1984a), is investigated for the problem in question. Moreover, in order to verify both analytical orbit error theories, a comparison is made with a so-called synthetical radial orbit error. This synthetical error is generated by means of the radial differences of two numerically integrated altimetric orbits each based on existing geopotential models.

Chapter 5 discusses the effect one may expect of the gravitational radial orbit error on two observation types frequently employed in the processing of satellite altimeter data. The two observation types are the earlier mentioned crossover differences and repeating measurements along altimeter profiles (namely collinear – or repeat arc differences) which are used for studying the variations of the sea surface with respect to time, compare (Cheney, Marsh and Beckly,1983). The analyses pursued in chapter 5 are based on the properties of the time tags which are characteristic for the observations in question. On basis of this information it is already possible to conclude whether a particular observation type is sensitive to certain effects in the orbit.

In chapter 6 the problem of recovering a radial orbit error from simulated crossover – and collinear differences is investigated. For the latter observation type it is merely a verification that collinear differences behave invariant with respect to short periodic perturbations caused by the geopotential which are not modulated by the long periodic oscillations originating from the near secular motion of the argument of perigee. However the contrary is true for crossover differences which are partially sensitive for radial orbit errors. This problem is investigated in chapter 6 for several global crossover minimization schemes involving the least squares estimation of chronological segmented and continuous orbit error models.

In chapter 7 the most promising crossover minimization scheme is employed for estimating a radial orbit error function from the actual SEASAT crossover differences. An additional problem encountered in the processing of SEASAT altimeter data comes from the fact that orbit determination is performed in periods of 3 or 6 days, as is described by (Lerch, Marsh, Klosko and Williamson,1982a). The consequences of segmented orbit determination on the estimated radial orbit error function(s) are discussed in chapter 7.

In chapter 8 an integrated approach is sketched with the purpose to improve a geoid, an orbit and a PST field simultaneously from satellite altimeter data, cf. Wagner (1986,1988) and Engelis (1987). This approach does not necessarily require the application of crossover differences since stationary surface effects, consisting of the geoid and PST, are incorporated in the model.

In chapter 9 conclusions are drawn and recommendations are given for future research on satellite altimetry.

Chapter 2

The principles of satellite altimetry

2.1 Introduction

In this chapter we describe the principles of satellite altimetry. In their most basic form the observations consist of radar height measurements from the satellite to the sea surface. In addition to these height observations it must be known 1) at which location the satellite is 2) at what time the measurement is performed 3) whether the state of the satellite allows the altimeter to operate and 4) how the medium behaves through which the radar signal travels. This simplified sketch shows directly the aspects playing a role in satellite altimetry. Therefore in this chapter the measurement principle, the technique for orbit determination, the instrumental aspects, the expected error budget and the altimeter dataset as it has been used from SEASAT are introduced. SEASAT was an altimeter satellite operating from July 6, 1978 till October 10, 1978. A detailed description of the SEASAT mission is given by Lame & Born (1982).

2.2 The measurement principle

2.2.1 Altimeter observations

Taking the altimeter of SEASAT we demonstrate the instrumental characteristics. It is stated by Tapley, Born and Parke (1982a) that the altimeter possessed an instrumental accuracy of 10 cm. It consists of a short pulse (3 ns) nadir viewing microwave radar operating at a frequency of 13.5 GHz. The instrument returns some average height of the satellite above the sea surface in the footprint area of the radar which is computed from the travel time of the radar pulse. The footprint of the altimeter can be regarded as the illuminated spot on the sea surface being 2.4 to 12 km in diameter depending on the actual sea state, filtering the effect of windwaves on the sea surface. The roughness of the sea surface in the footprint area is extracted from the distribution in time of the received radar pulse, and is used to define the significant wave height (SWH or $H\frac{1}{3}$). Another quantity returned is the strength of the reflected radar pulse which is symbolized by the automatic gain control (AGC).

In addition, the altimeter included a tracker loop (an alpha-beta tracker) consisting of a low band pass filter. The purpose of this filter was to maintain the leading edge of the return pulse in the center of a set of time-equivalent waveform sample gates. The performance of this filter was nearly ideal over water where dynamic lag resulted in errors of less than 10 cm, as is stated in (Martin, Zwally, Brenner and Bindschadler,1983).

2.2.2 The altimetric configuration

In addition to the height observations defined as ρ we consider the position of the satellite to be known in an Earth fixed coordinate system. The ephemerides of SEASAT were supplied in geographical coordinates based on the geodetic reference system 1980, compare (Lerch et al.,1982a). From the ephemerides one can derive the height of the satellite above the reference ellipsoid, a quantity denoted h^*. The height observation ρ represents the shortest distance between the altimeter and the instantaneous sea surface. Furthermore we define the height of the actual sea surface above a reference ellipsoid as h and find the basic relation:

$$h^* = \rho + h. \tag{2.1}$$

(A slope of the sea surface and its effect on the shortest distance measurement ρ is not considered in eq. (2.1). The perpendicular distance above a tilted surface is approximately a factor $\rho\alpha^2$ shorter (for small values of α) than a distance measurement along h^*. Since $\rho \approx 8 \times 10^5$ m and $\alpha \approx 10^{-4}$ radians (e.g. 10 m per 100 km), $\Delta\rho \approx \rho\alpha^2 \approx 8$ mm which is negligible with respect to other effects)

In reality the altimetric configuration is somewhat more complicated than assumed in (2.1). The quantity h may be divided into N, the geoid height and H, the deviation of the sea surface with respect to the geoid. Hence we find

$$h^* = \rho + N + H. \tag{2.2}$$

Furthermore it is customary to split H in ς^p and ς^v respectively the permanent (or mean) sea surface topography and variable sea surface topography. Later on in this chapter the order of magnitude and accuracy of these quantities are described. The altimetric configuration is illustrated in figure 2.1.

2.3 Orbital aspects

Here the derivation of the quantity h^* is described in more detail. It is obtained from the orbit determination of the altimeter satellite and involves application of other measurements; the so-called tracking observations.

2.3.1 Choice of orbits

Aspects playing an important role in the choice of the nominal orbits are firstly, that the altitude variation has to be minimized (an instrumental requirement of the altimeter) and secondly, that the ground track pattern of the altimeter covers the Earth's surface globally.

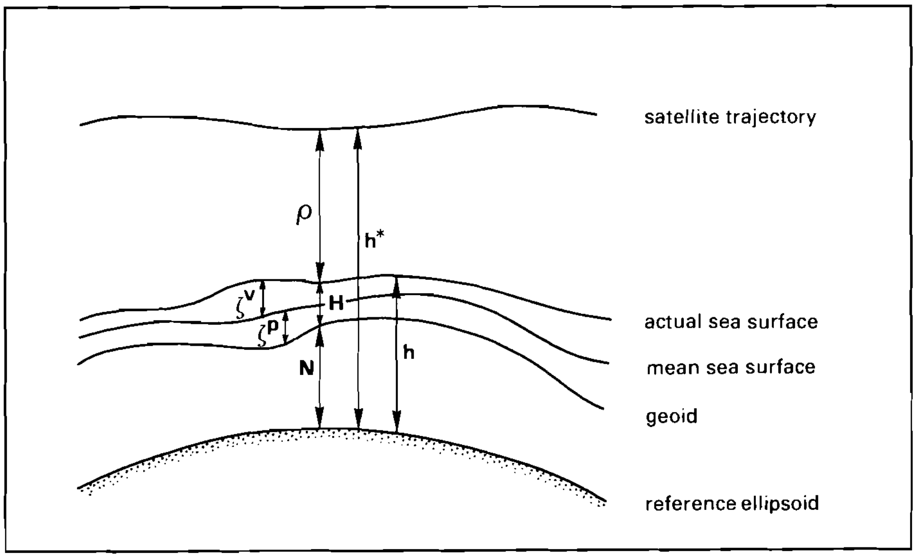

Figure 2.1: The altimetric configuration.

Additional requirements can be for instance a full sun orbit (e.g. as initially anticipated for SEASAT) or a sun synchronous trajectory (ERS-1). In the latter case, viewed from the satellite, the illumination of the Earth's surface is always from the same direction, facilitating the operation of remote sensing instruments on board the spacecraft. The concept of ERS-1 consists of an Earth Remote Sensing satellite on which the radar altimeter is placed as a 'second priority' instrument.

For certain oceanographic applications a trajectory can be chosen in such a way that the ground track repeats itself after a certain period, known as the repeat period. A comparison of successive height measurements over a repeating ground track enables to observe variations of the sea surface heights in time, compare (Cheney et al.,1983).

The classes of orbits applied for altimeter satellites are all low eccentric at an altitude of approximately 800 to 1400 km with relatively high inclinations above 60°, compare table 2.1.

name	h (km)	e	I	rev/day
GEOS-3	843	10^{-3}	115.0	14.13
SEASAT	780	8×10^{-4}	108.0	14.33
GEOSAT	780	8×10^{-4}	108.0	14.33
TOPEX/POSEIDON	1334	1.5×10^{-3}	63.4	12.82
ERS-1	780	10^{-3}	98.5	14.33

Table 2.1: The approximate orbital elements of altimeter satellites.

As mentioned before, an important requirement of the altimeter itself is a limited altitude variation with respect to the sea surface in the nadir of the satellite. In orbits having a small eccentricity a limited altitude variation is acquired by eliminating the secular perigee drift. A straightforward approach, employing the properties of the effect of the flattening term J_2 of the Earth's gravitational field on a satellite orbit, is applied in the mission of TOPEX/POSEIDON. In this mission it is planned to 'freeze' the argument of perigee at $\omega = 270°$ by adopting the critical inclination of 63.4° and a special eccentricity.

In a similar approach, applied in the last month of the SEASAT mission, the secular perigee drift is eliminated by fixing the argument at 90° while using a specific eccentricity. The relation between eccentricity and argument of perigee in this type of orbit is given by Cook (1966). A description of the relation between the argument of perigee and eccentricity due to the zonal effects of the gravitational field is given in appendix A.

The 'Cook' orbit is unstable due to the various perturbing forces and requires periodical corrections (about once per month) by means of firing thrusters on-board the satellite. A discussion about the corrections required to maintain a 'Cook' orbit can be found in (Colombo,1984b).

2.3.2 Orbit determination

During its mission the spacecraft is followed by a network of tracking stations for the purpose of orbit determination. Typical tracking observations are laser range measurements, Doppler range-rates, radar (USB, unified S-band) range and range rates, altimeter height measurements, cf. chapter 8, or SST range rates as in the case of ATS-6 to GEOS-3. During orbit determination the tracking observations are coupled to a dynamical model which describes the relation of a satellite state vector and time. The state vector consists of 3 position and 3 velocity components which are defined in an inertial coordinate system. The dynamical model takes the form of a system of second-order differential equations which are called the equations of motion. The motion of a point mass moving in the gravitational field of a planet represented in an inertial coordinate frame is given by:

$$\ddot{\vec{x}} = \nabla V + \vec{f}_1 + \cdots + \vec{f}_n \tag{2.3}$$

where $\ddot{\vec{x}}$ represents the acceleration vector of the satellite. The term V represents the gravitational potential of the Earth, $\vec{f}_1 + \cdots + \vec{f}_n$ denote additional force models for atmospheric drag, radiation pressure effects, tidal effects, and others, compare Lerch et al. (1982a).

The objective of orbit determination is to find an orbit that matches in the least squares sense the tracking observations. Adequate software is capable of handling a variety of observation types. The least squares adjustment model applied for the processing of these observations contains unknowns for:

- an initial state vector; the unknowns are the six state vector components at the epoch where integration of the equations of motion starts,
- parameters in the force models; typically the unknowns pertain to atmospheric drag, radiation pressure, gravity, or other models,

- tracking instrument parameters; such as clock offset and drift terms at a tracking station and
- geographical coordinates of the tracking stations.

The common method applied during orbit determination is to integrate (2.3) with respect to time numerically. High-order multistep integration methods, such as an Adams Moulton procedure described in (Martin, Oh, Eddy and Kogut, 1976), may be applied for these purposes. Integrated are the state vector itself and a transition matrix which relates the changes of the actual state vector with respect to the initial state vector.

The numerical integration starts at an a-priori state vector using an approximate force model. This results in an apparent trajectory which is used for linearization of the adjustment model. Eventually, the purpose is to update the approximate values of the parameters by a least squares adjustment. In general, this procedure is repeated a number of times till convergence occurs. Usually not all unknowns are treated in one step, instead the process of orbit determination is sub-divided into several phases (inner and outer iterations) in which separate groups of unknowns are treated individually. A detailed description of the so-called differential orbit correction technique as it is implemented in GEODYN is given by Martin et al. (1976).

For the purpose of improved orbit computations of SEASAT tailored gravity models were developed by application of laser, USB tracking data including altimeter observations of SEASAT and GEOS-3. They were combined with gravity field constraints from other satellites. The development of a tailored gravity model for SEASAT is given by Lerch et al. (1982a).

2.3.3 Orbit accuracy

As described in §2.3.2, h^* is determined by orbit determination resulting in an *apparent* satellite trajectory. As a result there remains a radial orbit error with respect to the actual trajectory of the altimeter satellite. In (Tapley et al.,1982a) it is mentioned that the most important sources of the orbit error may be divided into four categories which are: the gravitational field, atmospheric drag effects, solar radiation and station location effects. All these influences have a long wavelength behavior of which the dominant effect can be assigned to gravity field mismodeling. In the case of SEASAT it is known that its trajectory deviates radially about 1.5 to 2 m from the *actual* trajectory, compare also (Tapley et al.,ibid). The radial orbit error as function of the time is denoted $\Delta r(t)$.

The value of 1.5 to 2 m dates from a situation of almost 10 years ago. Nowadays, using advanced trajectory computation techniques, the estimated orbit error of SEASAT is on the level of 50 cm, compare e.g. (Marsh et al.,1986). *However* this is only the case for those orbits which have been *included* in the solution of e.g. GEM-T1, compare (Marsh et al.,ibid). In this context Wagner (1988), pg. 27, points out that the projected errors for orbits *not* included in this solution may become much higher (even up to a factor 5 to 10 with respect to the accurate orbits). Apparently GEM-T1 is not as accurate in predicting new orbits as it is in describing existing orbits. In other words, the problem of gravitational orbit errors will probably remain in the future.

2.4 Instrumental aspects

In the following some details concerning the instrumental aspects of the SEASAT altimeter are described. In view of eq. (2.1) we discuss the quantity ρ, the shortest distance between the altimeter and the instantaneous sea surface. In principle the measurements ρ are derived from the turn around time of the radar pulse. However a number of corrections are involved for meaningful application of the measurements. They are characterized by:

- Instrumental effects.
    1. Center of mass correction of the altimeter.
    2. Instrument bias and drift.
    3. Time tag corrections.
- Geophysical effects.
    1. Instrument bias due to the SWH.
    2. Ionospheric effects.
    3. Tropospheric effects.

2.4.1 Corrections for instrumental effects

The altimeter on board the spacecraft is usually not located in the center of mass, a point which motion is computed by trajectory computation. For instance, the shape of SEASAT without appendages (synthetic aperture radar (SAR) antenna and solar panels) resembles an approximate cylinder of 10 m height and 2 m diameter where the altimeter radar is located at the end of the cylinder, compare also the GDR (geophysical data record) handbook (Lorell, Parke and Scott,1980). SEASAT is an example of a gravity gradient stabilized satellite: the cylinder is positioned along the local gravity vector, which is approximately along h^*. The difference in location from the center of mass of the satellite to the phase center of the antenna of the altimeter is approximately 5 m. This requires a correction which is called the center of mass correction of the altimeter.

Another effect is the instrument bias of the distance measurements. The bias is due to internal instrumental delay and needs to be calibrated before the launch of the spacecraft. In addition, a calibration of the altimeter is done during the actual mission. In the last month of SEASAT's mission the satellite passed several times (while in 3 day repeat mode) over a laser site at the island of Bermuda. The overflight passes provided the primary information for the absolute bias calibration and stability analyses of the altimeter, compare (Kolenkiewicz & Martin,1982).

A last effect is the time tag correction of the satellite clock. It means that the time assigned to the observables ρ differs from the time at which the (ϕ, λ, h^*)

values are computed by orbit determination. Time tag differences do ***not*** affect the actual measurements ρ but have their influence through the term dh^*/dt, the vertical velocity component of the spacecraft above the reference ellipsoid. The effect and the approach to correct for it is described in (Marsh and Williamson,1982a).

2.4.2 Corrections for geophysical effects

A typical effect is the altimeter height bias due to wind waves on the sea surface. The bias tends to be a function of the significant wave height and is corrected by adding 0.07 × $H_{\frac{1}{3}}$ to the sea surface height, compare also (Born, Richards and Rosborough,1982).

As the radar signal travels through a medium consisting of ionosphere and troposphere, corrections are needed to remove refraction effects resulting in signal delay.

The ionospheric refraction effect depends on the electron content along the signal path as well as on the frequency of the radar. A remedy for this effect is to measure at two or more frequencies, as is done in Doppler and GPS receivers. However SEASAT's altimeter operated at only one frequency requiring the application of external ionospheric models, compare (Lorell, Colquitt and Anderle,1982).

The tropospheric 'dry' effect depends on the atmospheric pressure along the path of the radar signal through the troposphere. This correction requires the application of tropospheric models, compare (Lorell et al.,1980).

Another correction concerns the tropospheric 'wet' effect which depends on the water vapor pressure along the path of the radar signal. There are two possibilities for correcting this effect. Either radiometer data from the SMMR (scanning multichannel microwave radiometer) is used or the effect is compensated using an external model, (FNOC wet tropospheric correction), compare (Lorell et al.,1980) and (Tapley, Lundberg and Born,1982b). In our computations the FNOC correction is applied.

2.5 Geophysical effects and sea surface heights

After orbit computation and after all required corrections to ρ the instantaneous sea surface h (still not corrected for radial orbit errors) is obtained from eq. (2.1). The instantaneous sea surface height is the height above the reference ellipsoid. It contains the variable (or dynamic) sea surface effect ς^v, see figure 2.1. In order to eliminate ς^v as far as possible the following model corrections are applied:

- Earth and ocean tides affecting h,
- Inverse barometer behavior of the sea surface.

The ocean tide effect is taken into account by means of a global model of Schwiderski (1978) involving the M2, S2, N2, K1, O1, and P1 components of the tide. Another tidal model available on the SEASAT GDR tapes is described in (Parke and Hendershott,1980) involving the M2, S2 and K1 components of the global ocean tide. Both models are valid in open oceans far from shallow waters close to the coast as is mentioned by Rowlands (1981).

Earth tides result in a deformation of the solid Earth coming from the sun and the moon. They are corrected by means of an Earth tide model, compare (Melchior,1978).

Inverse barometer effects manifest as variations in the sea surface height due to meteorological effects. (1 mb corresponds to 1 cm height variation) This correction involves knowledge of the instantaneous atmospheric pressure, the average surface density and gravity, compare the GDR handbook (Lorell et al.,1980).

2.5.1 GDR data structure and editing

The GDR tapes contain:

- h^*, ϕ, λ derived from orbit determination, and t corrected for time tag bias.
- ρ including the corrections for instrumental effects (center of mass, calibration, inverse barometer) and geophysical effects (ionosphere, 'wet' and 'dry' troposphere effects).
- AGC (automatic gain control of the altimeter) in decibel (dB) and SWH in meter.
- Ocean tide (Schwiderski or Parke Hendershott model) and Earth tide information, (Melchior,1978).
- Editing information, (edit byte).
- Auxiliary information. (e.g. a low degree and order geoid model, sea surface temperature)

The next step is to apply editing on the data in its raw form, for the purpose of eliminating erroneous observations. The procedure is described in (Marsh and Martin,1982b). We used a slightly modified version during the processing of altimeter data. Raw altimeter data appeared to be hampered by a number of effects such as:

- Spikes in h, sudden unrealistic high values for h, likely to be caused by incidental radar reflections e.g. coming from land or sea ice.
- Invalid tidal corrections in some notorious regions such as the Hudson Bay.

Editing removes most of the effects mentioned. The procedure is to:

- check the TOIL (Time-tagged, Ocean, Ice, Land) and other editing information on tape. (eliminates: most land reflections, data hampered by excessive tilt of the satellite, blunders in other quantities),
- avoid those observations in which the corrected h deviates more than 10 m from an a-priori geoid model (only during an adjustment step),
- ignore those observations with AGC > 36 dB,
- skip observations with SWH=0 at $\phi \leq -55°$ or $\phi \geq 65°$, (ice reflections)
- avoid observations or to apply other tidal models in those regions where this information is invalid.

2.6 The error budget

In table 2.2 an abbreviated version of the SEASAT altimeter error budget is presented. It is important to note that the main error sources in altimetry, see figure 2.1, come from the orbit through the term h^* and from the geoid through N. As already mentioned both effects are mostly due to gravitational model errors. It indicates a principal problem in satellite altimetry:

- A typical objective of physical geodesy and geophysics is to recover a highly detailed geoid by means of satellite altimetry. The geoid is directly related *(non-dynamically)* to the gravity model. There is no relation by means of additional differential equations with variables dependent of time.
- Another geodetic objective might be to improve the orbit which is very attractive since an altimeter provides a good coverage of the trajectory. This information may be used to improve gravity models with benefits to satellite geodesy. If it is assumed that most of the orbit error is due to gravitational modeling then the problem is to recover a ***dynamical*** orbit error effect. It will be shown that there exists a relation of the orbit error with respect to the gravitational model by means of additional differential equations (the Lagrange planetary equations and the Hill equations) with variables dependent of time.

In the case of orbit error removal the problem may be formulated as a selective filter which is only sensitive to a radial orbit error and *not* for geoid model errors. This filter was introduced by Rummel et al. (1977) and takes the form of a least squares adjustment in which the discrepancies of h on ground track intersection points, known as crossovers, are minimized. Observations in the form of crossover differences are insensitive to N and ς^p whereas this is not the case for most parts of the radial orbit error signal.

In chapter 3 an example of a local crossover adjustment is described for the purpose of introducing a selective filter for radial orbit errors.

2.7 Conclusions

In this chapter the principles of satellite altimetry were reviewed. Two important items are the orbit determination process and the altimeter instrumental aspects. Two dominant error sources are the radial position error of the spacecraft and the modeling error of the geoid which are respectively of the order of 1.4 m and 2 m (situation: 1980), compare table 2.2. Both effects are far larger than the instrumental accuracy of the altimeter radar.

Observations which are invariant to stationary surface effects are known as crossover differences. It is likely that the height differences on crossovers are caused by a radial orbit error effect which in its turn originates dominantly from the uncertainties of the gravitational field used in the process of orbit determination. A sketch of a reduction of the orbit error by means of crossover difference minimization is given in chapter 3.

Type of Error	Source of Error	Amplitude (cm)	Residual (cm)	Wavelength (km)
Altimeter	Noise		5.0	
Altimeter	Bias	10	2.0	
Sea state related bias	Waveheight and tracker biases	$7 \pm 2\% \times H_{\frac{1}{3}}$	$2\% \times H_{\frac{1}{3}}$	500–1000
Troposphere	Mass of Air	240	0.7	1000
Troposphere	Water Vapor	10–40	3.0	50–500
Ionosphere	Free Electrons	2–20	3.0	50–10,000
Liquid Water	Clouds, rain	10–100	—	30–50
Orbital error	Gravity	10 km.	140	40,000
Orbital error	Drag	300	30.0	10,000
Orbital error	Solar radiation	300	30.0	10,000
Orbital error	Station location	100	10.0	10,000
Timing	Time tag bias		5.0	20,000
Depression of sea level	Atmospheric pressure	50	3.0	200–1000
Geoid	Mass of Earth	100 m.	200	2000-5000
Earth tide	Lunar, Solar tide	20	2	20,000
Ocean tide	Lunar, Solar tide	100	10	500–1000

Table 2.2: SEASAT altimeter error budget, cf. (Tapley et al.,1982a). It shows the type and source of the error, amplitude in cm of the unmodeled effect, residual (1σ) in cm after modeling and the wavelength of the effect in km.

Chapter 3

Introduction to local adjustment of altimeter data

3.1 Introduction

The goal of this chapter is to introduce some theoretical and practical problems related to the adjustment of altimeter data. For this purpose we describe a local adjustment of crossover differences in the North-east Atlantic. Similar studies of other geographical areas are described by e.g. (Rummel et al.,1977), Vermeer (1983), (Marsh, Cheney, McCarthy and Martin,1984), (Knudsen,1987), (Zandbergen, Wakker and Ambrosius,1988) and many others. The practical applications of local crossover minimization are numerous. Usually local crossover minimization is applied for local gravity field improvement and sea surface variability computations. In our study the adjustment is divided into two parts:

- Crossover differences, as they are derived from SEASAT altimeter data, are minimized. This results in a sea surface entirely determined by altimetry.
- Discrepancies between the altimetric sea surface solved in step 1 and an a-priori 'reference' surface are minimized.

Crossover minimization poses a singular problem. For instance a bias present in the radial orbit error does not reveal in the crossover differences. Later it will be shown that the 'bias' singularity belongs to a so-called null space of the normal equations formed by crossover minimization. It will also be shown that, depending on the choice of the adjustment model, other null space components show up. One might for instance obtain a tilt of the entire altimetric surface without affecting the crossover differences. In short: there exist transformations of the unknowns (which are the coefficients of so-called error functions over short arc segments solved by the adjustment of crossover differences) having the property not to affect the crossover differences. These transformations are called, in analogy to the adjustment of terrestrial geodetic networks, singularity transformations, compare (Teunissen,1985).

This leads to the second step which is the minimization of the altimetric surface to an a-priori reference surface. Here we carry out the transformation such that its degrees of freedom fall inside the null space of the crossover minimization problem.

In reality the reference surface is formed by e.g. an a-priori geoid model or, as is suggested in (Sandwell, Milbert and Douglas,1986), a few bench marks in the form of radar transponders.

As mentioned before, the two stage process of adjustment of altimeter data is demonstrated for a local region in the North-east Atlantic. Firstly it is described how we define the observations, the parameters (unknowns) to be estimated and their mutual relation: the observation model. The observation model consists of observation equations and an a-priori covariance matrix of the observations which are both used in a least squares adjustment (LSA). Due to the inherent singularity of the system of normal equations we split the solution in two groups: a homogeneous and a particular part. The general solution of the problem is found by combining both parts. As a consequence there is no unique solution of the problem. However it will be shown that there exists a set of possible solutions which *all* fulfill the minimization problem on which the LSA of crossover differences is based.

Also the covariance matrix of the estimated unknowns has to be considered when performing a LSA of crossover differences. This problem is far from a simple one since certain undesired effects are introduced by the homogeneous part of the 'general' solution of the crossover minimization problem. In order to eliminate these effects we arrive at the transformations of the covariance matrix of the unknowns which are known as the S-transformations; compare (Baarda,1973). The latter is essential when the quality of the estimated unknowns is considered.

3.2 The observation model

In this paragraph we introduce the observation model for adjusting altimeter data. Firstly some definitions are clarified.

3.2.1 Definitions

The nominal orbit

For the nominal orbit we assume a near circular trajectory from which the altimeter measures in the nadir viewed from the position of the spacecraft. This nominal orbit is only used for describing an approximate ground track. We remark that the footprint of the altimeter varies in the order of 2.4 to 12 km diameter (according to the SEASAT specifications) depending on the sea state. As a result the nominal orbit has to be accurate to some 10 km in cross – and along track direction. (Cross – and along track refer respectively to in the direction perpendicular to the orbital plane and perpendicular to the radial direction.)

The circular motion is described by a Kepler ellipse including the secular precession of the elements Ω, ω and M. Without these precession terms the model would not suffice. Consider for instance the orbit of SEASAT where Ω drifts at a rate of $\approx 2^\circ$ per day, which is equivalent to a longitude shift of the equator transit point of approximately 200 km.

A second assumption in the definition of the nominal orbit concerns the coordinate systems being used. Normally, the equations of motion are formulated in an inertial coordinate system. For ground track representation a transformation is performed into an Earth fixed coordinate system. For this purpose we assume the z-axes of the inertial and Earth fixed coordinate system to coincide. Furthermore we consider the Earth rotation rate ($\dot{\theta}$) as constant for the definition of the nominal orbit. As a result we find a description of the nominal orbit, as given in figure 3.1, by the parameters $\omega_e = \Omega - \theta$, $\omega_o = \omega + M$, I and r. (the subscript "o" refers to orbit, the subscript "e" refers to Earth)

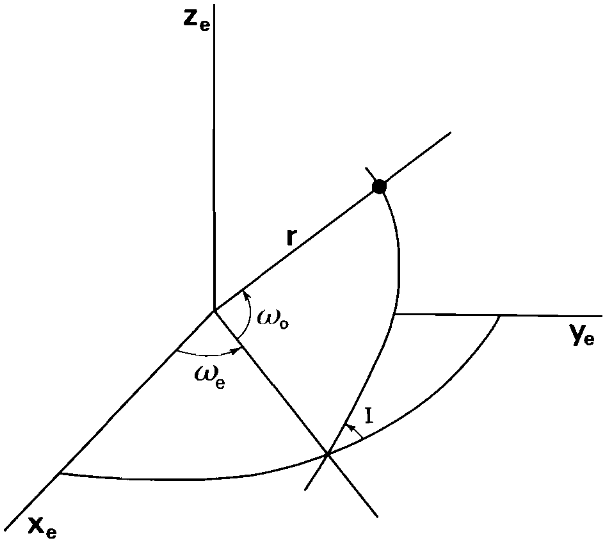

Figure 3.1: The nominal orbit in an Earth fixed coordinate system

Arc segments and crossovers

It is easy to verify that the satellite never exceeds the extreme latitudes compatible with the inclination of the orbital plane. In case of SEASAT the inclination equals to 108° which causes the ground track not to exceed above +72° or below −72° latitude. The path of the sub-satellite point over the Earth's surface from one extreme latitude to the other is defined as an *arc segment*. Each full revolution of the satellite contains two arc segments, an ascending one going from the southern hemisphere to the northern and a descending segment in which the satellite moves in the opposite direction. The situation is illustrated in figure 3.2. In the nominal orbit crossovers can only occur where an ascending arc segment intersects with a descending. This is an important property which is used in the analytical prediction of the crossover time tags and their geographical locations. This typical behavior indicates the topology of the crossover minimization problem. Later on, when certain parameters are estimated per individual arc segment, it will be shown that the crossover topology causes the normal matrix to be subdivided in two parts. In an ideal case (where all possible crossovers actually occur), one can show that this structure may be reduced to a circular Toeplitz form of the normal matrix, compare (Rummel,1985). It is mentioned that this structure can be solved in a very efficient

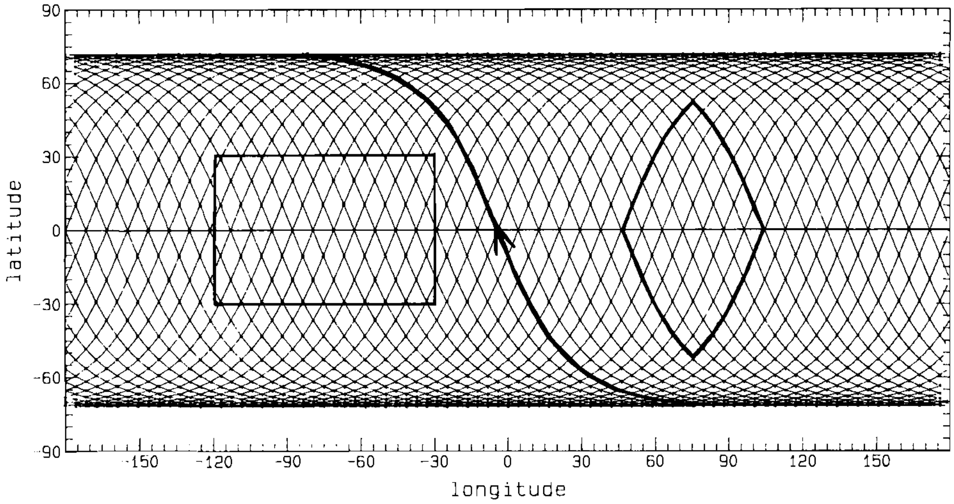

Figure 3.2: Ground tracks and arc segments on the Earth's surface

manner by application of fast Fourier transformations (FFT) which are described by Cooley & Tukey (1965) and Singleton (1969).

In reality, where crossovers are missing because they are located on land, a Toeplitz structure is not found. For this reason the normal equations are solved in two parts, known as partitioning. This technique allows a considerable reduction of computing effort when solving the normal equations. However, it does not prevent that the resulting system to solve (e.g. by Choleski decomposition or any other method) is nearly full.

Definition of local areas

A straightforward method for defining a local region would be to adopt boundaries for the geographical latitude ϕ and longitude λ, as is illustrated in figure 3.2. Here such an area definition is inconvenient since the length of arc segments inside the region varies from short ones in the corners to approximately equal length in the center. Later on in this chapter it is demonstrated that this particular phenomenon may result in numerical problems in the LSA of crossover differences. Short arc segments are not compatible with long ones when the same amount and type of parameters is estimated. A remedy for this problem may be a down-weighting of observations belonging to short arc segments. However here it was chosen to apply segments of approximately the same length in time. For this reason we define for local adjustments a so-called diamond shaped area. Instead of bounding the ϕ and λ values we select a certain set of arc segments with equator transit longitudes located between two arbitrarily chosen values. This is done separately for as well the ascending as descending arc segments, compare figure 3.2.

3.2.2 The crossover differences

A practical problem was to actually derive the crossover differences and positions from the GDR data. It is a procedure consisting of three steps: the first step is the creation of an arc segment catalog, the second step is the analytical prediction of crossover locations and timings and the third step is the numerical improvement of this data.

The arc segment catalog

Crossover computation requires an arc segment catalog which is derived from the GDR data. The catalog contains as many records as there are arc segments each describing the characteristic data belonging to an individual entry. A catalog record describes at the beginning, the equator transit and at the end of each segment the geographical location and GDR time respectively. The arc segment catalog itself is ***essential*** for the construction of crossover data since it defines the topology of arc segments and crossovers. Moreover it contains the valuable equator transit data which is required for the analytical prediction.

Analytical prediction

It is possible to predict the approximate crossover locations and timings by application of the properties of a nominal orbit. In the sequel this procedure is known as an analytical prediction of crossovers. The analytical prediction (described in chapter 5) turns out to be accurate to approximately 1.5 s which is rather large for interpolating the GDR data from tape.

Numerical improvement

In a second step the GDR altimeter data on tape is evaluated at the analytically predicted times. This procedure enables an iterative improvement by using the improved crossovers as new predictions until some threshold is fulfilled. More details about the method of crossover computation are given in chapter 5.

The resulting crossover dataset

For the diamond shaped area in the North-east Atlantic we used the first 1350 arc segments of SEASAT altimeter data. Eventually it results in 9098 applicable crossover differences formed out of 127 descending and 101 ascending arc segments.

3.2.3 Relating observations to parameters

In order to minimize the crossover differences we attempt to estimate the parameters of a radial error function defined along an arc segment. The radial error function is denoted $\Delta r(t)$ with t relative to an arbitrarily chosen reference time defined within an arc segment. A convenient choice could be the equator transit time of the arc segment, or the actual beginning at a boundary of the diamond shaped area.

The radial orbit error is often modelled by so-called tilt and bias functions taking the form of $\Delta r(t) = a_0 + b_0(t - t_0)$ with respectively a_0 the bias, b_0 the tilt and t_0 the reference time of the error function. An error function of this type may be applied up to a certain length in time. Above this maximum the deviations of Δr from the actual orbit error become too large introducing unrealistic high crossover differences after the LSA. The behavior of several error functions will be investigated in chapter 6.

In addition to the truncation behavior of Δr, there exists a problem of overparameterization of, usually short, arc segments. Too many parameters in Δr allow the removal of virtually all the crossover difference signal even if it is caused by short periodic effects other than the long periodic radial orbit errors.

Moreover, the superfluous parameters tend to be poorly estimable. This effect showed up in our first attempts where the technique had been applied for rectangular shaped areas. The mentioned problematic corner segments were solved for tilt and bias resulting in an artificial singularity, although the actual problem constrained with the minimal amount of master arc segments should behave regular.

Later on it will be demonstrated that it is more realistic to solve for Fourier error functions for longer arc segments. This approach is followed in chapters 6 and 7 where global altimetric surfaces are constructed by means of least squares crossover minimization. In this chapter we restrict ourselves to the local approach with observation equations taking the form of:

$$\Delta h_{ij} = \Delta r_i(t_{ij}) - \Delta r_j(t_{ji}) \tag{3.1}$$

where Δh_{ij} represents the crossover difference of arc segments i and j related to the error functions Δr_i and Δr_j. The error functions are evaluated at the times t_{ij} and t_{ji} both defined inside the arc segments. The notation is as follows: t_{ij} is the intersection time inside arc segment i with arc segment j.

Along track influences and time tagging problems

In the observation equation for crossover differences *no* correction is assumed for the differences between the internal satellite time and the ground based tracking network time. According to the GDR handbook (Lorell et al.,1980) two corrections are applied to the time tags of the altimeter observations. Due to the instrumental delay and signal propagation effects a correction of −0.0794 s appeared necessary. Furthermore, there is a variable correction for the time difference between the signal reflection on the sea surface and the receipt of the signal on board the spacecraft.

If there would be no vertical velocity component of the satellite above the sea surface then it would hardly matter whether the measured distances match with the computed positions of the satellite. However, for three reasons there exists a vertical velocity $\dot{h}^*$ and acceleration $\ddot{h}^*$ of the spacecraft above the footprint area. They are caused by a moderate eccentricity effect in the orbit, J_2 periodic perturbations and flattening of the Earth's surface.

As a result, the vertical velocity is in the order of 10 m/s as is stated in (Marsh et al.,1982a). The −79.4 ms clock error results in a radial error effect of $10 \times 79.4 \times 10^{-3}$ m $\approx$ 80 cm since the satellite position is computed at 'the wrong time'. The clock offset problem can be filtered out of the altimeter data by using the property that the ascending and descending dh^*/dt differ considerably and behave in a well predictable way at a crossover location. (compare the lemniscate function shown in (Marsh et al.,ibid)).

In the case of SEASAT a correction for the timing bias has been computed from the crossover differences, compare (Marsh et al.,ibid). After correction the estimated accuracy of the time tags is of the order of 3 ms r.m.s. as stated by Marsh et al. (ibid).

3.3 A solution for the problem

In this paragraph we introduce the least squares minimization problem for crossover differences. Ideally a regular system of normal equations would have to be solved. However, one can easily show that the system of normal equations is singular. This leads to a separation of the solution of the minimization problem into particular and homogeneous part.

3.3.1 Least squares minimization of crossover differences

In order to solve a system of observation equations as given by (3.1) we consider a Gauss-Markoff model in the form of $\vec{y} = A\vec{x} + \vec{\epsilon}$ with $\vec{y}$ representing the stochastic observables gathered in a vector of dimension n and $\vec{x}$ a vector of parameters (or unknowns) of dimension m. The matrix A of m columns and n rows is known as the design matrix whereas $\vec{\epsilon}$ represents the vector of residuals of dimension n.

Additionally we consider a symmetric positive definite matrix Q_{yy} containing on the main diagonal the a-priori variance of each observable and off the diagonal the covariance of one observation to another. As the problem is given here there are approximately $m = \alpha p$ unknowns to be estimated where α equals to the amount of parameters per arc segment and p the number of segments. Furthermore there are, as explained before, approximately $(\frac{1}{2}p)^2$ observations in the form of crossover differences. Accordingly, the observation equations result in an over-determined system of linear equations for $p > 2\alpha$.

According to e.g. Lanczos (1964) and Teunissen (1985) one may consider the design matrix A as a linear operator from the parameter space $\mathcal{M}$ to the observation space $\mathcal{N}$. In order to find a unique solution for the inverse problem we pose a least squares minimum norm for the residual vector $\vec{\epsilon}$, taking the form of $\vec{\epsilon}^t Q_{yy}^{-1} \vec{\epsilon} = \min$. It is easy to show that the least squares minimum is obtained by:

$$(A^t Q_{yy}^{-1} A)\hat{x} = A^t Q_{yy}^{-1} \vec{y} \tag{3.2}$$

which are the normal equations. A more convenient notation is $N\hat{x} = \vec{r}$ where N is called the normal matrix, $\hat{x}$ the vector of parameters estimated in the least squares sense, whereas $\vec{r}$ forms the right hand side (RHS) of the system.

Properties of the normal matrix

Theorem 3.1 *The normal matrix is symmetric and positive provided that Q_{yy} is symmetric and positive definite.*

Proof: The symmetric and positive definite covariance matrix Q_{yy} may, according to Lanczos (ibid), be decomposed in:

$$Q_{yy} = R\Lambda R^t \;\Rightarrow\; Q_{yy}^{-1} = R\Lambda^{-1}R^t$$

where R represents an orthogonal matrix (inverse equals to transposed form) and Λ a diagonal matrix containing the eigenvalues of Q_{yy}. An expansion of Q_{yy} into N gives:

$$N = A^tR\Lambda^{-1}R^tA = B^t\Lambda^{-1}B = C^tC$$

The eigenvalues in Λ are always real and greater than zero due to the fact that Q_{yy} is symmetric positive definite. Any element N_{ij} of N is always formed by an inner product of the column vectors of C denoted respectively as C_i and C_j. Due to the commutative property of the inner product we find $N_{ij} = (C_i, C_j) = (C_j, C_i) = N_{ji}$.

One can also show that the normal matrix is positive. A positive matrix N dimensioned $m \times m$ fulfills the condition that $\vec{x}^tN\vec{x} \geq 0 \;\forall \vec{x} \in \mathcal{R}^m \,|\, \vec{x} \neq \vec{0}$. Here $N = C^tC$ with C dimensioned $n \times m$. Hence N is positive when $\vec{x}^tC^tC\vec{x} \geq 0$ $\forall \vec{x} \in \mathcal{R}^m \,|\, \vec{x} \neq \vec{0}$. This is equivalent to $\vec{b}^t\vec{b} \geq 0 \;\forall \vec{b} \in \mathcal{R}^m$. Note that $\vec{b} = \vec{0}$ exists since it is allowed that $C\vec{x} = \vec{0} \,|\, \vec{x} \neq \vec{0}$. It is trivial that $\vec{b}^t\vec{b} = (\vec{b}, \vec{b}) \geq 0 \;\forall \vec{b} \in \mathcal{R}^m$.
□

Now it is shown that N is symmetric and positive we can follow Lanzcos' (ibid) approach where the properties of self-adjoint systems of equations are described.

3.3.2 Singularity of the LSA

For the problem at hand one can show that there exists a linear dependency between the column vectors of the design matrix. The cause of this linear dependency shall be explained later on. Here we mention that there exists a rectangular matrix E of m rows and l linear independent columns such that $AE = 0$. The result is that a null space $\mathcal{L}$ of N is described. The basis of the null space is formed by the column vectors of the E matrix, the dimension of the null space is l. Apparently there exists a vector $\vec{z} \in \mathcal{L}$ such that

$$A\vec{z} = \vec{0} \;\Rightarrow\; A^tQ_{yy}^{-1}A\vec{z} = \vec{0} \;\Rightarrow\; N\vec{z} = \vec{0} \tag{3.3}$$

where $\vec{z} = E\vec{s}$. The vector $\vec{s}$ is denoted as a shift vector, it forms the linear combinations of the columns of E describing the vectors $\vec{z}$ all lying in the null space $\mathcal{L}$. The nature of the E matrix depends for crossover minimization problems on several assumptions related to the observation equations (3.1).

3.3.3 Treatment of the normal equations

We conclude that:

- There exist normal equations in the form of $N\hat{x} = \vec{r}$. The matrix N (dimension $m \times m$) is a symmetric matrix with positive properties. This means that N possesses real eigenvalues all greater than or equal to zero.

- There exists a set of vectors $\vec{z}$ such that $N\vec{z} = \vec{0}$. Besides, it is known that $\vec{z}$ may be written in the form $\vec{z} = E\vec{s}$ where E is a matrix of m rows and l linear independent columns describing a so-called null space $\mathcal{L}$ of N. The vector $\vec{s}$ is called a shift vector having the dimension l.

Here we pose the question: does there exist a solution for the system of normal equations despite the fact it is singular? If this solution exists then we must also prove under which conditions it is unique. Hence we consider the eigenvalue problem

$$N\vec{u}_i = \lambda_i \vec{u}_i \tag{3.4}$$

where $\vec{u}_i$ are the eigenvectors and λ_i the eigenvalues of N. This form is now rewritten in the matrix product:

$$NU = U\Lambda \tag{3.5}$$

where the columns of U contain the eigenvectors whereas Λ takes the form of a diagonal matrix of eigenvalues. We substitute (3.5) in the normal equations $N\vec{x} = \vec{r}$ (for simplicity we use a vector notation for $\hat{x}$) and find:

$$U\Lambda U^t\vec{x} = \vec{r} \Leftrightarrow \Lambda U^t\vec{x} = U^t\vec{r} \Leftrightarrow \Lambda\vec{x}' = \vec{r}' \tag{3.6}$$

where $\vec{x}' = U^t\vec{x}$ and $\vec{r}' = U^t\vec{r}$. We know there exist $m - l$ non-zero eigenvalues and l zero eigenvalues forming the system:

$$\begin{pmatrix} \lambda_1 & & & & & \\ & \ddots & & & & \\ & & \lambda_{m-l} & & & \\ & & & 0 & & \\ & & & & \ddots & \\ & & & & & 0 \end{pmatrix} \begin{pmatrix} x'_1 \\ \vdots \\ \vdots \\ \vdots \\ \vdots \\ x'_m \end{pmatrix} = \begin{pmatrix} r'_1 \\ \vdots \\ \vdots \\ \vdots \\ \vdots \\ r'_m \end{pmatrix} \tag{3.7}$$

A solution is feasible if:

$$\lambda_i x'_i = r'_i \begin{cases} i \in [1, m-l] & \Rightarrow x'_i = \lambda_i^{-1} r'_i \\ i \in [m-l+1, m] & \Rightarrow r'_i = 0 \end{cases} \tag{3.8}$$

In case $i \in [1, m-l]$ a so-called particular solution is found. In the sequel we denote this solution as $\vec{x}_p$. In the other case we *must* demand that r'_i equals to zero. The latter has the consequence that, according to (3.6):

$$U_i^t \vec{r} = \vec{0}, \tag{3.9}$$

where U_i^t, $i \in [m-l+1, m]$ represents a sub-matrix of U^t with rows being the eigenvectors belonging to the zero eigenvalues of N spanning the null-space. Eq. (3.9) forms the so-called compatibility conditions which, as a direct consequence of (3.8), *must* be fulfilled. A geometrical interpretation of (3.9) is that the RHS vector $\vec{r}$ is orthogonal to each eigenvector $\vec{u}_i$, $i \in [m-l+1, m]$ of the null-space of N. Hence we consider:

$$N\vec{u}_i = \vec{0} \;\; \forall i \in [m-l+1, m] \tag{3.10}$$

which may be conveyed into

$$N\vec{z} = \vec{0} \tag{3.11}$$

where $\vec{z}$ is a linear combination of the eigenvectors $\vec{u}_i \in \mathcal{L}$,

$$\vec{z} = \sum_{i=m-l+1}^{m} \alpha_i \vec{u}_i = E\vec{s} \tag{3.12}$$

for arbitrarily chosen scalars α_i. In the sequel $\vec{z}$ fulfilling (3.11) is called a homogeneous solution of the normal equations. A substitution of $\vec{z}$ in (3.9) shows directly that the homogeneous solution $\vec{z}$ must be ***orthogonal*** to the RHS vector $\vec{r}$ of the normal equations. Lanczos (ibid) mentions that this is a necessary and sufficient condition for the solvability of a self-adjoint linear system with vanishing eigenvalues. We verify the latter for our case and find that:

$$\vec{z} = E\vec{s} \wedge \vec{r} = A^t Q_{yy}^{-1} \vec{y} \Rightarrow \vec{r}^t \vec{z} = (\vec{y}^t Q_{yy}^{-1} A)(E\vec{s}) = 0. \tag{3.13}$$

(note that $AE = 0$). As a consequence, for the problem at hand, the compatibility conditions are *always* fulfilled. The general solution $\vec{x}_g$ of a compatible self-adjoint system is obtained by adding to an arbitrary particular solution $\vec{x}_p$ an arbitrary solution of the homogeneous equation $N\vec{z} = \vec{0}$. The general solution $\vec{x}_g$ of the system takes the following form:

$$\vec{x}_g = \vec{x}_p + \vec{z} = \vec{x}_p + E\vec{s}. \tag{3.14}$$

3.3.4 Structure of the E–matrix

The structure and dimension of the E matrix is directly related to the observation equations used in the adjustment of the crossover differences. The E matrix is dimensioned as m rows by l columns and contains linear independent column vectors all lying in the null space of the normal matrix. The number of rows is identical to the number of unknowns of the problem. The number of columns is equivalent to the dimension of the null space of the problem.

The structure of the observation equation given in (3.1) indicates that a crossover difference Δh_{ij} is modeled by the difference of 2 error functions $\Delta r_i(t_{ij})$ and $\Delta r_j(t_{ji})$ which belong to arc segments "i" and "j". It was mentioned that Δr is chosen as a linear function with respect to time defined inside an arc segment, e.g. $\Delta r_i(t_{ij}) = a_i + b_i t_{ij}$. The terms a_i and b_i represent unknowns and are kept in the vector $\hat{x}$, compare (3.2). The rows in the design matrix A formed by the observation equations contain in the columns belonging to a_i a 1 and to b_i the value of t_{ij}.

A problem in the derivation of the E matrix from the A matrix constructed by means of these observation equations is the distribution of the times t_{ij} and t_{ji} in the crossover file. Hence in order to derive a proper formulation of the E matrix more insight is required in the actual distribution of the crossover timings t_{ij} and t_{ji}. This problem is discussed in more detail in chapter 5. It will be shown for an idealized circular satellite motion that:

- The values of t_{ij} and t_{ji} behave antisymmetric ($t_{ij} = -t_{ji}$) when they are considered relative to the equator transit time.

- The value of t_{ij} and the latitude ϕ are uniquely determined by the longitude *difference* $\Delta\lambda$ of the ascending and descending equator transit point. As a result the crossover configuration behaves invariant with respect to rotation about the z axis of the Earth fixed coordinate system.

Crossover timings as they are on the true ground track intersections resemble closely this pattern, deviations are caused by various perturbations of the satellite motion. The range of the value of t_{ij} is, in case of circular orbits at 800 km height, in between approximately -1500 and +1500 sec. The deviations from the nominal crossover pattern are of the order of 0.1 to 0.2% with respect to the value of t_{ij}.

A normal matrix N derived from the actual (unmodified) crossover times t_{ij} possesses a peculiar eigenvalue spectrum. The spectrum resembles that of a poorly conditioned system of equations with corresponding eigenvalues ranging from 10^{-15} to 10^{+10}. As a result the condition number $(\lambda_{max}/\lambda_{min})$, representing a measure for the numerical stability of the system, is of the order of 10^{25}. In an ideal situation the condition number should lie in the range from 1 to 10^3. According to Conte & de Boor (1986) one could pose that approximately $\log(\lambda_{max}/\lambda_{min})$ digits are lost when computing unknowns from a system of equations having extreme eigenvalues of λ_{min} and λ_{max}. The floating point arithmetic of the computer employed (a VAX 750 using FORTRAN double precision variables) is consistent to approximately 16 significant digits (which refers to the mantissa). The exponential range of these floating point variables is limited from 10^{-38} to 10^{+38}.

The only cause of the poor condition number can be the observation equations themselves, the values of t_{ij} and t_{ji} are considerably larger than 1, i.e. the 'bias' coefficient in the design matrix. This effect is artificial and can easily be avoided by a re-parameterization of the observation equations. The observation equations become instead $\Delta r_i(t^*_{ij}) = a_i + b^*_i t^*_{ij}$ with $b^*_i = \alpha b_i$ and $t^*_{ij} = t_{ij}/\alpha$. The factor α is referred to as a regularization factor. A suitable value might be the actual length of an arc segment.

The normal matrix N, found after regularization of the observation equations, shows an eigenvalue spectrum having the following properties:

- 1 eigenvalue is of the order of 10^{-16} to 10^{-15},
- 3 eigenvalues are of the order of 10^{-6} to 10^{-5},
- for other eigenvalues it is found that $1 \leq \lambda \leq 10^3$.

These values are *approximations* and depend e.g. on the amount of arc segments involved in a crossover adjustment. The 'singular' eigenvalue in the range of 10^{-16} to 10^{-15} is a direct consequence of the bias singularity in the normal equations. It is allowed to add an arbitrary constant to all a_i parameters in the observation equations *without* affecting the crossover residuals.

The remaining subsystem without the bias singularity is still poorly conditioned and results in unstable estimates of the tilt and bias parameters. Cause of the poor conditioning are the three eigenvalues in the range of 10^{-6} to 10^{-5}. In the sequel we pose the problem to arrive at a self-adjoint compatible system of normal equations having an acceptable eigenvalue spectrum:

- A number of eigenvalues are allowed to be equal to zero, the eigenvectors belonging to these eigenvalues should be known.
- The remaining subsystem, with eigenvalues $\lambda > 0$, should have an acceptable condition number.

In the situation considered here this is possible by a conversion of the actual crossover timings t_{ij} and t_{ji} into approximated model times.

Conversion of crossover timings

In the local diamond shaped region it was recognized that crossover timings coming from SEASAT behave nearly as linear congruent. The situation is illustrated in figure 3.3. The diamond shaped region is bounded by the ascending segments "1" and "2" and the descending segments "3" and "4". It is assumed that all other segments intersect the boundary in the following way:

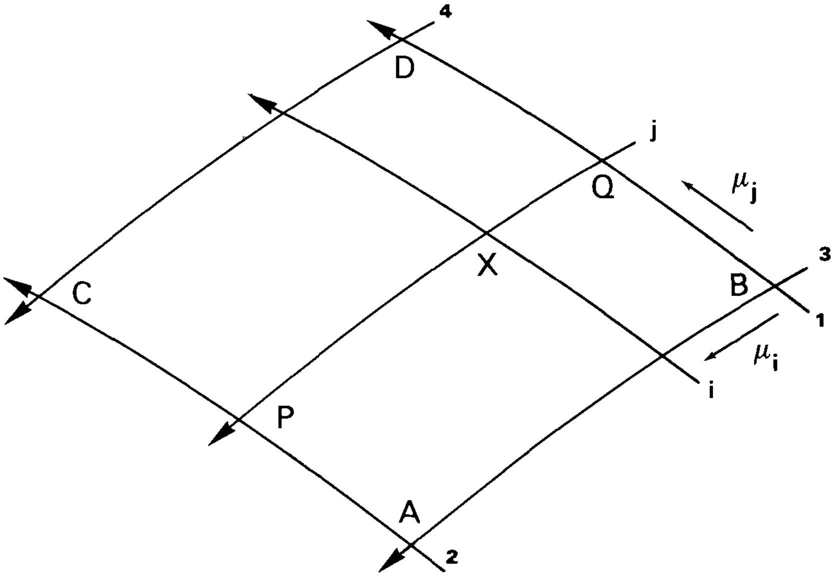

Figure 3.3: Linear congruent behavior of crossover timings in a local area.

- Ascending arc segments form an intersection firstly with segment "3" in between points A and B and secondly with "4" in between C and D.
- Descending arc segments form an intersection firstly with "1" in between B and D and secondly with "2" in between A and C.

This is illustrated for segment "j" forming a crossover Q with segment "1" followed by P with "2". The intersection time t_{1j} at crossover Q is transformed to a dimensionless quantity μ_{1j} by $\mu_{1j} = (t_{1j} - t_{13})/(t_{14} - t_{13})$. Note that the values of t_{13} and t_{14} at the crossovers A B C and D are defined by the choice of the boundary.

Analogously to μ_{1j} a dimensionless parameter μ_{2j} is defined where arc segment "2" intersects "j", accordingly $\mu_{2j} = (t_{2j} - t_{23})/(t_{24} - t_{23})$. Analysis of all arc segments involved in the regional crossover file reveals that the parameters μ_{1j} and μ_{2j} differ approximately 1 to 2%. In the sequel the average of μ_{1j} and μ_{2j} is assumed to represent a characteristic parameter μ_j for arc segment j.

More important is the reconstruction of the crossover times by means of the parameters μ_i and μ_j. This is illustrated in figure 3.3 with an ascending arc segment "i" with its corresponding parameter μ_i intersecting "j" at crossover X. The actual crossover timings t_{ij} and t_{ji} at the crossover X turn out to be equal to:

$$t_{ji} \approx \mu_i(t_{j2} - t_{j1}) + t_{j1} \quad \text{and} \quad t_{ij} \approx \mu_j(t_{i4} - t_{i3}) + t_{i3} \tag{3.15}$$

The accuracy of this approximation is also of the order of 1 to 2% with respect to the length in time of an arc segment. Substitution of (3.15) in the observation equation belonging to the crossover difference X formed by the arc segment "j" and "i" results in:

$$\Delta h_{ij} = \Delta r_i(\mu_j) - \Delta r_j(\mu_i). \tag{3.16}$$

For linear functions Δr_i and Δr_j we find:

$$\Delta h_{ij} = (a_i + b_i\mu_j) - (a_j + b_j\mu_i) \tag{3.17}$$

in which a and b represent the model bias and tilt parameter respectively. Observation equations of this type are convenient for investigating the structure of the E matrix. Consider for instance the structure of the design matrix of a crossover adjustment where 3 ascending and 3 descending arc segments are involved. This configuration is shown in figure 3.4. The observation vector $\vec{y}$ is arranged as:

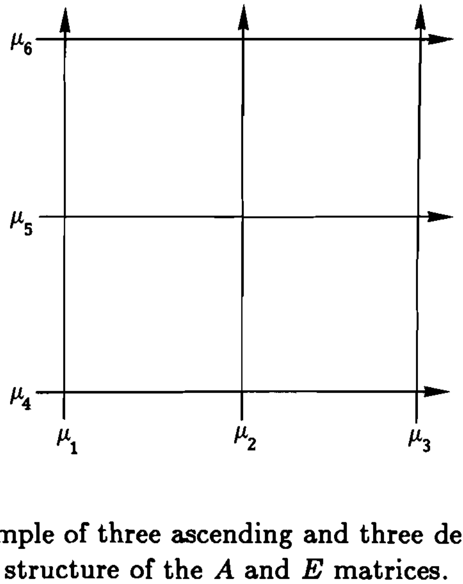

Figure 3.4: An example of three ascending and three descending arc segments used to demonstrate the structure of the A and E matrices.

$$\vec{y} = [\Delta h_{14}, \Delta h_{15}, \Delta h_{16}, \Delta h_{24}, \Delta h_{25}, \Delta h_{26}, \Delta h_{34}, \Delta h_{35}, \Delta h_{36}]^t$$

The vector of unknowns $\vec{x}$ equals to:

$$\vec{x} = [a_1, b_1, a_2, b_2, \cdots, a_6, b_6]^t$$

The corresponding structure of the design matrix A becomes:

$$A = \left[\begin{array}{cccccc|cccccc}
1 & \mu_4 & & & & & -1 & -\mu_1 & & & & \\
1 & \mu_5 & & & & & & & -1 & -\mu_1 & & \\
1 & \mu_6 & & & & & & & & & -1 & -\mu_1 \\
 & & 1 & \mu_4 & & & -1 & -\mu_2 & & & & \\
 & & 1 & \mu_5 & & & & & -1 & -\mu_2 & & \\
 & & 1 & \mu_6 & & & & & & & -1 & -\mu_2 \\
 & & & & 1 & \mu_4 & -1 & -\mu_3 & & & & \\
 & & & & 1 & \mu_5 & & & -1 & -\mu_3 & & \\
 & & & & 1 & \mu_6 & & & & & -1 & -\mu_3
\end{array}\right] \tag{3.18}$$

It is easy to recognize that the E matrix becomes:

$$E = \left[\begin{array}{cccc}
1 & \mu_1 & 0 & 0 \\
0 & 0 & 1 & \mu_1 \\
1 & \mu_2 & 0 & 0 \\
0 & 0 & 1 & \mu_2 \\
1 & \mu_3 & 0 & 0 \\
0 & 0 & 1 & \mu_3 \\
\hline
1 & 0 & \mu_4 & 0 \\
0 & 1 & 0 & \mu_4 \\
1 & 0 & \mu_5 & 0 \\
0 & 1 & 0 & \mu_5 \\
1 & 0 & \mu_6 & 0 \\
0 & 1 & 0 & \mu_6
\end{array}\right] \tag{3.19}$$

Accordingly the rank defect of the normal equations derived from observation equations of the form of (3.17) equals to 4. This was verified by means of an eigenvalue analysis of the normal equations showing that 4 eigenvalues become close to zero (10^{-16} to 10^{-15}) while the remaining eigenvalues are in the range of 1 to 10^3.

3.3.5 Implementation

In this section the implementation of the theory presented in the previous subsections will be discussed. Firstly a particular solution $\vec{x}_p$ for the crossover minimization problem is derived. Additionally we relate this problem to the choice of master arc segments. Secondly the transformation from one particular solution to another by application of (3.14) is treated. It is customary to denote this as a singularity transformation. Thirdly it will be shown that there exists a unique solution which adapts the altimetric surface in an optimal sense to a reference field. The latter is identical with finding a suitable shift vector $\vec{s}$ in (3.14) for a particular solution $\vec{x}_p$ such that a selected criterion is fulfilled for $\vec{x}_g$.

Partitioning

As mentioned earlier, the structure of the normal equations allows a partitioning of the normal equations in two groups: an ascending and a descending part. This is possible since crossover observations affect only those columns in the design matrix which belong to both partitions, compare (3.18). Inside each partition inner products between columns of A result in blocks of α times α on the diagonal of the normal matrix. Here α equals to the number of parameters to be solved per arc segment. The structure of these sub-matrices is called block-diagonal. In contrary the mixed matrix showing up between both partitions is mostly full since nearly every arc segment in one group is connected with every member of the other group. The non-zero structure of the normal matrix is represented in figure 3.5. The corresponding normal equations take the form:

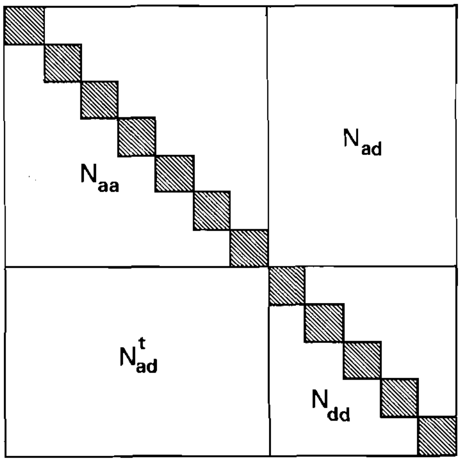

Figure 3.5: The non-zero structure of the normal matrix. The matrices N_{aa} and N_{dd} are block diagonal whereas N_{ad} is nearly full.

$$\begin{array}{rcl} N_{aa}\vec{x}_a + N_{ad}\vec{x}_d & = & \vec{r}_a \\ N_{ad}^t\vec{x}_a + N_{dd}\vec{x}_d & = & \vec{r}_d \end{array} \tag{3.20}$$

where N_{aa} and N_{dd} are block diagonal whereas N_{ad} equals to an almost full matrix. Pre-multiplication of the first equation by $N_{ad}^tN_{aa}^{-1}$ and subtraction of the second results in a solution for the descending unknowns:

$$(N_{ad}^tN_{aa}^{-1}N_{ad} - N_{dd})\vec{x}_d = N_{ad}^tN_{aa}^{-1}\vec{r}_a - \vec{r}_d. \tag{3.21}$$

Pre-multiplication of the second equation by $N_{ad}N_{dd}^{-1}$ and subtraction of the former results in a solution for the ascending unknowns:

$$(N_{ad}N_{dd}^{-1}N_{ad}^t - N_{aa})\vec{x}_a = N_{ad}N_{dd}^{-1}\vec{r}_d - \vec{r}_a. \tag{3.22}$$

Both (3.21) and (3.22) are a solution of (3.20). The inverses of N_{aa} and N_{dd} take no effort since they are block diagonal. Also the computation of the matrix on the LHS and the vector on the RHS of (3.21) and (3.22) are no more than matrix multiplications. Moreover only the smallest system of (3.21) and (3.22) needs to be solved, the other one is found by a substitution in (3.20) followed by an inversion of a block diagonal matrix. Computations in the test area revealed that solving (3.20) by (3.21) and/or (3.22) saves approximately up to a factor 8 in computing time when compared with an inversion of the full normal matrix in an unpartitioned way.

For some purposes it may be desirable to compute the inverse of the normal matrix which is called Q. (The letter Q is chosen for Quality, inverses of the normal matrix are the a-posteriori covariance matrices of the estimated unknowns as will be shown later on in this chapter). The inverse of N is derived from the matrix product:

$$\left[\begin{array}{c|c} N_{aa} & N_{ad} \\ \hline N_{ad}^t & N_{dd} \end{array}\right] \left[\begin{array}{c|c} Q_{aa} & Q_{ad} \\ \hline Q_{ad}^t & Q_{dd} \end{array}\right] = \left[\begin{array}{c|c} I & 0 \\ \hline 0 & I \end{array}\right] \tag{3.23}$$

and takes the form

$$\begin{array}{rcl} Q_{aa} & = & -\left[N_{ad}N_{dd}^{-1}N_{ad}^t - N_{aa}\right]^{-1} \\ Q_{dd} & = & -\left[N_{ad}^tN_{aa}^{-1}N_{ad} - N_{dd}\right]^{-1} \\ Q_{ad} & = & -Q_{aa}N_{ad}N_{dd}^{-1} \\ Q_{ad}^t & = & -Q_{dd}N_{ad}^tN_{aa}^{-1} \end{array} \tag{3.24}$$

A particular solution

In order to find a particular solution for the crossover minimization problem we solve the system of normal equations such that a number of so-called master arc segments remain fixed. It means that *certain* arc segments are not solved in the adjustment. However, the observations to these segments are still used for the construction of the normal equations. In the algorithm it is accomplished by pivoting the unknowns belonging to the master arc segments to the first rows and columns of the normal matrix. The decomposition or reduction algorithm is applied on the remaining subsystem.

As a result one finds the estimated parameters on the basis of a set of master arc segments. In analogy to terrestrial geodetic networks it is customary to call the minimal number of master arc segments that are required to regularize the normal equations a datum.

A regular datum shift

The particular solution found by this approach depends on the choice of the master arc segments. Such an approach is undesirable since it results in an arbitrary particular solution of the crossover minimization problem. A realistic solution of the altimetric surface is only found when it is assured that the error contribution of the master arc segment(s) is low or known in some way, compare Rapp (1983). The transformation of one particular solution into another would in principle require that a new system of normal equations has to be solved. However this can be avoided since it is nothing more than adding a suitable homogeneous part $\vec{x}$ to $\vec{x}_p$ such that $\vec{x}_{p(new)}$ becomes the new solution fulfilling the alternative particular condition. Accordingly:

$$\vec{z} = \vec{x}_{p(new)} - \vec{x}_{p(old)}. \tag{3.25}$$

Usually it is easy to derive $\vec{z}$ for an actual problem. It is convenient to use the property that $\vec{x}_{p(new)}$ contains zeros at the positions of the new estimates of the master arc segment parameters. Hence one finds a form which is essentially an evaluation of (3.25) for the unknowns belonging to the *new* master arc segments i, j. We demonstrate the singularity transform where observation equations in the form of (3.17) are applied. In case the solution is transformed to two ascending master arc segments then:

$$\begin{bmatrix} 0 \\ 0 \\ 0 \\ 0 \end{bmatrix} = \begin{bmatrix} a_i \\ b_i \\ a_j \\ b_j \end{bmatrix} + \begin{bmatrix} 1 & \mu_i & 0 & 0 \\ 0 & 0 & 1 & \mu_i \\ 1 & \mu_j & 0 & 0 \\ 0 & 0 & 1 & \mu_j \end{bmatrix} \begin{bmatrix} s_1 \\ s_2 \\ s_3 \\ s_4 \end{bmatrix}. \tag{3.26}$$

In case the solution is transformed to two descending master arc segments then:

$$\begin{bmatrix} 0 \\ 0 \\ 0 \\ 0 \end{bmatrix} = \begin{bmatrix} a_i \\ b_i \\ a_j \\ b_j \end{bmatrix} + \begin{bmatrix} 1 & 0 & \mu_i & 0 \\ 0 & 1 & 0 & \mu_i \\ 1 & 0 & \mu_j & 0 \\ 0 & 1 & 0 & \mu_j \end{bmatrix} \begin{bmatrix} s_1 \\ s_2 \\ s_3 \\ s_4 \end{bmatrix}. \tag{3.27}$$

From (3.26) and (3.27) one has to solve the components of the shift vector $s_1 \cdots s_4$. The analytical datum shift technique described above has been verified for the region in the North-east Atlantic. It was demonstrated that (3.26) & (3.27) are accurate to the rounding level (10^{-15} relative) of the computer when compared with a numerical datum shift, i.e. adjustment with two other master arc segments.

A singular datum shift

There are two cases where a datum shift cannot be performed:

1. If $\mu_i = \mu_j$, i.e. a transformation to overlapping master arc segments. This is easy to verify since eqns. (3.26) and (3.27) become respectively:

$$-\begin{bmatrix} a_i \\ a_j \\ b_i \\ b_j \end{bmatrix} = E' \begin{bmatrix} s_1 \\ s_2 \\ s_3 \\ s_4 \end{bmatrix} \quad \wedge \quad -\begin{bmatrix} a_i \\ a_j \\ b_i \\ b_j \end{bmatrix} = E' \begin{bmatrix} s_1 \\ s_3 \\ s_2 \\ s_4 \end{bmatrix} \tag{3.28}$$

   where

$$E' = \begin{bmatrix} 1 & \mu_i & 0 & 0 \\ 1 & \mu_j & 0 & 0 \\ 0 & 0 & 1 & \mu_i \\ 0 & 0 & 1 & \mu_j \end{bmatrix} \tag{3.29}$$

   from which it follows that E' is singular if $\mu_i = \mu_j$.

2. If arc segments "i" and "j" are forming an intersecting ascending/descending basis. In this case (ascending "i" and descending "j")

$$-\begin{bmatrix} a_i \\ b_i \\ a_j \\ b_j \end{bmatrix} = \begin{bmatrix} 1 & \mu_i & 0 & 0 \\ 0 & 0 & 1 & \mu_i \\ 1 & 0 & \mu_j & 0 \\ 0 & 1 & 0 & \mu_j \end{bmatrix} \begin{bmatrix} s_1 \\ s_2 \\ s_3 \\ s_4 \end{bmatrix} \Rightarrow \begin{vmatrix} 1 & \mu_i & 0 & 0 \\ 0 & 0 & 1 & \mu_i \\ 1 & 0 & \mu_j & 0 \\ 0 & 1 & 0 & \mu_j \end{vmatrix} = 0. \quad (3.30)$$

The nature of the homogeneous solution

We assume that the observation equations are of the form of (3.17). They are used to define a system of normal equations as given in (3.2). Furthermore we assume that a particular solution $\vec{x}_p$ is known by choosing two non-intersecting and non-overlapping master arc segments and solving the normal equations. According to the properties of compatible self-adjoint systems one is always allowed to add an arbitrary homogeneous solution $\vec{z} = E\vec{s}$ to $\vec{x}_p$ forming a general solution $\vec{x}_g$, compare (3.14). The minimization condition posed by the crossover problem does not change by this manipulation of the particular solution $\vec{x}_p$. If this is true then it should also be possible to substitute the general solution in any arbitrary observation equation without affecting the observables. In the sequel we verify this transformation of the unknowns in the observation equations (3.17), (ascending arc segments "i", descending arc segments "j", compare figure 3.3):

$$\Delta h_{ij} = \Delta r_i(\mu_j) - \Delta r_j(\mu_i) = (a_i + b_i\mu_j) - (a_j + b_j\mu_i). \quad (3.31)$$

The general solution $\vec{x}_g = [a_i, b_i, a_j, b_j]^t$ is formed by the sum of a particular solution $\vec{x}_p = [a_i^*, b_i^*, a_j^*, b_j^*]^t$ and the homogeneous solution $E\vec{s}$. Considering the structure of the E matrix as given in (3.19) the general solution becomes:

$$\begin{bmatrix} a_i \\ b_i \\ a_j \\ b_j \end{bmatrix} = \begin{bmatrix} a_i^* \\ b_i^* \\ a_j^* \\ b_j^* \end{bmatrix} + \begin{bmatrix} 1 & \mu_i & 0 & 0 \\ 0 & 0 & 1 & \mu_i \\ 1 & 0 & \mu_j & 0 \\ 0 & 1 & 0 & \mu_j \end{bmatrix} \begin{bmatrix} s_1 \\ s_2 \\ s_3 \\ s_4 \end{bmatrix} \quad (3.32)$$

Substitution of (3.32) in $\Delta r_i(\mu_j)$ results in:

$$\begin{aligned} \Delta r_i(\mu_j) &= (a_i^* + s_1 + s_2\mu_i) + (b_i^* + s_3 + s_4\mu_i)\mu_j \\ &= \Delta r_i^*(\mu_j) + D(\mu_i, \mu_j) \end{aligned} \quad (3.33)$$

Substitution of (3.32) in $\Delta r_j(\mu_i)$ results in:

$$\begin{aligned} \Delta r_j(\mu_i) &= (a_j^* + s_1 + s_3\mu_j) + (b_j^* + s_2 + s_4\mu_j)\mu_i \\ &= \Delta r_j^*(\mu_i) + D(\mu_i, \mu_j) \end{aligned} \quad (3.34)$$

In (3.33) and (3.34) the functions $\Delta r_{i,j}^*$ depend on the particular solution $\vec{x}_p$. In both equations the term $D(\mu_i, \mu_j)$ takes the form of:

$$D(\mu_i, \mu_j) = s_1 + s_2\mu_i + s_3\mu_j + s_4\mu_i\mu_j. \quad (3.35)$$

This function depends on the components of the shift vector $\vec{s}$ in the homogeneous solution $\vec{z} = E\vec{s}$. Note that the crossover observables Δh_{ij} are *not* affected by the function $D(\mu_i, \mu_j)$ since it cancels in the difference of $\Delta r_i(\mu_j)$ and $\Delta r_j(\mu_i)$.

In the sequel we consider the function $D(\mu_i, \mu_j)$ to represent a polynomial deformation surface. This is possible since one may consider that μ_i and μ_j behave as ordinates for the location of the crossover Δh_{ij} in the diamond shaped area, compare figure 3.3. The nature of the surface polynomial $D(\mu_i, \mu_j)$ is entirely determined by the components of the shift vector $\vec{s}$. The polynomial deformation surface comprises: a bias term (s_1), an ascending tilt term (s_3), a descending tilt term (s_2), and a torsion term (s_4). Apparently one is allowed to add a surface function $D(\mu_i, \mu_j)$ to the sea surface formed by the particular solution $\vec{x}_g$ *without* affecting the crossover observables Δh_{ij}.

The nature of the homogeneous solution in a general case

The homogeneous solution of the local crossover minimization problem based on observation equations of the form of eq. (3.31) manifests as a polynomial deformation surface of the form of eq. (3.35). In a more general case the orbit error per arc segment is chosen as a polynomial of degree N. These polynomials take the form of:

$$P(\alpha) = \sum_{i=0}^{N} p_i \alpha^i \quad \wedge \quad Q(\alpha) = \sum_{i=0}^{N} q_i \alpha^i \tag{3.36}$$

which are respectively the error functions belonging to an ascending and a descending arc segment. The purpose of the crossover adjustment is always to determine the coefficients p_i and q_i in eq. (3.36). Furthermore the argument α in eq. (3.36) serves as μ_i or μ_j in eq. (3.31). The general crossover difference observation equations take the following form:

$$\Delta h(\alpha, \beta) = P(\alpha) - Q(\beta) = \sum_{i=0}^{N} p_i \alpha^i - \sum_{j=0}^{N} q_j \beta^j \tag{3.37}$$

In the following we will demonstrate the invariance of (3.37) to error functions $P(\alpha)$ and $Q(\beta)$ originating from the projection of the surface function:

$$D(\alpha, \beta) = \sum_{i=0}^{N} \sum_{j=0}^{N} d_{ij} \alpha^i \beta^j \tag{3.38}$$

on the linear congruent crossover configuration as shown in figure 3.3. The expression of (3.38) along the variable α for constant β results in an error function:

$$P(\alpha) = \sum_{i=0}^{N} p_i \alpha^i \tag{3.39}$$

with

$$p_i = \sum_{j=0}^{N} d_{ij} \beta^j. \tag{3.40}$$

Similarly the expression of (3.38) along β for constant α results in:

$$Q(\beta) = \sum_{j=0}^{N} q_j \beta^j \tag{3.41}$$

with

$$q_j = \sum_{i=0}^{N} d_{ij} \alpha^i. \tag{3.42}$$

Substitution of (3.40) and (3.42) in (3.37) results in:

$$\begin{aligned} \Delta h(\alpha,\beta) &= P(\alpha) - Q(\beta) = \sum_{i=0}^{N} p_i \alpha^i - \sum_{j=0}^{N} q_j \beta^j \\ &= \sum_{i=0}^{N} \sum_{j=0}^{N} d_{ij} \beta^j \alpha^i - \sum_{j=0}^{N} \sum_{i=0}^{N} d_{ij} \alpha^i \beta^j \\ &= 0. \end{aligned} \tag{3.43}$$

This equation shows that (3.38) projected on the linear congruent crossover configuration cannot be detected from $\Delta h(\alpha,\beta)$ denoting the crossover differences.

(Note: this reasoning might not appear 'waterproof' to the reader since it could be followed for any surface function that is projected similar to discussed above. The reader should remind that not all possible surface functions evaluated along the variables α and β result in polynomial expressions of the form of (3.39) and (3.41). For this reason (3.38) is chosen as a general polynomial deformation surface).

Hence it has been shown that there exists a polynomial deformation surface $D()$ containing $(N+1)^2$ degrees of freedom. The number of coefficients in $D()$ equals to the rank defect of the normal equations. They are determined by a datum which is any set of arc segments that defines (3.38) in a unique way. We conclude that the rank defect of the normal equations equals to $(N+1)^2$ provided that $P()$ and $Q()$ are chosen as polynomial error functions of degree N.

Connection to a reference field

In this approach we search for a unique solution $\vec{x}_g = \vec{x}_p + \vec{z}$ such that it fulfills certain properties. A possible choice is a minimal discrepancy between an arbitrary particular solution of the altimetric surface and a chosen reference geoid. Here we chose e.g. the geoid model of GEM-10B (Lerch, Wagner and Klosko,1981), or GEM-T1 (Marsh et al.,1986) or any other realistic field.

We imagine a unique solution $\vec{x}_g$ evaluated along arc segments that is subtracted from the sea surface measured by the altimeter. This forms the RHS of the observation equation, the LHS equals to the contribution of the reference field. As a result we find at the crossover Δh_{ij} for ascending arc segment "i" (Note that corrections found by LSA have to be subtracted from the observations)

$$N_{ij}^{ref} = h_{ij} - \Delta r_i(\mu_j) + \vec{\epsilon}, \tag{3.44}$$

where N_{ij}^{ref} equals to the contribution of the reference field at a crossover point between arc segment i and j located inside the diamond shaped region and h_{ij} the observed sea surface height at that point. Substitution of (3.33) in (3.44) results in:

$$h_{ij} - N_{ij}^{ref} - \Delta r_i^*(\mu_j) = D(\mu_i, \mu_j) + \vec{\epsilon}. \tag{3.45}$$

A similar situation occurs at crossover Δh_{ij} on the descending arc segment "j":

$$N_{ij}^{ref} = h_{ji} - \Delta r_j(\mu_i) + \vec{\epsilon},$$

in which we substitute (3.34) resulting in:

$$h_{ji} - N_{ij}^{ref} - \Delta r_j^*(\mu_i) = D(\mu_i, \mu_j) + \vec{\epsilon}. \tag{3.46}$$

Equations (3.45) and (3.46) form the observation equations for a so-called optimal adjustment to the reference field where the LHS symbolizes an observation and the RHS a linear relation to the unknowns: i.e. the components of the shift vector $\vec{s}$. The result is a unique solution $\vec{x}_g$ since $\vec{s}$ forming the homogeneous part is estimated dependently of an arbitrary particular solution. It is trivial that the unique solution $\vec{x}_g = \vec{x}_p^1 + E\vec{s}^1 = \vec{x}_p^2 + E\vec{s}^2$.

It should be mentioned that the LHS of eqns. (3.45) and (3.46) are correlated since Δr_i^* and Δr_j^* are solved by the crossover adjustment. Propagation of the a-posteriori covariances of the coefficients of these functions is not considered in this approach of an optimal adjustment.

3.3.6 Results of a test computation

The area in the North-east Atlantic was formed by 127 descending and 101 ascending arc segments. Here we choose all ascending arc segments to intersect the equator between $-25° < \lambda < +50°$ and the descending arc segments between $-80° < \lambda < -20°$. The boundaries of the area including shore lines are drawn in figure 3.7.

In total 9098 applicable crossover points were formed of which we present the a-priori/a-posteriori histogram in figure 3.6. Before LSA the mean value of the crossover differences is -0.284 m and the r.m.s. 1.08 m. The crossover differences after LSA, by fixing two arbitrarily chosen non-intersecting and non-overlapping master arc segments, equal to 11.7 cm r.m.s.

It was a two step process to acquire these results. Firstly we adjusted with 9447 crossovers of which 349 were eliminated since their discrepancy after the adjustment was larger than 3σ, with $\sigma = 19.9$ cm. In a second pass arc segments are eliminated when the corresponding unknowns possess unrealistic high a-posteriori variances. Later on in this chapter the latter problem will be discussed in more detail.

The value of 11.7 cm r.m.s. is independent of the choice of master arcs. Any arbitrary homogeneous solution may be added to the particular solution without altering the minimum norm found after LSA of crossovers. It means that the a-posteriori crossover r.m.s. is representing an internal accuracy of the estimated sea surface which is caused by variability, remaining orbit errors and other errors. It does not bear any information about the absolute position of the sea surface since

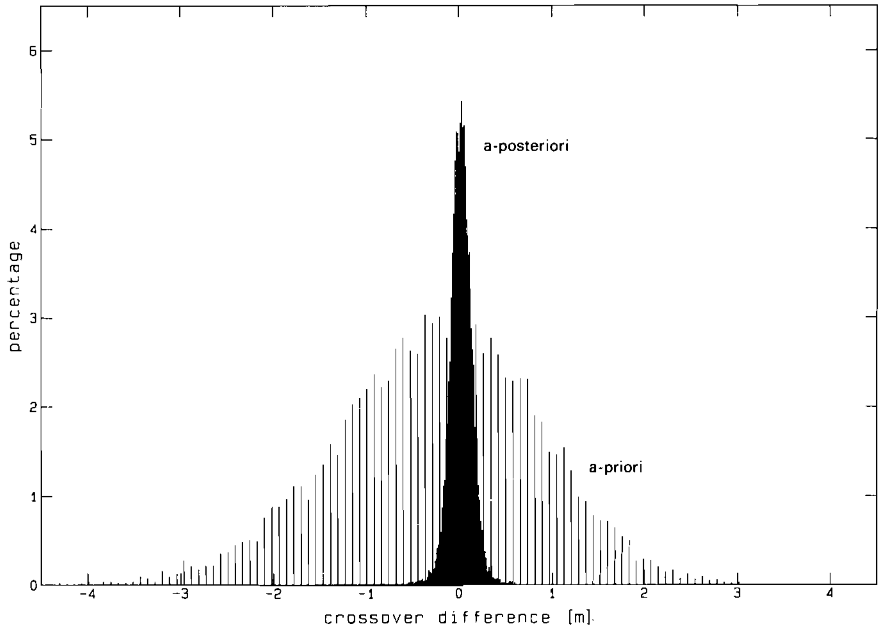

Figure 3.6: A-priori/A-posteriori histogram of crossover differences.

a manifold of homogeneous solutions added to the particular solution preserve the internal accuracy of 11.7 cm r.m.s.

All relations hold for the unknowns and observations as they are defined in the adopted model. This does not imply that the tilt and bias parameters evaluated by LSA for the arc segments at the actual crossover times yield the same internal accuracy as the model does with conventional crossover times. Depending on the magnitude of the homogeneous correction a modest deterioration of the internal accuracy is found, compare table 3.1. The difference is caused by the crossover time tag corrections which are needed to acquire a suitable matrix E, compare (3.19).

The next problem is to find a homogeneous part $\tilde{z}$ such that the general solution (and absolutely positioned altimeter surface) fits in optimal sense to a reference field. Here we choose GEM-10B, GEM-T1, OSU-81 and OSU-86F: GEM-10B had GEOS-3 altimeter data included; GEM-T1 was entirely based on non-altimetric data and OSU-81/OSU-86F were partially derived from SEASAT and GEOS-3 altimeter data combined with terrestrial gravity anomalies. Compare (Lerch et al.,1981); (Marsh et al.,1986); (Rapp,1983) and (Rapp and Cruz,1986a). The results are represented in table 3.1.

3.4 Quality of the estimated parameters

In this paragraph we describe the theory of quality control concerning the parameters estimated by the LSA of crossover differences. It is desirable to develop an algorithm indicating whether the parameters computed by LSA behave realistically. For this purpose we describe the properties of the covariance matrix of the estimated

Reference geoid	σ_{IA} [cm]	σ_{IM} [cm]	σ_E [m]
GEM-10B	12.5	11.7	1.46
GEM-T1	14.5	11.7	1.80
OSU-81	12.5	11.7	0.70
OSU-86F	12.5	11.7	0.57

Table 3.1: Comparison of the actual internal r.m.s. σ_{IA} the model internal r.m.s. σ_{IM} and the external r.m.s. σ_E of the SEASAT altimeter solution with respect to the reference geoid.

unknowns, in the sequel denoted as Q_{xx}. It will be shown that Q_{xx} equals to the inverse of the normal matrix which is singular for the crossover minimization problems considered here. Due to singularity only the 'particular part' of the normal equations is inverted resulting in a master arc dependent result.

A possible solution for this problem is to convey the particular covariance matrix into a minimum trace form as suggested by Mittermayer (1971, 1972). This avoids the non-uniqueness problem but has the disadvantage that no direct physical interpretation may be given to the transformed Q_{xx} matrix. An extension to the precision theory described by Baarda (1973) will be considered as an alternative.

3.4.1 The covariance matrix for a regular problem

For the non-singular least squares parameter estimation problem

$$\hat{x} = A^{\#}\vec{y} \tag{3.47}$$

with

$$A^{\#} = (A^t Q_{yy}^{-1} A)^{-1} A^t Q_{yy}^{-1} \tag{3.48}$$

propagation of variances is applied

$$Q_{xx} = A^{\#} Q_{yy} (A^{\#})^t \tag{3.49}$$

where Q_{xx} equals to the covariance matrix of the estimated unknowns. The notation $A^{\#}$ is used to indicate a generalized inverse (g-inverse) of the A matrix as is described by Rao (1973) and Bjerhammar (1973). An evaluation of (3.49) results in:

$$\begin{aligned} Q_{xx} &= [(A^t Q_{yy}^{-1} A)^{-1} A^t Q_{yy}^{-1}] Q_{yy} [(A^t Q_{yy}^{-1} A)^{-1} A^t Q_{yy}^{-1}]^t \Rightarrow \\ Q_{xx} &= N^{-1}. \end{aligned} \tag{3.50}$$

We conclude that the inverse of the normal matrix equals to the covariance matrix Q_{xx} of the estimated unknowns.

Typical for LSA is the independence of $\hat{x}$ and the linear dependence of Q_{xx} of a scale factor λ of Q_{yy}. Consider the problem $\vec{y} = A\vec{x} + \vec{\epsilon}$ under the condition $\vec{\epsilon}^t(\lambda Q_{yy})^{-1}\vec{\epsilon} = \min$. Accordingly:

$$\begin{aligned} \hat{x} &= (A^t \lambda^{-1} Q_{yy}^{-1} A)^{-1} A^t \lambda^{-1} Q_{yy}^{-1} \vec{y} \\ &= \lambda N^{-1} \lambda^{-1} \vec{r} = N^{-1} \vec{r} \end{aligned}$$

which shows that $\hat{x}$ is invariant $\forall\lambda \in \mathcal{R}|\lambda \neq 0$. However Q_{xx} is not anymore invariant to λ since

$$Q_{xx} = \{A^t\lambda^{-1}Q_{yy}^{-1}A\}^{-1} = \lambda N^{-1}.$$

This shows that λQ_{yy} results in λQ_{xx}.

3.4.2 The covariance matrix for a singular problem

Due to the singular behavior of N one cannot apply eq. (3.50) to compute Q_{xx}. For this reason the original problem $\vec{y} = A\vec{x} + \vec{\epsilon}$ with $\vec{\epsilon}^tQ_{yy}^{-1}\vec{\epsilon} = \min$ is reformulated into the problem:

$$\min \vec{\epsilon}^tQ_{yy}^{-1}\vec{\epsilon} \quad \left\{ \begin{array}{ll} \vec{y} = A\vec{x} + \vec{\epsilon} & \text{(a)} \\ \vec{c} = B\vec{x} & \text{(b)} \end{array} \right. \tag{3.51}$$

where eq. (3.51b) is chosen such that a minimum number of constraints are forced on the unknowns $\vec{x}$. It is known that the general solution $\vec{x}_g$ of eq. (3.51a) may be formulated as

$$\vec{x}_g = \vec{x}_p + E\vec{s} \tag{3.52}$$

which is substituted in eq. (3.51b) resulting in

$$\vec{c} = B(\vec{x}_p + E\vec{s}). \tag{3.53}$$

From this equation $\vec{s}$ is solved as:

$$\vec{s} = (BE)^{-1}(\vec{c} - B\vec{x}_p). \tag{3.54}$$

As a result one must demand that:

1. There are exactly as many constraint equations as the rank defect of the normal matrix.
2. The matrix product BE is regular.

One may substitute (3.54) in (3.52) if both conditions hold. It results in:

$$\begin{aligned} \vec{x}_g &= (I - E(BE)^{-1}B)\vec{x}_p + E(BE)^{-1}\vec{c} \\ &= P_1\vec{x}_p + P_2\vec{c} \end{aligned} \tag{3.55}$$

At this point there are *two* possibilities for variance propagation of eq. (3.55). In the most general form $\vec{x}_p$ and $\vec{c}$ possess stochastic properties which would be the case when constraint equations are minimized under the least squares norm simultaneously with the observation equations. As a result:

$$Q_{x_gx_g} = P_1Q_{x_px_p}P_1^t + 2P_1Q_{x_pc}P_2^t + P_2Q_{cc}P_2^t. \tag{3.56}$$

In case the constraint equations are not weighted ($Q_{x_pc} = 0$ and $Q_{cc} = 0$) we find the form:

$$Q_{x_gx_g} = P_1Q_{x_px_p}P_1^t \tag{3.57}$$

which are called the S-transformations, cf. (Baarda,1973), (Teunissen,1985) and (Strang van Hees,1982), of $Q_{x_px_p}$, a covariance matrix belonging to a particular solution $\vec{x}_p$.

Properties of S-transformations

A first property of the matrix P_1 concerns its idempotent behavior:

$$\begin{aligned} P_1P_1 &= (I - E(BE)^{-1}B)(I - E(BE)^{-1}B) \\ &= (I - 2E(BE)^{-1}B + E(BE)^{-1}BE(BE)^{-1}B) \\ &= (I - E(BE)^{-1}B) \\ &= P_1 \end{aligned} \tag{3.58}$$

Secondly P_1 is not unique. It depends on the matrix B which can be chosen freely provided that $(BE)^{-1}$ exists. In (Strang van Hees,1982) P_1 is written in the form of

$$P_1 = (I - EE^{\#}) \tag{3.59}$$

where $E^{\#} = (BE)^{-1}B$ denotes the g-inverse, cf. (Rao,1973) and (Bjerhammar,1973), of E. It is easy to verify that $EE^{\#}E = E$ which is a necessary and sufficient condition for a g-inverse $E^{\#}$ of E. However a manifold of S-transformations exist due to the non-uniqueness of $E^{\#}$. Further specification is possible by fulfilling at least one of the following conditions.

$$\begin{array}{rcll} E^{\#}EE^{\#} &=& E^{\#} & \text{(a)} \\ (E^{\#}E) &=& (E^{\#}E)^t & \text{(b)} \\ (EE^{\#}) &=& (EE^{\#})^t & \text{(c)} \end{array} \tag{3.60}$$

In the sequel (3.59) is substituted in (3.60) in order to verify (a) (b) and (c).

Condition (3.60a) is always fulfilled:

$$\begin{aligned} E^{\#}EE^{\#} &= [(BE)^{-1}B]E[(BE)^{-1}B] \\ &= (BE)^{-1}B \\ &= E^{\#} \quad \square \end{aligned}$$

Condition (3.60b) is always fulfilled:

$$\begin{aligned} E^{\#}E &= [(BE)^{-1}B]E \\ &= I \\ &= (E^{\#}E)^t \quad \square \end{aligned}$$

Condition (3.60c) is only fulfilled when $B = E^t$:

$$(EE^{\#})^t = [E(BE)^{-1}B]^t = B^t[(BE)^{-1}]E^t$$

If $B^t = E$ then $(EE^{\#})^t = E(BE)^{-1}B = EE^{\#}$ $\square$

$E^{\#}$ is unique and called a Penrose Moore inverse of E in case conditions (3.60a) (b) and (c) are fulfilled. It equals to:

$$E^{\#} = (E^tE)^{-1}E^t$$

from which it follows that

$$P_1 = I - E(E^t E)^{-1} E^t \tag{3.61}$$

Substitution of (3.61) in (3.57) results in the so-called free net transformation of $Q_{x_p x_p}$. The consequence is that $Q_{x_g x_g}$ behaves as a minimum trace covariance matrix of all unknowns, as is stated by Mittermayer (1971,1972). A free net transformation is unique (due to $E^{\#}$) but has the disadvantage that no direct physical interpretation can be assigned to $Q_{x_g x_g}$.

Another type of S-transformation introduced by (Baarda,1973) is designed to convey an arbitrary particular form $Q_{x_p x_p}$ into any other. As $Q_{x_p x_p}$ is derived it belongs to a chosen datum in the arc segment configuration, a situation comparable to that of a geodetic network. For this purpose B is defined such that a minimum trace covariance matrix is obtained for a subset of the unknowns. The B matrix takes the form of

$$B = \left(\frac{E_1}{E_2} \right) \tag{3.62}$$

with E_1 and E_2 representing sub-matrices of E. Here $E_1 = 0$ and $E_2 \neq 0$ such that the new unknowns to transform to coincide with the range of E_2. It can be verified that $E^{\#}$ fulfills the properties (3.60a) and (b) but not (c).

3.4.3 Extension to a quality control criterion

In order to derive a criterion for quality control of the estimated parameters Baarda (ibid) suggests to investigate the eigenvalues λ of the general eigenvalue problem $|G - \lambda H| = 0$ where G represents a $Q_{x_p x_p}$ matrix and H a model covariance matrix of the parameters. The eigenvalues are 'datum' independent since H is defined on the same 'datum' as G. However from practical point of view there are some obstacles:

- it is required to define an a-priori model matrix H,
- it is necessary to solve the general eigenvalue problem $|G - \lambda H| = 0$.

The first obstacle may be solved by studying the characteristic behavior of covariance matrices of arc segment configurations. The second obstacle can become, due to the dimensions of the matrices involved, a dilemma for crossover adjustments. Compare (Stoer and Bulirsch,1983) where the technique of eigenvalue computation is discussed.

In an actual implementation diagonal elements of as well $Q_{x_g x_g}$ (in a free net form) as $Q_{x_p x_p}$ have been investigated. In both forms peculiar arc segments were recognized by comparing the diagonal elements relative in magnitude. Relative comparison is necessary since it is known that a covariance matrix of the unknowns depends linearly on a scale factor λ in Q_{yy}. All comparisons revealed that variances of poorly connected arc segments were up to 10 times as large as the average value of well controlled segments. The crossovers along the arc segments with a poor data distribution in the test area are shown in figure 3.7. Typical is the behavior of those arc segments which possess a poor distribution of crossovers. They nearly all reside in

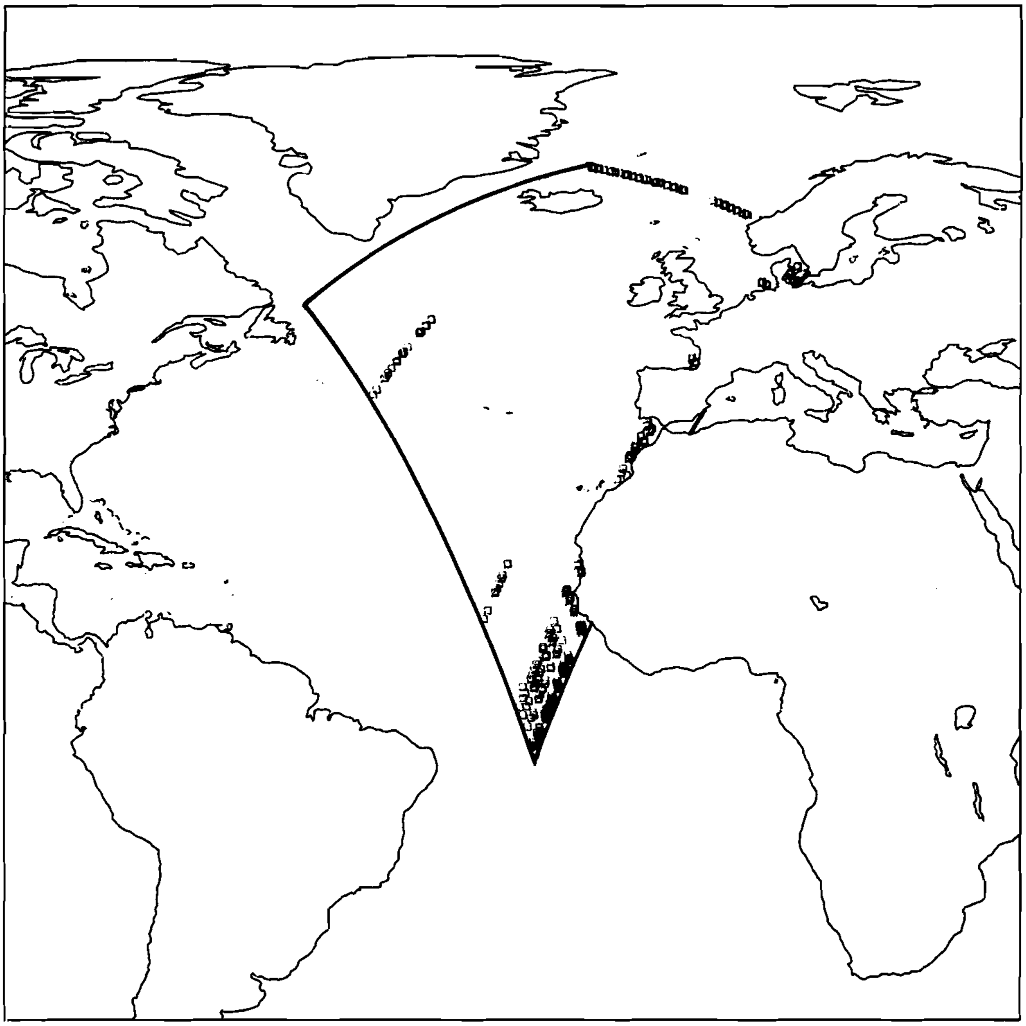

Figure 3.7: The area in the North-east Atlantic including crossovers along arc segments with unrealistic parameter variances.

the Eastern part of the test area showing a 'weak' connection to other arc segments. Apparently their tilt and bias parameters are not well estimated. Surprising was the fact that the parameters and the minimum trace variances estimated for well controlled segments were not altered significantly after a second LSA without the arc segments having a poor data distribution. Apparently the configuration remains stable even though a number of poorly connected arc segments are included.

3.5 Conclusions

In this chapter we described the LSA of crossover differences of SEASAT altimeter data for a test area in the North-east Atlantic. The choice of the test area is arbitrary. Its purpose is to demonstrate the technique of LSA of crossover differences in a local region. Minimization is accomplished by solving tilt and bias parameters belonging to an error function per arc segment modeling the behavior of a radial orbit error along the segment. It is found that crossover minimization results in a compatible self-adjoint system of normal equations allowing a manifold of solutions for the minimization problem. The general solution of the minimization problem is a combination of a particular and a homogeneous solution of a compatible self-adjoint system of equations.

Regularization of the crossover timings in a local diamond shaped area has been applied. The purpose of regularization to find 1) a convenient formulation for the homogeneous part of the system of normal equations and 2) a well conditioned numerical stable solution for the particular part of the system. One can show that a system of normal equations behaves as poorly conditioned if it is based on the original unmodified crossover timings.

An arbitrary particular solution of the normal equations is found by fixing a minimum amount of so-called master arc segments which provide control to the configuration. However, an arbitrary homogeneous solution may always be added to the particular solution without altering the minimum norm found by the LSA of crossover differences. Homogeneous solutions belonging to arbitrary particular solutions have been computed such that:

- datum shifts from one particular solution to any other were found,
- a second minimization criterion, a minimum discrepancy between a reference geoid and the altimetric surface, is fulfilled.

Additionally criteria were defined to identify those arc segments which possess poorly estimated parameters. For this purpose the diagonal elements of a minimum trace transformed covariance matrix of the estimated unknowns are investigated. It was recognized that poorly connected arc segments possess inaccurately estimated parameters.

In chapter 6 we will extend the crossover minimization technique from a local approach into a global (chronological) LSA. In the global chronological approach error functions are solved which are valid over the entire range of an arc segment. The technique is called chronological since the error functions will be chained in a chronological order enabling to describe a radial orbit error. The purpose of the global chronological approach, e.g. as described by (Zandbergen et al.,1988), is to:

- obtain a world-wide consistent sea surface model defined by altimeter data,
- extract in a non-dynamical way a radial error effect by means of minimizing the crossover discrepancies.

Local approaches can hardly be used for reconstructing a complete radial orbit error since only a small part of the total error effect is modeled. Instead in the alternative global approach a full coverage is possible. In many publications, cf. (Colombo,1984b) and (Wakker, Ambrosius and Aardoom,1983), it is mentioned that a radial error resembles a close to once per revolution oscillation modulated by a number of periodic effects. In chapter 4 the phenomenon is described in more detail.

Chapter 4

The radial orbit error

4.1 Introduction

From all errors present in the altimeter data radial orbit errors are the dominating ones. Whereas the instrumental accuracy is on the level of 10 cm, the orbit is uncertain at an order of magnitude of 1.5 to 2 meters, mainly due to errors in the gravitational model. As a consequence elimination of a radial orbit error from altimeter data has been a topic of research since the very beginning of altimetry.

In (Rummel et al.,1977) a procedure is sketched in which geoid undulation and gravity anomaly estimation is performed using GEOS-3 altimeter data in the North Atlantic. In total 64 arc segments were used consisting of data taken between 21 April 1975 and 20 May 1975. Crossover differences were minimized by solving empirical orbit error functions consisting of first degree Legendre polynomials per arc segment. Additionally the altimetric surface was minimized with respect to the GEM-7 geoid, at that time the most accurate of its type.

A similar procedure has been followed in the processing of SEASAT altimeter data as is described by Rowlands (1981) and Rapp (1983). The altimetric solution combined with land and sea gravity data including other data have made it possible to produce a global gravity model with a resolution of 1° × 1° or even 0.5° × 0.5°. This is equivalent to a spherical harmonic expansion till degree and order 180 or 360 respectively, a remarkable resolution which is hard to obtain without the aid of satellite altimetry.

In the processing of both GEOS-3 and SEASAT data crossover differences were used as observations for estimating an empirical radial orbit error function from the satellite ephemerides. In case of SEASAT the crossover residuals decrease typically from 1.6–1.8 m before the adjustment to approximately 10–30 cm after it. On the first hand there appears no problem until the characteristics of crossover differences and the orbit error are compared. In (Goad, Douglas and Agreen,1980) it has been pointed out that crossovers possess peculiar time differences characteristics with respect to the orbit error. The minimum time difference of two crossover time tags is equal to *at least* 98% of a revolution of the satellite (here SEASAT).

This justifies a more detailed study of the orbit error effect. In the past, orbit errors have been modeled by means of empirical functions such as 'tilt and bias' – or other elementary functions. The characteristics, based upon an interaction between the gravitational field and orbital perturbations, have not really been taken into account.

This has been the motivation for several studies, compare (Colombo,1984b) and (Wagner,1985,1986,1988). In (Colombo,1984b) the orbital and tidal effects in satellite altimetry are investigated. Another approach is that of Wagner (1985) where the linear perturbations theory, as described by Kaula (1966), is employed for the description of the radial variations of a satellite in a near circular trajectory. The goal of both investigations is to find a linear relation between the radial perturbations and the main cause of the phenomenon: uncertainties in the gravitational field. Another sophistication is the simultaneous recovery of the geoid and the permanent sea surface topography as is described in (Wagner,1986,1988) and (Engelis,1987).

Other publications of Sandwell et al. (1986), Tapley & Rosborough (1985) and Zandbergen, Wakker and Ambrosius (1988) note the existence of a geographically correlated orbit error. A part of the orbit error is not recoverable from crossover differences since its contribution is the same on both crossing arc segments.

4.2 A description of the radial orbit error

A numerical integration of the equations of motion followed by an improvement of the initial state vector and certain parameters of the force models is the modern method for precise orbit determination. Such methods are necessary for doing the production work, unfortunately they do not provide insight in the nature of a radial orbit error, cf. Taff (1985), pp. 392 ff. In order to obtain a better physical insight in the problem analytical orbit theories are introduced. Here we consider an analytical perturbations theory for orbits which are:

- near circular, a property required for the instrument,
- perturbed only by the gravitational field,
- not longer than about 10 days, i.e. the utmost period considered for orbit determination of altimeter satellites.

These requirements can be satisfied by the linear perturbations theory (LPT) introduced by Kaula (1966) and the Hill equations (HE), compare Kaplan (1976) and Colombo (1984a). In the sequel it will be attempted to describe both methods and their consequences for modeling a radial orbit error. It will be shown that, under certain realistic assumptions, both methods result in an identical formulation of the problem.

4.2.1 Linear perturbations theory

The conventional method for describing orbital perturbations is based on the Lagrange planetary equations (LPE). They describe the behavior of the Keplerian elements caused by a conventional perturbing force function R which comprises (for our purposes) all the terms of the gravitational field, except the central force term. In general, for most formulations of R, it will be difficult to find an exact solution for the six (coupled) differential equations forming the LPE.

In the LPT this problem is avoided by a linearization of the LPE in the neighborhood of a conveniently chosen reference orbit consisting of three constant and three precessing Keplerian elements. The precession effect is caused by the even zonal coefficients of the gravitational field of which the flattening term $\overline{C}_{20}$ dominates.

Eventually the perturbation formulas are derived by an integration of the LPE 'about' the nominal orbit. These perturbation formulas hold for the Keplerian elements and require a transformation into an expression for the radial part.

The Lagrange planetary equations

A tedious derivation of the LPE is avoided here since it can be found in most textbooks concerning celestial mechanics, such as Taff (1985) pp. 300–316 or Kaula (1966). The LPE are derived by a conversion of the perturbed equations of motion expressed in an inertial coordinate system into a new set of elements, in this case the Keplerian elements. Conversions into other elements are also possible and were derived by a number of famous mathematicians such as Gauss and Delaunay. The original planetary equations are derived by Lagrange:

$$\begin{aligned}
\frac{da}{dt} &= \frac{2}{na}\frac{\partial R}{\partial M} \\
\frac{de}{dt} &= \frac{1-e^2}{na^2e}\frac{\partial R}{\partial M} - \frac{\sqrt{1-e^2}}{na^2e}\frac{\partial R}{\partial \omega} \\
\frac{d\omega}{dt} &= -\frac{\cos I}{na^2\sqrt{1-e^2}\sin I}\frac{\partial R}{\partial I} + \frac{\sqrt{1-e^2}}{na^2e}\frac{\partial R}{\partial e} \\
\frac{dI}{dt} &= \frac{\cos I}{na^2\sqrt{1-e^2}\sin I}\frac{\partial R}{\partial \omega} - \frac{1}{na^2\sqrt{1-e^2}\sin I}\frac{\partial R}{\partial \Omega} \\
\frac{d\Omega}{dt} &= \frac{1}{na^2\sqrt{1-e^2}\sin I}\frac{\partial R}{\partial I} \\
\frac{dM}{dt} &= n - \frac{1-e^2}{na^2e}\frac{\partial R}{\partial e} - \frac{2}{na}\frac{\partial R}{\partial a}, \quad \text{with} \\
n &= \sqrt{\frac{\mu}{a^3}}
\end{aligned} \tag{4.1}$$

In equation (4.1) a, e, I, Ω, ω and M represent the Keplerian elements, semi-major axis, eccentricity, inclination, right ascension of the ascending node, argument of perigee and mean anomaly, respectively. The constant μ represents the gravitational constant times the mass of the Earth. Characteristic of (4.1) is an apparent separation between the elements $\{a, e, I\}$ and $\{\Omega, \omega, M\}$. There are for instance *no* elements other than $\{a, e, I\}$ in the coefficients multiplied by the partial derivatives of R.

The force function

The gravitational potential V considered here fulfills the Laplace condition outside the attracting masses of the Earth:

$$\Delta V = \frac{\partial^2 V}{\partial x^2} + \frac{\partial^2 V}{\partial y^2} + \frac{\partial^2 V}{\partial z^2} = 0 \tag{4.2}$$

in which x, y and z are given in a geocentric Earth fixed coordinate system. A potential function V fulfilling (4.2) can be expressed as a sum of spherical harmonics:

$$V(r,\phi,\lambda) = \frac{\mu}{a_e} \sum_{l=0}^{lmax} \sum_{m=0}^{l} \left(\frac{a_e}{r}\right)^{l+1} \left[\overline{C}_{lm} \cos m\lambda + \overline{S}_{lm} \sin m\lambda\right] \overline{P}_{lm}(\sin\phi) \tag{4.3}$$

in which r (radius), ϕ (latitude) and λ (longitude) represent the geocentric spherical coordinates. Other parameters are a_e, $\overline{C}_{lm}$ and $\overline{S}_{lm}$ representing the mean equatorial radius and the normalized potential coefficients respectively. The terms $\overline{P}_{lm}$ denote associated normalized Legendre functions of degree l and order m, compare (Hobson,1965).

For an evaluation of the LPE it is required to evaluate the derivatives of the force function R with respect to the Keplerian elements. Therefore an expression of (4.3) is required in $\{a, e, I, \Omega, \omega, M\}$. In Kaula (1966) the formulation of V in terms of Keplerian elements is given as:

$$\begin{aligned}
V &= \sum_{l=0}^{lmax} \sum_{m=0}^{l} V_{lm}, \\
V_{lm} &= \frac{\mu a_e^l}{a^{l+1}} \sum_{p=0}^{l} \overline{F}_{lmp}(I) \sum_{q=-\infty}^{\infty} G_{lpq}(e) S(\psi_{lmpq}), \\
S(\psi_{lmpq}) &= A_{lm} \cos\psi_{lmpq} + B_{lm} \sin\psi_{lmpq} \\
(A_{lm}, B_{lm}) &= \begin{cases} (\overline{C}_{lm}, \overline{S}_{lm}), & l-m: \text{ even} \\ (-\overline{S}_{lm}, \overline{C}_{lm}), & l-m: \text{ odd} \end{cases} \\
\psi_{lmpq} &= (l-2p)\omega + (l-2p+q)M + m(\Omega - \theta)
\end{aligned} \tag{4.4}$$

where θ represents the argument of longitude of the Earth. The terms $\overline{F}_{lmp}(I)$ are known as normalized inclination functions and arise when transforming the potential V, given in (4.3), to the inclined orbital plane. The functions $G_{lpq}(e)$ are the Hansen coefficients which are used to convert the potential from a circle to an ellipse, compare Kaula (1966).

The purpose of (4.4) is to obtain a disturbing function R which may be differentiated with respect to the Keplerian elements. In the sequel the partial derivatives of R are substituted in (4.1), and the result is integrated with respect to time. Before this item is treated the inclination and eccentricity functions have to be discussed.

Eccentricity functions

The eccentricity functions describe the transformation of the mean anomaly (M) to the true anomaly (f). The transformation takes the form of:

$$\left(\frac{r}{a}\right)^{l'} \exp(im'f) = \sum_{p'=-\infty}^{\infty} \chi_{p'}^{l',m'}(e) \exp(ip'M) \tag{4.5}$$

where $l' = -l-1$, $m' = l-2p$ and $p' = l-2p+q$, compare Kaula (1966) pp. 35 ff. The terms $\chi_{p'}^{l',m'}$ are the Hansen coefficients which are related to the eccentricity functions:

$$G_{lpq}(e) = \chi_{l-2p+q}^{-l-1,l-2p}(e). \tag{4.6}$$

An approximation of (4.5) results in:

$$\chi_{p'}^{l',m'}(e) = (-e/2)^{p'-m'} \sum_{q'=0}^{p'-m'} \frac{(-p')^{q'}}{q'!} \begin{pmatrix} l'-m'+1 \\ p'-q'-m' \end{pmatrix} + O(e^{p'-m'+2}), \quad (p' \geq m'). \tag{4.7}$$

A symmetry property holds for the eccentricity functions:

$$\chi_{p'}^{l',m'} = \chi_{-p'}^{l',-m'} \tag{4.8}$$

which can be applied to evaluate (4.7) when $p' < m'$. It can be shown by an evaluation of (4.7) that the first-order approximations for the eccentricity functions become, compare Wagner (1985) and Allan (1967)

$$\begin{aligned} G_{l,p,0}(e) &= 1 \\ G_{l,p,-1}(e) &= (-l+4p+1)e/2 \\ G_{l,p,+1}(e) &= (3l-4p+1)e/2 \end{aligned} \tag{4.9}$$

and for $q \in \{-2, +2\}$ we find the expression:

$$G_{l,p,q}(e) = \left[(l'-m')(l'-m'+1)/2 - p'(l'-m'+1) + \frac{1}{2}(p')^2\right] \frac{1}{4}e^2 \tag{4.10}$$

where for

$$q = 2 \left\{ \begin{array}{c} l' = -l-1 \\ m' = l-2p \\ p' = l-2p+2 \end{array} \right\} \quad \text{and} \quad q = -2 \left\{ \begin{array}{c} l' = -l-1 \\ m' = 2p-l \\ p' = 2p-l+2 \end{array} \right\}$$

Due to the damping term $(e/2)^q$ in (4.7) rapid convergence for the eccentricity functions is guaranteed for near circular orbits. In the case of most circular applications it is sufficient to restrict $q \in [-1, 1]$ in the evaluations of the disturbing force functions.

Normalized inclination functions

The computation of inclination functions is a problem in itself. The formulation in terms of binomial coefficients of Allan (1967) appears to be unstable beyond degree 55 as well as the recursive relation given by Gooding (1971) which tends to be unstable at high degrees as is stated in Wagner (1983). A comparison of several numerical and analytical methods can be found in (Kostelecký, Klokočník and Kalina,1986). A recently developed algorithm for normalized inclination functions is given by Goad (1987).

The method applied in the software used here is the algorithm described by Wagner (ibid) including precautions for 1) numerical underflow in the recurrence relations of Legendre functions and 2) singularities at inclinations of 90°.

It was proposed by Wagner (ibid) to formulate the problem in terms of an unit potential function developed along a great circle with inclination I. The unit potential function V_{lm} is defined as:

$$\begin{aligned} &\mu = a_e = a = r = \overline{C}_{lm} = \overline{S}_{lm} = 1, \\ &\Omega = \theta = e = 0 \quad \wedge \quad \omega + M = u \end{aligned} \tag{4.11}$$

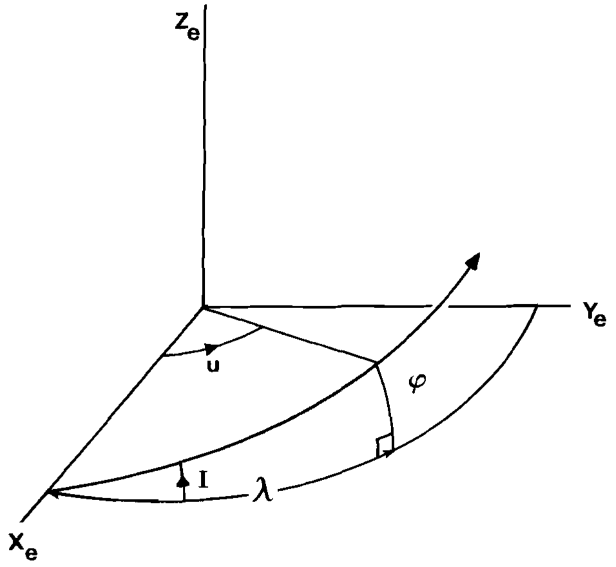

Figure 4.1: The relation between the coordinates (ϕ, λ) and (u, I).

where u is called the argument of latitude. In this context, compare figure 4.1, the relation between (ϕ, λ) and (u, I) is

$$\begin{aligned} x &= \cos\phi\cos\lambda &&= \cos u \\ y &= \cos\phi\sin\lambda &&= \sin u\cos I \\ z &= \sin\phi &&= \sin u\sin I \end{aligned} \tag{4.12}$$

Substitution of (4.11) into (4.3) results in:

$$V_{lm} = (\cos m\lambda + \sin m\lambda)\overline{P}_{lm}(\sin\phi) \tag{4.13}$$

Substitution of (4.11) into (4.4) results in:

$$V_{lm} = \sum_{p=0}^{l} \overline{F}_{lmp}(I) \left\{ \begin{array}{ll} \sin(l-2p)u + \cos(l-2p)u & l-m: \text{ even} \\ \sin(l-2p)u - \cos(l-2p)u & l-m: \text{ odd} \end{array} \right. . \tag{4.14}$$

Equation (4.14) is equivalent to a Fourier expansion of V_{lm} along the great circle with inclination I. We transform it into a harmonic expansion in u:

$$V_{lm} = \sum_{i=0}^{l} C_i \cos iu + S_i \sin iu \tag{4.15}$$

which is equivalent with (rearranging the summation indices of (4.14)):

$$V_{lm} = \sum_{j=-l}^{l} \left\{ \begin{array}{ll} \overline{F}_{lmp}(I)\cos ju + \overline{F}_{lmp}\sin ju & l-m: \text{ even} \\ -\overline{F}_{lmp}(I)\cos ju + \overline{F}_{lmp}\sin ju & l-m: \text{ odd} \end{array} \right. \tag{4.16}$$

with $l - 2p = j$. In this summation the variable j is always of the same parity as l, opposite parity is not defined. As a result we find the relation between inclination functions and Fourier coefficients:

$$\begin{array}{rcll} \overline{F}_{l,m,l/2} & = & C_0 & \text{for even } l \text{ and even } m \\ \overline{F}_{l,m,l/2} & = & -C_0 & \text{for even } l \text{ and odd } m \\ \overline{F}_{l,m,(l+i)/2} & = & (C_i - S_i)/2 & \text{for } l,m \text{ same parity} \\ \overline{F}_{l,m,(l-i)/2} & = & (C_i + S_i)/2 & \text{for } l,m \text{ same parity} \\ \overline{F}_{l,m,(l+i)/2} & = & (-C_i - S_i)/2 & \text{for } l,m \text{ opposite parity} \\ \overline{F}_{l,m,(l-i)/2} & = & (-C_i + S_i)/2 & \text{for } l,m \text{ opposite parity} \end{array} \tag{4.17}$$

where l and i have the same parity. The coefficients C_i and S_i are derived by computing the unit potential at discrete points along the great circle using (4.12) and (4.13) and secondly by performing a FFT (fast Fourier transformation) of the discrete values. The algorithm for the computation of normalized inclination functions may be summarized as follows:

- In (4.12) for a chosen inclination I and degree l the variable u is defined as $u = i\Delta u$ where $i \in [0, \alpha - 1]$. Here $\Delta u = 2\pi/\alpha$ where $\alpha \geq 2l$ due to the number of C_i and S_i coefficients in (4.15). Besides α is chosen such that a FFT may be computed with the mixed radix algorithm described by Singleton (1969).

- The unit potential defined by (4.13) is evaluated at the discrete points for $u \in [0, 2\pi]$. Note that the order m may be chosen freely for $m \in [0, l]$ without altering the value of α whose value depends on l. Hence recursions for Legendre functions are chosen such that for equal degree l all orders m are found. This is possible by application of special stabilized Legendre recursion formulas as is described in Schrama (1986b).

- In order to optimize the algorithm two symmetry properties of Legendre polynomials are applied. In fact the polynomials are developed only in the first quadrant of the argument of latitude where $u \in [0, \pi/2]$. The second quadrant, where $u \in [\pi/2, \pi]$, has the same latitudes ϕ as the first. Accordingly the values of $\overline{P}_{lm}(\sin\phi)$ are symmetric. Another property of Legendre polynomials used in the algorithm concerns the equatorial symmetry:

  $$\begin{array}{rcll} \overline{P}_{lm}(\sin\phi) & = & \overline{P}_{lm}(-\sin\phi) & l,m: \text{ same parity} \\ \overline{P}_{lm}(\sin\phi) & = & -\overline{P}_{lm}(-\sin\phi) & l,m: \text{ opposite parity.} \end{array}$$

  allowing to compute quadrant 3 and 4 from 1 and 2.

- Once the unit potential function is evaluated, (4.17) is applied to derive the actual values of the inclination functions. A similar procedure is followed for the derivatives of inclination functions with respect to I, compare Schrama (1986b).

The nominal orbit

A direct substitution in the LPE of the partial derivatives of the disturbing force function as given in equation (4.4) with respect to the Keplerian elements would in principle result in a set of six differential equations which have to be solved in order to find the perturbations in the Keplerian elements. However due to the complicated behavior of (4.1) it is very difficult to find an analytical solution.

For this reason a linearization is carried out with respect to a reference orbit. The elements of the reference orbit are substituted on the right hand side of the LPE and result in the perturbations in the elements. In the sequel we will concentrate on the derivation of a suitable reference orbit.

Firstly we note that the force function R may take two forms: it may be *dependent* or *independent* of the variable ψ. This depends on the indices $\{l, m, p, q\}$ in (4.4). Independency of ψ occurs for the even zonal coefficients of the gravity field:

$$V_{l,0} = \frac{\mu a_e^l}{a^{l+1}} \overline{F}_{l,0,l/2}(I)\, G_{l,l/2,0}(e) \overline{C}_{l0} \tag{4.18}$$

with even l, $m = 0$, $p = l/2$, $q = 0$. If we insert the derivatives of this function into the LPE we find:

$$\begin{aligned} (\dot{a}, \dot{e}, \dot{I}) &= \vec{0} \\ (\dot{\Omega}, \dot{\omega}, \dot{M}) &= \vec{f}(a, e, I) \end{aligned} \tag{4.19}$$

The largest even zonal coefficient $\overline{C}_{20}$, which is about 1000 times greater than all other potential coefficients, is now used to define a reference orbit. A substitution of V_{20} with $p = 1$, $q = 0$ in (4.1) results in:

$$\begin{aligned} \frac{d\Omega}{dt} &= \frac{3nC_{20}a_e^2}{2(1-e^2)^2a^2} \cos I, \\ \frac{d\omega}{dt} &= \frac{3nC_{20}a_e^2}{4(1-e^2)^2a^2} [1 - 5\cos^2 I], \\ \frac{dM}{dt} &= n - \frac{3nC_{20}a_e^2}{4(1-e^2)^{3/2}a^2} [3\cos^2 I - 1] \end{aligned} \tag{4.20}$$

in which C_{20} is unnormalized ($C_{20} = -0.00108263$). From (4.20) follows the well known fact that the flattening term of the gravitational field results in a secular precession in the elements Ω, ω and M. These drift rates are well observable in the orbit of e.g. SEASAT, where the orbital plane rotates about the z axis in inertial space with a period of 170 days. The effect $\dot{\omega}$ causes a rotation of ω in a period of -207 days ($\dot{\omega} < 0$) which is known as the apsidal period. These statistics are based on the first two months of SEASAT. In its last two months the perigee was frozen at 90°. There exists a specific combination of eccentricity and argument of perigee ($e \approx 10^{-3}$ and $\omega = 90°$) causing $\dot{e} = 0$ and $\dot{\omega} = 0$, compare appendix A.

Another noticeable effect in the SEASAT orbit is the quite large twice per revolution oscillation in the semi-major axis. The amplitude of this phenomenon equals to approximately 5 to 10 km, caused by time dependent force functions coming from the C_{20} term. Later on it will be shown that the latter phenomenon does not appear to restrict severely the applicability of the linear perturbations theory. A treatment of the oscillating perturbations in the Keplerian elements caused by C_{20} effects is described by Kozai (1961), Engelis (1987) and many others.

Perturbations in the elements

The perturbation formulas are found by a substitution of the nominal elements in (4.1). An integration with respect to time of the LPE is avoided and replaced by an integration with respect to ψ causing the term $\dot{\psi}$ to appear in the denominator of all formulas.

$$\Delta E = \int f(t)\, dt \quad \Rightarrow \quad \Delta E \approx \frac{1}{\dot{\psi}} \int f(\psi)\, d\psi \tag{4.21}$$

(where E symbolizes an arbitrary element) Under this assumption the perturbation formulas become, compare Kaula (1966):

$$\begin{aligned}
\Delta a &= \frac{\mu a_e^l}{n a^{l+2} \dot{\psi}} 2 \overline{F}_{lmp} G_{lpq} (l - 2p + q) S_{lmpq} \\
\Delta e &= \frac{\mu a_e^l}{n a^{l+3} e \dot{\psi}} \overline{F}_{lmp} G_{lpq} \sqrt{1 - e^2} [\sqrt{1 - e^2} (l - 2p + q) - (l - 2p)] S_{lmpq} \\
\Delta \omega &= \frac{\mu a_e^l}{n a^{l+3} \dot{\psi}} [\sqrt{1 - e^2} e^{-1} \overline{F}_{lmp} G'_{lpq} - \cot(I) (1 - e^2)^{-1/2} \overline{F}'_{lmp} G_{lpq}] \overline{S}_{lmpq} \\
\Delta I &= \frac{\mu a_e^l}{n a^{l+3} \sqrt{1 - e^2} \sin(I) \dot{\psi}} \overline{F}_{lmp} G_{lpq} [(l - 2p) \cos(I) - m] S_{lmpq} \\
\Delta \Omega &= \frac{\mu a_e^l}{n a^{l+3} \sqrt{1 - e^2} \sin(I) \dot{\psi}} \overline{F}'_{lmp} G_{lpq} \overline{S}_{lmpq} \\
\Delta M &= \frac{\mu a_e^l}{n a^{l+3} \dot{\psi}} [-(1 - e^2) e^{-1} G'_{lpq} + 2(l + 1) G_{lpq}] \overline{F}_{lmp} \overline{S}_{lmpq} \\
&\text{where } \overline{S}_{lmpq} = \int S_{lmpq}(\psi)\, d\psi.
\end{aligned} \tag{4.22}$$

in which the perturbations of the elements are given for a particular $\{l, m, p, q\}$ combination. Resonance shows up when $\dot{\psi}$ approaches 0, a well observed phenomenon in most satellites orbits, compare Wagner (1975,1977,1981) and Schrama (1986a).

Resonance

Due to the choice of the reference orbit in the LPT the term ψ in (4.4) is divided in a constant and a linear part, hence:

$$\begin{aligned}
&\psi = \psi_0 + \dot{\psi} t \;\text{ with} \\
&\psi_0 = k(\omega_0 + M_0) + m(\Omega_0 - \theta_0) - q\omega_0 \;\text{ and} \\
&\dot{\psi} = k(\dot{\omega} + \dot{M}) + m(\dot{\Omega} - \dot{\theta}) - q\dot{\omega} \;\text{ with} \\
&k = (l - 2p + q)
\end{aligned} \tag{4.23}$$

(The subscript 0 is used to specify the elements at the reference time) The term $\dot{\psi}$ determines the frequency of the perturbations whereas ψ_0 determines the phase. In this expression there appear three basic frequencies:

- An 'once per revolution' component $(\dot{\omega} + \dot{M}) = \dot{\omega}_o$

- A 'daily' component $(\dot{\Omega} - \dot{\theta}) = \dot{\omega}_e$
- An 'apsidal' component $\dot{\omega}$

The influence of $\dot{\omega}$ can be regarded as a long periodic modulation, especially when the perturbations are considered in the relative short time interval of some 10 days.

Another remarkable effect is the clustering of frequencies for the same order m and index k. Considering (4.23) there appear to be a multiple of $\{l, m, p, q\}$ combinations which result in the same term $\dot{\psi}$. Take for instance: $l = 12$, $m = 10$, $p = 6$, $q = 0$ and $l = 14$, $m = 10$, $p = 7$, $q = 0$ which both result in $\dot{\psi} = 10(\dot{\Omega} - \dot{\theta})$. The consequence is rather important: perturbations caused by potential coefficients of the same order m over all degrees l overlap on the same frequency.

Radial perturbations

The perturbations in the elements may be used for various purposes, as may be concluded from the many publications on this subject. One may derive e.g. the observation equations in a SST configuration, compare Wagner (1983), Kaula (1983) and Schrama (1986b). Here the radial perturbations are of importance. They are found by inearization of a Kepler ellipse for near circular orbits:

$$\begin{aligned} r &= a(1 - e\cos E) \quad \Rightarrow \\ r &\simeq a(1 - e\cos M) \quad (\text{small } e) \quad \Rightarrow \\ \Delta r &\simeq \Delta a - (a\Delta e + e\Delta a)\cos M + ae\Delta M \sin M \end{aligned} \tag{4.24}$$

Accordingly we substitute (4.22) in (4.24) assuming first-order approximations of eccentricity functions as in (4.9). The components of (4.22) with a significant contribution become:

$$\begin{aligned} \Delta a_{lmpq} &= \frac{\mu a_e^l}{n a^{l+2}\dot{\psi}} 2\overline{F}_{lmp} G_{lp0}(l-2p) S_{lmp0}(\psi) \quad (q=0) \\ \Delta e_{lmpq} &= \frac{\mu a_e^l}{n a^{l+3}\dot{\psi}} \overline{F}_{lmp} G'_{lpq} q S_{lmpq}(\psi) \quad (q=\pm 1) \\ e\Delta M_{lmpq} &= -\frac{\mu a_e^l}{n a^{l+3}\dot{\psi}} \overline{F}_{lmp} G'_{lpq} \overline{S}_{lmpq}(\psi) \quad (q=\pm 1) \end{aligned} \tag{4.25}$$

The following step is to substitute (4.25) in (4.24). Wagner (1985) shows that this substitution results in:

$$\Delta r(t) = \sum_{m=0}^{l_{max}} \sum_{k=-l_{max}}^{k=l_{max}} [A_{km} \cos \dot{\psi} t + B_{km} \sin \dot{\psi} t] \tag{4.26}$$

$$(A_{km}, B_{km}) = \sum_{l=m}^{l_{max}} H_{lmk} [\begin{bmatrix} \overline{C}_{lm} & \overline{S}_{lm} \\ -\overline{S}_{lm} & \overline{C}_{lm} \end{bmatrix}_o^e \cos \psi_0 + \begin{bmatrix} \overline{S}_{lm} & -\overline{C}_{lm} \\ \overline{C}_{lm} & \overline{S}_{lm} \end{bmatrix}_o^e \sin \psi_0]$$

$$H_{lmk} = \frac{\mu (a_e/a_0)^l}{n_0^2 a_0^2} \overline{F}_{lm(l-k)/2}(I_0) \left[\frac{\beta(l+1) - 2k}{\beta(\beta^2 - 1)} \right]$$

$$\begin{aligned}\beta &= \dot{\psi}/n_0\\ \psi_0 &= k(\omega_0 + M_0) + m(\Omega_0 - \theta_0)\\ \dot{\psi} &= k(\dot{\omega} + \dot{M}) + m(\dot{\Omega} - \dot{\theta})\end{aligned}$$

in which the summation over l is evaluated *only* for l and k having the same parity. Besides e and o symbolize $l - m$: even or $l - m$: odd. Eq. (4.26) provides the desired analytical relationship between radial orbit perturbations and coefficients of the gravitational field.

4.2.2 An alternative approach: Hill equations

An alternative to the LPT are the Hill equations (HE) which are, in contrast to the LPE, a direct approximation of the equations of motion. The HE presented here are closely related to Hill's original problem concerning the motions in the Earth–Moon–Sun system. The HE describe the actual satellite motion in an orthogonal radial, cross – and along track triad that is moving along a nominal satellite trajectory. The reference orbit is by definition circular along which the satellite is orbiting at a constant rotation rate.

In this section we describe the derivation of the HE which take the form of three differential equations. The force free or *homogeneous* solution as well as the forced or *particular* solutions of the HE are considered.

Hill equations

In order to derive the HE the equations of motion are transformed into an uniformly rotating coordinate system. In this context we express the equations of motion as:

$$\ddot{\vec{x}} = \nabla V \quad \text{or,} \quad \begin{bmatrix} \ddot{x} \\ \ddot{y} \\ \ddot{z} \end{bmatrix} = \begin{bmatrix} \partial V/\partial x \\ \partial V/\partial y \\ \partial V/\partial z \end{bmatrix}, \tag{4.27}$$

in which the x, y axes are inside the orbital plane while the z axis lies orthogonal to it in the direction of the angular momentum vector, compare figure 4.2. The relation between $\{x, y, z\}$ and $\{\alpha, \beta, \gamma\}$ is described by a rotation about the z axis:

$$\vec{x} = R(\theta)\vec{\alpha} \quad \Leftrightarrow \quad \begin{bmatrix} x \\ y \\ z \end{bmatrix} = \begin{bmatrix} \cos\theta & -\sin\theta & 0 \\ \sin\theta & \cos\theta & 0 \\ 0 & 0 & 1 \end{bmatrix} \begin{bmatrix} \alpha \\ \beta \\ \gamma \end{bmatrix} \tag{4.28}$$

where due to the uniform rotation of $\{\alpha, \beta, \gamma\}$:

$$\dot{\theta} = n = \sqrt{\frac{\mu}{r^3}} = \text{constant.} \tag{4.29}$$

In the following (4.27) is worked out using (4.28) and (4.29). Differentiation of (4.28) twice with respect to the time results in:

$$\ddot{\vec{x}} = R\ddot{\vec{\alpha}} + 2\dot{R}\dot{\vec{\alpha}} + \ddot{R}\vec{\alpha} \quad \Leftrightarrow \quad \begin{bmatrix} \ddot{x} \\ \ddot{y} \\ \ddot{z} \end{bmatrix} = R(\theta) \begin{bmatrix} \ddot{\alpha} - 2n\dot{\beta} - n^2\alpha \\ \ddot{\beta} + 2n\dot{\alpha} - n^2\beta \\ \ddot{\gamma} \end{bmatrix} \tag{4.30}$$

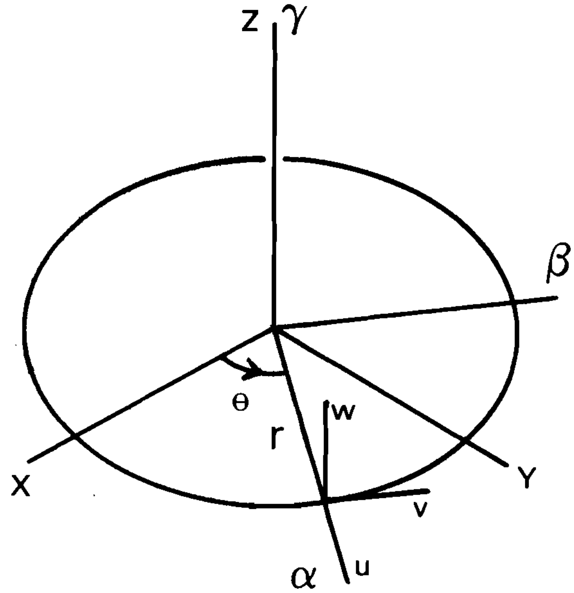

Figure 4.2: Definition of the Hill coordinates $\{u, v, w\}$, the $\{\alpha, \beta, \gamma\}$ system, and the inertial frame $\{x, y, z\}$

The RHS of (4.27) in $\{\alpha, \beta, \gamma\}$ using (4.28) becomes:

$$\begin{bmatrix} \partial V/\partial x \\ \partial V/\partial y \\ \partial V/\partial z \end{bmatrix} = \begin{bmatrix} \partial\alpha/\partial x & \partial\beta/\partial x & \partial\gamma/\partial x \\ \partial\alpha/\partial y & \partial\beta/\partial y & \partial\gamma/\partial y \\ \partial\alpha/\partial z & \partial\beta/\partial z & \partial\gamma/\partial z \end{bmatrix} \begin{bmatrix} \partial V/\partial\alpha \\ \partial V/\partial\beta \\ \partial V/\partial\gamma \end{bmatrix} = R(\theta) \begin{bmatrix} \partial V/\partial\alpha \\ \partial V/\partial\beta \\ \partial V/\partial\gamma \end{bmatrix} \tag{4.31}$$

Substitution of (4.30) and (4.31) in (4.27) allows to eliminated the rotation matrix $R(\theta)$:

$$\begin{bmatrix} \partial V/\partial\alpha \\ \partial V/\partial\beta \\ \partial V/\partial\gamma \end{bmatrix} = \begin{bmatrix} \ddot{\alpha} - 2n\dot{\beta} - n^2\alpha \\ \ddot{\beta} + 2n\dot{\alpha} - n^2\beta \\ \ddot{\gamma} \end{bmatrix} \tag{4.32}$$

Consider now a linearization at $\alpha = r$, $\beta = 0$ and $\gamma = 0$, see figure 4.2. Accordingly on the LHS of eq. (4.32) a first order Taylor expansion of the spherical potential function μ/r is performed about the nominal orbital height r to the actual position of the spacecraft. Instead of writing $\Delta\alpha$, $\Delta\beta$ and $\Delta\gamma$ the variables u, v and w are chosen.

$$\begin{bmatrix} \partial V/\partial\alpha \\ \partial V/\partial\beta \\ \partial V/\partial\gamma \end{bmatrix} = \begin{bmatrix} -\mu/r^2 \\ 0 \\ 0 \end{bmatrix} + \begin{bmatrix} 2\mu u/r^3 \\ -\mu v/r^3 \\ -\mu w/r^3 \end{bmatrix} + \begin{bmatrix} \partial T/\partial u \\ \partial T/\partial v \\ \partial T/\partial w \end{bmatrix} + \ldots \tag{4.33}$$

where T denotes the disturbance potential ($V = \mu/r + T$). Note that T itself is not linearized. Linearized toward the actual satellite position is the spherical part of the potential. The truncation error in (4.33) consists of the higher order spherical terms and the linearization error of the disturbance potential. Eventually it results in the Hill equations:

$$\begin{aligned} \partial T/\partial u &= f_u = \ddot{u} - 2n\dot{v} - 3n^2 u \\ \partial T/\partial v &= f_v = \ddot{v} + 2n\dot{u} \\ \partial T/\partial w &= f_w = \ddot{w} + n^2 w \end{aligned} \tag{4.34}$$

Note that the w-equation is uncoupled from the others, allowing a separate treatment. The HE, especially the w-equation, resemble a mass-spring system oscillating at its natural frequency n. The homogeneous part resembles a force free ($f_u = f_v = f_w = 0$) oscillation of the system whereas the particular part resembles a perturbed oscillation of a mass-spring system, compare (Colombo,1986).

The homogeneous solution

The homogeneous part is obtained by $(f_u, f_v, f_w) = \vec{0}$. The homogeneous solution describes the response of the system to an initial state vector effect. Kaplan (1976) and Colombo (1984a) have shown that the homogeneous solution can be expressed as:

$$\begin{aligned} u(t) &= a_u \cos nt + b_u \sin nt + c_u \\ v(t) &= a_v \cos nt + b_v \sin nt + c_v + d_v t \\ w(t) &= a_w \cos nt + b_w \sin nt \end{aligned} \tag{4.35}$$

where the coefficients a_u through b_w are determined by the initial conditions which are the initial state vector disturbances at a reference time. It is common to consider the initial conditions at t=0, resulting in:

$$\begin{aligned} u(t) &= (-3u_0 - \frac{2}{n}\dot{v}_0) \cos nt + \frac{\dot{u}_0}{n} \sin nt + (4u_0 + \frac{2}{n}\dot{v}_0) \\ v(t) &= \frac{2\dot{u}_0}{n} \cos nt + (6u_0 + \frac{4\dot{v}_0}{n}) \sin nt + (-6nu_0 - 3\dot{v}_0)t + (v_0 - 2\frac{\dot{u}_0}{n}) \\ w(t) &= w_0 \cos nt + \frac{\dot{w}_0}{n} \sin nt \end{aligned} \tag{4.36}$$

An example of a satellite motion as a result of radial and along–track initial state vector disturbances is illustrated figure 4.3. A practical application of the homogeneous solution of the HE is found in rendez-vous maneuvers of a target and a chase satellite as is described in Kaplan (ibid).

An obstacle encountered was the actual derivation of the formulas shown in equation (4.36). The ones presented above may be derived manually e.g. by substituting the results found by Kaplan (ibid) and Colombo (ibid) in the HE. However the risk of errors increases if the equations become more complicated as in the case of the particular solution of the Hill equations. For this purpose the formula manipulation program REDUCE, described by Hearn (1985), was used to derive and verify (4.36) including other solutions which will be discussed later on.

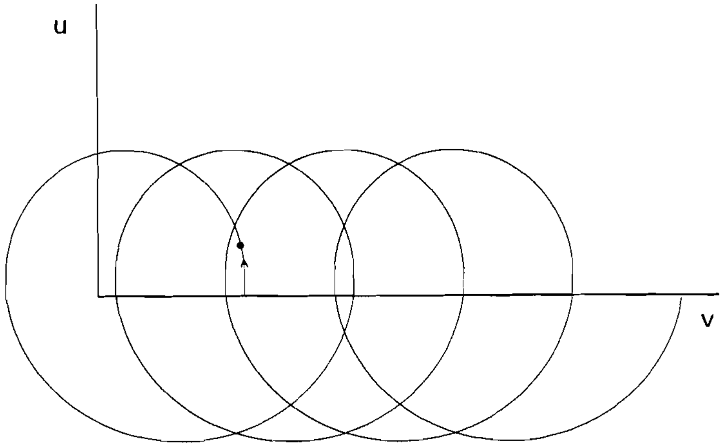

Figure 4.3: The unperturbed motion of a satellite in radial (u) and along track (v) direction with respect to the reference orbit.

The non-resonant particular solution

Kaplan (ibid) states that the particular solution of the HE cannot be given for an arbitrary force function. For certain choices of force functions, e.g. the ones expressed in a Fourier series, an analytical solution exists, compare Colombo (1986). In this case the particular solution is found by solving the system:

$$\begin{aligned} P_u \cos\omega t + Q_u \sin\omega t &= \ddot{u} - 2n\dot{v} - 3n^2 u \\ P_v \cos\omega t + Q_v \sin\omega t &= \ddot{v} + 2n\dot{u} \\ P_w \cos\omega t + Q_w \sin\omega t &= \ddot{w} + n^2 w \end{aligned} \tag{4.37}$$

where P_u through Q_w symbolize constants originating from the disturbing force function. The solution of this system becomes (REDUCE was used to obtain these expressions):

$$\begin{aligned} u(t) &= \frac{-2nQ_v + \omega P_u}{\omega(n^2-\omega^2)} \cos\omega t + \frac{2nP_v + \omega Q_u}{\omega(n^2-\omega^2)} \sin\omega t \\ v(t) &= \frac{(3n^2+\omega^2)P_v + 2n\omega Q_u}{\omega^2(n^2-\omega^2)} \cos\omega t + \frac{(3n^2+\omega^2)Q_v - 2n\omega P_u}{\omega^2(n^2-\omega^2)} \sin\omega t \\ w(t) &= \frac{P_w}{(n^2-\omega^2)} \cos\omega t + \frac{Q_w}{(n^2-\omega^2)} \sin\omega t \end{aligned} \tag{4.38}$$

The particular solution of the system represents the response to an oscillating perturbing force at a frequency ω, in this context not to be confused with the argument of perigee. Noteworthy is the amplification of the perturbations when $\omega \approx 0$ or when $\omega \approx \pm n$. This is the *resonant* case of the system where either a *constant* or an oscillating force at *once per revolution* acts on the satellite. Important is that each non-resonant periodic force function at a frequency of ω results in a disturbance of u, v, w at a frequency ω.

A general solution of the HE is not given here since the homogeneous part may become rather complex. It can easily be shown that the general solution consists of the sum of all particular solutions and one homogeneous expression in which the constants a_u through b_w are determined by the *initial conditions* and the coefficients P_u through Q_w of *each* particular part, as will be shown for the solution of (4.39).

Later on in this chapter a computer simulation is discussed in which radial perturbations of a numerically integrated satellite trajectory are compared with predicted analytical disturbances. In this comparison the homogeneous and exact resonant contribution of the HE are considered as undesired effects which are filtered out of the numerically predicted radial perturbation spectrum.

The resonant solution

As can be concluded from (4.38) the general particular response is no more valid when either $\omega = 0$ or $\omega = \pm n$. Such situations must be treated independently by solving the system:

$$\begin{aligned} P_u \cos nt + Q_u \sin nt + R_u &= \ddot{u} - 2n\dot{v} - 3n^2 u \\ P_v \cos nt + Q_v \sin nt + R_v &= \ddot{v} + 2n\dot{u} \\ P_w \cos nt + Q_w \sin nt + R_w &= \ddot{w} + n^2 w \end{aligned} \tag{4.39}$$

It can be shown, compare Colombo (1986), that a solution for the radial term exists in the form of:

$$u(t) = (a_u^0 + a_u^1 t)\cos nt + (b_u^0 + b_u^1 t)\sin nt + (c_u^0 + c_u^1 t) \tag{4.40}$$

in which the coefficients are represented by (accomplished by means of REDUCE):

$$\begin{aligned} a_u^0 &= \frac{1}{n^2}(-3n^2 u_0 - 2n\dot{v}_0 - 2Q_v - R_u) \\ a_u^1 &= \frac{1}{2n}(-2P_v - Q_u) \\ b_u^0 &= \frac{1}{2n^2}(2n\dot{u}_0 - 4R_v + 2P_v + Q_u) \\ b_u^1 &= \frac{1}{2n}(-2Q_v + P_u) \\ c_u^0 &= \frac{1}{n^2}(4n^2 u_0 + 2n\dot{v}_0 + 2Q_v + R_u) \\ c_u^1 &= \frac{2}{n}R_v \end{aligned}$$

For the along-track term we find:

$$v(t) = (a_v^0 + a_v^1 t)\cos nt + (b_v^0 + b_v^1 t)\sin nt + (c_v^0 + c_v^1 t + c_v^2 t^2) \tag{4.41}$$

in which the coefficients are represented by:

$$a_v^0 = \frac{1}{n^2}(2n\dot{u}_0 - 4R_v + 3P_v + 2Q_u)$$

$$
\begin{aligned}
a_v^1 &= \frac{1}{n}(-2Q_v + P_u) \\
b_v^0 &= \frac{1}{n^2}(6n^2 u_0 + 4n\dot{v}_0 + 5Q_v + 2R_u - P_u) \\
b_v^1 &= \frac{1}{n}(2P_v + Q_u) \\
c_v^0 &= \frac{1}{n^2}(n^2 v_0 - 2n\dot{u}_0 + 4R_v - 3P_v - 2Q_u) \\
c_v^1 &= \frac{1}{n}(-6n^2 u_0 - 3n\dot{v}_0 - 3Q_v - 2R_u) \\
c_v^2 &= -\frac{3}{2}R_v
\end{aligned}
$$

and finally in cross-track direction:

$$
w(t) = (a_w^0 + a_w^1 t)\cos nt + (b_w^0 + b_w^1 t)\sin nt + c_w^0 \tag{4.42}
$$

in which the coefficients are represented by:

$$
\begin{aligned}
a_w^0 &= \frac{1}{n^2}(n^2 w_0 - R_w) \\
a_w^1 &= \frac{-1}{2n}Q_w \\
b_w^0 &= \frac{1}{2n^2}(2n\dot{w}_0 + Q_w) \\
b_w^1 &= \frac{1}{2n}P_w \\
c_w^0 &= \frac{1}{n^2}R_w
\end{aligned}
$$

Here the complete solution for the particular resonant effect is given including the initial conditions at $t = 0$. Characteristic are the time dependent Fourier coefficients like $(a_u^0 + a_u^0 t)$ in the perturbations of u, v and w. These terms may be considered as a long periodic modulation of the signal similar to the perigee drift, compare Colombo (1986).

The non-resonant radial solution

In the previous paragraphs all possible solutions of the HE are discussed. For a comparison with the radial perturbations resulting from the LPE the particular radial part for the non-resonant case of the HE is worked out.

The problem is to evaluate the u-equation of (4.38) in which the terms P_u, Q_u, P_v and Q_v, the derivatives of the potential with respect to the 'Hill' coordinates, are substituted. Hence the first step is to develop the disturbing potential along a nominal satellite trajectory. Considering the same nominal orbit as in the LPT we find for the disturbance potential T in the circular case:

$$
T(t) = \sum_{m=0}^{lmax} \sum_{k=-lmax}^{lmax} \left[A_{km}\cos\psi_{km} + B_{km}\sin\psi_{km}\right]
$$

$$\psi_{km} = k\overline{\omega}_o + m\overline{\omega}_e \rightarrow \begin{cases} \overline{\omega}_o = \omega_o + \dot{\omega}_o t, & \omega_o = (\omega + M) \\ \overline{\omega}_e = \omega_e + \dot{\omega}_e t, & \omega_e = (\Omega - \theta) \end{cases} \tag{4.43}$$

$$(A_{km}, B_{km}) = \mu \sum_{l=m}^{l_{max}} \frac{(a_e/r)^l}{r} \overline{F}_{lm(l-k)/2}(I) \begin{bmatrix} \overline{C}_{lm} & \overline{S}_{lm} \\ -\overline{S}_{lm} & \overline{C}_{lm} \end{bmatrix}_{l-m:odd}^{l-m:even}$$

The summation is evaluated only when there exists an equal parity between l and k. The terms f_u, f_v and f_w in the HE can be found by differentiating (4.43) with respect to u, v and w. However the disturbing potential T in (4.43) is given in the coordinate system (ω_o, ω_e, r) whereas the Hill elements are represented by (u, v, w). It can be shown that (assuming a constant inclination):

$$\Delta u = \Delta r, \ \Delta v = r(\Delta\omega_e \cos I + \Delta\omega_o), \ \Delta w = -r\Delta\omega_e \cos\omega_o \sin I \tag{4.44}$$

and

$$\Delta r = \Delta u, \ \Delta\omega_o = \frac{\Delta v}{r} + \frac{\Delta w \cos I}{r\cos\omega_o \sin I}, \ \Delta\omega_e = \frac{-\Delta w}{r\cos\omega_o \sin I} \tag{4.45}$$

Accordingly the f_u, f_v and f_w terms become:

$$f_u = \frac{\partial T}{\partial r}, \ f_v = \frac{1}{r}\frac{\partial T}{\partial \omega_o}, \ f_w = \frac{1}{r\cos\omega_o \sin I}\{\frac{\partial T}{\partial \omega_o}\cos I - \frac{\partial T}{\partial \omega_e}\} \tag{4.46}$$

The terms f_u and f_v which are required in (4.38) take the form:

$$f_u = \frac{dT}{dr} = \sum_{m=0}^{l_{max}} \sum_{k=-l_{max}}^{l_{max}} [A^u_{km}\cos\psi_{km} + B^u_{km}\sin\psi_{km}], \text{ and}$$

$$f_v = \frac{1}{r}\frac{dT}{d\omega_o} = \sum_{m=0}^{l_{max}} \sum_{k=-l_{max}}^{l_{max}} [A^v_{km}\cos\psi_{km} + B^v_{km}\sin\psi_{km}] \text{ where}$$

$$(A^u_{km}, B^u_{km}) = \sum_{l=m}^{l_{max}} \frac{\mu a_e^l}{r^{l+2}}(-l-1) \begin{bmatrix} \overline{C}_{lm} & \overline{S}_{lm} \\ -\overline{S}_{lm} & \overline{C}_{lm} \end{bmatrix}_{l-m:odd}^{l-m:even}$$

$$(A^v_{km}, B^v_{km}) = \sum_{l=m}^{l_{max}} \frac{\mu a_e^l}{r^{l+2}} k \begin{bmatrix} \overline{S}_{lm} & -\overline{C}_{lm} \\ \overline{C}_{lm} & \overline{S}_{lm} \end{bmatrix}_{l-m:odd}^{l-m:even} \tag{4.47}$$

with $(l-k)/2 = p$ and parity(k, l). The next step is to evaluate the u-equation in (4.38) whereby $P_u = A^u_{km}$, $P_v = A^v_{km}$, $Q_u = B^u_{km}$ and $Q_v = B^v_{km}$. It results in:

$$u(t) = \sum_{m=0}^{l_{max}} \sum_{k=-l_{max}}^{l_{max}} [C^*\cos\psi_{km} + S^*\sin\psi_{km}] \tag{4.48}$$

where C^* equals to the 'cosine' term of the u-equation in (4.38):

$$C^* = \frac{-2nQ_v + \omega P_u}{\omega(n^2 - \omega^2)} = \frac{-2nB^v_{km} + \omega A^u_{km}}{\omega(n^2 - \omega^2)} =$$

$$= \sum_{l=m}^{l_{max}} \frac{\mu(a_e/r)^l}{n^2 r^2} \left\{\frac{\beta(l+1) - 2k}{\beta(\beta^2 - 1)}\right\} \begin{bmatrix} \overline{C}_{lm} \\ -\overline{S}_{lm} \end{bmatrix}_{l-m:odd}^{l-m:even}$$

and S^* to the 'sine' term of (4.38):

$$S^* = \frac{+2nP_v + \omega Q_u}{\omega(n^2 - \omega^2)} = \frac{+2nA^v_{km} + \omega B^u_{km}}{\omega(n^2 - \omega^2)} =$$
$$= \sum_{l=m}^{l_{max}} \frac{\mu(a_e/r)^l}{n^2 r^2} \left\{ \frac{\beta(l+1) - 2k}{\beta(\beta^2 - 1)} \right\} \begin{bmatrix} \overline{S}_{lm} \\ \overline{C}_{lm} \end{bmatrix}^{l-m:even}_{l-m:odd}$$

Here $\beta = \omega/n$ and $\omega = \dot{\psi}_{km}$. In the next step the term ψ_{km} is separated in two parts $(\psi_{km} = \psi^0_{km} + \dot{\psi}_{km} t)$

$$u(t) = \sum_{m=0}^{lmax} \sum_{k=-lmax}^{lmax} [C^{\#} \cos \dot{\psi}_{km} t + S^{\#} \sin \dot{\psi}_{km} t]$$
$$(C^{\#}, S^{\#}) = (C^*, S^*) \cos \psi^0_{km} + (S^*, -C^*) \sin \psi^0_{km} =$$
$$= \sum_{l=m}^{lmax} H_{lmk} \left[\begin{bmatrix} \overline{C}_{lm} & \overline{S}_{lm} \\ -\overline{S}_{lm} & \overline{C}_{lm} \end{bmatrix} \cos \psi^0_{km} + \begin{bmatrix} \overline{S}_{lm} & -\overline{C}_{lm} \\ \overline{C}_{lm} & \overline{S}_{lm} \end{bmatrix} \sin \psi^0_{km} \right]^e_o$$
$$H_{lmk} = \frac{\mu(a_e/r)^l}{n^2 r^2} \left\{ \frac{\beta(l+1) - 2k}{\beta(\beta^2 - 1)} \right\} \tag{4.49}$$

where e and o denote $l - m$: *even* and $l - m$: *odd*. This expression is identical with (4.26), the form Wagner (ibid) derived for the radial orbit error by application of the LPT.

However, there is a principal difference between both approaches. The LPE are exact differential equations and result in approximate perturbation equations after linearization with respect to a reference orbit. The HE are (1) implicitly linearized (2) represent a spherical approximation of the latter and (3) give exact solutions of the resulting differential equations.

Apparently it doesn't matter whether a first order LPT or the HE are employed since the two formulations for the radial orbit error are equivalent. Yet the LPT is more versatile than the HE since it can be used to e.g. derive elliptical solutions. In contrary to the LPE underlying the LPT are the HE which turn out to be more suitable for 'educational purposes'.

4.3 Comparison with numerically integrated orbits

In this section the validity of the analytical radial perturbations theory as given by (4.26) or (4.49) is discussed. The purpose of the analytical model is only to describe the residual radial differences since the major parts of the low-degree gravity field are already relatively well known.

The comparison of the analytical model with numerical integrated trajectories is confined to short arcs, i.e. up to a duration of 10 days. This period resembles the nowadays commonly used maximum period in orbit determination of altimeter satellites. It is likely that there is no particular need to model long periodic effects, e.g. induced by the perigee drift rate.

A second remark concerns the behavior of certain resonance phenomena which are caused by the term $(\beta(l+1)-2k)/(\beta(\beta^2-1)), \beta = \dot{\psi}_{km}/n_0$ in (4.49). Considering the amplitudes of the perturbations we conclude that they become large when:

- $\dot\psi_{km} \rightarrow 0$, a situation which occurs due to resonance of potential coefficients of a particular order $m, m \neq 0$. Resonance may become extreme when the ratio of $\dot\omega_o$ and $\dot\omega_e$ approaches an integer value.
- $\dot\psi_{km} \rightarrow \pm n_0$, showing up for odd zonal terms. This causes long periodic oscillations due to the secular motion of the argument of perigee.

It is obvious that both situations require a special treatment for which a non-linear theory may be required. Taking into account the range of applications of the analytical theory there is no need for a non-linear theory here. In the process of orbit determination long periodic effects are simply absorbed in the initial state vector adjustment and the estimation of drag and solar radiation parameters.

In the experiment conducted we integrated numerically a 10 day orbit twice using different potential coefficient models. For the reference orbit we applied the gravitational model GEM-10B, (Lerch et al.,1981). No effects other than perturbations due to the gravitational field were taken into account. The nominal elements were chosen in agreement with the three day repeat orbit of SEASAT: firstly the repeat ratio $((\dot\omega + \dot M)/(\dot\Omega - \dot\theta))$ was chosen -43/3, which implies that after 43 revolutions the ground track coincides with the initial one, secondly the eccentricity was kept small ($e \approx 0.002$) and thirdly the inclination of the orbital plane was chosen 108°. The initial elements employed in this experiment are listed in table 4.1.

GEM-10B reference	
$a = 7160472.5590$ m	$\Omega = 0°$
$e = 0.001$	$\omega = 90°$
$I = 108°$	$M = 0°$
PGS-S4 adjusted to GEM-10B	
$a = 7160471.0680$ m	$\Omega = 359.999978154°$
$e = 0.000999962108$	$\omega = 89.948286077°$
$I = 107.999983752°$	$M = 0.051778873°$
Common data	
epoch 05/11/86 till 15/11/86	
$a_e = 6378137$ m and $\mu = 3.986005 \times 10^{14}$ m^3/s^2	
11th order Cowell predictor-corrector	
75 s fixed step size	

Table 4.1: Initial elements and other data used in the numerical orbit generation and data reduction by GEODYN.

It should be remarked that the amount of frequencies appearing in the perturbation spectrum of repeating orbits is less than those of non-repeating orbits. Take for example a perturbing frequency caused by the combination $k = 1$; $m = 14$ which is identical in frequency, but shifted in phase by 180°, with the combination $k = 2$; $m = 29$:

$$\dot\psi_{km} = k\dot\omega_o + m\dot\omega_e, \quad \text{with } \dot\omega_e = -\frac{3}{43}\dot\omega_o \Rightarrow$$

$$\dot{\psi}_{km} = (k - \frac{3}{43}m)\dot{\omega}_o \Rightarrow$$

$$k = 1, m = 14 \rightarrow (1 - \frac{42}{43})\dot{\omega}_o = +\frac{1}{43}\dot{\omega}_o$$

$$k = 2, m = 29 \rightarrow (2 - \frac{87}{43})\dot{\omega}_o = -\frac{1}{43}\dot{\omega}_o$$

For gravity field recovery it is preferable to consider orbits which do not repeat in a short period since their spectra contain less individual frequencies than non-repeating orbits. As a consequence different combinations of k and m, generating separate frequencies in the non-repeating case, result here in one overlapping frequency.

The second orbit in the experiment was integrated numerically using the potential coefficient model PGS-S4, a tailored gravity model for SEASAT developed by Lerch et al. (1982a). The choice of both gravity models is entirely arbitrary and not considered critical or relevant for the experiment. The objective is, as stated before, merely to verify the analytical perturbations theory.

The initial state vector of the 'PGS-S4' orbit is adjusted in several iterations in order to minimize the differences between both trajectories. The initial elements recovered by GEODYN for the PGS-S4 orbit are listed in table 4.1. The adjustment of the initial elements takes place in x, y, z and $\dot{x}, \dot{y}, \dot{z}$. For readability the initial elements are represented in the form of Keplerian elements.

In both cases the program GEODYN (Martin et al.,1976) was used. A more detailed treatment of the numerical orbit generation and initial state vector improvement is given in §4.3.1. The outcome of the experiment, being the radial differences of two trajectories integrated with independent gravity models, is the basis for further investigations.

4.3.1 Orbit generation and initial state vector improvement

A numerical technique commonly employed for integrating satellite trajectories is known as the Cowell method. Thereby the equations of motion are integrated numerically using a high-order Runge-Kutta or multistep predictor-corrector method such as Adams-Moulton or Adams-Bashforth, compare Conte et al. (1986), or Taff (1985) pp. 392-393.

Characteristic of Runge-Kutta integrators is that they evaluate the function to be integrated, being an 'expensive' summation in spherical harmonics, a number of times depending on the order of the method. In contrast multistep methods are more efficient since they re-use the previous state vectors and their derivatives with respect to the time in the prediction and correction of the new state vector. Each prediction and correction step takes one function evaluation independent of the order of the integrator.

The high orders (e.g. above 8) of the integrators are required to diminish the inherent truncation error of the integration method. Cowell's method is by nature sensible for truncation effects. Irrespective of the order of the integrator instability will occur after a certain time, compare Taff (1985).

The system of differential equations to be integrated by Cowell's method is derived by a transformation of the equations of motion into 6 first order differential equations:

$$
\begin{aligned}
&\ddot{\overline{S}} = \nabla V + \sum_j \overline{f}_j \quad \Rightarrow \\
&\frac{\partial \dot{S}_i}{\partial t} = \frac{\partial V}{\partial S_i} + \sum_j \frac{d\overline{f}_j}{dt}, \quad i = 1 \cdots 3 \\
&\frac{\partial S_i}{\partial t} = \dot{S}_i, \quad i = 1 \cdots 3
\end{aligned}
\tag{4.50}
$$

where $\overline{S} = (x, y, z)$ represents the position part of the state vector in an inertial coordinate system. The function V represents the gravitational potential whereas $\overline{f}_i$ represents disturbing forces other than the gravitational.

For the experiment an initial state vector estimation was carried out for the purpose of minimizing the state vector differences between both trajectories. This resembles the real-world situation of orbit determination where discrepancies between the 'model' satellite orbit (starting at an estimated initial state) and tracking measurements are minimized. Ideally one likes to improve:

- the initial state vector consisting of $\overline{S}(t_0)$ and $\dot{\overline{S}}(t_0)$,
- terms in $\overline{f}_i$, usually C_d (drag) and C_r (radiation pressure) coefficients,
- terms in the gravitational model V,
- other parameters such as tracking station coordinates.

It is convenient to merge the unknown parameters in a single vector $\overline{\beta}^*$:

$$
\overline{\beta}^* = (\underbrace{x, y, z, \dot{x}, \dot{y}, \dot{z}}_{\text{state vector}}\ \underbrace{\overline{C}_{lm}, \overline{S}_{lm}, \ldots}_{\text{V}}\ \underbrace{C_d, C_r, \ldots}_{\overline{f}_i}) \tag{4.51}
$$

in which for our needs only the first six terms are used. The next step is to differentiate the right as well as the left hand side of (4.50) with respect to the first 6 elements of $\overline{\beta}^*$, which for sake of brevity is denoted as $\overline{\beta}$. This results in a system of 36 first order differential equations known as the *variational equations:*

$$
\begin{aligned}
&\frac{\partial^2 \dot{S}_i}{\partial \beta_k \partial t} = \frac{\partial^2 V}{\partial S_i \partial S_j} \frac{\partial S_j}{\partial \beta_k} \quad i, j = 1 \cdots 3, \ k = 1 \cdots 6 \\
&\frac{\partial^2 S_i}{\partial \beta_k \partial t} = \frac{\partial \dot{S}_i}{\partial \beta_k}
\end{aligned}
\tag{4.52}
$$

The purpose of the variational equations is to derive a transition matrix Φ relating the variations in the state vector at a certain epoch to the initial state vector at $t = t_0$. The terms $\partial \dot{S}_i / \partial \beta_k$ and $\partial S_i / \partial \beta_k$ form the elements of the transition matrix which is updated continuously at each integration step. The transition matrix becomes:

$$\Phi(t,t_0) = \begin{bmatrix} \partial x(t)/\partial x_0 & \partial x(t)/\partial y_0 & \cdots & \partial x(t)/\partial \dot{z}_0 \\ \partial y(t)/\partial x_0 & \partial y(t)/\partial y_0 & \cdots & \partial y(t)/\partial \dot{z}_0 \\ \vdots & \vdots & \ddots & \vdots \\ \partial \dot{z}(t)/\partial x_0 & \partial \dot{z}(t)/\partial y_0 & \cdots & \partial \dot{z}(t)/\partial \dot{z}_0 \end{bmatrix}. \tag{4.53}$$

Note that $\Phi = I$ at $t = t_0$. The actual computation of Φ requires that 42 differential equations are integrated simultaneously. In order to reduce the amount of computing work in an orbit determination algorithm the second order derivatives in (4.52) are evaluated up to limited degree (e.g. 4) which is usually sufficient for convergence in the initial state vector estimation process. For our problem the transition matrix is used as a coefficient matrix in a least squares adjustment in which the initial state vector is estimated from the state vector differences between both trajectories. The observation equations become:

$$\vec{\beta}_{\text{PGS-S4}}(t) - \vec{\beta}_{\text{GEM-10B}}(t) = \Phi(t,t_0)\Delta\vec{\beta}(t_0). \tag{4.54}$$

Summarizing, the procedure of orbit generation and initial state vector improvement consists of the following steps:

1. Integration of the equations of motion, as given in (4.50), starting at a well chosen initial state vector using the potential coefficient model GEM-10B (the method of determining the first initial state vector is discussed in chapter 6),
2. the first initial state vector to start the integration of the PGS-S4 orbit is set to the initial state vector employed in step 1,
3. integration of the equations of motions as given in (4.50) including the variational equations as given in (4.52) while using the PGS-S4 model,
4. computation of $\overline{\Delta\beta}$ using (4.54) in a least squares adjustment,
5. updating of the initial state vector, i.e. the existing initial state vector is improved by $\overline{\Delta\beta}$.
6. repeat from 3 on until convergence, i.e. no more significant improvement of the state vector differences between both trajectories.

Under normal circumstances only 3 to 4 iterations are required for convergence. The final result is a radial difference signal between both trajectories which is the basis for a comparison with the analytical model.

4.3.2 Comparison with the analytical model

A number of experiments have been carried out for the actual comparison.

Firstly the radial differences between the reference (GEM-10B) and the perturbed (PGS-S4) orbit have been transformed into the frequency domain using a mixed radix FFT subroutine, compare Singleton (1969). The time signal and the power

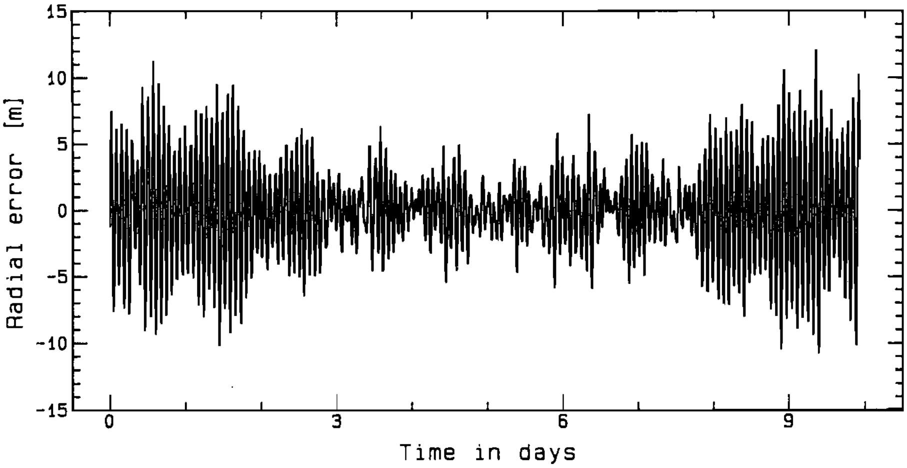

Figure 4.4: The radial orbit error in the simulation experiment caused by the full differences of the potential coefficient models GEM-10B and PGS-S4. On the horizontal axis the time is represented in days, on the vertical axis the radial perturbation in meters.

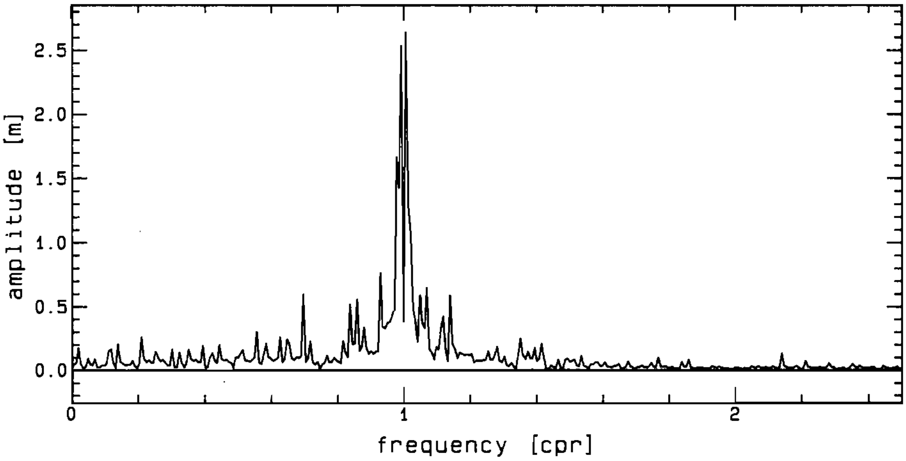

Figure 4.5: The amplitude spectrum of the radial perturbations in the simulation experiment. On the horizontal axis the frequency is represented in cycles per revolution, on the vertical axis the power density is represented in units of m per 1/129 c.p.r.

spectrum of residual radial differences are shown in figures 4.4 and 4.5. From these figures we can conclude that most of the radial difference signal is concentrated near the once per revolution frequency. Computations have shown that most of the signal is concentrated below three cycles per revolution, the remaining signal > 3 c.p.r. has a total power of 15 cm. Both effects agree with the analytical model: radial perturbations are amplified near once per revolution and decrease rapidly at higher frequencies. The mechanism can be compared with that of a band-pass filter.

In the time signal as given in figure 4.4 we note the 'butterfly' or bow tie (⋈) type of pattern. Typically the radial difference signal is large at the edges and small in the center of the figure. This phenomenon can be explained by a long periodic modulation of the signal due to constant and once per revolution perturbing forces. The phenomenon can be modeled by the special (resonant) particular solution of the HE. The c_u^0 and c_u^1 terms in (4.40) do not show up since these terms were already removed by the initial state vector adjustment.

A similar analysis as presented in figures 4.4 and 4.5 has been performed by Wakker et al. (1983,1987). Their analysis of orbital errors simulated by differences of gravitational models is nearly identical to the results presented here.

Secondly the analytical spectrum is derived by an evaluation of (4.49) using as potential coefficients the differences between the GEM-10B and the PGS-S4 model. The analytical model requires knowledge of a number of variables which are derived from the numerical satellite trajectory. The combinations $\omega(t_0) + M(t_0)$ and $\Omega(t_0) - \theta(t_0)$ determine the *phase* behavior of the perturbation spectrum and hold at the starting point of the trajectory. They have to coincide with the orbital elements at the offset time used in the computation of the numerical spectrum. The *frequency* behavior of the spectrum is determined by a combination of the terms $\dot{\omega} + \dot{M}$ and $\dot{\Omega} - \dot{\theta}$. These terms are computed from the average revolution period of the satellite and the longitude displacement of the ascending equator transit points. Let the average revolution period be defined as τ ($\approx$ 6045.5 sec.) and the mean longitude displacement as $\Delta\lambda$ ($\approx -25.1°$), the relation with $\dot{\omega} + \dot{M}$ and $\dot{\Omega} - \dot{\theta}$ is:

$$\dot{\omega}_o = \dot{\omega} + \dot{M} = \frac{2\pi}{\tau} \quad \wedge \quad \dot{\omega}_e = \dot{\Omega} - \dot{\theta} = \frac{\Delta\lambda}{180}\frac{\pi}{\tau}. \tag{4.55}$$

The resemblance between the numerical – and the analytical spectrum is poor at frequencies very close to once per revolution, compare also (Wagner,1985). This is not surprising since there are a number of overlapping effects close to once per revolution. Wagner (ibid) mentions the effect due to the odd zonal coefficients of the gravitational field which are in deep resonance for $k = \pm 1$ and $m = 0$. However unsolved initial state vector effects are also contributing to the once per revolution signal. For this reason no further attempts are made to describe this exact once per revolution effect.

Instead the numerical spectrum is filtered by removing a function of the form of (4.40) from the raw signal. After this precaution the filtered numerical spectrum agrees well with the analytically generated spectrum. Most real and imaginary terms differ typically up to 1–5%. The frequencies of the perturbations match more accurately, usually in the order of 0.25% counted in cycles per revolution. Included is figure 4.6 containing the numerical filtered spectrum and figures 4.7 and 4.8, representing the differences between the numerical and the analytical power and phase spectra.

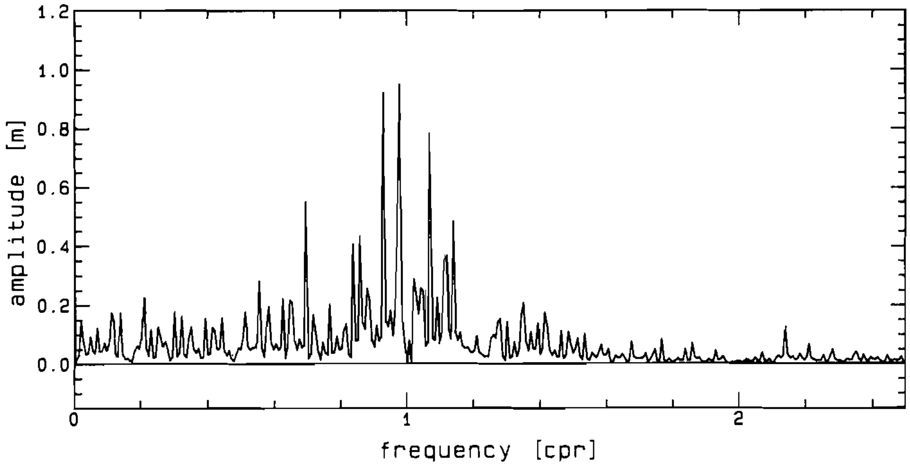

Figure 4.6: The radial perturbation amplitude spectrum filtered for resonant particular Hill effects. On the horizontal axis the frequency is represented in cycles per revolution, on the vertical axis the power density is given in m per 1/129 c.p.r.

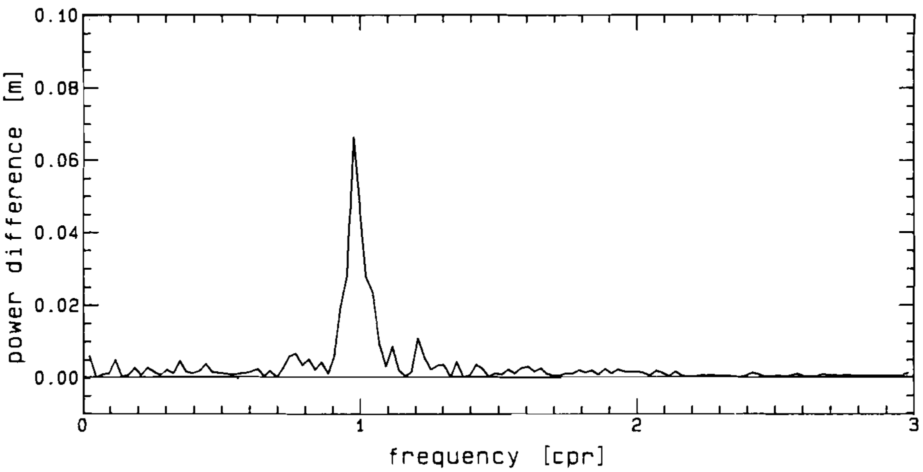

Figure 4.7: The residual radial perturbation amplitude spectrum. The residual consists of the difference between the filtered numerical radial orbit error and the analytical radial orbit error. On the horizontal axis the frequency is represented in cycles per revolution, on the vertical axis the power density is given in m per 1/43 c.p.r.

It can be concluded from this comparison that the analytical model differs mostly from the numerical results close to once per revolution. The phase differences are

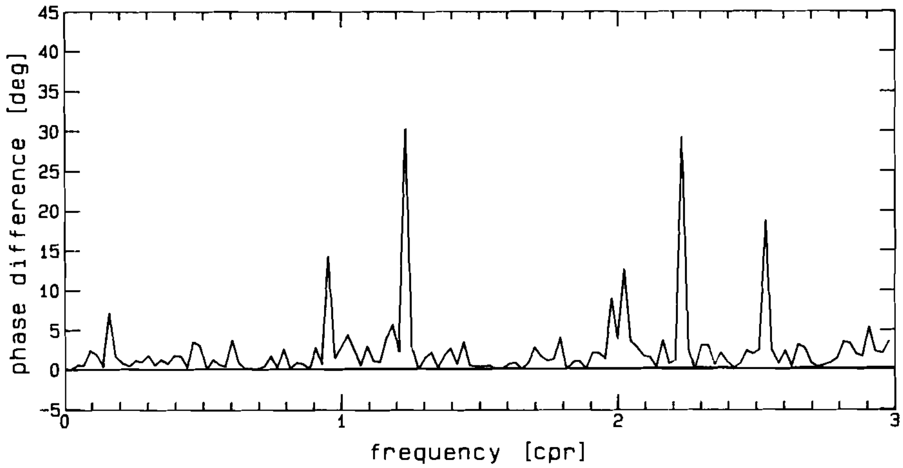

Figure 4.8: The residual radial perturbation phase spectrum. The residual consists of the difference between the filtered numerical radial orbit error and the analytical radial orbit error. On the horizontal axis the frequency is represented in cycles per revolution, on the vertical axis the phase distortion is given in degrees per 1/43 c.p.r.

in the order of 5° to 10° and show a number of outliers at locations in the spectrum where hardly any signal is found.

4.4 Conclusions

In this chapter we discussed the characteristics of a radial orbit error $\Delta r(t)$ for near circular satellite trajectories caused by uncertainties of potential coefficients. In first instance the linear perturbations theory, as introduced by Kaula (1966), is applied to derive an expression for $\Delta r(t)$. The LPT is based on the Lagrange planetary equations which are solved with the aid of a general perturbations technique. This results in six equations describing the perturbations of the Keplerian elements about a nominal orbit. The latter expressions are used to derive radial perturbation equations in which the deviations of the satellite are related to potential coefficients of the gravitational model.

Two approximations have been used to come from the exact LPE to a convenient model describing radial perturbations. The first concerns the derivation of the perturbations in the elements from the LPE with respect to a nominal orbit. The second concerns the transformation of these elements into a convenient radial expression. In the latter transformation long periodic oscillations induced by the argument of perigee are neglected. For our purposes it should be kept in mind that a perturbations theory is needed for (1) near circular orbits and for (2) periods up to 10 days.

As an alternative, the Hill equations have been used to verify the radial perturbations as found by the conventional LPT. The HE consist of three differential equations describing radial (u) along track (v) and cross track (w) components of a satellite moving in an uniformly rotating coordinate system. Implicitly the HE describe, in contrast to the LPE, an idealized circular situation. The three differential equations forming the HE can be solved undisturbed or disturbed resulting in the homogeneous and particular solutions respectively.

The homogeneous case describes the behavior of the u,v and w terms in absence of any disturbing force function. The result is equivalent to perturbations caused by initial state vector disturbances. The nature of the homogeneous radial perturbations is an exact once per revolution oscillation and a radial bias. The magnitudes of the constants in is radial expression are determined by the initial conditions of the homogeneous system.

The particular solutions describe the behavior of the u, v and w terms as a result of perturbing forces acting on the satellite. The perturbing forces were expressed in a Fourier series. Solutions are shown for two cases, a 'normal' and a 'special' or 'resonant' case.

In the normal particular case oscillating disturbing forces are chosen at any frequency except for two singular frequencies. These singular frequencies are at zero and once per revolution. Characteristic is the linear response of the system in normal particular cases: a perturbing force at the frequency ω causes oscillations in the terms u, v and w at the same frequency ω. The normal particular case has been evaluated for gravitational disturbances. It could be shown that it results in an identical analytical formulation as coming from the LPT.

In the special particular case the oscillating disturbing forces are chosen at the two singular frequencies. The solution of this problem can be regarded as a long periodic modulation of the u term resulting in a function resembling a 'butterfly' or 'bow tie' pattern.

The normal particular solution has been compared with the radial differences that occur between two 10 day numerically derived SEASAT trajectories. The differences between the trajectories are only caused by different gravitational models, here GEM-10B and PGS-S4. It was demonstrated by means of this simulation that a good agreement can be achieved between the predicted analytical radial perturbations and the numerical results. This indicates that the analytical perturbations theory is valid to describe the altimetric situation, provided that arc length is less than 10 days.

In the following chapters the analytical perturbations model is used as a tool to study the influence of radial orbit errors in satellite altimetry.

Chapter 5

Identification and spectral characteristics of crossover and repeat arc differences

5.1 Crossover differences

The main reason to apply crossover observations instead of the direct distance measurement of the radar altimeter above the sea surface was already discussed in chapter 2. On intersections of the ground tracks the geoid error contribution is eliminated since it may be considered as a stationary surface. As a consequence crossover differences are mainly caused by the radial orbit error, and secondarily by unmodeled tidal effects and ocean variability. Eliminated by means of the crossover technique are all permanent structures which determine the shape of the sea surface such as the geoid and the permanent sea surface topography. Hence for the purpose of 'orbit error removal' it seems useful to minimize the height differences at crossovers by means of a least squares adjustment of parameters of error functions defined along individual arc segments, compare chapter 3.

In this section we first consider a more elementary problem: how does one efficiently compute the actual crossover locations, timings (so-called time tags) and height differences from a given altimeter dataset such as described in chapter 2.

Then some characteristics of crossovers are described such as their cluster forming at equal differences of the crossover time tags. This property is used to get a better insight in the spatial distribution of the crossovers. Furthermore cluster forming is also used to analyze the spectral behavior of the crossover differences, compare (Goad et al.,1980) and (Douglas, Agreen, Sandwell,1984). Of special interest are the invariances of crossover differences to certain parts of the orbit error.

These invariances are closely related to the fact that crossover differences behave invariant with respect to geographically correlated radial orbit errors. These effects show an equal signal for the ascending and descending arc segment at a particular location. For this reason a part of the radial orbit error cancels after subtraction of the ascending and descending sea surface heights. This phenomenon has been mentioned by various authors, compare Anderle & Hoskins (1977), Tapley et al. (1985) and Sandwell et al. (1986).

5.1.1 Computation of crossover data

The actual computation of 1) crossover locations, 2) times at which they occur and 3) sea surface heights at these times are typical problems that have to be solved during processing of radar altimeter data. Here the computation of crossover data is done in several steps.

In the prediction step crossover time tags are estimated by assuming a circular motion of the satellite. The resulting crossovers possess some interesting properties which are considered later on in the derivation of the eigenvectors spanning up the null space of the normal matrices of global chronological crossover adjustments.

In the refinement step the given altimeter data on the GDR dataset is interpolated at the predicted crossover times. Additionally, it is possible to perform successive iterations of the interpolation procedure in order to arrive at improved crossover positions and time tags.

Prediction of crossovers

In first instance we consider the modeling of the nominal ground track of the satellite. Taking into account the properties of altimeter orbits, ground tracks resemble sine waves functions mirror symmetric with respect to the equator, compare figure 3.2.

Essential quantities which determine the nature of the nominal ground track are the inclination of the orbital plane I, the variable ω_o representing $(\omega + M)$ and ω_e which is equal to $(\Omega - \theta)$. The behavior of these quantities is conform the linear perturbations theory, cf. chapter 4. Hence ω_o and ω_e are linear functions of time whereas I behaves as a constant. As a result the nominal satellite motion in an Earth fixed coordinate system becomes:

$$\overline{x}_e = R_3(-\omega_e)R_1(-I)\begin{pmatrix} r\cos\omega_o \\ r\sin\omega_o \\ 0 \end{pmatrix} \tag{5.1}$$

Here $\overline{x}_e$ equals to the position vector in an Earth fixed coordinate system, whereas R_1 and R_3 denote Euler rotation matrices for rotations about the x and z axis, respectively. Here we assume the z axes of the inertial and Earth fixed coordinate system to coincide. An evaluation of (5.1) results in:

$$\begin{pmatrix} x \\ y \\ z \end{pmatrix} = r\begin{pmatrix} \cos\omega_e\cos\omega_o - \sin\omega_e\cos I\sin\omega_o \\ \sin\omega_e\cos\omega_o + \cos\omega_e\cos I\sin\omega_o \\ \sin I\sin\omega_o \end{pmatrix} \tag{5.2}$$

Simulations have demonstrated that (5.1) is accurate to approximately ± 10 km about the true orbit. Effects ignored in (5.1) are the eccentricity and other oscillating perturbations caused by the flattening parameter J_2 of the Earth's gravitational field.

It has been demonstrated by simulations that the largest radial perturbations with respect to the nominal orbit could easily be modeled by an auxiliary function. This function resembles the special (resonant) solution of the HE including a twice per revolution term to model the J_2 perturbations. After addition of the auxiliary function the remaining differences are usually less than ± 100 m with respect to the true orbit. Compare also Rosborough (1986) where the radial perturbations of the TOPEX satellite are discussed.

For the purpose of computing the predicted crossover positions and times at which they occur one should be aware of the facts that:

- The footprint diameter of a pulse limited radar is of the order of 2.4 to 12 km, a value depending on the sea surface roughness in the footprint area. The height observations can be considered as some average value of the sea surface height over the footprint area.
- On the GDR's the sample interval of the altimeter data is approximately 1 second which is equivalent to some 7 km in along track direction. (This refers to the SEASAT GDR's, GEOSAT measurements are supplied at 10 observations per second) The consequence is that interpolation has to be performed in order to determine the proper values at the intersection point.

As a result it is probably sufficient to compute predictions of preliminary crossovers by (5.1) which is accurate to ≈ 10 km. Hence for the purpose of crossover prediction the following procedure is applied:

- Arc segments are defined: A segment starts at the lowest and ends at the highest latitude (or visa versa). For each segment, which is either ascending or descending, the equator transit longitude and time is computed.
- From the equator transit data the terms $\dot{\omega}_e$ and $\dot{\omega}_o$ are determined, compare equation (4.55).
- Eventually, for each ascending arc segments against all descending ones, equation (5.1) is solved for both arc segments resulting in a crossover position and two time tags, compare figure 5.1. The topology of the situation shows that $N_a \times N_d$ crossovers will be generated out of N_a ascending and N_d descending arc segments.

Properties of predicted crossovers

In the sequel we distinguish between ***absolute*** and ***relative*** time tags of crossovers. Absolute time tags are defined in the time system used during orbit determination, relative time tags are counted from the current equator transit time in the arc segment forming the crossover. From the procedure described above we find predicted crossovers fulfilling three important properties.

Antisymmetry: The relative time tags of the ascending and the descending part of the predicted crossovers in equation (5.1) are of an opposite sign. In order to demonstrate this we consider at a crossover the condition:

$$\begin{aligned} \omega_e^a &= \lambda_{\phi=0}^a + \dot{\omega}_e \Delta t^a & \omega_e^d &= \lambda_{\phi=0}^d + \dot{\omega}_e \Delta t^d - \pi \\ \omega_o^a &= \dot{\omega}_o \Delta t^a & \omega_o^d &= \dot{\omega}_o \Delta t^d + \pi \end{aligned} \qquad (5.3)$$

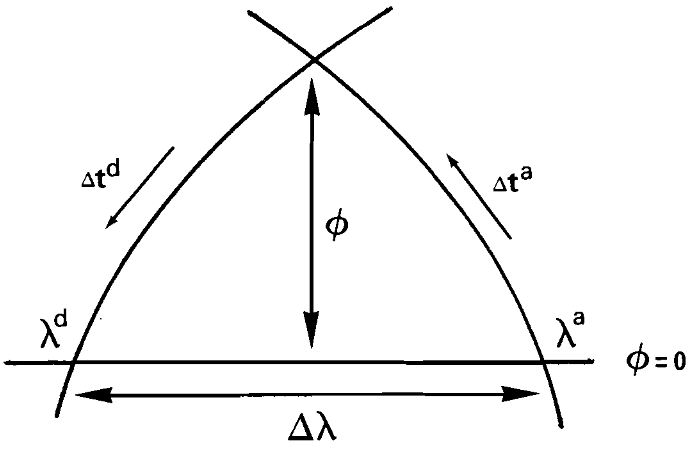

Figure 5.1: Analytically predicted crossovers in the nominal orbit.

where $\lambda_{\phi=0}$ denotes the transit longitude and Δt the relative time tag. The superscripts indicate whether the quantities affect an ascending or a descending arc segment. The corrections $+\pi$ and $-\pi$ to respectively ω_o^d and ω_e^d are required to convey the arc segment from ascending into descending. Substitution of (5.3) in the z-equation of (5.1) results in:

$$z^a = z^d \quad \Rightarrow \quad \sin(\dot{\omega}_o \Delta t^a) = \sin(\dot{\omega}_o \Delta t^d + \pi) \quad \Rightarrow \quad \Delta t^a = -\Delta t^d \tag{5.4}$$

which is a necessary condition at a crossover point. In the sequel, crossovers fulfilling this property are referred to as antisymmetric. The relative time tag $\Delta t = \Delta t^a = -\Delta t^d$ of antisymmetric crossovers fulfills the condition $|\Delta t| < \tau/4$ where τ represents the satellite revolution period.

Time tag versus latitude: The magnitude of the relative time tag Δt is only dependent of the latitude ϕ provided that the inclination I and $\dot{\omega}_o$ are constant. This follows directly from eq. (5.1): $\sin\phi = \sin I \sin(\dot{\omega}_o \Delta t)$.

Longitude separation dependency: The relative time tag Δt and the latitude ϕ of an antisymmetric crossover are only determined by the quantity $\Delta\lambda = \lambda^a_{\phi=0} - \lambda^d_{\phi=0}$, compare figure 5.1. In order to demonstrate this property we substitute (5.3) in (5.1) and demand that $x^a = x^d$ and $y^a = y^d$, it follows that:

$$\begin{bmatrix} x^a \\ y^a \end{bmatrix} = R(\omega_e^a)\,\overline{v}(\omega_o^a) = \begin{bmatrix} x^d \\ y^d \end{bmatrix} = R(\omega_e^d)\,\overline{v}(\omega_o^d) \quad \text{where}$$

$$R(\alpha) = \begin{bmatrix} \cos\alpha & -\sin\alpha \\ \sin\alpha & \cos\alpha \end{bmatrix} \quad \text{and } \overline{v}(\beta) = \begin{bmatrix} \cos\beta \\ \cos I \, \sin\beta \end{bmatrix}$$

Since $R(\alpha_1 + \alpha_2) = R(\alpha_1)\,R(\alpha_2)$ and $R(-\alpha) = R^{-1}(\alpha)$ and $\Delta t^a = -\Delta t^d = \Delta t$ we find:

$$R(\lambda^a_{\phi=0} + \dot{\omega}_e \Delta t)\,\overline{v}(\dot{\omega}_o \Delta t) = R(\lambda^d_{\phi=0} - \dot{\omega}_e \Delta t - \pi)\,\overline{v}(-\dot{\omega}_o \Delta t + \pi) \Rightarrow$$

$$R(2\dot{\omega}_e\Delta t + (\lambda^a_{\phi=0} - \lambda^d_{\phi=0}))\,\overline{v}(\dot{\omega}_o\Delta t) + \overline{v}(-\dot{\omega}_o\Delta t + \pi) = 0 \tag{5.5}$$

This expression shows that Δt is determined by $\Delta\lambda = \lambda^a_{\phi=0} - \lambda^d_{\phi=0}$. Apparently the relative crossover time tags are invariant to rotation about the z axis of the Earth fixed coordinate system.

An interesting consequence of eq. (5.5) is that there exists a functional relation between Δt, ϕ and $\Delta\lambda = \lambda^a_{\phi=0} - \lambda^d_{\phi=0}$ in the form of:

$$\Delta t = F(\lambda^a_{\phi=0} - \lambda^d_{\phi=0}) \;\wedge\; \phi = G(\lambda^a_{\phi=0} - \lambda^d_{\phi=0}) \tag{5.6}$$

It will be obvious that (5.4) and (5.5) become helpful when the predicted crossovers are computed. For computing efficiency, a function like (5.6) is computed only once and tabulated in a crossover prediction algorithm.

A numerical approach is applied to solve the prediction problem. From the various approaches tested it was found that the following results in accurate roots within usually less than 5 iterations. The procedure is as follows:

1. Let $\overline{p}$ denote the position vector at the ascending equator transit point and $\overline{q}$ its descending counterpart. (the vectors $\overline{p}$ and $\overline{q}$ are derived from (5.1)).

2. The orbital plane through $\overline{p}$ (spanned up by the in-plane vectors $\overline{p}$ and $\dot{\overline{p}}$) and the orbital plane through $\overline{q}$ are intersected to yield an approximate crossover position vector with the relative time tags Δt^a and Δt^d.

3. The vectors $\overline{p}$ and $\overline{q}$ are replaced by the new predicted ones which are computed by (5.1) using the relative time tags found in the previous step.

4. If $|\overline{p} - \overline{q}| > \epsilon$ then repeat from 2 on.

An example of (5.6) is evaluated and presented in figure 5.2 for the simulated orbit described in chapter 4. We conclude that predicted crossovers possess the following characteristics:

- A large number of crossovers reside at the high latitudes. Figure 5.2 shows that if $75^\circ < |\Delta\lambda| < 180^\circ$ then $|\phi| > 60^\circ$. We conclude that more than 50% is located above or below $\pm 60^\circ$ latitude. (we assume that ground track transit longitudes are homogeneously distributed over the equator). The situation deteriorates for higher inclinations, e.g. at $I = 90^\circ$ there exist crossovers only at $|\phi| \neq 90^\circ$ if $-12.5^\circ < \Delta\lambda < 12.5^\circ$. (approximately the longitude displacement in one revolution of the satellite.) As a result only $\frac{25}{360}100\% \approx 7\%$ of the crossovers is actually applicable.

- The geometry of the configuration shows that solutions of (5.6) are only of interest when $|\Delta t| \leq \tau/4$, with τ representing the revolution period and $|\Delta\lambda| < 180^\circ$. Due to (5.1) $|\phi| \leq I$ is always fulfilled.

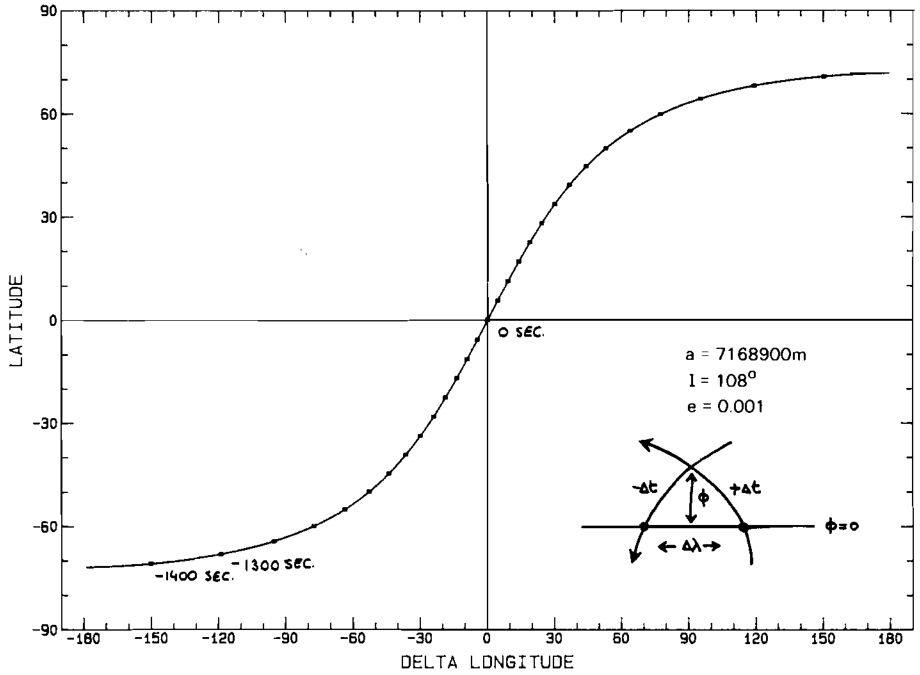

Figure 5.2: The horizontal axis represents the longitude separation and the vertical axis the latitude of a predicted crossover. The relative time tags of the ascending ground track are represented by dots along the function at a 100 second interval starting at -1400.

Improvement of predicted crossovers

In reality, the true ground track tends to deviate from the nominal. Hence 'real world' crossovers differ slightly from antisymmetric crossovers. For this reason eq. (5.6) is applied for predicting the absolute crossover time tags in the given altimeter dataset.

In a second iteration the improved crossovers are derived by computing at the predicted points the intersections of the tangents of the ground track as given on the altimeter tape, compare Rowlands (1981). The tangents of the local ground track are estimated from the supplied ground track position samples. Computations have shown that time tag corrections in the order of 1.5 s occur in the second iteration.

The result is an improved crossover file which can serve again as a prediction for successive iterations. It was verified that the crossover time tag corrections in a third iteration step were in the order of 10^{-3} s. This indicates that one prediction and one improvement step is required for accurate crossover computation.

Efficiency of the crossover algorithm

The algorithm described above is rather efficient especially when a-priori tabulated F and G functions, as given in (5.6), are used in the prediction step. As an extra option one could avoid the prediction of crossovers on land or outside a local area, either rectangular or diamond shaped. This restricts the number of predicted crossovers to be stored and increases the efficiency of the algorithm.

Unfortunately the improvement steps are more 'expensive' since they consist of (1) sorting the predicted absolute time tags and (2) input output operations to large tape datasets. Especially this last step tends to be 'expensive' on most computer systems. Theoretically the resulting crossover file may become quite large growing quadratically in time. In the case of SEASAT this results in 10^6 crossovers formed by ≈ 2000 arc segments. Whether it is required or not to compute all the crossovers is a topic that will be discussed later on.

5.1.2 Spectral characteristics of crossover differences

In this section we describe the spectral characteristics of crossover differences on basis of the separation of the absolute time tags, compare Goad et al. (1980) and Douglas et al. (1984). The first step is to verify that the absolute time tag differences, represented by δt, are clustered in groups inside an uninterrupted orbital period. Secondly it is possible to model the height difference signal of the crossovers inside a cluster by means of one unique function. The characteristics of this function including the way it is sampled typifies the behavior of crossover differences.

Clustering of absolute time tag differences

The absolute time tag difference at a crossover is defined as $\delta t = t^a - t^d$ where t^a and t^d represent respectively the ascending and descending time tag. As mentioned before the relative time tags Δt^a and Δt^d are related to t^a and t^d by:

$$t^a = t^a_{\phi=0} + \Delta t^a \ \wedge \ t^d = t^d_{\phi=0} + \Delta t^d \tag{5.7}$$

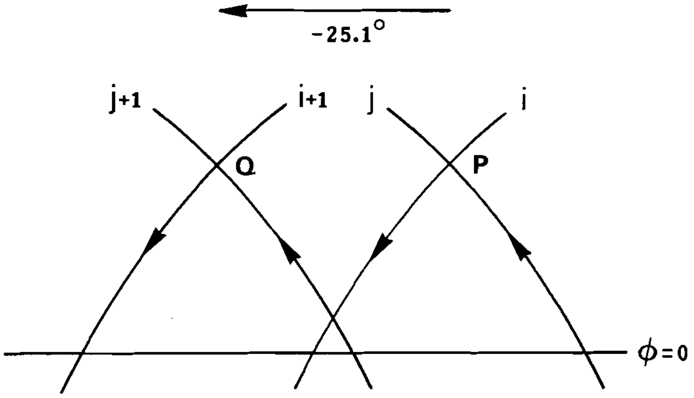

Figure 5.3: Cluster forming of crossovers on latitude bands.

where $t^a_{\phi=0}$ and $t^d_{\phi=0}$ represent the equator transit times of respectively the ascending and descending ground track forming the crossover. For crossovers formed by the nominal orbit we concluded that Δt^a and Δt^d possess the same magnitude but an opposite sign. Furthermore we concluded that their values were determined only by the longitude separation $\Delta\lambda$ of the ascending and descending equator transit longitudes.

It is easy to verify that there are several crossovers having an equal longitude separation. This is illustrated in figure 5.3 where it is assumed that arc segments i and j form a crossover P. Imagine that exactly one revolution period τ is added to both absolute time tags forming the crossover. This results in an equivalent configuration of intersecting arc segments $i+1$ and $j+1$ having an identical longitude separation $\Delta\lambda$ and crossing in Q. The consequence is that the crossovers P and Q possess the same antisymmetric relative time tags Δt and latitude ϕ. The absolute time tag difference δt is also unchanged in this situation since $t^a_{\phi=0}$ and $t^d_{\phi=0}$ are both advanced by exactly one revolution period τ. The same manipulation of absolute crossover time tags may be rehearsed again on arc segments $i+1$ and $j+1$. It is now easy to recognize that crossovers are clustered in bands of equal latitude ϕ. Crossovers forming a parallel all have an identical absolute time tag difference δt.

The longitude separation $\Delta\lambda$ between arc segments i and j, as given in figure 5.3, is also preserved in magnitude, but reversed in sign, when a *half* revolution period is added to $t^a_{\phi=0}$ and $t^d_{\phi=0}$. This causes the ascending segment j to become a descending and the descending segment i to become ascending. The consequence is that $\Delta\lambda$ and accordingly Δt and ϕ will change sign, compare (5.5). It is easy to verify that also the absolute time tag difference δt changes sign.

For a cluster of crossovers having an equal value of $|\delta t|$ this results in two latitude bands symmetrical with respect to the equator.

Response of a crossover cluster to radial orbit errors

In the previous section it was described how the time tag differences δt show up on crossovers. The differences δt are constant for a cluster of crossovers located on the same latitude. In addition to this clustering effect mirror symmetry with respect to the equator shows up for values of $-\delta t$.

For each value of δt we consider the radial orbit error $\Delta r(t)$ in the form of a Fourier series, compare chapter 4, equations (4.26) and (4.49):

$$\Delta r(t) = \sum_{k,m} A_{km} \cos \dot{\psi}_{km} t + B_{km} \sin \dot{\psi}_{km} t \ . \tag{5.8}$$

In the following we derive the way crossover differences manifest by a transformation of (5.8) into:

$$\Delta h(t + \delta t, t) = \Delta r(t + \delta t) - \Delta r(t). \tag{5.9}$$

The function $\Delta h(t + \delta t, t)$ represents the height differences for a cluster of crossovers and becomes:

$$\Delta h(t) = \sum_{k,m} A^*_{km} \cos \dot{\psi}_{km} t + B^*_{km} \sin \dot{\psi}_{km} t \ . \tag{5.10}$$

where the coefficients A^*_{km} and B^*_{km} are related to the original coefficients A_{km} and B_{km} by:

$$\begin{bmatrix} A^*_{km} \\ B^*_{km} \end{bmatrix} = \begin{bmatrix} \cos(\dot{\psi}_{km}\delta t) - 1 & \sin(\dot{\psi}_{km}\delta t) \\ -\sin(\dot{\psi}_{km}\delta t) & \cos(\dot{\psi}_{km}\delta t) - 1 \end{bmatrix} \begin{bmatrix} A_{km} \\ B_{km} \end{bmatrix} \tag{5.11}$$

which is a linear transformation of the Fourier coefficients A_{km} and B_{km}. However, the problem is to derive – given Δh – the coefficients A_{km} and B_{km} from A^*_{km} and B^*_{km}, which requires the inverse relation of (5.11). This inverse relation of (5.11) does not exist when the determinant of the transformation matrix equals to zero:

$$\begin{vmatrix} \cos(\dot{\psi}_{km}\delta t) - 1 & \sin(\dot{\psi}_{km}\delta t) \\ -\sin(\dot{\psi}_{km}\delta t) & \cos(\dot{\psi}_{km}\delta t) - 1 \end{vmatrix} = 2 - 2\cos(\dot{\psi}_{km}\delta t) = 0 \ . \tag{5.12}$$

This can only be the case when $\dot{\psi}_{km}\delta t = 2\pi l$ where l represents an arbitrary integer. Another interpretation is that singularity occurs when:

$$\frac{\dot{\psi}_{km}}{n_0} = l\frac{2\pi}{\delta t n_0} \quad \Rightarrow \quad \beta_{km} = l\beta_c \ \ (n_0\text{: mean motion}) \tag{5.13}$$

where β_{km} represents the perturbation frequency and β_c the singular cluster frequency both in units of cycles per revolution.

For $l = 0$ a trivial solution is found, the zero frequency (bias) cannot be recovered from any crossover cluster. In order to demonstrate the effect of other values of β_{km} we present in table 5.1 the sorted values in ascending order of β_c coming from the simulated orbit discussed in chapter 4. This table contains in ascending order the clusters of equal δt in units of revolutions, their singular frequency β_c in cycles per revolution and the amount of crossovers in the cluster.

Table 5.1 shows that the 'earliest crossovers' occur at $\approx$ 98% of the revolution period. It may be concluded that all successive crossover clusters appear to have a value of δt at close multiples of the crossover clusters with the earliest δt. This is in agreement to what has been published by Goad et al. (1980), Douglas et al. (1984) and Colombo (1984b).

nr	$\|\delta t\|$	β_c	amount	nr	$\|\delta t\|$	β_c	amount
1	0.979	1.022	85	8	7.438	0.134	71
2	1.955	0.511	83	9	8.282	0.121	69
3	2.927	0.341	81	10	9.183	0.109	67
4	3.891	0.257	79	11	10.123	0.099	65
5	4.839	0.207	77	12	11.083	0.090	63
6	5.754	0.174	75	13	12.053	0.083	61
7	6.617	0.151	73	14	13.029	0.077	59

Table 5.1: The first 14 clusters of absolute time tag differences on crossovers in the simulated orbit.

For successive clusters of crossovers one can always find an integer l which causes a singularity close to once per revolution. However this is where most of the radial orbit error is concentrated. It is obvious that a more detailed analysis is required to judge upon observability of the A_{km} and B_{km} coefficients from A^*_{km} and B^*_{km}. In reality, A_{km} and B_{km} are estimated from all possible values of δt. Furthermore it is likely that A^*_{km} and B^*_{km} may not be estimated easily from a given crossover file. Firstly it may be due to the sampling of (5.10), secondly not all crossovers inside a cluster may be available since some are e.g. located on land.

As a preliminary conclusion one could pose that it is likely that crossover data alone is ***insufficient*** for an complete orbit error recovery. In other words crossover observations form a ***necessary*** but not a ***sufficient*** condition for orbit error recovery.

5.2 Repeat arc differences

A completely different type of information from satellite altimetry can be extracted from the repeated measurement of the sea surface over the same ground track. In such a configuration the ground track of the satellite appears to 'bite in its own tail' after a certain time, known as the repeat period. The necessary and sufficient condition for obtaining a repeating ground track is that there exists an integer ratio between the quantities $(\dot{\omega} + \dot{M})$ and $(\dot{\Omega} - \dot{\theta})$, compare Colombo (1984b):

$$\frac{(\dot{\omega} + \dot{M})}{(\dot{\Omega} - \dot{\theta})} = \frac{\dot{\omega}_o}{\dot{\omega}_e} = \frac{\alpha}{\beta} \quad \text{where } \alpha, \beta : \text{ integer.} \tag{5.14}$$

The repeat period δt is derived from (5.14):

$$\delta t = \alpha \frac{2\pi}{\dot{\omega}_o} = \beta \frac{2\pi}{\dot{\omega}_e} \tag{5.15}$$

Its physical interpretation is that the ground track repeats itself after α revolutions of the satellite in the orbital plane and after β revolutions of the orbital plane itself about the z axis of the Earth fixed coordinate system.

In reality nearly every circular trajectory resembles a repeating one for the simple reason that any real value of $\dot{\omega}_o/\dot{\omega}_e$ may be approximated by a ratio of two integer numbers α and β. A practical problem might be that the integer values become quite large for an accurate approximation of the $\dot{\omega}_o/\dot{\omega}_e$ ratio. Therefore we employ a second condition: the repeat period should be less than a few months or so.

Up to now two altimeter satellites have been arranged in repeat mode. SEASAT had in its last month a repeat orbit at $h = 790$ km, $e = 0.001$ and $I = 108°$ with $\alpha/\beta = -43/3$. Accordingly its repeat period was $43 \times \tau$ which equals to 3.01 days. The longitude spacing of the ground tracks on the equator equals to $360°/43 = 8.37°$. Currently GEOSAT is placed at $h = 785$ km, $e = 0.001$ and $I = 108°$ with $\alpha/\beta = -244/17$ causing δt to be 17.05 days. In this case the longitude separation is much denser: $360°/244 = 1.48°$.

5.2.1 Spectral characteristics of repeat arc differences

Let the 'repeat arc difference' be defined as:

$$\Delta h(t) = \Delta r(t + \delta t) - \Delta r(t) \tag{5.16}$$

which is equivalent in its form to (5.9) except that δt is defined as a constant depending on the choice of the ground track configuration. It is now easy to investigate the impact on the radial perturbations caused by uncertainties of the potential coefficients of the gravitational field. Equation (4.22) shows that the perturbations in an arbitrary element 'E' take the form of:

$$\Delta r(t) = \sum_{l,m}\sum_{p,q} H_{lmpq}\left[A_{lm}\cos(\psi_{lmpq}) + B_{lm}\sin(\psi_{lmpq})\right] \tag{5.17}$$

with H_{lmpq} representing a function of the nominal elements and other time independent parameters whereas A_{lm}, B_{lm} depend directly on potential coefficients of the gravitational field. The time dependent term ψ_{lmpq} equals to $(l-2p)\omega + (l-2p+q)M + m(\Omega - \theta)$. We substitute condition (5.15) into the ψ_{lmpq} term and find:

$$\begin{aligned}
\psi_{lmpq}(t) &= (\dot{\psi}_{km} - q\dot{\omega})t, \\
\dot{\psi}_{km} &= k(\dot{\omega} + \dot{M}) + m(\dot{\Omega} - \dot{\theta}) \quad (k = l - 2p + q) \\
\psi_{lmpq}(t + \delta t) &= k(\dot{\omega} + \dot{M})(t + \frac{2\pi\alpha}{(\dot{\omega} + \dot{M})}) + m(\dot{\Omega} - \dot{\theta})(t + \frac{2\pi\beta}{(\dot{\Omega} - \dot{\theta})}) - q\dot{\omega}(t + \delta t) \\
\psi_{lmpq}(t + \delta t) &= \psi_{lmpq}(t) + 2\pi(k\alpha + m\beta) - q\dot{\omega}\delta t
\end{aligned} \tag{5.18}$$

The latter equation shows that all perturbations in the elements are exactly in phase over one repeat period. The only exception is formed by the term $-q\dot{\omega}\delta t$, the precession of the argument of perigee. Hence repeat arc differences in the form of (5.16) behave as a natural filter eliminating all short periodic perturbations implied by gravitational errors, compare Colombo (1984b). In case of a frozen repeat orbit the situation is slightly different since $\dot{\omega} \approx 0$. In this case we can expect an even lesser effect of $-q\dot{\omega}\delta t$ on $\Delta h(t)$.

It is not surprising that repeat arc differences are not hampered by short periodic gravitational errors for the simple physical fact that evaluation of the force function in the integration of the equations of motion takes place at the same location in the gravitational field.

5.3 Conclusions

In this chapter we described an efficient method for computing the crossover positions and time tags. Furthermore we discussed three properties which crossovers fulfill whenever 1) a circular orbit is considered and 2) ω_e and ω_o are linear expressions and I a constant. A consequence of the first property is that the relative ascending time tag at a crossover is opposite in sign with respect to the relative descending time tag. The times are considered with respect to the equator transit times. The second property tells that the relative time tag and the latitude are uniquely connected, the third property results in latitude and time tags of crossovers that are only determined by the longitude separation of the equator transit points.

Considering the spectral characteristics of crossover differences it may be concluded that it will not be feasible to recover a complete orbit error as far as crossover data alone is used. A simple example is a bias term which cannot be recovered from crossover data. More drastic are the recovery problems for frequencies near once per revolution. It has been verified for a 3-day SEASAT repeat orbit, that singular frequencies in the inverse transformation of crossovers to the orbit errors exist in the spectral band where most of the signal is concentrated. The spectral characteristics suggest that crossover differences *alone* are insufficient for a complete orbit error recovery.

Another observation type described is the repeated measurement of the sea surface over the same ground track. It has been shown that 'repeat arc differences' behave as an almost perfect filter for all short periodic perturbations caused by the gravitational field. This implies that radial orbit errors – full or in part – cannot be recovered from repeat arc differences except for the long periodic modulation caused by the precession of the argument of perigee.

Chapter 6

Processing of simulated observables

6.1 Introduction

The previous chapters describe the behavior of the radial orbit error and the spectral characteristics of crossover and repeat arc differences. It has been found that the relation between the radial orbit error and uncertainties in the gravitational field can be modeled by means of numerical orbit integration and analytical perturbation theories. The numerical results, which are exact to the level of a negligible integration error resemble closely the non-resonant particular solution of the Hill equations.

In a real world altimeter experiment one is faced with an adjustment problem; the recovery (or elimination) of the radial position inaccuracy of the satellite from observables derived from direct height measurements, crossover and repeat arc differences. In order to gain more insight in the behavior of the adjustment problem a simulation is carried out. The purpose of the simulation is:

- to generate an artificial orbit including a radial orbit error,
- to compute crossover – and repeat arc differences from this data,
- to investigate the recovery problem using simulated observables.

As a source we apply the simulated three day repeat orbit having a total duration of 10 days as is described in chapter 4. In first instance we verify the spectral characteristics of the simulated repeat arc differences, from which it is expected that they behave as a natural filter for all short periodic perturbations implied by the gravitational field. In the second and third part of this chapter we describe three versions of a global crossover adjustment based on simulated observables from which it is attempted to reconstruct the original radial orbit error.

6.2 Repeat arc differences

6.2.1 Generation of the observables

In general the conditions for the prototype orbit 'biting in its own tail' are:

- the trajectory has to be nearly circular (instrumental requirement),
- the repeat ratio $\dot{\omega}_o/\dot{\omega}_e$ equals to a certain integer ratio,
- although this is not relevant in this context, one might demand for calibration of the altimeter that the repeating ground track passes over a specific geographical location, compare Kolenkiewicz et al. (1982).

In this context only the first two conditions are of interest where we choose the repeat ratio as -43/3, a value compatible with that of the orbit of SEASAT in its last month. The following steps are carried out in order to find a suitable initial state vector for this problem:

- Based upon the secular behavior of the Keplerian elements caused by the flattening term of the gravitational field (J_2) the ratio of $(\dot{M}+\dot{\omega})/(\dot{\Omega}-\dot{\theta})$ is fixed on the desired integer ratio (α/β). The problem is to determine the root of equation (5.14):

  $$\frac{(\dot{M}+\dot{\omega})}{(\dot{\Omega}-\dot{\theta})}-(\frac{\alpha}{\beta})=0 \text{ with } \alpha,\beta: \text{integers},$$

  by variation of the semi major axis 'a' in (4.20) which is accomplished by a Newton-Raphson procedure.

- The first step results in an initial state vector used to start a numerical integration with the full gravitational field GEM-10B which is carried out over 10 revolutions. The equator transit longitudes and timings are used to improve the repeat ratio. For this purpose the semi-major axis is gradually changed until the repeat condition is met. (This is accomplished by a Newton-Raphson technique in which the derivative of the repeat ratio with respect to the semi-major axis is derived by means of numerical differentiation.)

Eventually the repeat ratio is accurate to $\approx 10^{-4}$ with a mean eccentricity of $\approx 2.4\times10^{-3}$ which is slightly higher than the actual three-day repeat orbit of SEASAT. Hence the simulated orbit fulfills the repeat condition, but is not frozen repeat, compare appendix A.

The trajectory found by numerical integration of the GEM-10B gravitational model is re-integrated with the PGS-S4 model while solving for initial state vector effects. For more details see chapter 4.

6.2.2 Numerical analysis

The next step is to evaluate the repeat arc differences defined by the relation $\Delta h(t) = \Delta r(t+\delta t) - \Delta r(t)$ where δt represents the length of exactly one repeat period, $\Delta r(t)$ the simulated orbit error formed by the radial differences of the GEM-10B and the PGS-S4 trajectories and $\Delta h(t)$ the simulated repeat arc difference. For computing the spectrum of $\Delta h(t)$ a mixed radix FFT is applied, compare Singleton (1969). In total two full repeat periods of data (6 days) have been used to compute the spectrum. The logarithmical power spectrum of the quantity $\Delta h(t)$ is given

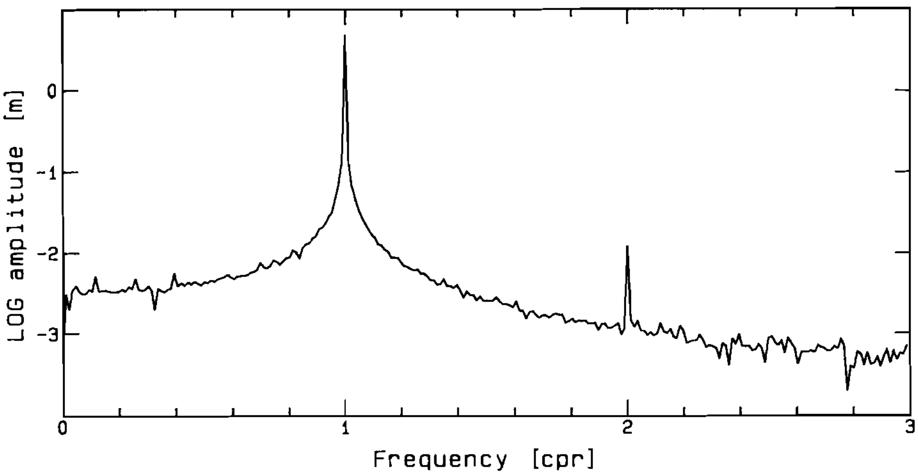

Figure 6.1: The logarithmical power density spectrum of a simulated repeat arc difference only caused by gravitational effects. The horizontal and vertical axes represent the frequency in cycles per revolution and the logarithmical power density in m per 1/43 c.p.r. respectively

in figure 6.1 showing a concentration of signal dominantly at once and to a lesser extent at twice per revolution. Comparison of figure 4.5 with 6.1 shows that all the modulated signal of Δr (the spikes in the spectrum other than very close to once per revolution) has vanished. This phenomenon was predicted by (5.18): repeat arc differences are insensitive for short periodic perturbations caused by the gravitational field. If this is true then how can we explain the remaining signal in figure 6.1? The signal appears quite significant and requires more attention.

Further analysis of the simulated repeat arc differences reveals that the signal may be described by an once per revolution oscillation and a long periodic bow tie effect, compare eq. (4.40). The remaining signal after modeling a bow tie function consists of noise with an total r.m.s. of approximately 2 cm.

6.2.3 The nature of the bow tie effect in repeat arc differences

In the sequel we attempt to analyze the nature of the bow tie effect which shows up as well in the radial orbit error as in the repeat arc differences derived from the simulation experiment. The bow tie effect in a radial orbit error is predicted by the resonant case of the HE, compare (4.39), of which it is known that constant or once per revolution perturbing forces give rise to a bow tie effect in the simulated $\Delta r()$. However (4.39) *cannot* explain a bow tie effect as found in the simulated repeat arc differences. (Terms like a_u^1, b_u^1 and c_u^1 cancel in a function $\Delta h(t) = u(t+\delta t) - u(t)$ if $\delta t = 2\pi\alpha/\dot{\omega}_o$, where u takes the form of eq. (4.40)) This is the main reason to analyze this particular effect in more detail. The bow tie effect is caused by a long periodic modulation implied by $\dot{\omega}$ which is related to the uncertainties in the zonal coefficients of the gravitational field.

The dominant precession of the argument of perigee comes from the combined effect of the even zonal coefficients, especially J_2 as is described by (4.20). However the even zonals are quite well known and their uncertainty is too small to explain the bow tie effect in the simulated radial orbit error. The apsidal period of ≈ 208 days shows a difference of $\approx 10^{-7}$ days according to both gravity models used in the simulation.

Besides the precession effect of ω due to the even zonals there is also an odd zonal effect which causes the non-singular variables $u = e \cos\omega$ and $v = e \sin\omega$ to describe a circular motion with radius A centered around an imaginary point at $(0, C/\dot{\omega})$ in the u, v plane, compare appendix A equation (A.11).

In the simulation experiment it was recognized that the bow tie effect in the simulated orbit error and the related repeat arc differences can be explained by uncertainties in modeling the non-singular variables u and v. A significant contribution is expected from the differences of $C/\dot{\omega}$ of the reference and the perturbed trajectory. The $C/\dot{\omega}$ value computed by equations (A.4) ff. equals 7.945×10^{-4} and 8.024×10^{-4} for the GEM-10B and the PGS-S4 trajectory respectively. In the computation we take the total effect of the odd zonal coefficients up to degree and order 36 with $a = a_e + 780$ km and $I = 108°$.

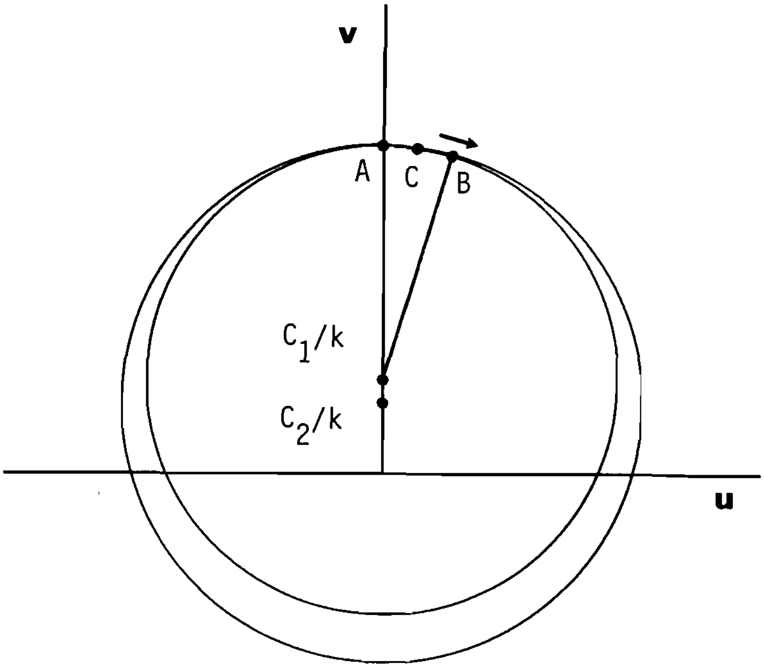

Figure 6.2: The non-centric configuration of the simulated trajectories in the u,v plane.

In figure 6.2 the circular motion of the non-singular variables u and v is presented as in the case of the simulation experiment. The motion is clockwise starting at A and ending at B. Due to the initial state vector adjustment applied the circles coincide at C located in the middle of A and B. The total precession of the argument of perigee from A to B equals to 17° which is related to the length of 10 days of the orbits relative to the apsidal period of 208 days. ($17^\circ \approx 10/208 \times 360^\circ$).

The next step is to evaluate the effect of the non-centric situation in the simulated radial orbit error and the repeat arc differences derived from this data. In this context we consider for near circular orbits:

$$r \approx a(1 - e\cos(\omega_o - \omega)) \tag{6.1}$$

where $\omega_o = \omega + M$. An expression in the non-singular variables u and v becomes:

$$r \approx a(1 - u\cos\omega_o - v\sin\omega_o) \tag{6.2}$$

The value of 'a' shows (as a result of numerical analysis) no precession effects due to zonal coefficients; it is more likely that Δr is caused by errors in the non-singular variables u and v:

$$\Delta r \approx a(-\Delta u\cos\omega_o - \Delta v\sin\omega_o). \tag{6.3}$$

This expression shows that Δr resembles an once per revolution oscillation with a total amplitude of the order of $a[\Delta u^2 + \Delta v^2]^{1/2}$. Of significant influence is the factor 'a' with a magnitude of $\approx 7 \times 10^6$ m. It explains that small deviations in Δu and Δv of the order of 10^{-6} to 10^{-5} cause oscillations in Δr of several meters to several tens of meters (7-70 m respectively).

As a result of the non-centric situation Δu and Δv may be modeled by a Fourier series in the form of:

$$\begin{aligned}\Delta u(t) &= a_u\cos\dot{\omega}t + b_u\sin\dot{\omega}t\,,\\ \Delta v(t) &= a_v\cos\dot{\omega}t + b_v\sin\dot{\omega}t\,.\end{aligned} \tag{6.4}$$

For short periods of $\approx 17^\circ$ of the total precession of the apsidal period $\dot{\omega}t$ remains small. One may approximate (6.4) linearly resulting in:

$$\begin{aligned}\Delta u(t) &= a_u + b_u\dot{\omega}t + O((\dot{\omega}t)^2),\\ \Delta v(t) &= a_v + b_v\dot{\omega}t + O((\dot{\omega}t)^2).\end{aligned} \tag{6.5}$$

A substitution in (6.3) explains the bow tie effect found in the simulated radial orbit error. For repeat arc differences we find the form:

$$\Delta h(t) = \Delta r(t + \delta t) - \Delta r(t) \tag{6.6}$$

which is equal to:

$$\Delta h(t) = a[-\Delta u^*\cos\omega_o - \Delta v^*\sin\omega_o] \tag{6.7}$$

with (assuming no influence of the $\dot{\omega}_o\delta t$ terms due to the repeat condition):

$$\begin{aligned}\Delta u^*(t) &= a_u^*\cos\dot{\omega}t + b_u^*\sin\dot{\omega}t\,,\\ \Delta v^*(t) &= a_v^*\cos\dot{\omega}t + b_v^*\sin\dot{\omega}t\end{aligned} \tag{6.8}$$

and

$$\begin{bmatrix} a_{u,v}^* \\ b_{u,v}^* \end{bmatrix} = \begin{bmatrix} \cos(\dot{\omega}\delta t) - 1 & \sin(\dot{\omega}\delta t) \\ -\sin(\dot{\omega}\delta t) & \cos(\dot{\omega}\delta t) - 1 \end{bmatrix} \begin{bmatrix} a_{u,v} \\ b_{u,v} \end{bmatrix}.$$

Expression (6.8) allows, similar as in (6.4), a linear approximation explaining a bow tie type of function in the repeat arc differences. We conclude that a function of the form of:

$$\Delta h(t) = (a_0 + b_0 t)\cos\omega_o + (a_1 + b_1 t)\sin\omega_o \tag{6.9}$$

is capable of modeling the repeat arc differences. Further analysis confirmed that a filter of the form of (6.9) is sufficient to describe nearly all the repeat arc difference signal. The remaining effect in the repeat arc differences after estimating eq. (6.9) from the difference data resembles white noise with a r.m.s. of $\approx$ 2 cm.

As a result it is feasible to reduce most of the long periodic error signal in the repeat arc differences (compared with the relatively short periodic effects of oceanographic phenomena) by a simple filter function of the form of (6.9) which spans the duration of an orbit determination period. A further conclusion is that analyzing the difference signal does not help to improve the gravitational field. The only phenomenon caused by gravitational effects that might eventually be recovered from the repeat arc difference signal is the long term motion of the argument of perigee which in its turn is related to the zonal terms of the gravity field. What remains in the repeat arc differences are short periodic variations caused by instrumental noise, model noise (e.g. tropospheric, ionospheric and tidal effects), and most of all, mesoscale variability phenomena, compare Cheney et al. (1983).

6.3 Global chronological crossover adjustment

6.3.1 Introduction

In chapter 3 a local crossover adjustment experiment has been described. The purpose of this experiment was to get an insight into the properties of a regional adjustment. Emphasis is being placed on the adjustment theoretical aspects, especially the singularity problem. In this chapter a second orbit error recovery experiment is worked out. In this experiment

- crossover differences are generated from the simulated orbit error and,
- the simulated radial orbit error is reconstructed by means of crossover minimization.

The computation of crossover differences, their geographical locations and times at which they occur was already introduced in chapter 3 and worked out in more detail in chapter 5. Hence the first problem – generation of crossover differences from the simulated orbit – is essentially a direct application of the technique described in chapter 5. For the simulated orbit 290 arc segments were found: 145 ascending and 145 descending.

For the recovery of the simulated radial orbit error only the first repeat period consisting of three days of data is used. It results in $2 \times 43 = 86$ arc segments forming $43 \times 43 = 1849$ crossover differences. (this value includes the so-called 'land' crossovers). It is justified to use this subset since the remaining repeat cycles of the radial orbit error may be connected to the first three day repeat era by minimization of repeat arc differences. (from which it is known that this particular minimization hardly helps to improve the gravitational field.)

The chronological LSA of crossover differences shows a considerable analogy with the local LSA of crossover differences discussed in chapter 3:

- Parameters of error functions are defined inside the (time) range of an arc segment and solved by means of LSA of crossover differences.
- Crossover time tag regularization is applied in order to obtain a numerical stable particular solution of the normal equations.
- A datum problem showing up as a rank defect of the normal equations is recognized. It is found by analyzing the homogeneous part of a self-adjoint system of normal equations formed by the crossover minimization problem.
- Singularity transformations of the unknowns are derived from the structure of the homogeneous solution of the normal equations.

In chapter 3 the information obtained by solving the unknowns of the observational model was only used to derive an internal consistent surface. Here this information is applied, as well, for the recovery of a simulated radial orbit error. For this purpose the adjusted error functions are arranged in a chronological order, i.e. the recovered Δr functions are set 'head to tail' forming a stepwise radial orbit error function.

In this section two chronological models are considered. In the first model error functions are only solved by minimizing the crossover residuals, i.e. only the minimal number of constraints are forced on the system. The second model is similar to the first except that additional smoothness constraints are introduced at the boundaries of successive arc segments.

In both cases a comparison between the chronological stepwise recovered and the originally simulated radial orbit error is made. The solutions found by minimization of crossover differences represent the particular solution of the crossover problem showing a discrepancy with the simulated radial orbit error. For this purpose the homogeneous part is recovered such that the general solution coincides in an optimal way with the simulated radial orbit error. In a real world altimeter configuration it is impossible to carry out this step for the simple reason that the real orbit error is unknown. Here the comparison with the simulated radial orbit error is made in order to *verify* whether the homogeneous part of the crossover solution is capable of describing the discrepancies between the particular solution and the simulated radial orbit error.

6.3.2 The choice of a stepwise error function

An important choice to make in the segmented chronological adjustment of crossover differences is the type of error function to be solved for per arc segment. In chapter 3 a well known choice was made: a 2 parameter 'tilt' and 'bias' error function for relatively short arc segments not longer than 1000 sec. Directly related to the choice of any stepwise error function is the length in time over which it is defined. Computations have shown that linear error functions are adequate over short time

len	min 1	max 1	rms 1	min 2	max 2	rms 2	min 3	max 3	rms 3
250	-0.06	0.06	0.02	-0.01	0.01	0.002	-0.003	0.004	0.001
500	-0.26	0.23	0.06	-0.04	0.04	0.01	-0.02	0.03	0.004
1000	-0.90	0.80	0.22	-0.15	0.18	0.04	-0.09	0.10	0.02
2000	-3.65	2.72	0.82	-0.78	0.92	0.17	-0.27	0.24	0.06
3000				-2.27	2.11	0.44	-0.59	0.63	0.15
4000							-1.11	1.74	0.31

Table 6.1: Fitting accuracy of polynomial error functions with respect to the simulated radial orbit error.

intervals of approximately 1/6 of a revolution. However linear functions show an increasing approximation error in the modeling of Δr over longer time intervals and are not anymore applicable over e.g. the full length of an arc segment.

The validity of the polynomial error functions is investigated by analyzing their ability to follow the simulated radial orbit error. In this context a polynomial error function of degree i_{max} is defined as: (t equals to the relative time within an arc segment, τ equals to the absolute length in time of the segment)

$$\Delta r(t) = \sum_{i=0}^{i_{max}} \beta_i (t/\tau)^i. \tag{6.10}$$

In order to verify the approximation error of these polynomials the following procedure is applied:

- The simulated orbit error is subdivided in chronological parts of equal length in time. The first day of the simulated radial orbit error, consisting of 1440 one minute samples, is used as a source of data.
- The coefficients β_i of a stepwise polynomial error function of a chosen degree i_{max} are estimated in each interval consisting of the simulated radial orbit error samples.
- Computed are the r.m.s. and the extreme deviations of all stepwise functions with respect to the simulated orbit error.

Results of polynomial fits up to degree 3 are given in table 6.1. In table 6.1 the dimensions are in seconds for the length (len) and meters for the extreme and r.m.s. values. The nine columns min 'i', max 'i' and rms 'i' for i=1..3 indicate respectively the minimum –, maximum extreme and the r.m.s. found for stepwise polynomials of degree 'i'.

The results confirm that linear error functions are not able to describe accurately the simulated orbit error signal when they are solved over intervals longer than approximately 1000 seconds. (r.m.s. limit of 20 cm) Remarkable is the fact that quadratic polynomial error functions will not fit better than 44 cm r.m.s. with respect to the simulated radial orbit error when solved over a full arc segment of 3000 sec. More suitable appear 3^{th} degree (cubic) polynomial error functions requiring

4 unknowns to be solved per arc segment. More accurate results were found for stepwise functions taking the form of:

$$\Delta r(t) = a_0 \cos(nt) + b_0 \sin(nt) + c_0 \tag{6.11}$$

and

$$\Delta r(t) = (a_0 + a_1 \frac{t}{\tau}) \cos(nt) + (b_0 + b_1 \frac{t}{\tau}) \sin(nt) + (c_0 + c_1 \frac{t}{\tau}) \tag{6.12}$$

where n represents the mean motion and τ the revolution period of the satellite. Function (6.11) is found by linearization of a Kepler ellipse as described by equation (4.24). Its physical justification is discussed by Colombo (1984b), Rummel (1985), Wagner (1985) and Zandbergen et al. (1988). Function (6.12) is found by solving the special resonant case of the Hill equations, as is shown by equation (4.39). The results of fitting (6.11) and (6.12) up to intervals of 6000 seconds are given in table 6.2. This table is organized in the same way as 6.1: columns with i=1 represent the results for (6.11) and i=2 for (6.12). Apparently (6.12) is capable of fitting accurately the simulated radial orbit error even up to one revolution. However in our situation, where an error function is defined per arc segment, the price to pay is a larger system of normal equations due to the fact that 6 unknowns are introduced for each arc segment.

len	min 1	max 1	rms 1	min 2	max 2	rms 2
1000	-0.13	0.16	0.03	-0.04	0.04	0.008
2000	-0.52	0.44	0.08	-0.10	0.10	0.03
3000	-0.83	0.64	0.17	-0.17	0.22	0.05
4000	-1.15	1.06	0.25	-0.30	0.32	0.08
5000				-0.37	0.36	0.10
6000				-0.47	0.50	0.12

Table 6.2: Fitting accuracy of alternative error functions with respect to the simulated radial orbit error.

More economic is an error function of the form of (6.11) requiring only 3 parameters per arc segment. From this function it should be possible to recover the simulated radial orbit error with a r.m.s. of approximately 17 cm which is considered acceptable for simulation purposes. As expected this function gives more accurate results than obtained by a linear or quadratic polynomial error functions. Moreover (6.11) requires fewer parameters than cubic polynomial error functions and its fitting accuracy is 'on the same level' as the cubic polynomial error function. For these reasons (6.11) is chosen as a stepwise error function in the global chronological adjustment of the crossover differences.

6.3.3 Adjustment

We consider the crossover residuals Δh_{ij} , between an ascending arc segment 'i' and a descending arc segment 'j', to be modeled by observation equations in the form of:

$$\Delta h_{ij} = \Delta r_i(t_{ij}) - \Delta r_j(t_{ji}) \tag{6.13}$$

As mentioned in §6.3.2 the error functions $\Delta r_i()$ and $\Delta r_j()$ are chosen according to (6.11) which is defined inside the time range of an arc segment. As a result the observation equations become:

$$\Delta h_{ij} = [a_i \cos(nt_{ij}) + b_i \sin(nt_{ij}) + c_i] - [a_j \cos(nt_{ji}) + b_j \sin(nt_{ji}) + c_j] \qquad (6.14)$$

where t_{ij} and t_{ji} represent the time tags at the crossover point. Observation equations in the form of (6.14) are used to construct the design matrix A. The crossover differences are stored in the observation vector $\vec{y}$ and the unknowns a_i b_i and c_i for each arc segment i are contained in the vector of unknowns $\vec{x}$. Accordingly we find $\vec{y} = A\vec{x} + \vec{\epsilon}$ from which the unknowns are solved by minimization of $\vec{\epsilon}^t Q_{yy}^{-1} \vec{\epsilon}$, where Q_{yy} represents the covariance matrix of the observations taking the form of a unit matrix. Minimization results in the well known normal equations:

$$(A^t Q_{yy}^{-1} A)\hat{x} = A^t Q_{yy}^{-1} \vec{y} \Rightarrow N\hat{x} = \vec{r}. \qquad (6.15)$$

The dimension of the matrix N is 258 × 258 (258 = 86 × 3), where 1849 crossover differences have been used to derive the normal equations.

The LSA of Δh_{ij} is analogous to the local LSA described in chapter 3. However this is not anymore the case for the rank defect of the normal matrix. It is caused by a different structure of the observation equations. Eigenvalue analysis of the normal matrix as given in (6.15) in its unaltered form derived from the original crossover time tags using (6.14) have revealed that [a] one eigenvalue equals to -5.73×10^{-15} which may be considered as zero due to the round-off level of the floating point arithmetic [b] two eigenvalues are equal to respectively 1.81×10^{-8} and 9.53×10^{-8} and [c] other eigenvalues in the range of $\approx 10^{-3}$ to $\approx 10^{+2}$. Theoretically the rank defect equals to 1 which is, as will be clarified in the sequel, due to the bias singularity induced by the c_i & c_j terms in (6.14).

The remaining subsystem, compare (3.7), with eigenvalues not equal to zero is unfortunately poorly conditioned. The condition number of the subsystem equals to approximately $10^2/1.81 \times 10^{-8} \approx 10^{10}$ meaning that some 10 digits are lost in the computation of the vector of unknowns.

It is found that regularization of the crossover time tags, a procedure where the original crossover time tags are replaced by approximated model timings, may be applied in order to force the two small eigenvalues in category [b] to zero. Application of the predicted crossover time tags, compare (5.4), in the observation equations results in a system of normal equations with a rank defect of 3. Regularization results in antisymmetric crossover time tags with respect to the equator transit times. Hence an extra condition, namely $t_{ij} = -t_{ji}$, is built into the observation equations:

$$\Delta h_{ij} = [a_i - a_j] \cos(nt_{ij}) + [b_i + b_j] \sin(nt_{ij}) + [c_i - c_j]. \qquad (6.16)$$

Observation equations of the form of (6.16) are convenient for deriving the rank defect of the normal equations. In order to recover the defect we search for linear combinations of the columns of the A matrix ($c := \cos(nt_{ij})$ & $s := \sin(nt_{ij})$):

$$A = \left[\begin{array}{ccccccccc|ccccccc}
c & s & 1 & & & & & & & -c & s & -1 & & & & \\
c & s & 1 & & & & & & & & & & -c & s & -1 & \\
 & \vdots & & & & & & & & & & & & & & \ddots \\
 & & & c & s & 1 & & & & -c & s & -1 & & & & \\
 & & & c & s & 1 & & & & & & & -c & s & -1 & \\
 & & & & \vdots & & & & & & & & & & & \ddots \\
 & & & & & & c & s & 1 & -c & s & -1 & & & & \\
 & & & & & & c & s & 1 & & & & -c & s & -1 & \\
 & & & & & & & \vdots & & & & & & & & \ddots
\end{array}\right] \tag{6.17}$$

The matrix E fulfilling the condition that $AE = 0$ becomes:

$$E = \left[\begin{array}{ccc}
1 & 0 & 0 \\
0 & 1 & 0 \\
0 & 0 & 1 \\
 & \vdots & \\
\hline
1 & 0 & 0 \\
0 & -1 & 0 \\
0 & 0 & 1 \\
 & \vdots &
\end{array}\right] \tag{6.18}$$

The rank defect of the normal equations derived from the design matrix as given in (6.17) equals to 3. A particular solution of the normal equations is found by fixing one master arc segment, compare also Rowlands (1981). Eigenvalue analysis reveals that the condition number of the subsystem of normal equations with $\lambda \neq 0$ equals to approximately 10^5.

The adjustments showed that the crossover residuals decrease from 4.17 m r.m.s. before to 14.4 cm after the LSA. The a-posteriori r.m.s. of 14.4 cm is unaltered by adding an arbitrary homogeneous solution $\vec{z} = E\vec{s}$ to the particular solution $\vec{x}_p$ found by fixing one master arc. Computations have shown that it is possible to transform the unknowns of an arbitrary master arc solution into any other arbitrary master arc solution by adding a suitable homogeneous solution $\vec{z}$ to $\vec{x}_p$. The problem is identical to eqs. (3.26) and (3.27) except that the E matrix differs in structure. Moreover the datum of the altimeter solution is formed by fixing only 1 master arc segment.

The homogeneous solution as a deformation surface

In order to verify the nature of the homogeneous solution we substitute the general solution $\vec{x}_g$ into the observation equations (6.16), compare also (3.32) ff. The general solution of an arbitrary ascending segment 'i' and its corresponding descending segment 'j' equals to $\vec{x}_g = [a_i, b_i, c_i, a_j, b_j, c_j]^t$. The particular solution found by fixing one master arc segment equals to $\vec{x}_p = [a_i^*, b_i^*, c_i^*, a_j^*, b_j^*, c_j^*]^t$ whereas the homogeneous part equals to $\vec{z} = E\vec{s}$. By using the structure of the E matrix in (6.18) we find:

$$\begin{bmatrix} a_i \\ b_i \\ c_i \\ a_j \\ b_j \\ c_j \end{bmatrix} = \begin{bmatrix} a_i^* \\ b_i^* \\ c_i^* \\ a_j^* \\ b_j^* \\ c_j^* \end{bmatrix} + \begin{bmatrix} 1 & 0 & 0 \\ 0 & 1 & 0 \\ 0 & 0 & 1 \\ 1 & 0 & 0 \\ 0 & -1 & 0 \\ 0 & 0 & 1 \end{bmatrix} \begin{bmatrix} s_1 \\ s_2 \\ s_3 \end{bmatrix} \tag{6.19}$$

Substitution of the general solution into $\Delta r_i(t_{ij})$ eq. (6.13) results in:

$$\begin{aligned} \Delta r_i(t_{ij}) &= (a_i^* + s_1)\cos(nt_{ij}) + (b_i^* + s_2)\sin(nt_{ij}) + (c_i^* + s_3) \\ &= \Delta r_i^*(t_{ij}) + D(t_{ij}). \end{aligned} \tag{6.20}$$

Substitution of the general solution into $\Delta r_i(t_{ij})$ eq. (6.13) results in:

$$\begin{aligned} \Delta r_j(t_{ji}) &= (a_j^* + s_1)\cos(nt_{ji}) + (b_j^* - s_2)\sin(nt_{ji}) + (c_j^* + s_3) \\ &= \Delta r_j^*(t_{ji}) + D(t_{ij}). \end{aligned} \tag{6.21}$$

The term $D(t_{ij})$ takes the form of:

$$D(t_{ij}) = s_1\cos(nt_{ij}) + s_2\sin(nt_{ij}) + s_3 \tag{6.22}$$

which depends on the components of the shift vector $\vec{s}$ of the homogeneous solution. The deformation function $D(t_{ij})$ is equal for the ascending and descending sea surface height and cancels in the difference when forming crossovers. In analogy to the deformation surface polynomial found in the local case, compare (3.35), one can give a similar interpretation here. For antisymmetric crossover time tags formed by the nominal orbit it is found that the value of t_{ij} is determined *only* by the latitude ϕ of the crossover location, compare (5.6). The antisymmetric relative time tag $t_{ij}(= -t_{ji})$ is found to be invariant with respect to rotation about the z-axis of the Earth fixed coordinate system. As a result $D(t_{ij})$ in (6.22) represents a strictly zonal deformation surface.

Included is figure 6.3 indicating the nature of this zonal deformation surface as it shows up after a singularity transformation of an arbitrarily chosen master arc segment with respect to the simulated radial orbit error. The deformation surface itself is smooth, the dips at the north-south boundaries are an artifact of the interpolation method employed in the plotting software.

The homogeneous solution as a time series

For a chronological chain of arc segments it is possible to plot the time history of the function $D()$ given in (6.22). The time history is presented in figure 6.4 for the three individual components of this function. We conclude from figure 6.4 that the 's_2' and the 's_3' component result in a continuous smooth function. Thereby it is assumed that the boundaries of the arc segments are located at $t = \pm\tau/4$ relative to the equator transit time. However 's_1', compare figure 6.4, causes a discontinuous time derivative of $D()$ at the boundaries of successive arc segments. This effect is also observed in arbitrary particular solutions found by fixing one master arc

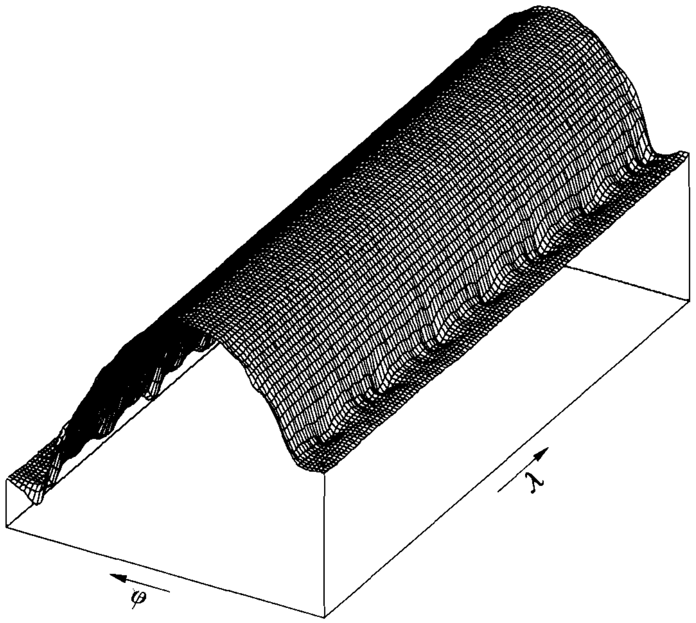

Figure 6.3: A perspective view on a deformation surface as it shows up after a singularity transformation of a global segmented crossover solution to a simulated radial orbit error.

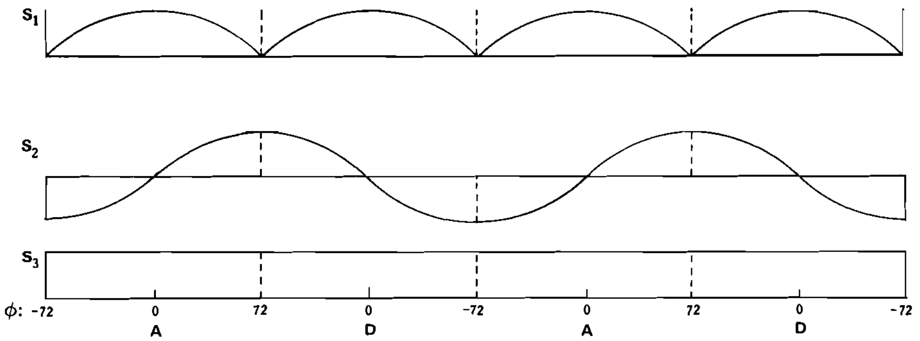

Figure 6.4: The time history of the three individual components of the homogeneous solution belonging to the segmented global crossover model.

segment. Naturally a radial orbit error does not show these discontinuities. For this reason the effect is considered artificial.

An example is shown in figure 6.5 where the time series of the radial orbit error is plotted as a chronological chain of stepwise error functions. The solution is found by a chronological segmented LSA of simulated crossover differences. From this figure we can see a velocity discontinuity effect: the upper envelope of the recovered orbit error signal is folded which is due to the s_1 component in the homogeneous solution.

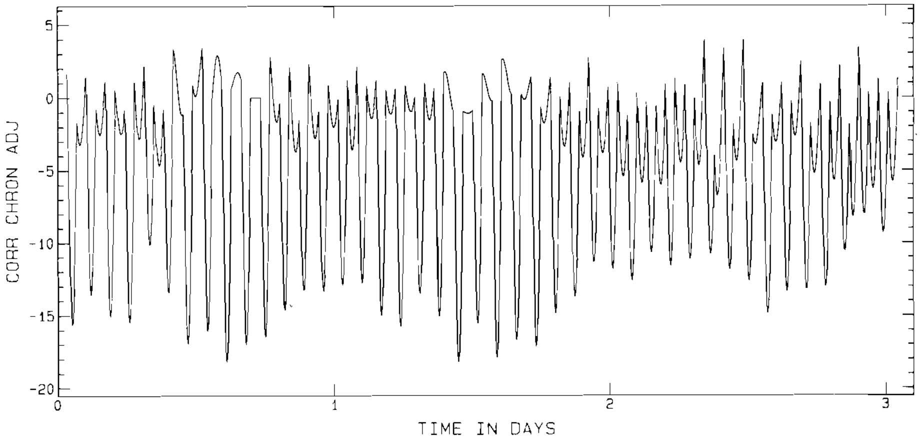

Figure 6.5: The orbit error found after a chronological segmented LSA of simulated crossover differences. On the vertical axis the radial orbit error is shown in m as it is found by fixing 1 master arc segment (at t=0.71 days). The horizontal axis represents the time in days.

In an attempt to minimize the discontinuity effect so-called smoothness conditions are forced on the stepwise error functions. The smoothness conditions of successive arc segments 'i' and 'j' take the following form:

$$\begin{array}{c} \left.\frac{dr}{dt}\right|_i (t=+\tau/4) = \left.\frac{dr}{dt}\right|_j (t=-\tau/4) \quad \Rightarrow \\ n(-a_i \sin(\frac{\pi}{2}) + b_i \cos(\frac{\pi}{2})) = n(-a_j \sin(\frac{-\pi}{2}) + b_j \cos(\frac{-\pi}{2})) \quad \Rightarrow \\ 0 = a_i + a_j \end{array} \tag{6.23}$$

Smoothness conditions in the form of (6.23) included as pseudo observation equations in the design matrix have shown to reduce the rank defect from 3 to 2. It is easy to verify that the first column vector of the E matrix as given in (6.18) is eliminated by including smoothness conditions of the form of (6.23). As a result one is not anymore free to fix a complete master arc segment for finding a particular solution. This would result in a so-called over-constrainted system.

Actually the radial orbit error is now considered to be one continuous function. In order to find a particular solution so-called initial conditions are included. It is assumed that e.g. $\Delta r_i(t=0)=0$ and $\Delta\dot{r}_i(t=0)=0$ for an arbitrary chosen i. The effect of constraints on unknowns is described in chapter 3.

Optimal adjustment to the simulated orbit error

A particular solution $\vec{x}_p$ of the normal equations is found by [a] fixing one master arc segment or [b] by employing 2 initial conditions in case smoothness conditions are forced on the system. Any other general solution of the unknowns may be found by a suitable singularity transformation of the particular solution. An optimal adjustment is chosen such that the simulated orbit error is followed in the best possible way. The observation equations employed in the optimal adjustment take for an ascending segment 'i' the form of:

$$\Delta r(t^i_{\phi=0} + \Delta t) - \Delta r_i(\Delta t) = s_1 \cos n\Delta t + s_2 \sin n\Delta t + s_3 + \vec{\epsilon} \tag{6.24}$$

or when smoothness conditions are employed:

$$\Delta r(t^i_{\phi=0} + \Delta t) - \Delta r_i(\Delta t) = s_2 \sin n\Delta t + s_3 + \vec{\epsilon}. \tag{6.25}$$

Here the term $\Delta r(t^i_{\phi=0} + \Delta t)$ represents the simulated radial orbit error at the absolute time $t^i_{\phi=0} + \Delta t$ where $t^i_{\phi=0}$ equals to the equator transit time for arc segment 'i' and Δt the time relative to the equator transit of a simulated sample. The term $\Delta r_i(\Delta t)$ is derived from a particular solution of the normal equations. In case of a descending arc segment 'j' the observation equations become:

$$\Delta r(t^j_{\phi=0} + \Delta t) - \Delta r_j(\Delta t) = s_1 \cos n\Delta t - s_2 \sin n\Delta t + s_3 + \vec{\epsilon} \tag{6.26}$$

or when smoothness conditions are employed:

$$\Delta r(t^j_{\phi=0} + \Delta t) - \Delta r_j(\Delta t) = -s_2 \sin n\Delta t + s_3 + \vec{\epsilon}. \tag{6.27}$$

The unknowns to be solved for by means of the optimal adjustment are the components of the shift vector $\vec{s}$ on the RHS of (6.24) to (6.27).

Residual analysis

For the 86 arc segments involved in the LSA of the simulated crossover differences it was recognized that a *systematic* difference shows up between the simulated orbit error and the optimally adjusted 'crossover' solution. The systematic differences were found for the unknowns solved by the segmented chronological models both with and without additional smoothness conditions. The power spectrum of the systematic difference signal between the chronological model not including smoothness conditions and the simulated radial orbit error is presented in figure 6.6. Remarkable is the concentration of the difference signal at the frequencies belonging to $2\omega_e$, $\omega_o - \omega_e$, $\omega_o + \omega_e$ and $2\omega_o - 2\omega_e$ which are the spikes in figure 6.6. Unfortunately the homogeneous solution cannot resolve this effect since the frequencies of the systematic difference are far from the zero and once per revolution frequency. Also the k times per revolution effects ($k = 2,3,...$), which appear when smoothness conditions are not included, cannot be described by the homogeneous solution of the system of normal equations. This analysis shows that the general solutions of the global segmented crossover minimization problems described earlier on in this

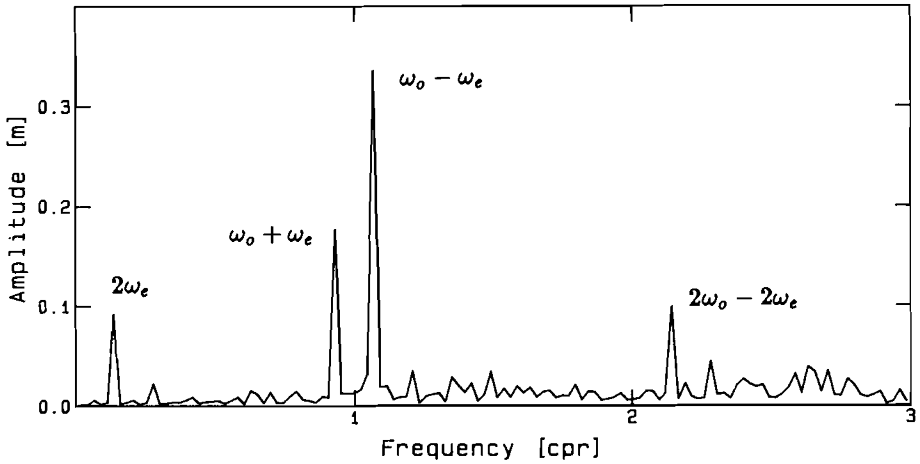

Figure 6.6: Power density spectrum of the systematic differences between a chronological optimally adjusted crossover solution and the simulated orbit error. On the horizontal axis the frequency is given in c.p.r., the vertical axis shows the amplitude in m per 1/43 c.p.r.

chapter are **inadequate** for describing a radial orbit error. The problem appears to be improperly posed.

However it was found that the systematic effect can be modeled by mapping a surface function expressed in spherical harmonics along the nominal trajectory. This idea originates from Sandwell et al. (1986) where the geographically correlated part of the radial orbit error is modeled. A surface function $D(\phi, \lambda)$ developed in spherical harmonics takes the form of:

$$D(\phi,\lambda) = \sum_{l=0}^{lmax} \sum_{m=0}^{l} [C_{lm} \cos m\lambda + S_{lm} \sin m\lambda] P_{lm}(\sin \phi) \qquad (6.28)$$

where C_{lm} and S_{lm} represent the surface function coefficients. Mapping of this function along a nominal orbit with a constant inclination I, satellite rotation rate $\dot{\omega}_o$ and the rotation rate $\dot{\omega}_e$ of the orbital plane about the z axis of the Earth fixed coordinate system takes, in analogy to Sandwell et al. (1986), the form of:

$$D(\phi,\lambda) = \sum_{l=0}^{lmax} \sum_{m=0}^{l} \sum_{p=0}^{l} F_{lmp}(I)[A_{lm} \cos \psi_{lmp} + B_{lm} \sin \psi_{lmp}] \qquad (6.29)$$

where

$$A_{lm} = \left\{ \begin{matrix} C_{lm} \\ -S_{lm} \end{matrix} \right\}_{l-m:odd}^{l-m:even} \quad \text{and} \quad B_{lm} = \left\{ \begin{matrix} S_{lm} \\ C_{lm} \end{matrix} \right\}_{l-m:odd}^{l-m:even}$$

and

$$\psi_{lmp} = (l-2p)\overline{\omega}_o + m\overline{\omega}_e$$

with

$$\overline{\omega}_o = \dot{\omega}_o t + \omega_o^0 \text{ and } \overline{\omega}_e = \dot{\omega}_e t + \omega_e^0.$$

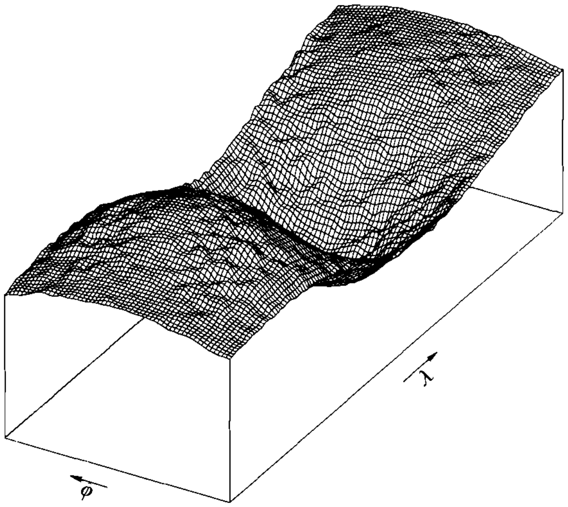

Figure 6.7: A perspective view on the surface function estimated from the systematic difference signal between the solution of an optimally adjusted chronologically segmented crossover LSA and the simulated radial orbit error.

Modeling of the systematic differences found between the optimally adjusted crossover solution and the simulated orbit error has shown to be possible by solving in the least squares sense for the surface functions coefficients C_{lm} and S_{lm}. Typically the peaks in the residual power spectrum presented in figure 6.6 disappear when the surface function is solved. In our case we solve for coefficients up to degree and order 2. The observation equations are given by (6.29); unknowns are the C_{lm} and S_{lm} coefficients, observations are the systematic differences discussed before.

Included is figure 6.7 showing a perspective view of the systematic difference spectrum as in figure 6.6. Also here one may observe some remaining "interpolation noise" which is due to the plotting software.

We conclude that there exists a part in the radial orbit error signal that *cannot* be recovered by the general solution of the crossover minimization problem posed here. The analysis above has shown that this part of the radial orbit error behaves as geographically correlated. The nature of the geographical correlation in the radial orbit error appears to be a surface function with coefficients C_{lm}, S_{lm} up to degree and order 2. Mapping of surface function coefficients above this degree and order is not expected to describe geographical correlation due to the characteristic damping of the radial orbit error at higher frequencies.

6.4 Global crossover adjustment without arc segments

6.4.1 Introduction

In §6.3 crossover minimization was performed by solving the unknowns of individual error functions defined inside the time range of an arc segment. In a second step a description of the radial orbit error is found by a chronological ordering of the stepwise error functions solved by LSA. Some problems encountered in the segmented chronological approach raise questions about the applicability of this method.

Firstly it is shown that the choice of an error function plays a critical role. The fitting accuracy, i.e. the ability to follow the simulated orbit error signal, depends directly on the length of an arc segment and the type of error function in effect. For the problem considered in §6.3 arc segments were chosen equally long in time. Land crossovers were included in the LSA of crossover differences. In a real world situation these observations do not exist; land crossovers are of an inferior quality due to instrumental reasons. Hence in reality a segmented global LSA of crossover differences as sketched in §6.3 would *always* be hampered by the fact that arc segments are not equally long in time. Especially the variance behavior of the unknowns estimated by LSA of segments which are poorly connected by means of crossovers to other segments remains problematical.

Secondly, it was found that the form of the homogeneous solution of the segmented crossover problem depends on the choice of an error function and crossover time tag regularization. In a global segmented approach it is possible to include e.g. smoothness constraints in order to minimize the velocity discontinuity effect of successive arc segments. These smoothness constraints have shown to reduce the rank defect of the normal equations from 3 to 2.

Thirdly it was found that a general solution of the segmented crossover problem is still inadequate to follow the simulated radial orbit error. It was found for both crossover minimization problems sketched in §6.3 that the general solutions of both systems are *not* able to follow the simulated radial orbit error. There remains a systematic difference signal which can be explained by fitting the Fourier series resulting from a surface function up to degree and order 2 mapped along the nominal orbit.

The problems mentioned above lead to the investigation of other minimization models enabling to recover the radial orbit error from the crossover difference data. In this approach the unknowns of one continuous and differentiable function are solved for. It takes the form of a Fourier expansion up to 2.3 cycles per revolution (c.p.r.) in steps of 1/43 c.p.r. including a two parameter function modeling a long periodic modulation of the signal.

It will be demonstrated that this approach possesses some attractive properties avoiding some of the problems encountered in segmented chronological models. A typical advantage of this approach is that the Fourier coefficients to compute represent physically meaningful quantities allowing a clear interpretation in terms of orbital mechanics. The Fourier coefficients could be used as observations in lumped coefficient equations for potential coefficients as is described in Schrama (1986a).

6.4.2 The model

In this context the continuous differentiable function to be solved for takes the form:

$$\Delta r(t) = \frac{a_0 t}{\kappa r}\cos(nt) + \frac{b_0 t}{\kappa r}\sin(nt) + c_0 + \sum_{k=1}^{kmax}\left[a_k\cos(k\Delta\omega nt) + b_k\sin(k\Delta\omega nt)\right] \quad (6.30)$$

where $\Delta r(t)$ represents the estimated radial orbit error at time t, whereas a_0 and b_0 symbolize two unknowns belonging to the resonant solution of the Hill equations, compare also (4.39). The term c_0 stands for the bias term and a_k, b_k represent the Fourier coefficients of the orbit error spectrum. The known constant τ denotes the average revolution period of the spacecraft in seconds whereas n equals to the mean motion. The constant κ is chosen such that $\kappa\tau$ equals to the full period over which (6.30) is defined. The purpose is to obtain values around 1 in the design matrix which is favorable for the numerical properties of the system of normal equations. The other constants $\Delta\omega$ and $kmax$ are chosen such that:

- An optimal resolution is obtained in the orbit error spectrum. The orbit repeats itself after 43 revolutions which equals to the largest period that can be recovered from any frequency analysis. For this reason the value of $\Delta\omega$ is chosen as 1/43.
- The orbit error spectrum is followed with sufficient accuracy. Computations have shown that after 2.3 c.p.r. (=100 × 1/43) a r.m.s. of $\approx$ 15 cm is found for the remaining orbit error signal. This noise signal is not modeled.

Crossover difference observation equations are written in the from of $\Delta h_{ij} = \Delta r(t_i) - \Delta r(t_j)$ where t_i and t_j refer to the *absolute* time tags of a crossover point. Unknowns are the coefficients a_0, b_0, c_0 and a_k, b_k with $k \in [1, kmax]$. It results directly in the relation $\vec{y} = A\vec{x} + \vec{\epsilon}$ since (6.30) is a linear expression with respect to the unknowns. The vector $\vec{y}$ contains the crossover differences Δh_{ij} and $\vec{x}$ the unknowns.

In a first attempt the crossover difference observations are equally weighted, i.e. a unit matrix is assumed for Q_{yy}. The design matrix A is unfortunately *not* anymore sparse as in the segmented method(s) and cannot be partitioned in an ascending and a descending part.

It should be noticed that a considerable amount of computing time is needed to form the normal equations. In order to compute one element of the normal matrix $N = A^t Q_{yy}^{-1} A$, n floating point operations in the form of one multiplication and one addition are required. Here n equals to the amount of crossover difference observations involved in the problem. In the simulated orbit 1849 crossover are found of which 711 are located on land and 1138 on sea. Due to symmetry of N, $\frac{1}{2}m(m+1)$ elements have to be computed by an inner product of the columns of the design matrix, where m is the amount of unknowns involved in the problem, $m = 2 \times kmax + 3 = 203$. Accordingly $\frac{1}{2}m(m+1)n$ ($\approx 80 \times 10^6$) floating point operations are required to compute the N matrix. The reduction and backward substitution of the normal equations is performed in less time, requiring of the order of $\frac{1}{3}m^3$ ($\approx 2.8 \times 10^6$) floating point operations, compare also (Conte et al.,1986).

6.4.3 Singularity of the normal equations

It is not surprising that the normal equations derived from observation equations in the form of $\Delta h_{ij} = \Delta r(t_i) - \Delta r(t_j)$ where $\Delta r()$ is given by (6.30) results in a singular system. This is confirmed by an eigenvalue analysis of the normal matrix. The results of this analysis are presented under "land+sea 1" in table 6.4. The computed eigenvalues of the normal matrix show 9 small eigenvalues indicating one true singularity (the first eigenvalue) and in addition a system which is poorly conditioned. The problem is 1) to explain how the normal equations have to be treated in order to find a numerical stable solution and 2) to demonstrate the characteristics of this solution.

As discussed in chapter 3 singularity of the normal equations is caused by linear dependency of the column vectors in the design matrix A. In the sequel we search for a set of linear independent base vectors $\vec{u}_i$ having the dimension of m which multiplied by A result in a zero vector of dimension n:

$$\vec{0} = A\vec{u}_i, \quad i \in [1, \ldots, \ell]. \tag{6.31}$$

The base vectors $\vec{u}_i$ span the null space of A which has the dimension ℓ. It is customary to gather these base vectors in a matrix E of m rows and ℓ columns such that $AE = 0$. It will be shown for this problem that the elements of the E matrix consist of linear combinations of F_{lmp} functions evaluated at the inclination of the nominal orbit, here 108°.

For this purpose we consider a spherical harmonic expansion of a surface function $D(\phi, \lambda)$, compare (6.28), mapped along the nominal orbit, compare (6.29). From this expression one can derive the Fourier series of the signal mapped along the orbit belonging to an individual C_{lm} coefficient of the surface function:

$$D^c_{lm}(t) = C_{lm} \sum_{p=0}^{l} F_{lmp} \begin{bmatrix} \cos\psi_{lmp} \\ \sin\psi_{lmp} \end{bmatrix}_{l-m:odd}^{l-m:even} \tag{6.32}$$

For an individual S_{lm} coefficient it is found that:

$$D^s_{lm}(t) = S_{lm} \sum_{p=0}^{l} F_{lmp} \begin{bmatrix} \sin\psi_{lmp} \\ -\cos\psi_{lmp} \end{bmatrix}_{l-m:odd}^{l-m:even} \tag{6.33}$$

In (6.32) and (6.33) it is possible to replace the summation by an inner product of two vectors $\vec{u}$ and $\vec{v}$. Here the sequence of the elements in the vectors is chosen conform the ordering of the unknowns in the design matrix:

$$D^c_{lm}(t) = C_{lm}(\vec{u}^{\,c}_{lm}, \vec{v}(t)) \tag{6.34}$$

$$D^s_{lm}(t) = S_{lm}(\vec{u}^{\,s}_{lm}, \vec{v}(t)) \tag{6.35}$$

where $\vec{v}(t)$ represents a vector with time dependent components, compare (6.30):

$$\vec{v}(t) = \left(\frac{t}{\kappa\tau}\cos(nt), \frac{t}{\kappa\tau}\sin(nt), 1, \ldots, \cos(k\Delta\omega nt), \sin(k\Delta\omega nt), \ldots\right). \tag{6.36}$$

Two remarks concerning $\vec{v}$: 1) For each ψ_{lmp} combination in (6.34) and (6.35) there exists a corresponding $k\Delta\omega nt$ term in (6.30); 2) The first two elements in $\vec{v}$ are not contributing to the inner products in eqs. (6.34) and (6.35). The location of the elements in the $\vec{u}^{\,c}_{lm}$, $\vec{u}^{\,s}_{lm}$ and $\vec{v}$ vectors depends on the values of the indices l, m and p. In our case where the highest frequency to recover equals to 2.3 c.p.r. there exist 9 possible $\vec{u}^{\,c}_{lm}$, $\vec{u}^{\,s}_{lm}$ vectors ($lmax = 2$ in (6.28)). The higher degree and order $\vec{u}^{\,c}_{lm}$ and $\vec{u}^{\,s}_{lm}$ vectors fall outside the frequency range of the model based on (6.30) and cannot be used to describe linear dependence between column vectors of the design matrix. For each surface coefficient C_{lm} or S_{lm} one base vector $\vec{u}^{\,c}_{lm}$ or $\vec{u}^{\,s}_{lm}$ is found. The corresponding expressions in the form of (6.34) & (6.35) (from which the structure of the $\vec{u}^{\,c}_{lm}$ and $\vec{u}^{\,s}_{lm}$ vectors follows) become, compare (Sandwell et al.,1986):

$$
\begin{aligned}
D^c_{00} &= C_{00}[F_{000}] \\
D^c_{10} &= C_{10}[(F_{100} - F_{101})\sin\omega_o] \\
D^c_{20} &= C_{20}[F_{201} + (F_{200} + F_{202})\cos 2\omega_o] \\
D^c_{11} &= C_{11}[F_{111}\cos(\omega_o - \omega_e) + F_{110}\cos(\omega_o + \omega_e)] \\
D^s_{11} &= S_{11}[-F_{111}\sin(\omega_o - \omega_e) + F_{110}\sin(\omega_o + \omega_e)] \\
D^c_{21} &= C_{21}[F_{211}\sin\omega_e - F_{212}\sin(2\omega_o - \omega_e) + F_{210}\sin(2\omega_o + \omega_e)] \\
D^s_{21} &= S_{21}[-F_{211}\cos\omega_e - F_{212}\cos(2\omega_o - \omega_e) - F_{210}\cos(2\omega_o + \omega_e)] \\
D^c_{22} &= C_{22}[F_{221}\cos 2\omega_e + F_{222}\cos(2\omega_o - 2\omega_e) + F_{220}\cos(2\omega_o + 2\omega_e)] \\
D^s_{22} &= S_{22}[+F_{221}\sin 2\omega_e - F_{222}\sin(2\omega_o - 2\omega_e) + F_{220}\sin(2\omega_o + 2\omega_e)]
\end{aligned}
\tag{6.37}
$$

From (6.37) it can be shown that the $\vec{u}^{\,c}_{lm}$ and $\vec{u}^{\,s}_{lm}$ vectors are linear independent. Furthermore it is easy to show that any $\vec{u}^{\,c}_{lm}$ or $\vec{u}^{\,s}_{lm}$ vector multiplied by the design matrix A results in a zero vector. In other words, they fulfill the properties of the base vectors $\vec{u}_i$ in (6.31)! In order to demonstrate this property we consider an arbitrary row vector $\vec{a}_{ij}$ of the design matrix containing the coefficients of the crossover difference observation equation $\Delta h_{ij} = \Delta r(t_i) - \Delta r(t_j)$. This row vector equals to:

$$\vec{a}_{ij} = \vec{v}(t_i) - \vec{v}(t_j). \tag{6.38}$$

Multiplication of $C_{lm}\vec{u}^{\,c}_{lm}$ or $S_{lm}\vec{u}^{\,s}_{lm}$ by the design matrix results in:

$$(\vec{a}_{ij}, C_{lm}\vec{u}^{\,c}_{lm}) = C_{lm}(\vec{v}(t_i) - \vec{v}(t_j), \vec{u}^{\,c}_{lm}) = D^c_{lm}(t_i) - D^c_{lm}(t_j) = 0 \tag{6.39}$$

or

$$(\vec{a}_{ij}, S_{lm}\vec{u}^{\,s}_{lm}) = S_{lm}(\vec{v}(t_i) - \vec{v}(t_j), \vec{u}^{\,s}_{lm}) = D^s_{lm}(t_i) - D^s_{lm}(t_j) = 0. \tag{6.40}$$

Remember that D^c_{lm} and D^s_{lm} are the result of a mapping operation of a surface function D along a nominal orbit. The time tags t_i and t_j hold along this nominal orbit and form a crossover point at the geographical location (ϕ, λ). It is obvious that $D^c_{lm}(t_i) - D^c_{lm}(t_j) = 0$ and $D^s_{lm}(t_i) - D^s_{lm}(t_j) = 0$ since the difference of a surface function with itself at the same geographical location equals to zero. In reality the crossover differences are not exactly equal to zero when D^c_{lm} and D^s_{lm} are mapped along the actual simulated trajectory. Cause of the effect are the small deviations of the order of a few seconds with respect to the nominal trajectory. This explains the existence of the 9 small – instead of zero – λ's recovered by the eigenvalue analysis of the normal matrix. Later on in this chapter a more detailed analysis is made of the non–orthogonality of the $\vec{u}^{\,c}_{lm}$ and $\vec{u}^{\,s}_{lm}$ vectors with respect to the vectors $\vec{v}$.

6.4.4 Attempts to solve the problem

In this section three numerical experiments are conducted for the purpose of solving the system of normal equations which are singular since it was shown in §6.4.3 that linear combinations of the columns of the design matrix exist. The experiments concern respectively a hybrid norm solution, the inclusion of a minimal number of so-called direct height measurements and an alternatively constrained solution of the normal equations.

Hybrid norm solution

An easy to realize solution of the normal equations can be found by minimizing a hybrid norm. The hybrid norm minimization takes the form of:

$$\vec{\epsilon}^{\,t} Q_{yy}^{-1} \vec{\epsilon} + \vec{x}^{\,t} P_{xx}^{-1} \vec{x} = \min \tag{6.41}$$

with P_{xx} the a-priori covariance matrix of the *unknowns*. The purpose of hybrid norm minimization is partly the same as that of least squares minimization, namely to minimize the norm of the vector $\vec{\epsilon}$. In addition in (6.41) one attempts to find the 'smoothest' solution for $\vec{x}$ by minimizing $\vec{x}^{\,t} P_{xx}^{-1} \vec{x}$. It can be shown that a minimum is found by solving the system of equations:

$$(A^t Q_{yy}^{-1} A + P_{xx}^{-1}) \hat{x} = A^t Q_{yy}^{-1} \vec{y} \tag{6.42}$$

The numerical consequences of a hybrid norm minimization are obvious. The inverse of the regular P_{xx} matrix is added to the singular normal matrix. This affects directly the eigenvalues of the matrix on the LHS of (6.42). A problem encountered while minimizing the hybrid norm given in (6.41) is the proper choice of the Q_{yy} and P_{xx} matrices. For Q_{yy} a diagonal matrix is assumed to describe the variance/covariance behavior of the crossover differences. This assumes that all observations are equally weighted and uncorrelated. In the literature, cf. (Engelis,1987), some critical remarks are made about this point. Crossover differences occur more frequently at higher latitudes and should therefore be down-weighted with respect to the ones on lower latitudes. Undoubtedly this is true, on the other hand satisfactory results are already obtained by assuming a unit diagonal matrix for Q_{yy}, compare the results of the chronological crossover adjustment.

For modeling the P_{xx} matrix a-priori information concerning the orbit error spectrum is required. Here one could apply the property that most of the signal is concentrated near 1 c.p.r. and that a rapid decrease of $\Delta r(t)$ is expected at higher frequencies. A proper formulation of the P_{xx} matrix may be derived from the radial solution of the HE, compare (4.49) in conjunction with an error degree variance model of potential coefficients of the gravitational field.

Here we assume a modest approach which mildly affects the unknowns to be estimated by means of a hybrid norm minimization. The P_{xx} matrix is chosen as a scaled unit matrix λI where the scalar λ is taken as large as possible for regularization of the normal matrix. The effect of this particular hybrid norm minimization is that all eigenvalues of the normal matrix are increased by λ^{-1}. Computations have shown that $\lambda^{-1} = 10^{-5}$ is sufficient for regularizing the system of equations

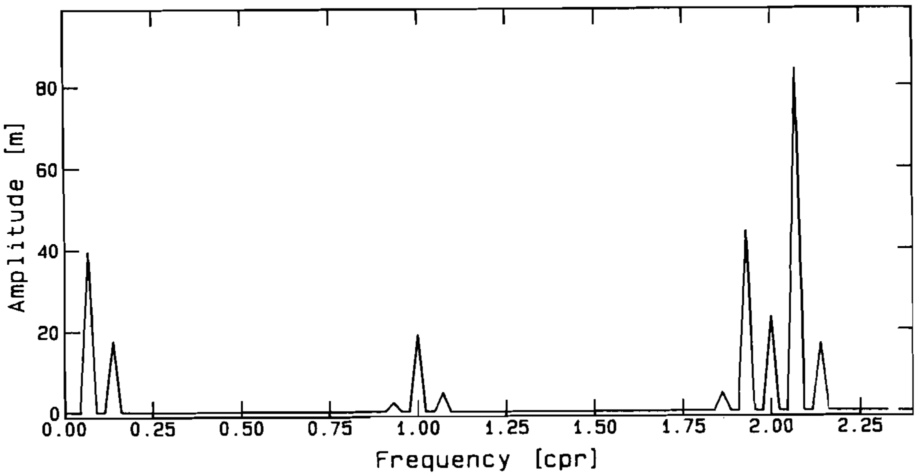

Figure 6.8: A power spectrum of the difference signal between hybrid norm minimization and the simulated radial orbit error. On the horizontal axis the frequency is represented in cycles per revolution, on the vertical axis the amplitude is represented in m per 1/43 c.p.r.

given in (6.42). It implies that a uniform a-priori variance of 10^5 is assigned to the unknowns involved in the problem.

The power spectrum of the differences between the hybrid norm solution with respect to the simulated radial orbit error is given in figure 6.8. In this figure the results are shown for $\lambda = 10^5$ where it is noted that similar results were found for other values of λ. Remarkable is the fact that most frequencies of the recovered signal, even for different values of λ, tend to follow accurately the simulated radial orbit error. (The apparent offset between the bottom line of figure 6.8 and the 'non singular' frequencies is an artifact of the plotting program employed.) However there appear to exist a number of 'singular' frequencies at 0 (which is not plotted in figure 6.8), ω_e, $2\omega_e$, ω_o $2\omega_o$, $\omega_o \pm \omega_e$, $2\omega_o \pm \omega_e$ and $2\omega_o \pm 2\omega_e$ (which are the peaks in figure 6.8). This test confirms the expected singular behavior of the normal matrix as it would arise whenever a least squares minimum norm is defined, compare §6.4.3.

Unfortunately it was *not* possible to reduce the differences between the hybrid norm solution and the simulated orbit error significantly. The remaining differences stay in the order of 40 m, whereas one would expect that the residual between the 'hybrid norm' solution and the simulated $\Delta r()$ could be described by a surface function mapping.

The eigenvalues above 9 are hardly affected since λ^{-1} is a factor 10^4 to 10^8 smaller, from which one may conclude that the regular part of the normal equations remains intact. This explains why the 'regular' frequencies – those not equal to the peaks shown in figure 6.8 – are followed with satisfactory accuracy (even up to a few cm difference signal).

However the first 9 eigenvalues of the least squares normal matrix shown in table 6.4 (column "land+sea 1") are of the same magnitude or even much smaller than λ^{-1}. This explains the 11 singular frequencies shown in figure 6.8.

The only conclusion drawn from the hybrid norm minimization in its current form is that the expected singular frequencies predicted in §6.4.3 show up in the difference signal. It is remarkable that a simple ad hoc solution as discussed in this section results in these singular frequencies. What is not understood is why the "hybrid norm" orbit error cannot be reduced significantly to the simulated error. More investigations are required to investigate this problem which is probably due to the unrealistic choice of the P_{xx} matrix.

Minimum constrained solutions

In order to find a solution for the normal equations it is possible to include a number of constraints in the form of additional observation equations. The question is 1) what sort of constraints are allowed to be included and 2) how many constraints are required for regularizing the problem? This problem is described in eqs. (3.51) ff.

In order to find a general solution, by forcing additional constraints on the unknowns, one must demand that exactly as many constraints are included as the dimension of the null space of A. By definition under-constrained systems are singular. Over-constrained solutions imply that the original minimization problem is *altered*, i.e. the solution will satisfy the observation equations *including* the constraints. Whether the latter type of solution is desirable or not from physical point of view will not be discussed here. However solutions of this type do *not* fall in the category of general solutions of the original minimization problem.

Direct height constraints

A first suggestion for additional constraints has been put forward by Sandwell et al. (1986). The constraints are formed by direct height measurements from the altimeter to natural or artificial radar transponders in the form of 1) inland lakes 2) salt planes 3) sea surfaces near tide gauges or 4) active radar transponders on land. For all configurations it is required to know the position of the transponder in a consistent geocentric coordinate system. The position(s) could by derived by modern geodetic techniques and should be known within sub-decimeter accuracy.

Direct height measurements enable to form constraints having a physical relevance. The height h of the transponder above the reference ellipsoid can be derived from the geometrical coordinates which are known within a certain accuracy. The actual height h^* of the satellite above a reference ellipsoid is contaminated by a radial orbit error Δr. The height above the transponder location ρ, is measured. An evaluation of eq. (2.1) results in:

$$\Delta r = h + \rho - h^*. \qquad (6.43)$$

Direct height measurements of the altimeter to the transponder enable to derive, within a certain accuracy, an estimate for the actual Δr while the satellite passes over the transponder location. The technical details of transponder measurements, e.g. an identical coordinate system definition for trajectory computation and transponder coordinate determination, pose an additional problem but fall outside the scope of this work.

In a simulation one may include observation equations in the form of (6.30) in order to regularize the normal equations. Sandwell (ibid) mentions that 9 globally distributed transponders suffice for regularizing the problem. In fact 9 constraint equations in the form of $\vec{c} = B\vec{x}$ are included in the design matrix. One should verify whether the transponder constraints fulfill the condition that BE equals to a square regular matrix, compare eq. (3.51) ff. A simple counter example is a set of transponders distributed along the equator. Such a configuration cannot be used to determine the zonal terms of a geographically correlated orbit error function. Further investigations of this problem are required.

Alternative constraints

An alternative for finding a general solution of a self-adjoint system of normal equations is to include constraints in the form of $\vec{c} = E^t\vec{x}$ with $\vec{c} = \vec{0}$ and $B = E^t$, compare eqs. (3.51). The numerical advantage is obvious, the matrix product E^tE in (3.55) equals to a square matrix with regular properties due to the linear independence of the column vectors of the E matrix. Unfortunately, in contrary to the constraints obtained by direct height measurements to transponders, *no* physical meaning can be assigned to these constraint equations. Their *only* purpose is to help finding a general solution of the self-adjoint system of normal equations. In a secondary step this solution can be compared, by means of a singularity transformation, with the simulated trajectory.

A first numerical test is to check the orthogonality of the constraints with respect to the observation equations. For this purpose each base vector $\vec{u}^c_{lm}$ and $\vec{u}^s_{lm}$, compare (6.34) & (6.35), is multiplied by the design matrix A. In theory each product $A\vec{u}^c_{lm}$ or $A\vec{u}^s_{lm}$ should result in a zero observation vector. However, the crossover time tag distribution deviates slightly from the pattern expected from the nominal orbit. This causes the vectors $\vec{u}^c_{lm}$ and $\vec{u}^s_{lm}$ to be nearly orthogonal with respect to the observation equations. The results are presented in table 6.3 where each possible vector $\vec{u}^c_{lm}$, $\vec{u}^s_{lm}$ is multiplied by the A matrix. This table shows the mean value and the standard deviation of the elements in the vector

term	mean [m]	rms [m]
C_{00}	$+0.00$	0.00
C_{10}	$+3.86 \times 10^{-3}$	2.74×10^{-3}
C_{20}	-1.99×10^{-4}	8.17×10^{-3}
C_{11}	$+1.83 \times 10^{-5}$	3.80×10^{-3}
S_{11}	$+2.84 \times 10^{-6}$	3.74×10^{-3}
C_{21}	$+1.45 \times 10^{-5}$	9.26×10^{-3}
S_{21}	-7.35×10^{-6}	9.10×10^{-3}
C_{22}	-7.58×10^{-6}	1.33×10^{-2}
S_{22}	$+2.73 \times 10^{-5}$	1.33×10^{-2}

Table 6.3: Orthogonality of the constraint equations with respect to the observation equations.

$\vec{y}$ where $\vec{y} = A\vec{u}^{c}_{lm}$ or $\vec{y} = A\vec{u}^{s}_{lm}$. The values in this table may be interpreted as the discrepancies on the crossover points due to the constraints forced on the unknowns involved in the problem. The effect appears insignificant and is ignored in the sequel. The statistics mentioned above are based on all 1849 crossovers of the simulated dataset.

The following experiments concern the numerical treatment of the least squares normal equations which are augmented by constraints in the form of $\vec{0} = E^t\vec{x}$. Here we assumed that the constraints are assigned a same a-priori weight as the observation equations. We distinguish two problems, the so-called "land+sea" problem referring to an LSA involving all crossover differences and the "sea" problem where only marine crossovers are employed.

The improvement of the eigenvalue spectrum of the constrained normal equations is considerable. The 4 eigenvalue spectra of the "land+sea" and "sea" problem are shown in table 6.4. The eigenvalue analysis shows that constraint equations drastically improve the condition number of the normal matrix. The $\lambda_{max}/\lambda_{min}$ values become $\approx 10^5$ and $\approx 10^6$ respectively for the "land+sea" and "sea" problem.

nr	"sea" 1	"sea" 2	"land+sea" 1	"land+sea" 2
1	0.00	3.79×10^{-2}	0.00	0.11
2	2.47×10^{-9}	0.44	6.34×10^{-9}	0.44
3	5.74×10^{-9}	0.55	1.60×10^{-8}	0.55
4	1.60×10^{-8}	0.55	3.33×10^{-8}	0.55
5	3.89×10^{-6}	0.90	1.09×10^{-5}	0.90
6	5.71×10^{-6}	1.06	1.22×10^{-5}	1.06
7	1.50×10^{-5}	1.07	3.54×10^{-5}	1.31
8	2.35×10^{-5}	1.31	4.63×10^{-5}	1.31
9	3.44×10^{-2}	1.31	9.75×10^{-5}	3.27
10	3.79×10^{-2}	3.62	0.11	3.62
11	1.07	3.62	3.27	3.62
...				
203	3554	3554	4121	4121

Table 6.4: Eigenvalues of the normal matrices in case "sea 1": only sea crossovers are used, "sea 2": including constraints, "land+sea 1": all crossovers are used, "land+sea 2": including constraints.

The "land+sea" 1 column in table 6.4 shows the eigenvalues as they were found for the least squares normal matrix where 1) all crossover differences are employed and where 2) no constraints are used. It shows that there are 9 small eigenvalues causing condition numbers for the remaining subsystem greater than 10^8. Note the difference with the "sea" 1 case which is the same as the "land+sea" 1 case except that only the marine crossover differences are used. As a result the boundary between the "small" and the "large" eigenvalues is smeared out and it appears as if the rank defect becomes 8 instead of 9. It is not unlikely that the land-sea problem in altimetry leaves an effect on the rank defect of the normal equations.

In the following step the constrained solutions of the unknowns are compared with the simulated radial orbit error. This experiment could never be carried out in reality as is mentioned in the introduction of this chapter. However it gives an indication of the behavior of the constrained solution with respect to the simulated orbit error. The comparison is made at 433 samples regularly distributed at every 10 minutes along the simulated orbit (density of sampling equals to 10 per revolution over the first 3 day repeat period). The power spectrum of the residual for as well the "land+sea" and "sea" problem is similar to the difference spectrum shown in figure 6.6. Discrepancies occur dominantly at 0, ω_e, $2\omega_e$, $\omega_o \pm \omega_e$, ω_o, $2\omega_o$, $2\omega_o \pm \omega_e$ and $2\omega_o \pm 2\omega_e$. Modeling of this signal is possible by solving surface function coefficients C_{lm}, S_{lm} in (6.28). This is equivalent to performing a singularity transformation of the unknowns to the simulated $\Delta r()$.

For the constrained "land+sea" problem the a-priori / a-posteriori r.m.s. of the crossover residuals equals to respectively $\sigma_{i1} = 4.17$ / $\sigma_{i2} = 0.13$ m. Note that -10 to +10 cm uniformly distributed random noise was added to the a-priori simulated crossover residuals. This solution shows a r.m.s. of $\sigma_{e1} = 0.98$ m and a mean value of -3.84×10^{-4} with respect to the simulated radial orbit error. After solving the surface function coefficients C_{00} through S_{22} a r.m.s. of $\sigma_{e2} = 0.15$ m and a mean value of 0.00 m is found. For the constrained "sea" problem we found, under the same assumptions as in the former problem, $\sigma_{i1} = 4.17$, $\sigma_{i2} = 0.10$, $\sigma_{e1} = 0.99$ and $\sigma_{e2} = 0.18$. The corresponding surface function coefficients are shown in table 6.5.

coefficient	"land+sea" case	"sea" case
C_{00}	$+2.38 \times 10^{-3}$	-6.62×10^{-4}
C_{10}	$+0.75$	$+0.74$
C_{11}	$+1.54$	$+1.57$
S_{11}	-6.94×10^{-2}	-0.15
C_{20}	-1.83×10^{-2}	-1.78×10^{-2}
C_{21}	-2.84×10^{-2}	-2.85×10^{-2}
S_{21}	$+1.65 \times 10^{-2}$	$+2.02 \times 10^{-2}$
C_{22}	$+0.10$	$+9.90 \times 10^{-2}$
S_{22}	$+5.80 \times 10^{-2}$	$+5.60 \times 10^{-2}$

Table 6.5: The surface function coefficients recovered by a singularity transformation of the constrained solutions to the simulated radial orbit error. Column 1 represents the coefficient, column 2 its value in the "land+sea" case and column 3 its value in the "sea" case.

A last test concerns the variance behavior of the unknowns in the "sea" case. A-posteriori standard deviations of the unknowns are computed as the square roots of the diagonal elements of the inverse of the normal matrix. In this computation it is assumed that $Q_{yy} = I$, $Q_{cc} = I$ and $Q_{x_pc} = 0$, compare (3.51) ff. In our case this implies a 1 m a-priori variance estimate for the crossover differences. The estimated standard deviations for the A_k unknowns in (6.30) are given in figure 6.9, the values for the B_k unknowns are given in 6.10.

From this analysis we conclude that relatively high standard deviations occur at the predicted singular frequencies. The singularity of the unknowns at these

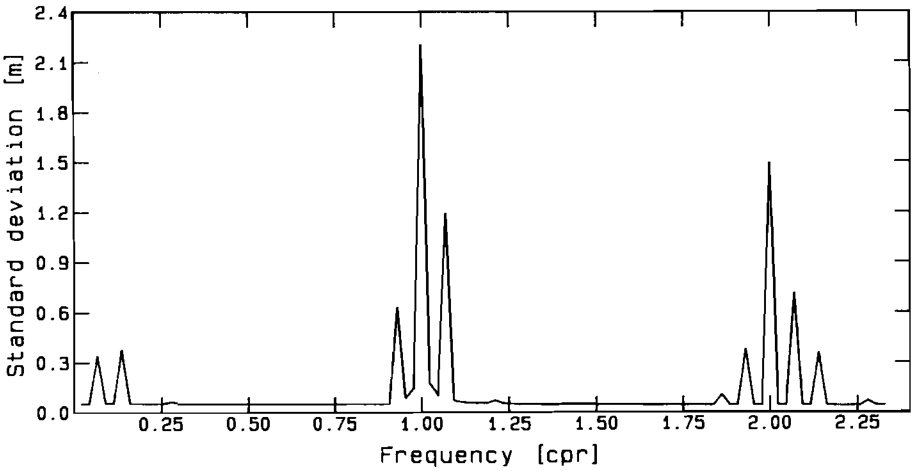

Figure 6.9: A-posteriori standard deviations of the A_k unknowns. The estimated standard deviations in m per 1/43 c.p.r. are given as a function of the frequency in c.p.r.

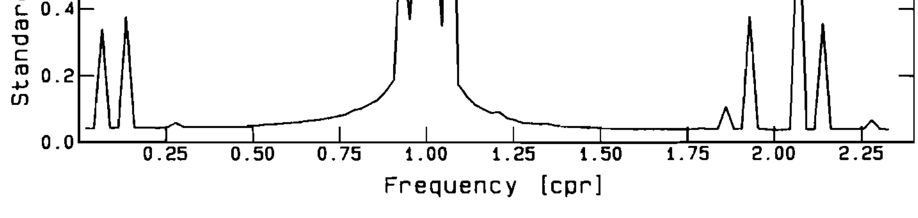

Figure 6.10: A-posteriori standard deviations of the B_k unknowns. The estimated standard deviations in m per 1/43 c.p.r. are given as a function of the frequency in c.p.r.

frequencies is *only* controlled by the constraints forced on the system. Furthermore we note that all the B_k terms in the band from ≈ 0.75 to ≈ 1.25 c.p.r. possess, compared with the corresponding A_k terms, relatively high standard deviations.

6.5 Conclusions

In this chapter observables derived from a dataset containing the simulated orbit superimposed with a synthetic radial orbit error were used to perform 1) a so-called collinear adjustment of repeat arc differences and 2) two versions of a global adjustment of crossover residuals. The first method for adjusting the crossover residuals is based on the conventional arc segment model. In the second crossover minimization model parameters are solved of a continuous and differentiable function which is defined over a full period of 3 days.

Repeat arc differences

Repeat arc differences caused by gravitational effects have shown to be inadequate for recovering most of the short periodic components in the simulated radial orbit error. This phenomenon was predicted in chapter 5 on basis of the results of the linear perturbations theory and confirmed by a numerical analysis of the simulated repeat arc differences. It is shown that the observed error signal present in the simulated repeat arc differences can be explained by a long periodic modulation caused by the precession of the argument of perigee. Especially the non-centricity in the u, v plane of the reference and the perturbed trajectory seems to explain most of the signal found in the simulated observables. As a result it is demonstrated that an adequate filter is capable of removing almost completely the simulated gravitational effect from the repeat arc differences. Repeat arc differences measured by a radar altimeter are particularly useful for studying ς^v induced by oceanographic phenomena such as eddies, meanders or rings.

Global chronological crossover adjustment

Global chronological crossover adjustment based on solving the parameters of stepwise error functions per arc segment is described in section 6.3 of this chapter. The type of error function to be introduced per arc segment plays an important role in this method since it determines the accuracy of the crossover minimization model. A compromise between accuracy of the stepwise error function and efficiency concerning the amount of unknowns to be solved for results in a stepwise 3 parameter Fourier function. This model also allows a physical interpretation in terms of the expected behavior of a radial orbit error. A crossover minimization problem derived from these error functions results in a self-adjoint compatible system of normal equations. Under assumption of anti-symmetry of crossover time tags it is shown that the rank defect of the normal equations equals to 3. This means that one so-called master arc segment can be used to fix the solution, i.e. to acquire a particular solution of the system of normal equations.

A singularity transformation of the unknowns allows to transform from one arbitrary master arc segment solution to any other without re-adjustment of the configuration while preserving the internal consistency of the altimeter solution. A remarkable property of the homogeneous solution of the system of normal equations is the velocity discontinuity effect at junctures of successive arc segments. The effect is considered artificial since it is known that a radial orbit error behaves as a smooth continuous function. Hence in a second global chronological model additional minimization conditions for velocity discontinuities are forced on the system of normal equations. Inclusion of additional smoothness conditions have shown to reduce the rank defect from 3 to 2.

In a next step a comparison is made between the general solution of the chronological crossover problem and the simulated radial orbit error. For this purpose a singularity transformation of the solution is carried out under the condition that the general solution coincides in an optimal way with the simulated radial orbit error signal. Computations have shown that an optimally adjusted crossover solution based on a chronological approach *fails* to describe some terms of the geographically correlated part of the radial orbit error. It is shown that additional surface function modeling is required to explain the differences between both solutions. In an ideal case the homogeneous solution of a crossover minimization model coincides with the geographical correlated part of the radial orbit error.

Global crossover adjustment without arc segments

In an alternative version of a global crossover adjustment, stepwise error functions along arc segments are not anymore used. The problem is to solve the parameters of one continuous and differentiable function modeling the radial orbit error over a full 3 day period. This function resembles the general solution of the Hill equations (homogeneous, particular and resonant case) taking the form of a Fourier series truncated at 2.3 cycles per revolution, including a two parameter expression describing the long periodic modulation of the signal.

This approach avoids in a convenient way a number of problems encountered with the segmented models. Shortly summarized, the problems inherent to arc segment models are: 1) discontinuity at the boundaries of arc segments 2) over-parameterization of short arc segments 3) poorly or even isolated segments with respect to the 'main' configuration. For completeness it is reminded that some of these problems formed real obstacles in the development of adequate software handling a segmented crossover adjustment.

Under suitable time tag regularization it is shown that the rank defect of the normal equations equals to 9. This presumes a cutoff frequency of 2.3 cycles per revolution in the Fourier series. Higher cutoff frequencies result in a larger rank defect! It is found that the base vectors of the E matrix used in the singularity transformation of the unknowns take the form of certain linear combinations of inclination functions.

Furthermore a verification of the column vectors of the E matrix with respect to the rows in the design matrix is performed. This reveals that the column vectors are almost orthogonal to the observation equations. However the effect of non-orthogonality is negligible with respect to the real crossover differences.

A first suggestion for additional constraints on the system of normal equations has been put forward by Sandwell et al. (1986). The constraints are formed by direct height measurements from the altimeter to natural or artificial radar transponders. Sandwell (ibid) mentions that 9 globally distributed transponders suffice for regularizing the problem which is equivalent to including 9 constraint equations in the form of $\vec{c} = B\vec{x}$ in the problem. The criteria for a proper choice of the transponder locations require further investigation.

The method for regularizing the normal equations employed here is to force 9 additional constraint equations on the unknowns. These constraint equations are chosen such that a general solution of the normal equations is found. This general solution may be transformed by a singularity transformation into any other solution without affecting the crossover problem. After a suitable singularity transformation an accurate comparison can be made with the simulated radial orbit error. Promising results are shown for solutions derived in this way.

Chapter 7

Processing of SEASAT altimeter data

7.1 Introduction

In this chapter the technique is described that is applied for removing a radial orbit error present in SEASAT altimeter data. The method employed here is identical with the LSA of crossover differences described in §6.4. It is based on solving a continuous and differentiable error function from crossover differences under assumption of several additional constraint equations. These constraint equations are necessary for regularizing the normal equations which are singular by definition. The motivation for using this particular technique instead of the approach of Rowlands (1981) is given in §7.2.1.

An inventory of the available altimeter data shows that there are five periods in the non-repeat era of the SEASAT mission which are suitable for processing with the technique considered here. The periods have been chosen such that they coincide with the orbital periods the GSFC (Goddard Space Flight Center) defined for computing the ephemerides of SEASAT.

In each of these periods defined by the GSFC an independent LSA of crossover differences is carried out. Firstly it will be shown that it is possible to apply the same model as discussed in §6.4.2. For this purpose assumptions will be discussed concerning the frequency resolution and the maximum cutoff frequency in the radial orbit error model.

The internal evaluation of crossover residuals is discussed in §7.3.1. The results show that the technique of global crossover minimization considered here can be performed effectively on SEASAT altimeter data. Furthermore some characteristics of the five computed orbit error functions are discussed. They concern the concentration of signal near 1 c.p.r. and correlations of the individual solutions. As a result of the high correlations it will be shown that it is feasible to consider a combined orbit error model. The latter implies a continuous error function overlapping a multiple of orbital periods that is solved by minimizing crossover differences.

The external evaluation describes the behavior of individual crossover solutions as a result of a singularity transformation. Here the singularity transformation is chosen such that an internal consistent crossover solution is minimized with respect to a reference geoid. Furthermore it will be shown that there exists a systematic effect in the shift vector of the singularity transformation. Whether this part is actually representing an unmodeled (physical) phenomenon is discussed in §7.3.2.

7.2 Description of the adjustment

7.2.1 Motivation

In this section a model is described that is applied in a global adjustment of SEASAT crossover differences. The method is analogous to the LSA described in §6.4 where a continuous and differentiable error function is solved from simulated observables. The reasons for choosing this approach instead of the alternative segmented method is discussed in the sequel.

A global segmented approach, where error functions are solved per individual arc segments, has been applied by Rowlands (1981). Rowlands solved for error functions in the form of tilt and bias expressions for segments longer than 212 seconds. Shorter segments were solved for bias only error functions. The purpose of Rowlands' work was to obtain a globally adjusted SEASAT altimeter dataset. There was no specific objective to reconstruct a radial orbit error function from the unknowns solved, neither was there any objective for improving the gravitational field from the radial orbit error recovered.

Similar versions of Rowlands' adjustment, using other error functions defined over arc segments as long as a half revolution of the satellite, are discussed in §6.3. There are a number of reasons to assume that Rowlands' results are 'contaminated' by effects similar to the shortcomings of the homogeneous solution of the segmented crossover minimization problem. Rowlands mentions that: "The primary arc which was fixed was a north-west heading arc starting south of Africa and finishing near Greenland". This means that Rowlands' solution is deformed by the full effect of a radial orbit error along this primary arc.

The counter measures mentioned by Rowlands (ibid) for suppressing the effect are presumably not adequate. "The primary arc has been formed out of the average of 8 repeat arcs and shows a good precision." In chapters 5 and 6 it is shown that minimization of repeat arc differences is hardly effective for improving a radial orbit error caused by short periodic gravitational effects. Yet these averaged arc segments may be useful for suppressing variability and other short periodic effects. The only hope for a well positioned primary arc comes possibly from the second reason Rowlands mentions for choosing a specific arc: "Secondly, it was an arc that could have been tracked from several laser stations."

Nevertheless, if Rowlands succeeded in finding a suitable primary arc, the results might still be contaminated with other geographically correlated radial orbit error components. Noteworthy is the mapping of surface harmonics up to degree and order 2 since the corresponding mapping frequencies occur close to the once per revolution region in the radial orbit error spectrum. Mapping of higher degree and order surface harmonic coefficients is not expected to be so problematical due to the expected rapid extinction of the radial orbit error signal at higher frequencies. Moreover, as our simulation showed, this effect cannot be described by a singularity transformation of the segmented solution.

In addition Rowlands' derivation of a singularity transformation (appendix F in

Rowlands (1981)) indicates that one primary arc segment suffices for regularizing his global segmented crossover minimization problem. This implies 2 degrees of freedom in the network of arc segments which is not sufficient for modeling the (more complex) geographically correlated part of the radial orbit error.

In an improved version of a global crossover adjustment the unknowns of a continuous and differentiable function taking the form of (6.30) are solved from the crossover differences. This method is invariant with respect to the geographically correlated part of the radial orbit error as shown in §6.4. By adding 9 constraint equations, which are derived from the base vectors spanning the null space of the normal equations, to the observation equations it is possible to regularize the normal equations. From a practical point of view the 'continuous' method has shown to be considerable easier for computer implementation than any segmented method.

The outline of this section is as follows. Firstly an inventory is discussed of the available SEASAT altimeter data. The inventory is necessary for selecting suitable orbital periods defined by the GSFC. In a second step the model itself is described.

7.2.2 Inventory of available data

Altimeter data in the form of GDR's is available over the entire period of 3 months of the SEASAT mission. In the GDR dataset used the earliest available data starts at 7-jul-1978 4:21:44 GMT and ends at 10-oct-1978 1:36:56 GMT. In first instance a catalog of arc segments is made from this dataset. Here the purpose of a catalog is to organize the GDR data in arc segments which is particularly useful for crossover computation, compare chapter 5. The arc segment catalog contains in total 1965 arc segments of which the first 1208 entries fall into the non-repeat and the last 757 into the 3 day repeat era.

The GDR structure itself keeps an revolution number which is increased by 1 whenever the satellite passes through the equator in an ascending way. In the 95 days of available data the GDR dataset indicates 1358 revolutions. Theoretically the amount of arc segments should be twice the amount of revolutions indicated by the GDR dataset. Unfortunately this is not the case due to the fact that it is 'contaminated' by a number data interruptions, in the sequel referred to as data gaps. The gaps in the altimeter data stream are caused by various effects. Short gaps in the data stream are mostly a result of the bad data removed during the editing procedure. Larger data gaps, lasting from several revolutions up to several days, are caused by the various interruptions in the operation of the altimeter. A number of times it occurred that the altimeter has been switched on and off or set in a standby mode as can be seen from the operations log listed in the GDR handbook, compare Lorell et al. (1980).

After launch, orbit insertion and engineering assessment in total 5 maneuvers were carried out during which the altimeter was switched off. Table 7.1 contains the 6 maneuver free periods encountered in the GDR dataset. It contains respectively: the starting and ending epochs in seconds with respect to the GDR offset time (01/01/78 00:00 GMT), the estimated revolution period in seconds (τ), the standard deviation of this value (σ_τ), the longitude displacement in degrees of an ascending equator transit longitude ($\Delta\lambda$), the standard deviation of this value ($\sigma_{\Delta\lambda}$) and the

start	end	τ	σ_τ	$\Delta\lambda$	$\sigma_{\Delta\lambda}$	$\dot{\omega}_o/\dot{\omega}_e$
–	19554068	6037.7057	0.0577	-25.082693	0.0005401	-14.3525
19554068	19813618	6036.2993	0.0548	-25.076746	0.0005538	-14.3559
19813618	20251236	6034.3844	0.0558	-25.068686	0.0005185	-14.3605
20251236	20510528	6035.7380	0.0572	-25.074408	0.0004831	-14.3573
20510528	21777022	6045.1774	0.0572	-25.114129	0.0005127	-14.3346
21777022	–	6045.6829	0.0656	-25.116424	0.0004279	-14.3333

Table 7.1: The maneuver free periods in the SEASAT GDR structure.

		beginning epoch			ending epoch		
nmr	per	date	time	GDR sec.	date	time	GDR sec.
1	1	06/07/78	00:00	16070400	09/07/78	00:00	16329600
2	1	09/07/78	00:00	16329600	15/07/78	00:00	16848000
3	1	15/07/78	00:00	16848000	21/07/78	00:00	17366400
4	1	21/07/78	00:00	17366400	27/07/78	00:00	17884800
5	1	27/07/78	00:00	17884800	02/08/78	00:00	18403200
6	1	02/08/78	00:00	18403200	08/08/78	00:00	18921600
7	1	08/08/78	00:00	18921600	14/08/78	00:00	19440000
8	1	14/08/78	00:00	19440000	15/08/78	07:43	19554180
9	2	15/08/78	07:43	19554180	18/08/78	07:48	19813680
10	3	18/08/78	08:49	19817340	23/08/78	09:22	20251320
11	4	23/08/78	09:22	20251320	26/08/78	09:27	20510820
12	5	26/08/78	09:28	20510880	01/09/78	00:00	20995200
13	6	05/09/78	00:00	21340800	10/10/78	01:05	24368700

Table 7.2: Beginning and ending epochs of the GSFC orbits according to the GDR handbook of Lorell et al. (1980)

corresponding $\dot{\omega}_o/\dot{\omega}_e$ ratio.

Another problem with the GDR altimeter dataset comes from the fact that the GSFC orbits are computed in periods of maximally 6 days, resulting, according to the GDR handbook, in 13 trajectories. The corresponding orbital periods are taken from the GDR handbook and are presented in table 7.2. This table contains respectively the orbit number (nmr), the maneuver free period number (per) referring to the corresponding row in table 7.1 and the beginning and the ending epochs. The epochs are given as date and time and the corresponding GDR seconds which are counted from the GDR offset time. In contrary to the NSWC orbits (which are available as a correction on the GDR tapes) no attempt was made to smooth the orbit altitude h^* at the juncture times listed in table 7.2, compare (Colquitt, Malyevac and Anderle,1980). As a result discontinuities are found in the orbit altitude h^* and the corresponding sea surface heights h.

7.2.3 Setup of the individual adjustments

As mentioned in §7.1 a global crossover adjustment is performed within the periods the GSFC defined for computing the trajectories of SEASAT. This is a necessary restriction of the method employed here. A continuous and differentiable function modeling the radial orbit error signal may not be expected to follow the discontinuities at the orbit junctions. Implicitly this limits the dimensions of a crossover problem. Six days of altimeter data consist maximally of $\approx 28 \times 6 = 168$ arc segments resulting in ≈ 7056 crossover differences. In reality, usually less than 50% of the crossovers remain due to data editing and land data.

The method employed for minimizing the crossover differences is described in §6.4. Crossover differences are minimized by means of solving, in the least squares sense, unknowns of one continuous and differentiable function taking the form of, compare (6.30):

$$\Delta r(t) = \frac{a_0 t}{\kappa \tau} \cos(nt) + \frac{b_0 t}{\kappa \tau} \sin(nt) + c_0 + \sum_{k=1}^{kmax} \left[a_k \cos(k\Delta\omega nt) + b_k \sin(k\Delta\omega nt)\right] \quad (7.1)$$

The characteristics of this function have been described in §6.4.2. Crossover observation equations take the form of:

$$\Delta h_{ij} = \Delta r(t_i) - \Delta r(t_j) \quad (7.2)$$

where t_i and t_j represent absolute crossover time tags. From a LSA based on (7.1) substituted in (7.2) the unknowns a_0, b_0, c_0 and a_k, b_k with $k \in [1, kmax]$ are solved. The constants n, κ, and τ in (7.1) are chosen conform the characteristics of the individual orbital periods which are listed in table (7.1). Furthermore t in equation (7.1) is defined with respect to an arbitrary ascending equator transit time inside an orbital period.

The constant $\Delta\omega$ in equation (7.1) determines the frequency resolution of the radial orbit error spectrum. The value of $\Delta\omega$ must be chosen such that the terms $k\Delta\omega nt$ in (7.1) coincide with the lumped coefficients $\psi_{km} = k\,\omega_o + m\,\omega_e$. For a three day repeat orbit, as considered in the crossover adjustment based on simulated observables described in §6.4, an choice for $\Delta\omega$ is easily made. Since the simulated orbit repeats itself after 43 revolutions $\Delta\omega = 1/43$. However the list of maneuver free periods, compare table 7.1, indicates that the values of $\dot{\omega}_o/\dot{\omega}_e$ vary in the range from -14.3605 to -14.3333. As a result the ψ_{km} terms do not coincide exactly with multiples of 1/43 of a c.p.r. This was verified by computing for all maneuver free periods all possible $\dot{\psi}_{km}/\dot{\omega}_o = k + m(\dot{\omega}_e/\dot{\omega}_o)$ values assuming: 1) a maximal spherical harmonic expansion up to degree and order 36 and 2) a cutoff frequency of 3 cycles per revolution. The extreme deviations of $\dot{\psi}_{km}/\dot{\omega}_o$ with respect to the nearest frequency being a multiple of 1/43 c.p.r. turned out to be less than 0.005 c.p.r. This discrepancy is too small to be detected from a time series having a duration of 6 days (86 revolutions). As a result there is no need to decrease the value of $\Delta\omega$ from 1/43 to for example 1/86.

The constant *kmax* determines the upper limit of the series expansion in equation (7.1). Care must be taken when choosing a value for *kmax* since it determines

case	nmr	start	end	a/d	cnt	M	σ
1	2	9/7 00:00	15/7 00:00	84/83	1606	-0.74	1.71
2	5	27/7 00:00	2/8 00:00	86/84	1813	-0.37	1.58
3	6	2/8 00:00	8/8 00:00	84/84	1892	-0.36	1.59
4	7	8/8 00:00	14/8 00:00	81/83	1402	-0.54	1.85
5	10	18/8 08:49	23/8 09:22	69/68	1256	+0.04	1.64

Table 7.3: The a-priori crossover statistics in 5 six day GSFC periods.

directly: 1) the cutoff frequency of the radial orbit error spectrum; 2) the corresponding rank defect of the normal equations derived by crossover minimization; and 3) the speed of the algorithm for the computation of the normal equations. Here the value of *kmax* is chosen conform the LSA of the simulated crossover differences described in §6.4, accordingly *kmax* = 100. This choice allows frequencies in the radial orbit error spectrum up to 2.3 c.p.r. The crossover r.m.s. after LSA could be used to verify (or justify) the value of *kmax*.

As mentioned before observation equations in the form of (7.2) will be used in a LSA of crossover differences where the covariance matrix of the observations Q_{yy} is chosen as a unit matrix. The rank defect of the normal equations derived by observation equations of the form of (7.2) has been discussed in §6.4.3. In order to find a general solution of the system of normal equations 9 additional constraints of the form of $\vec{c} = B\vec{x}$ with $B = E^t$ are included.

7.3 Internal and external evaluation

7.3.1 Internal evaluation

Crossover data considered in the analysis has been chosen such that 1) it falls in the 6 day GSFC periods 2) it is located in the non-repeat period of the SEASAT mission and 3) a sufficient amount of data is found. This results in 5 periods suitable for processing with the technique considered here. The other GSFC periods where either three days long or frequently interrupted. The a-priori crossover statistics in each of the five orbital periods are shown in table 7.3. This table shows column-wise; `nmr`: the corresponding GSFC orbit number as given in table 7.2; `start` & `end`: the beginning and ending date and time in 1978; `a/d`: the number of ascending and descending arc segments; `cnt`: the amount of crossover observations in this period; M, σ : the mean crossover difference (always ascending minus descending) and r.m.s. respectively.

For each period individually a crossover minimization is carried out as described in §7.2.3. This means that a function $\Delta r()$, in the form of (7.1), comprising 203 unknowns, is solved from the crossover differences. Furthermore 9 additional constraint equations are included. The constraints are only used for regularizing the system of normal equations. The internal (crossover) accuracy in the form of crossover difference statistics computed for each solution are shown in table 7.4. It indicates for each case respectively; `nmr1`: the amount of observations; `rms1`: the internal r.m.s.

case	nmrl	rmsl	min/maxl	nmr2	rms2	itr
1	1606	0.26	-1.245/+2.238	1600	0.25	3
2	1813	0.39	-2.802/+1.079	1779	0.36	3
3	1892	0.28	-1.115/+1.161	1886	0.28	2
4	1402	0.32	-1.085/+2.320	1392	0.30	3
5	1256	0.41	-1.429/+1.228	1215	0.36	4

Table 7.4: The a-posteriori crossover statistics in 5 six day GSFC periods.

after the first adjustment and `min/maxl`: the corresponding extreme deviations. No crossover data is eliminated by means of editing. The columns labelled **nmr2** and **rms2** in table 7.4 show the results after editing the crossover observations. Editing refers here to the rejection of crossover differences in case their discrepancy after LSA exceeds in magnitude a value of 3σ (with σ estimated as 30 cm). The procedure is applied in an iterative manner; the LSA is rehearsed with edited observations until rejections stop. Column 7 in table 7.4 shows the amount of iterations required to accomplish a solution.

The results show that the technique of global crossover minimization described in §7.2.3 can be performed effectively on SEASAT altimeter data. The internal accuracy found is comparable with Rowlands' results who found an a-priori r.m.s. of ±1.65 m that is reduced to ±0.28 m after the adjustment.

Variance behavior of the solutions

A point of concern is the a-posteriori variance behavior of the unknowns in (7.1) found by a LSA of crossover differences described above. The a-posteriori variances are shown in figure 7.1 from which it can be seen that the solutions 1 to 3 result in promising a-posteriori variances of the unknowns. The results are similar to what has been found in the crossover adjustment of simulated observables described in §6.4.2 ff. *However* this is not anymore true for solutions 4 and 5.

In figure 7.1 the a-posteriori standard deviations of the a_k unknowns are shown as a function of the frequency in c.p.r. where it is assumed that the a-priori covariance matrix of the observations Q_{yy} equals to an unscaled unit matrix. The horizontal axis represents the frequency in c.p.r. with a resolution of 1/43 c.p.r. The vertical axis shows the a-posteriori standard deviations of the unknowns in meters per 1/43 c.p.r. Case 1 is displayed with a vertical offset of 0 m whereas each following case is shown relative to successive vertical increments of 1.5 m. Two remarks: 1) the striped vertical lines in figure 7.1 coincide with the singular frequencies in the crossover solution, 2) a-posteriori standard deviations of the a_0, b_0 and c_0 terms in eq. (7.1) are not included in this figure.

It can be seen from figure 7.1 that some solutions, especially the fifth, are hampered by relatively high a-posteriori standard deviations of the unknowns concentrated in the lower frequency range of the spectrum (from 0 to 1 c.p.r.). Furthermore it appears that the high standard deviations occur for the non-singular frequencies in the radial orbit error spectrum.

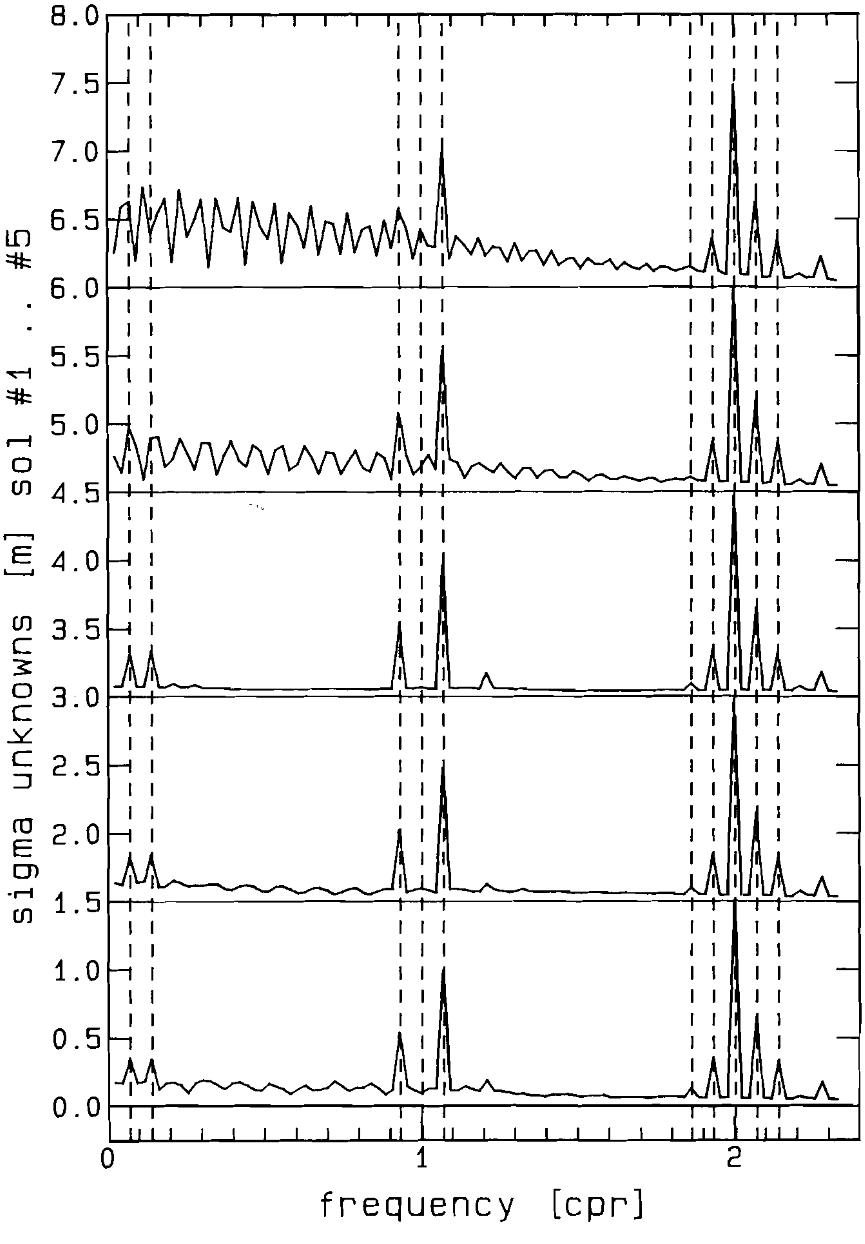

Figure 7.1: The a-posteriori standard deviations of the a_k unknowns in m per 1/43 c.p.r. (relative to a certain offset) as a function of the frequency in c.p.r. The figures show the results for the five crossover solutions computed from SEASAT altimeter data.

	1	2	3	4	5
1	1.00				
2	0.72	1.00			
3	0.51	0.48	1.00		
4	0.54	0.40	0.61	1.00	
5	0.34	0.28	0.54	0.40	1.00

	1	2	3	4	5
1	1.00				
2	0.94	1.00			
3	0.79	0.80	1.00		
4	0.64	0.64	0.51	1.00	
5	0.51	0.41	0.58	0.36	1.00

Table 7.5: The matrices of correlation coefficients as they are computed from 5 independent orbit perturbation spectra. On the left side the results are shown for all frequencies, on the right side the singular frequencies are excluded.

This phenomenon is most certainly caused by the poor data distribution in periods 4 and 5. Compare also table 7.4 where it is shown that the latter two periods contain the fewest amount of crossover differences. In this context it should be remarked that the mentioned a-posteriori standard deviations are found as the square roots of the diagonal elements of the inverse of the normal matrix $(A^tQ_{yy}^{-1}A)^{-1}$. The magnitude of the crossover residuals plays no role in the computation of the a-posteriori standard deviations of the unknowns. It is the structure of the design matrix A and the a-priori covariance matrix Q_{yy} that determine the a-posteriori variances.

Concentration of signal around once per revolution

All solutions found (the 'suspicious' variance solutions 4 and 5 inclusive) have shown to resemble the expected concentration of signal close to once per revolution. The five power spectra computed from the a_k and b_k unknowns are shown in figure 7.2. Figure 7.2 is arranged in the same way as figure 7.1. Here the vertical axis represents the amplitude in m per 1/43 c.p.r. defined as $\sqrt{a_k^2 + b_k^2}$. Again the a_0, b_0 and c_0 terms in eq. (7.1) are not included in figure 7.2.

Correlation of perturbation spectra

Another important result are the *high* correlations found between the independently determined perturbation spectra. The method which is applied for computing the optimal correlations by means of FFT techniques is discussed in appendix B.

The five independent solutions in the form of (7.1) obtained by crossover minimization have been compared by means of a correlation analysis. On the left side of table 7.5 the correlation coefficients are shown as they are found by comparing all possible combinations of perturbation spectra computed by LSA. Correlation is computed for all a_k and b_k terms in (7.1) except for the a_0, b_0 and c_0 terms. The a_0 and b_0 term are assumed to be characteristic for one orbital period since they originate from the particular resonant solution of the HE. The bias term c_0, whose value is negligible due to the constraints forced on the unknowns, is also not used in the correlation analysis.

The correlation coefficients as they are shown on the left side of table 7.5 are not "too convincing" (One should be aware of the fact that it might be difficult to

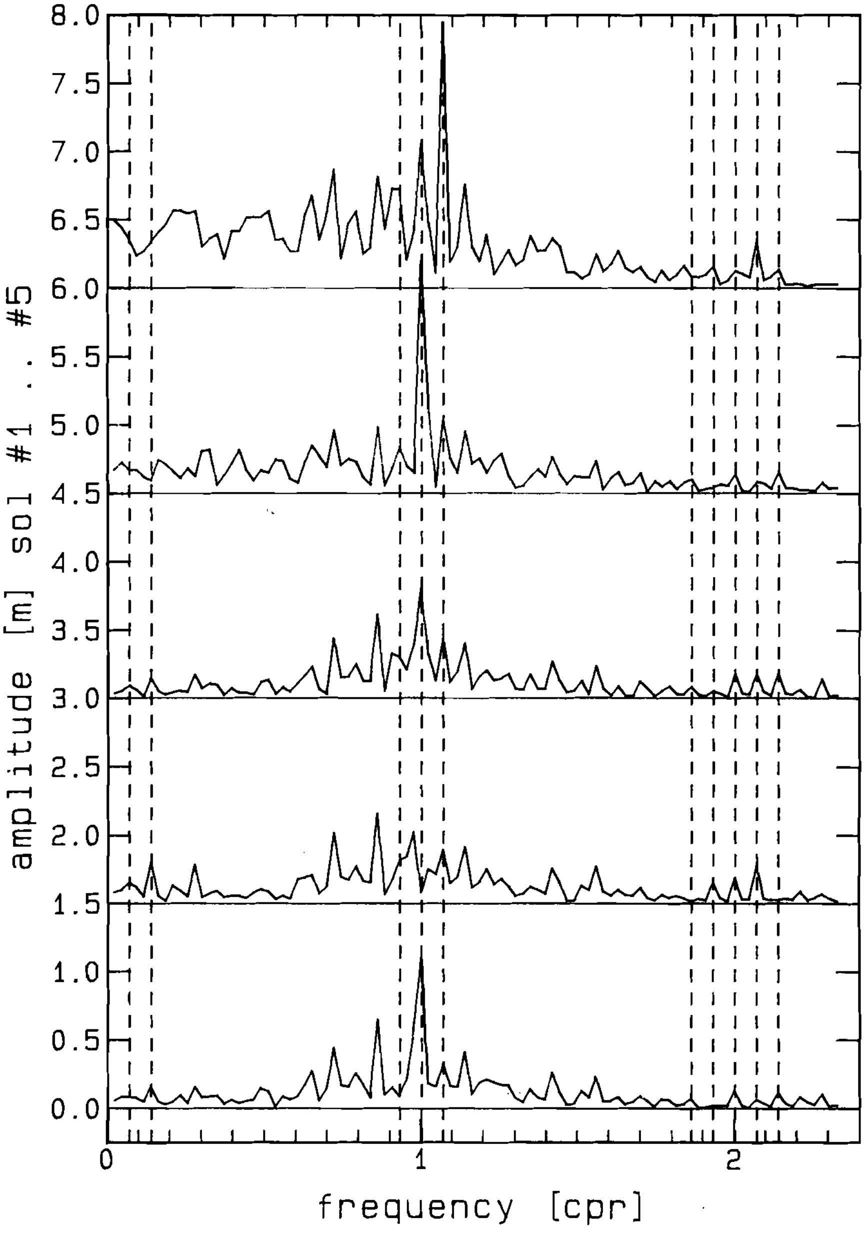

Figure 7.2: Five independently computed power spectra of the unknowns acquired by minimization of SEASAT crossover differences. The figure shows the amplitude in m per 1/43 c.p.r. (relative to a certain offset) as a function of the frequency in c.p.r.

interpret the values of the correlation coefficients). Higher correlation coefficients can be obtained after an elimination of the singular frequencies from the perturbation spectra (at 0, ω_e, $2\omega_e$, ω_o, $\omega_o \pm \omega_e$, $2\omega_o$, $2\omega_o \pm \omega_e$ and $2\omega_o \pm 2\omega_e$). The results where the singular frequencies are left out are shown on the right side of table 7.5.

These results are "more convincing" than those found in the former correlation analysis. Remarkable are the high correlations, up to 0.94, of the first three perturbation spectra. Note also the weak correlation of solution 4 with 5 and solutions 4 & 5 with the other solutions. This is not surprising due to the problematic a-posteriori variances of the unknowns of solutions 4 and 5.

Combined solutions

It is an important consequence that individual solutions free of 1) singular frequencies and 2) resonant Hill effects are highly correlated. These high correlations suggest the presence of a continuous disturbing effect, like unmodeled gravitational perturbations, acting on the satellite. In this case potential coefficients of the gravitational field may be estimated from the Fourier coefficients of the continuous function. In this separate parameter estimation process eq. (4.26) may be used to derive the observation equations. The implementation of the latter step is however not investigated in this work, instead it is recommended for further research on satellite altimetry.

Due to high correlations it is reasonable to assume that one can solve for one disturbing function $\Delta r_o(t)$ overlapping a number of orbital periods:

$$\Delta r_o(t) = \sum_{k=1}^{kmax} A_k \cos(k\Delta\omega n t) + B_k \sin(k\Delta\omega n t). \tag{7.3}$$

(compare (7.1), here excluding an exact once per revolution frequency). Included are a number of additional subfunctions $\Delta r_p^i(t)$ modeling specific perturbations for individual orbital periods:

$$\Delta r_p^i(t) = (a_0^i + a_1^i \frac{t - t_0^i}{\kappa^i \tau^i}) \cos(n^i(t - t_0^i)) + (b_0^i + b_1^i \frac{t - t_0^i}{\kappa^i \tau^i}) \sin(n^i(t - t_0^i)) + c_0^i \ . \tag{7.4}$$

These subfunctions model the resonant Hill effect for each orbital period "i". The variables are chosen conform (7.1) with an additional superscript "i" referring to the specific orbital period. If N multiple orbital periods are treated simultaneously in a crossover adjustment then $\Delta r(t) = \Delta r_o(t) + \Delta r_p^1(t) + \ldots + \Delta r_p^N(t)$. Note that any crossover observation equation in the form of (7.2) refers to Δr.

Constraint equations as applied in the crossover adjustment over one orbital period are necessary for regularizing the normal equations. Constraints affect the Δr_o function including the a_0, b_0 and c_0 term of an (arbitrarily chosen) Δr_p function. In figure 7.3 it is shown how one Δr_o and four Δr_p functions, including the constraints affecting 1 specific orbital period, might be arranged in a combined approach.

In an attempt to compute a combined solution two successive orbital periods (case 2 & 3 in table 7.3) are processed simultaneously. In total there are 7385 crossover differences of which 1813 reside in the 2^{nd} and 1892 in the 3^{rd} orbital

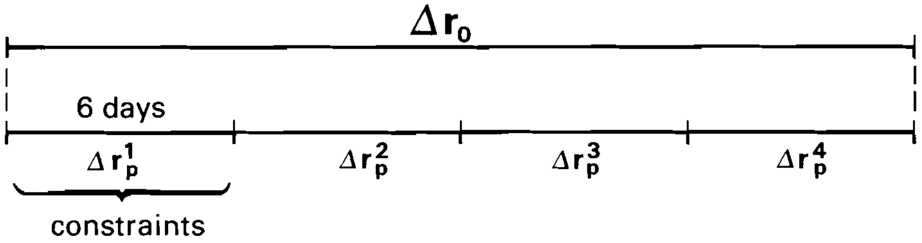

Figure 7.3: Arrangement of error functions in a combined approach.

		a-priori		a-posteriori	
case	cnt	M	σ	M	σ
period #2	1813	-0.37	1.58	0.00	0.57
period #3	1892	-0.36	1.59	-0.01	0.48
overlap	3680	-0.37	1.59	0.00	0.51
total	7385	-0.37	1.59	0.00	0.52

Table 7.6: Crossover statistics before and after a combined adjustment of orbital periods 2 and 3.

period. Furthermore there are 3680 additional crossover differences in the overlap of period 2 and 3. These combination crossovers have their ascending time tags in one orbital period and their descending time tags in the other orbital period.

The number of unknowns in this combined adjustment equals to 208; there are 203 unknowns conform an individual adjustment in the 2^{nd} orbital period and 5 unknowns for the subfunction $\Delta r_p()$ in the third orbital period. The results before and after the adjustment are shown in table 7.6. In table 7.6 column "cnt" refers to the amount of crossover differences, "M" refers to the average and "σ" to the r.m.s. of the crossover differences. The results are separated row-wise for period 2, 3, the overlap of 2 and 3 and the sum of 2 and 3.

The results in table 7.6 are typical for combined crossover solutions and show that the a-posteriori crossover r.m.s. tends to increase. However it was found that the a-posteriori standard deviations of the unknowns tend to decrease uniformly by a factor of 3 to 5 when compared with individual solutions. Most of the improvement in the variance spectra takes place in the lower frequency range. This is caused by the fact that about 4 times as much observations are used.

The results show, as suggested by the correlation analysis, that it is possible to solve one continuous overlapping function $\Delta r_o()$. This function models a continuous disturbing effect acting on the altimeter satellite which is unmodeled in the altimetric configuration. The fact that the crossover r.m.s. increases is probably due to the inability of the model to follow short periodic effects above 2.3 c.p.r. like remaining tropospheric or ionospheric effects acting on ρ. These effects are probably absorbed in individual adjustments where they result in a lower crossover r.m.s.

7.3.2 External evaluation

In §6.4 the characteristics of singularity transformations of continuous crossover solutions are discussed. In that section a singularity transformation of the unknowns is used to minimize the discrepancies between an internal consistent crossover solution and the simulated radial orbit error. For obvious reasons it is not possible to apply this experiment to actual altimeter data acquired from SEASAT.

A possibility for escaping this vicious circle is to transform the internal consistent crossover solutions to a known reference surface. In analogy with §3.3.5 it will be discussed how internal crossover solutions are minimized with respect to a chosen reference geoid. How these transformed solutions have to be interpreted is discussed later on in this section.

Theoretical background

Solved by means of a LSA of crossover differences are the unknowns a_k, b_k and a_0 b_0 and c_0 in (7.1) under the condition of 9 additional constraint equations. In the sequel we consider these unknowns to be collected in a vector $\vec{x}_{old}$ which is subject to a singularity transformation taking the form of $\vec{x}_{new} = \vec{x}_{old} + E\vec{s}$. The structure of the matrix E is discussed in §6.4 where it is shown that it consists of nine $\vec{u}^{c}_{lm}$ and $\vec{u}^{s}_{lm}$ vectors comprising linear combinations of inclination functions. These base vectors are found by mapping an artificial surface function along the nominal orbit. The shift vector $\vec{s}$ in the singularity transformation contains the surface function coefficients.

Minimization of the crossover solution $\vec{x}_{new}$ with respect to a reference geoid is accomplished by solving (by means of LSA) the components of the shift vector $\vec{s}$ in the singularity transformation. The observations employed in this LSA are the radial differences between the (crossover minimized) altimeter surface and a reference surface which is assumed to be a known geoid. Unknowns are the coefficients C_{lm} and S_{lm} of a surface function, see (6.28), which forms the observation equations.

The radial difference observations Δh in this experiment are modeled by $\Delta h(t) = h(t) - \Delta r(t) - N(t)$ where $h(t)$ represents the sea surface height derived from raw altimeter measurements, $\Delta r(t)$ the predicted correction in the form of (7.1) found by a LSA of crossover differences and $N(t)$ the geoid height at the sample point. Note that $\Delta r()$ represents a correction after LSA that needs to be subtracted from the observations. The influence of PST is ignored in this approach.

In the computations it is assumed that the direct sea surface height samples $h(t)$ are supplied at regular spaced 180 s intervals along the altimeter ground track. A smoothing procedure is used for computing $h(t)$ from the direct sea surface heights measured by the altimeter radar. The procedure consists of fitting a linear function of time through the measured sea surface height samples in a 180 s window. An evaluation of this linear function in the center of the window results in so-called 3 minute smoothed height samples. Smoothed height samples have the advantage that highly detailed surface structures are eliminated during the computation of the surface function coefficients belonging to a spherical harmonic expansion up to degree and order 2.

Another computational problem concerns the evaluation of geoid heights at intervals of 180 s distributed along the altimeter ground track. Here geoid heights are found by an evaluation of the Bruns equation $N = T/\gamma$ on a reference ellipsoid. This reference ellipsoid is defined by the geodetic reference system 1980, as is described by Moritz (1984), which is also used in the computation of the GDR dataset.

Here $T = W - U$ where W denotes the gravity potential whereas U refers to the so-called normal gravity potential. Due to its rotational symmetry about the z axis and its symmetry with respect to the equator, U may be written as a spherical harmonic expansion over the even zonal coefficients including a centrifugal term, compare Heiskanen & Moritz (1979). The centrifugal term cancels in T since it is identical in W and U

Essentially the computation of T consists of a direct series expansion in spherical harmonics analogous to (4.3). Instead of preforming the expensive series expansion at each 180 s sample it is chosen to follow a more economic approach in which the geoid heights are interpolated from a precomputed $1^\circ \times 1^\circ$ (λ, ϕ) grid. The grid of geoid heights is generated by means of fast Fourier synthesis as is described by Colombo (1981).

Interpolation in the (λ, ϕ) grid is accomplished by evaluating at the desired point a bilinear function separately defined in each square of the grid. The bilinear function is in the form of $a_0 + a_1x + a_2y + a_3xy$ where the coefficients a_0 through a_3 have been chosen such that it fits exactly through the four corner values of each square. Computations based on geoids evaluated up to degree and order 36 have shown that the worst case interpolation noise induced by this method is of the order of 4 cm standard deviation.

Results

In the computations it is assumed that crossover solutions are transformed to a reference geoid derived from the GEM-T1 model described by Marsh et al. (1986). The improvements of the direct height differences Δh of the altimeter surface with respect to the GEM-T1 geoid are shown in table 7.7. The statistics are shown for all 5 cases described in §7.3.1. In table 7.7 "nrsamp" refers to the amount of 180 s smoothed height samples in each case. The columns labelled $M_{\Delta h}$ and $\sigma_{\Delta h,1}$ represent respectively the mean of the height differences and the corresponding standard

case	nrsamp	$M_{\Delta h}$	$\sigma_{\Delta h,1}$	$\sigma_{\Delta h,2}$	$\sigma_{xo,1}$	$\sigma_{xo,2}$
1	1274	-0.65	1.68	1.46	0.2659	0.2666
2	1364	-0.56	1.74	1.48	0.3899	0.3908
3	1448	-0.61	1.72	1.45	0.2818	0.2829
4	1210	-0.80	1.87	1.57	0.3271	0.3279
5	1173	-0.45	2.45	1.53	0.4214	0.4300

Table 7.7: Statistics of direct height and crossover differences before and after a singularity transformation of 5 SEASAT "crossover" solutions to a GEM-T1 reference geoid.

deviations before the singularity transformation. The column labelled $\sigma_{\Delta h,2}$ represents the standard deviation of the height differences at the 180 s smoothed samples after the singularity transformation. These statistics indicate an improvement in the relative positioning after a suitable singularity transformation of the altimeter crossover solution to the reference geoid.

One should keep in mind that the $\sigma_{\Delta h}$ values are mainly caused by the differences in N at frequencies where $l > 36$ which is the cutoff degree of GEM-T1. A transformation to higher degree and order reference geoids results in values for $\sigma_{\Delta h}$ comparable to what has been shown for the local adjustments, compare table 3.1.

In theory the crossover residuals of each solution should not alter after a singularity transformation. However this transformation is derived from a nominal orbit instead of the actual altimeter trajectory causing small degradations in the internal crossover standard deviations before and after the singularity transformation. These statistics are shown in the columns labelled $\sigma_{xo,1}$ and $\sigma_{xo,2}$ in table 7.7. They indicate respectively the crossover difference r.m.s. before and after the transformation. It shows a negligible effect caused by the 'inaccuracy' of the singularity transformation.

In table 7.8 the surface function coefficients, i.e. components of the shift vector $\vec{s}$, are shown as they are solved for the five cases considered here. Note that all solutions are computed with respect to different reference times consisting of equator transit times.

	1	2	3	4	5
C_{00}	-0.670	-0.769	-0.675	-0.839	-0.342
C_{10}	-0.057	+0.709	+0.308	-0.325	+0.515
C_{11}	-0.404	-0.308	+0.749	+0.643	+2.953
S_{11}	+0.007	+0.792	-0.046	+0.915	+0.538
C_{20}	-1.905	-1.648	-1.829	-1.461	-1.974
C_{21}	-0.157	+0.002	-0.238	-0.114	-0.409
S_{21}	+0.039	-0.166	+0.208	+0.257	-0.208
C_{22}	+0.112	+0.086	-0.026	+0.036	-0.006
S_{22}	+0.008	-0.045	+0.078	-0.129	+0.087

Table 7.8: The surface function coefficients solved by minimizing the five SEASAT crossover solutions to the GEM-T1 geoid.

Remarkably consistent and independent of the choice of a reference time appear to be the values of the C_{00} and C_{20} coefficients. Yet the author is of the opinion that it is difficult to interpret these values. There are a number of reasons which might cause consistency in the recovered surface function coefficients:

1. Geographic correlation of the radial orbit error itself which is in the order of several decimeters as found in the simulated adjustments. Compare also the results presented table 6.5. A significant influence is expected in the C_{10}, C_{11} and S_{11} terms since they produce effects close to the once per revolution frequency.

2. The permanent sea surface topography effect, i.e. deviations of the sea surface with respect to a geoid due to permanent large scale currents in the oceans. Permanent sea surface topography has amplitudes up to ± 1 m in the region of the Antarctic circumpolar current, as is described by Levitus (1982). This phenomenon affects all the surface function coefficients in a singularity transformation. It is not unlikely that the consistent negative value of C_{20} is caused by this effect.

3. Modeling errors in the reference geoid which are expected to be small in the frequency band of 0 to 3 c.p.r. An interpretation of this effect will be given in chapter 8.

4. Tracking station coordinate system errors which are presumably of the order of several centimeters up to decimeters. Presumably this results in a shift of the center of the geocentric coordinate system affecting directly the C_{10}, C_{11} and S_{11} terms in the singularity transformation.

5. Unmodeled instrumental scaling effects which might explain the consistent negative value of C_{00}.

6. Errors introduced by the crossover model itself, e.g. the fact that sea surface heights are measured only over the oceans. Compare also table 6.5 where surface coefficients of the "land+sea" case and the "land" case are shown.

We conclude that it is rather difficult to judge upon the values of surface function coefficients found after a singularity transformation of an internal crossover solution to a reference geoid since these coefficients absorb a combination of phenomena listed above. Eventually it means that the transformed crossover solution after a singularity transformation is tailored to a specific reference geoid.

7.4 Conclusions

In this chapter the global crossover adjustment of SEASAT altimeter data is discussed. The SEASAT altimeter dataset is subdivided in two sort of time windows. First of all there are 6 so-called maneuver free periods each in between two orbit corrections. Secondly inside each maneuver free period there are at least one and usually more so-called orbital periods, i.e. time windows in which the GSFC computed one independent 6 day orbit. By definition maneuver free periods and orbital periods do not overlap. In the case of GSFC orbits no precaution was taken to smooth the satellite altitude h^* at the juncture times. This is in contrast with the NSWC orbits which are overlapping and smoothed at the juncture times, compare Colquitt et al. (1980).

The method of orbit error reduction employed in this chapter is nearly identical with the method described in §6.4. In analogy an attempt is made to solve, by means of minimizing crossover differences, a continuous and differentiable error function modeling the radial orbit error. This function takes the form of a Fourier series including an additional sub-function modeling specific perturbations per orbital period. A limiting factor in this approach is the inability of the model to follow orbit errors at the juncture times of two successive orbital periods. Accordingly the technique is applied on 5 six day GSFC periods in the non-repeat part of the SEASAT mission.

In §7.3 five independent perturbation spectra are shown which are derived by minimizing SEASAT crossover differences. The internal evaluation has shown that perturbation spectra 1 to 3 behave as realistic solutions. This is in contrast with solutions 4 and 5 which are hampered by high a-posteriori variances of the unknowns concentrated in the lower frequency range. The cause of this effect is presumably the poor data distribution in periods 4 and 5.

In all cases it was found that the crossover differences tend to decrease from ±1.65 m before the LSA of crossover differences to ±0.30 m after it. These statistics are comparable with the results Rowlands (1981) found in the global adjustment of SEASAT altimeter data. The internal solutions appear to show a concentration of signal in the neighborhood of 1 c.p.r. More important is the fact that individual crossover solutions tend to show a high correlation whereby it seems that singular frequencies are less correlated. High correlations might indicate a continuous unmodeled effect acting on the spacecraft mainly consisting of unmodeled gravitational perturbations.

High correlations between individual solutions suggest to solve for one error model overlapping several orbital periods. This model takes the form of one continuous function including additional sub-functions modeling specific perturbations inside each individual orbital period. This approach showed that the a-posteriori standard deviations of the crossover differences increased to approximately 50 cm. On the other hand the a-posteriori standard deviations of the unknowns of the continuous error function decrease which is due to the fact that about four times as much observations have been used for estimating the unknowns. The method enables to process those orbital periods which individually result (due to poor data distribution) in high a-posteriori variances of the unknowns.

The external evaluation discussed in §7.3.2 treats the adjustment of a crossover minimized surface to a chosen reference geoid derived from GEM-T1. Characteristic of this singularity transformation is the fact that the original crossover solution is not affected. However, it is necessary to assume a nominal orbit in the derivation of the singularity transformation causing a small (negligible) degradation of a theoretically consistent internal crossover r.m.s.

A singularity transformation of the crossover solution to a reference geoid has been performed for all cases. The height differences of the particular crossover solution with respect to the GEM-T1 reference geoid are taken at so-called 180 s smoothed height samples distributed along the altimeter ground track. Characteristic of the transformed orbit error spectra appear to be the consistent values of the C_{00} and C_{20} surface function coefficients which are the parameters of the singularity transformations. The nature of this effect is not well understood since there are a number of possible causes. The parameters of the singularity transformation tend to absorb a combination of these effects meaning that the eventual transformed crossover solution is tailored to a specific reference geoid.

Chapter 8

A sketch of an integrated approach

8.1 Introduction

In this chapter we compare a number of so-called integrated approaches for processing of satellite altimeter data. Firstly we concentrate on the objectives of an integrated approach, starting with a recently developed technique introduced by Wagner (1986,1988) and worked out in a slightly different version by Engelis (1987). In both cases the goal is to recover simultaneously the improvements of 1) the geoid 2) the radial position of the spacecraft and 3) the permanent part of the sea surface topography (PST). Parts 1) and 2), the geoid and the radial orbit error, are functions of corrections to the Earth's gravitational field. Items 1) and 3) shall be denoted as the 'lower' part whereas 2) represents the 'upper' part of the problem.

Both Wagner (ibid) and Engelis (ibid) develop for the upper gravitational part of the problem an analytical model for radial orbit errors Δr based on the Lagrange planetary equations. The lower gravitational part of the problem, consisting of a geoid N and its corresponding undulations corrections ΔN, is far easier to model than the upper part since no additional differential equations with variables dependent upon time are required as in the case of radial orbit errors. From the Bruns equations it follows directly that $N = T/\gamma$. An non-gravitational term in the lower part of the problem is the influence of PST, i.e. the term ς^p in eq. (2.2). This effect is modeled by mapping a surface function expressed in spherical harmonics along the altimeter ground track.

In the second part of this chapter results obtained by global crossover analysis are compared with the Wagner/Engelis approach. A discussion focussed on the estimability of the radial orbit error by means of global crossover minimization is given in chapters 6 and 7 where it is pointed out that crossover solutions allow to model only a subset of the radial orbit error. This is caused by the fact that a portion of the radial orbit error behaves as geographically correlated.

The results discussed in this work indicate that geographical correlation manifests as a low degree and order surface function. Geographical correlation of the radial orbit error has also been described by Rosborough (1986) whose results differ from the author's findings. This justifies a more detailed treatment of Rosborough's theory which is given in §8.3. As a key issue the question remains in what sense the geographically uncorrelated part of the radial orbit error can be used to improve a gravitational field.

The frequencies recovered in the orbit error spectrum, acquired by means of crossover minimization, may be applied in constraint equations for lumped coefficients of the gravitational field, as is described in Schrama (1986a). This indicates that also these results may contribute in an integrated approach. However on first sight a major difference between the method of global crossover minimization and the Wagner/Engelis approach appears to be the perspective of the latter to recover any low degree and order surface effect which shows up either in the form of geoid undulations or PST.

8.2 Remarks on simultaneous recovery experiments

The integrated approach of Wagner (1986) envisages to solve for improvements in the orbit, the geoid and the PST simultaneously. The method is clarified by considering the fundamental altimetric equation with ς^p representing the permanent and ς^v the variable part of the sea surface topography:

$$h^* + \boxed{\Delta r} = N + \boxed{\Delta N} + \rho + \varsigma^p + \boxed{\Delta\varsigma^p} + \varsigma^v \tag{8.1}$$

(compare (2.1)) from which the boxed terms Δr, ΔN and $\Delta\varsigma^p$ are considered. These terms denote models for the improvements of potential coefficients and surface function coefficients of the PST field, respectively. Uncertainties in the potential coefficients describe the radial perturbations of the satellite and the geoid errors. Improvements in the surface function coefficients pertaining to the PST field describe $\Delta\varsigma^p$. The other terms in eq. (8.1) are assumed to be known (either from a-priori models or measurements performed by the altimeter radar) or are simply ignored (like ς^v, assuming that tides are modeled by means of an independent model).

The motivation for a joint modeling of Δr and ΔN becomes apparent when the error budget in altimetry, e.g. as shown in table 2.2, is taken into account. This table confirms that dominating effects are caused by gravitational modeling errors manifesting in geoid errors ΔN and orbit errors Δr which are both far larger than the instrumental accuracy of the altimeter radar. In any crossover method the influence of ΔN is eliminated by definition. Here this property is not necessarily applied.

A completely *different* term in the altimetric equation, that is not coupled to gravitational influences, is $\Delta\varsigma^p$. It is curious that this term cannot be found in the altimetric error budget presented in table 2.2 originating from Tapley et al. (1982a): the influence of PST is of the order of 1 m as is shown in Levitus (1982). The following quotation comes from Wagner (1988,pp. 1–2) emphasizing the importance of PST:

> "Why is it important? Because this permanent water height above a level reference can only be maintained by permanent external forces acting on the ocean's surface layers, either prevailing wind stresses or dynamic forces associated with ocean currents such as the Coriolis forces which accompany the great ocean gyres that result from equator to pole heat

transport in the open oceans. Knowing the constant part of this topography would essentially determine the circulation of the surface waters in the deep ocean with great benefits to marine science, navigation and climatology."

8.2.1 Gravitational orbit errors

The effect of gravitational radial orbit errors in satellite altimetry has been discussed in chapter 4 and needs no further derivation here. Instead a brief summary is discussed of the radial solutions of the Hill equations.

The homogeneous solution of the HE shows radially an exact once per revolution term including a constant bias, compare eq. (4.36). Homogeneous effects are caused by unsolved initial state vector disturbances which are most certainly present in the altimeter orbit. The magnitude of this effect is unfortunately not known for e.g. SEASAT.

From the non-resonant particular solutions, given in eq. (4.38), it is found that the radial perturbations are amplified close to the once per revolution frequency. This is indicated by the leading term of (4.38) taking the form of $[\omega(n^2 - \omega^2)]^{-1}$ where ω represents the frequency of the perturbing force and n the mean motion of the spacecraft. An important property of the non-resonant particular solution of the Hill equations is the uniqueness in frequency response. It means that harmonic perturbing forces at a frequency of ω result in orbit errors at exactly the same frequency ω.

A first application of eq. (4.38) is the substitution of the disturbing potential T. This results, as is shown in §4.2.2, in the same solution Wagner (1985), Rosborough (1986) and Engelis (1987) derived from the linear perturbations theory which is based on the conventional Lagrange planetary equations.

The nature of the disturbing potential function, as given in eq. (4.43), suggests that certain clusters of potential coefficients contribute to the same frequency. These clusters form so-called *lumped* coefficients and occur for constant values of k and m in (4.43). Moreover only a limited number of (k, m) clusters are in effect as a result of the rapid decline of perturbations at higher frequencies. This problem is relevant for the estimability of potential coefficients from orbital perturbations, cf. (Schrama,1986a). Here, where one intends to improve potential coefficients from radial orbit errors, the problem is not any different. Yet in order to discuss the problem of estimability of potential coefficients in the integrated approach it is required to consider as well the second gravitational part of the problem which is formed by geoid undulations. This part will be described later on in this chapter.

Additionally the Hill equations allow a so-called resonant particular solution describing the radial orbit errors as a result of constant or exact once per revolution perturbing forces. This is a separate particular solution, taking the form of (4.39), since disturbing functions at $\omega = 0$ or $\omega = \pm n$ lead to singularities in the non-resonant particular solution of the Hill equations. The practical applications of the resonant solution combined with the homogeneous solution are important. These solutions tend to model a lot of the signal in the simulated radial orbit error, as is mentioned in chapter 4. An accurate comparison of the simulated radial orbit error with the particular solution appears *only* possible after removing the resonant particular & homogeneous effect. In a symbolical notation the complete form of the solution becomes:

$$\begin{aligned}\Delta r(t) &= \Delta r_h(n,t) \\ &+ \Delta r_{pr}(P_u, Q_u, R_u, P_v, Q_v, R_v, n, t) \\ &+ \sum_{\omega} \Delta r_{pn}(P_u, Q_u, P_v, Q_v, \omega, n, t)\end{aligned} \tag{8.2}$$

where Δr_h represents the homogeneous part, Δr_{pr} the resonant and Δr_{pn} the non-resonant part. The coefficients P_u, Q_u, R_u, P_v, Q_v and R_v may be related to the disturbing potential as is shown for equation (4.38). These terms are a function of the perturbing force and additional constants needed to define the potential, compare also (4.43) and (4.46). The comparison with a numerically integrated radial orbit error indicates that eq. (8.2) is suitable for modeling the simulated perturbations. This agrees with Wagner's (1985,p. 3035) findings showing that there is hardly any need to improve the gravitational radial orbit error model. He states that "second-order" linear effects ($e_0\Delta M$ with $q = 0$ and $q = \pm 2$, Δa with $q = \pm 1$ and Δe with $q = \pm 2$ in (4.24)) can be ignored in the altimetric problem.

Higher-order solutions

Both the linear perturbations theory and the Hill equations are based on the concept of a nominal trajectory: an ellipse precessing as a result of secular J_2 effects, compare also (4.20). In reality the nominal orbit is more complicated due to the 1) relatively large oscillations caused by the J_2 term and 2) odd zonal perturbations as is described in appendix A. This implies that perturbations in the elements, as shown in (4.22), should be derived by integration along a more complicated trajectory. In (Kovalevsky,1988) these sort of solutions are referred to as *second-order* solutions.

There is a *conflict* in terminology between (Kovalevsky,1988) and (Wagner,1985). The latter "second-order effects" are described in the scope of the linear perturbations theory. A more appropriate description would probably be: truncation effects in linear perturbations theory due to damping properties of eccentricity functions in near circular orbits. In order to distinguish between the terminology of Kovalevsky and Wagner we shall use "second-order" between double quotes for the latter.

Kovalevsky (1988) describes the derivation of second-order solutions from J_2 first-order solutions (i.e. the J_2 secular including the J_2 LPT solution). For this purpose the first-order solution is substituted in the LPE and integrated term by term resulting in expressions containing J_2^2. Kozai (1962) gives the complete second-order expression for the radius of an orbit of any eccentricity for low-degree zonal coefficients only.

There are two reasons why second and higher-order models have not been investigated in this study. A first reason is that these theories are probably not resulting in a drastic refinement of the analytical orbit error model. In chapter 4 the first-order results have shown to be quite appropriate for describing the simulated radial orbit error. Secondly, all the second and higher-order solutions tend to become very complicated and almost impossible to verify. The following quotation from Taff (1985) on page 321 should be a warning against higher-order theories:

> "Beyond first order results I know of no useful result from perturbation theory in celestial mechanics because all of the higher-order results have no firm mathematical basis. Frequently the second order approximation produces non-sensical (non-sensible?) results (the critical inclination, small divisors e.t.c.). There in no good analytical long-term perturbation theory."

8.2.2 Geoid undulations

A characteristic part in the integrated approach is the modeling of geoid undulations in connection with gravitational orbit errors. In §7.3.2 it is mentioned that the geoid itself may be computed by means of the Bruns equation: $N = T/\gamma$. The disturbing potential T is represented by $T = W - U$ where W equals to the full gravity potential and U the normal gravity potential of the reference ellipsoid. Besides $W = V + Z$ and $U = V' + Z$ where V equals to the gravitational potential, V' the normal gravitational potential and Z the centrifugal potential which cancels in T. The denominator γ in the Bruns equation represents the normal gravity of the reference ellipsoid. Here as well T as γ are evaluated at the sub-satellite point lying on the reference ellipsoid.

By means of inclination functions T is projected on the nominal ground track of the altimeter satellite. The corresponding potential function takes the form:

$$T(t) = \sum_{k=-lmax}^{lmax} \sum_{m=0}^{lmax} \left[A_{km} \cos\psi_{km} + B_{km} \sin\psi_{km}\right] \tag{8.3}$$

where

$$(A_{km}, B_{km}) = \frac{\mu}{r} \sum_{l=m}^{lmax} \left(\frac{a_e}{r}\right)^l \overline{F}_{lm(l-k)/2}(I) \begin{bmatrix} \overline{C}^*_{lm} & \overline{S}^*_{lm} \\ -\overline{S}^*_{lm} & \overline{C}^*_{lm} \end{bmatrix}^{l-m:\ even}_{l-m:\ odd} \tag{8.4}$$

and

$$T = W - U = V - V' \quad \Rightarrow \quad \begin{cases} \overline{C}^*_{lm} = \overline{C}_{lm} - \overline{C}^{V'}_{lm} \\ \overline{S}^*_{lm} = \overline{S}_{lm} - \overline{S}^{V'}_{lm} \end{cases} \tag{8.5}$$

where $\overline{C}^{V'}_{lm}$ and $\overline{S}^{V'}_{lm}$ represent the coefficients of the normal potential. Only the even zonal coefficients are taken into account since the normal potential originates from an ellipsoid which is symmetric with respect to the equator. The summation over l in (8.4) is carried out only for equal parity of the variables k and l. In a spherical approximation it is $r = a_e$ and $\gamma = \mu/a_e^2$. This results in, compare also Engelis (1987):

$$N(t) = \sum_{k=-lmax}^{lmax} \sum_{m=0}^{lmax} A^N_{km} \cos\psi_{km} + B^N_{km} \sin\psi_{km} \tag{8.6}$$

with

$$(A^N_{km}, B^N_{km}) = a_e \sum_{l=m}^{lmax} \left(\frac{a_e}{r}\right)^l \overline{F}_{lm(l-k)/2} \begin{bmatrix} \overline{C}^*_{lm} & \overline{S}^*_{lm} \\ -\overline{S}^*_{lm} & \overline{C}^*_{lm} \end{bmatrix}^{l-m:\ even}_{l-m:\ odd} \tag{8.7}$$

This equation shows that geoid undulations in spherical approximation expressed along the ground track possess 1) the same lumping effect as orbit errors and 2) uniqueness in frequency response, i.e. parasitic frequencies are not introduced in the problem.

Yet this is only true in spherical approximation, in ellipsoidal approximation the problem becomes more complicated since r (and γ) become, as a result of flattening of the reference ellipsoid, a function of the latitude ϕ, accordingly $r = h_r(\phi)$ (and $\gamma = h_\gamma(\phi)$). The A^N_{km} and B^N_{km} coefficients in (8.7) become instead:

$$(A^N_{km}, B^N_{km}) = \frac{\mu}{h_r(\phi)h_\gamma(\phi)} \sum_{l=m}^{lmax} \left(\frac{a_e}{h_r(\phi)}\right)^l \overline{F}_{lm(l-k)/2}(I) \begin{bmatrix} \overline{C}^*_{lm} & \overline{S}^*_{lm} \\ -\overline{S}^*_{lm} & \overline{C}^*_{lm} \end{bmatrix}^{l-m:\ even}_{l-m:\ odd} \tag{8.8}$$

compare also (Wagner,1988). In the latter publication the functions $h_r(\phi)$ and $h_\gamma(\phi)$ are developed in terms of f, (flattening of the reference ellipsoid) whereas f^2 and higher-order terms are ignored. The ellipsoidal approximation of the geoid along the altimeter ground track results in a so-called frequency splitting effect. This is due to the fact that $h_r(\phi)$ and $h_\gamma(\phi)$ in (8.8) symbolize sine-cosine functions dependent of time which are multiplied by the $\cos\dot{\psi}_{km}$ and $\sin\dot{\psi}_{km}$ terms in (8.6). This multiplication causes a frequency modulation introducing parasitic terms at $\dot{\psi}_{km} \pm 2\dot{\omega}_o$ in the problem, compare also Wagner (1988).

Another possibility would be an ellipsoidal representation of T instead of the spherical representation discussed above. For this problem we refer to (Moritz,1980) pp. 321–322 where T is developed in an ellipsoidal series expansion requiring Legendre functions of the second kind.

The problems sketched above, an ellipsoidal approximation of N in (8.6) by application of (8.8), or the development of T in an ellipsoidal series expansion will not be treated here. They are just mentioned to indicate the problems that might show up in a computation of N at a sub-satellite point, especially where it comes to geoids accurate to the level of a few centimeters.

Signal size, commission and omission errors

In the previous section it is discussed in which way N is computed at a sub-satellite point. The next problem concerns the behavior of this signal in the spectral domain. For the true geoid undulation N it is assumed that:

$$N = N_0 + \Delta N_c + \Delta N_o \tag{8.9}$$

where N_0 represents the undulation as it is computed in a spherical harmonic expansion up to a certain degree and order $lmax$, compare e.g. (8.6). The quantities ΔN_c and ΔN_o represent respectively the commission and the omission error in the geoid signal. The term ΔN_c represents the error signal that is included in the computation of N_0 due to uncertainties of the $\overline{C}_{lm}$ and $\overline{S}_{lm}$ coefficients. The term ΔN_o represents an error signal due to the fact that the spherical harmonic expansion is truncated at degree $lmax$.

The signal size, commission and omission errors in geoid heights and gravity anomalies can be investigated by an evaluation of high degree and order global geopotential solutions as is described in (Rapp,1986b). For the OSU-86F field, which is complete up to degree and order 360, undulations up to degree 36 have a r.m.s. magnitude of 30.43 m with an omission error of 1.58 m and a commission error of 79 cm. Undulations up to degree 180 in the OSU-86F field have a r.m.s. magnitude of 30.47 meter, an omission error of 23 cm and a commission error of 1 meter. These results are taken from (Engelis,1987).

This indicates that it is not allowed to simply truncate the spherical harmonic expansion at a low degree and order for accurate geoid computations. On the other hand, mostly for practical reasons, it is not possible to include potential coefficients up to degree and order 360 in an integrated approach. This would result in a least squares or hybrid norm parameter estimation problem with some $360^2 = 129600$ unknowns as will be discussed later on in this chapter. It is not surprising that Engelis (1987) reports:

> "From the discussion made so far, it is obvious that the solution of the combined altimeter problem is computationally extremely intensive. The computer resources that are required both in terms of computing time and memory are typical of a supercomputer environment."

This is one of the reasons to restrict the amount of unknowns, i.e. potential coefficients, in the problem. Accordingly the variable $lmax$ in the expansion of spherical harmonics is confined to an acceptable low value. Presumably for this reason Wagner (1986) employs in a simulation experiment a value of $lmax = 6$. Also Engelis (1987) used an $lmax = 10$. Yet limiting $lmax$ to a value of 10 introduces large omission errors in the geoid computation.

However this does ***not*** imply that the integrated approach cannot be used for geoid improvement and radial orbit error reduction. When we return to the fundamental altimetric equation (8.1) we will notice that the observations employed in an integrated approach represent so-called direct sea surface heights measured by the altimeter radar minus an a-priori geoid model minus an a-priori PST model. The observation equations in the integrated approach take the form of:

$$h^* - \rho - N - \varsigma^v - \varsigma^p = \Delta N - \Delta r + \Delta\varsigma^p \tag{8.10}$$

with on the LHS the measured (or modeled) quantities and on the RHS the unknowns. If ΔN, Δr and, as will be shown later in this chapter, $\Delta\varsigma^p$, are truncated at a low degree and order then it is also allowed to filter out the highly detailed surface structures on the LHS of (8.10). For this purpose a simple low pass filter as is described in §7.3.2 is sufficient. Compare also (Wagner,1988) who mentions that direct altimetric heights are smoothed over 550 seconds along the altimeter ground track. In (Tapley, Shum, Yuan, Ries and Schutz,1988) it is described how the integrated altimetric approach is employed in the development of an improved model for the Earth's gravity field named TEG-1. Also here a series expansion of the PST is confined to degree and order 8 whereas the gravitational field itself is evaluated up to degree and order 50. Tapley et al. (ibid) mention that the sea surface heights measured by the altimeter radar are smoothed to represent a spectrum consistent up to degree and order 50.

Omission errors in the lower frequency band

An *important* omission effect *not considered* by Wagner (ibid), Engelis (ibid) and Tapley et al. (ibid) is the contribution of the gravitational field above degree $lmax$ to the lower frequency band between e.g. 0 and 10 c.p.r. of Δr and ΔN. This signal is far more serious than any commission or omission error in the higher frequency range since it will persist even after a low-pass filter is applied on the residual sea surface heights.

Computations employing inclination functions have shown that this signal may be significant. With the OSU-81 field, cf. (Rapp,1983), using $I = 108°$, $\dot{\omega}_e/\dot{\omega}_o = -3/43$, $a_e = 6378137$ m and $r = a_e + 800$ km we found a total power (between 0 and 10 c.p.r. summarizing between degrees 37 and 180) of 79 cm for ΔN and 39 cm for Δr (excluding near resonant cases). For Δr most of this signal appears to come from the field between degrees 37 and ≈ 50. Similarly for ΔN, most of the signal appears to come from degrees 37 till ≈ 100. In a similar computation we computed the total power of ΔN and Δr between degrees 51 and 180 using the OSU-81 field in a frequency band between 0 and 10 c.p.r. It results in a total power of 55 cm for ΔN and only 5 cm for Δr.

Remind that the mentioned omission errors refer to the total power between 0 and 10 c.p.r. Whether all of this signal (or only a part of it) is affecting the estimation of the PST coefficients should be investigated.

Analogy with gravitational radial orbit errors

In spherical approximation geoid undulations take the form of (8.6) with A^N_{km} and B^N_{km} coefficients as given in (8.7). The series expansion of N in (8.6) can be compared directly with the non-resonant particular solution of the Hill equations as given in (4.38). In the following we consider the radial orbit error Δr and the geoid error ΔN to be caused solely by potential coefficient uncertainties $\Delta\overline{C}_{lm}$ and $\Delta\overline{S}_{lm}$. For the geoid error ΔN it is found that:

$$\Delta N(t) = \sum_{k=-lmax}^{lmax} \sum_{m=0}^{lmax} A^{\Delta N}_{km} \cos\psi_{km} + B^{\Delta N}_{km} \sin\psi_{km} \tag{8.11}$$

with $A^{\Delta N}_{km}$ and $B^{\Delta N}_{km}$ in spherical harmonic approximation ($r = a_e$, $\gamma = -\mu/a_e^2$):

$$(A^{\Delta N}_{km}, B^{\Delta N}_{km}) = \sum_{l=m}^{lmax} G_{lmk} \begin{bmatrix} \Delta\overline{C}_{lm} & \Delta\overline{S}_{lm} \\ -\Delta\overline{S}_{lm} & \Delta\overline{C}_{lm} \end{bmatrix}_{l-m:\ odd}^{l-m:\ even} \tag{8.12}$$

whereas the orbit error Δr is given by (4.38):

$$\Delta r(t) = \sum_{k=-lmax}^{lmax} \sum_{m=0}^{lmax} A^{\Delta r}_{km} \cos\psi_{km} + B^{\Delta r}_{km} \sin\psi_{km} \tag{8.13}$$

with

$$(A^{\Delta r}_{km}, B^{\Delta r}_{km}) = \sum_{l=m}^{lmax} H_{lmk} \begin{bmatrix} \Delta\overline{C}_{lm} & \Delta\overline{S}_{lm} \\ -\Delta\overline{S}_{lm} & \Delta\overline{C}_{lm} \end{bmatrix}_{l-m:\ odd}^{l-m:\ even} \tag{8.14}$$

where the summations over l in (8.12) and (8.14) are carried out *only* when there exists equal parity of k and l. The sensitivity coefficients G_{lmk} and H_{lmk} become:

$$G_{lmk} = a_e \overline{F}_{lm(l-k)/2} \tag{8.15}$$

and

$$H_{lmk} = r\left(\frac{a_e}{r}\right)^l \overline{F}_{lm(l-k)/2} \left\{\frac{\beta(l+1)-2k}{\beta(\beta^2-1)}\right\} \tag{8.16}$$

with, compare (4.38), r representing the mean height of the spacecraft, $\psi_{km} = k\overline{\omega}_o + m\overline{\omega}_e$, $\overline{\omega}_o = \omega_o + \dot{\omega}t$ and $\overline{\omega}_e = \omega_e + \dot{\omega}t$, $\dot{\omega}_o = n = (\mu/r^3)^{1/2}$, and $\beta = \psi_{km}/n$. A comparison between (8.15) and (8.16) shows clearly:

1. a damping factor $r(a_e/r)^l$ (due to the upward continuation of the disturbing potential causing the radial orbit errors) in contrast to a factor a_e in geoid errors,
2. a resonance factor $(\beta(l+1)-2k)/(\beta(\beta^2-1))$ unique for Δr.

In order to get a better insight in the relationship between Δr and ΔN a simulation is carried out. In this experiment $\Delta\overline{C}_{lm}$ and $\Delta\overline{S}_{lm}$ in (8.12) and (8.14) are simulated by the differences of the PGS-S4 and the GEM-10B field. In figure 8.1 the amplitude ratio's of $(A_{km}^{\Delta N}, B_{km}^{\Delta N})$ versus $(A_{km}^{\Delta r}, B_{km}^{\Delta r})$ are shown. The amplitude ratio Δp is

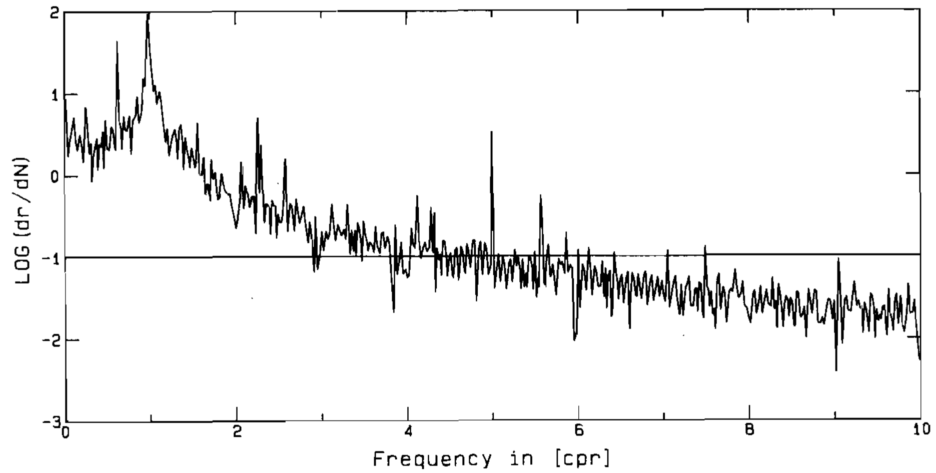

Figure 8.1: The amplitude ratio spectrum of the radial orbit error in relation to the geoid error for a SEASAT type of orbit. The disturbing potential is simulated by the differences of the PGS-S4 minus the GEM-10B field. The spectral resolution equals to 1/43 c.p.r.

defined by:

$$\Delta p = \sqrt{\frac{(A_{km}^{\Delta r})^2 + (B_{km}^{\Delta r})^2}{(A_{km}^{\Delta N})^2 + (B_{km}^{\Delta N})^2}} \tag{8.17}$$

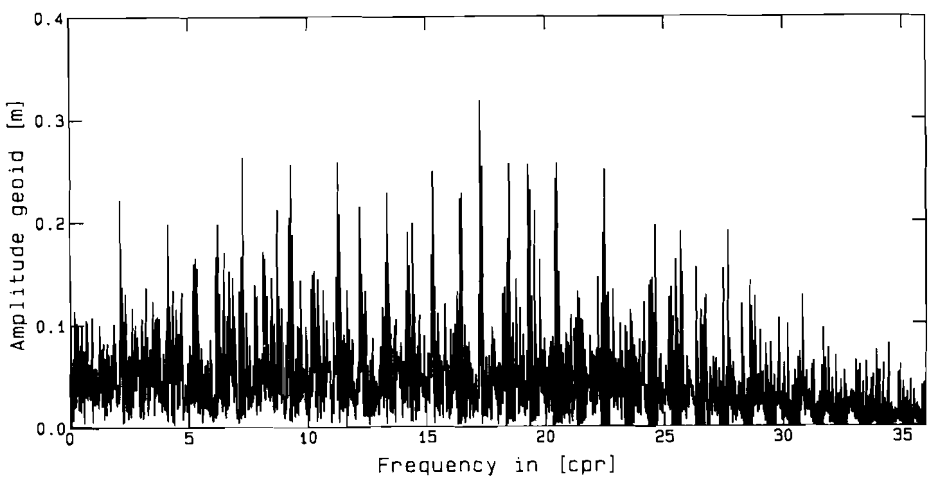

Figure 8.2: The geoid error amplitude spectrum along an altimeter ground track in spherical approximation based on simulated potential coefficient differences.

where coinciding $A_{km}^{\square}$ and $B_{km}^{\square}$ ($\square = \Delta r$ or ΔN) terms at each frequency are accumulated. The horizontal axis in figure 8.1 represents $|\beta|$, i.e. the absolute frequency in cycles per revolution, the vertical axis represents $\log_{10}(\Delta p)$. For simplicity exact resonance situations with $\beta = 0$ or $\beta = \pm 1$ are left out. Furthermore the constants μ, a_e and J_2 are chosen conform the GRS-80. Orbital parameters are chosen conform the nominal SEASAT trajectory: $r = a_e + 790$ km, $e = 0.001$ and $I = 108°$.

In figure 8.2 the geoid error amplitude spectrum is shown. The vertical axis shows the denominator of equation (8.17) which is computed under the same conditions as the radial orbit error. As can be seen from figure 8.1, Δr is dominating ΔN for $|\beta| <$ 2 c.p.r. The cause of this is the presence of a resonance factor in equation (8.16). In the range between 2 c.p.r. and 4 c.p.r. the geoid error is slightly higher than the orbit error. Above 4 c.p.r. the geoid error is more than a factor 10 greater than the orbit error. For example at $|\beta| \approx 15$ c.p.r., which corresponds to wavelengths of 2500 km, there are geoid errors of 30 cm and radial orbit errors of only 3 mm.

It is reasonable to assume that a joint modeling of Δr and ΔN is only successful whenever there exists a significant signal in *both* models. Under this assumption the range in the frequency spectrum is very limited for an integrated approach. Above a frequency of 4 to 6 c.p.r. one can simplify the joint recovery model and solve the unknowns for geoid errors only.

However the opposite is also true, in the frequency band of 0 to 2 c.p.r. there is a lot of amplification in Δr compared to that of ΔN. It can only mean that the geoid *must* be known rather accurate in this frequency range. If this were not the case then radial orbit errors should be far larger than the 1 to 2 meter level found for SEASAT.

8.2.3 Permanent sea surface topography

The model applied for PST in the integrated approach is almost identical to the series expansion in spherical harmonics used for modeling the geoid errors in spherical approximation. Accordingly:

$$\varsigma^p(\lambda,\phi) = a_e \sum_{l=1}^{lmax} \sum_{m=0}^{l} \left[\overline{C}_{lm,\varsigma} \cos m\lambda + \overline{S}_{lm,\varsigma} \sin m\lambda\right] \overline{P}_{lm}(\sin\phi) \qquad (8.18)$$

where $\overline{C}_{lm,\varsigma}$ and $\overline{S}_{lm,\varsigma}$ represent the PST coefficients of degree l and order m. Equation (8.18) describes a surface function representing the permanent deviations of the actual sea surface with respect to a geoid due to the effect of PST. Levitus (1982) presented maps of the PST in his "Climatological Atlas of the World Oceans". The results published by Levitus are based upon hydrographic measurements collected over a time span of 70 years. From this data the coefficients $\overline{C}_{lm,\varsigma}$ and $\overline{S}_{lm,\varsigma}$ have been estimated by means of spherical harmonic analysis, cf. (Engelis,1983,1985). In the regions where PST is not available (land, polar regions) ς^p is assumed to be equal to zero.

An important difference with the gravitational field are the ranges of the series expansion in (8.18) which start at degree one. The terms $\overline{C}_{10}$, $\overline{C}_{11}$ and $\overline{S}_{11}$ do not exist in any potential coefficient model since this would imply that the center of mass of the Earth is not located in the geocentric coordinate origin. These coefficients would indicate a shift over the z-axis and a shift in the x-y plane respectively. On the other hand for PST it is known that $\overline{C}_{10,\varsigma}$, $\overline{C}_{11,\varsigma}$ and $\overline{S}_{11,\varsigma}$ exist. Wagner (1988) mentions that $\overline{C}_{10,\varsigma}$ is caused by the dominant circumpolar Antarctic current manifesting in the latitude band between $\phi = -50°$ and $\phi = -70°$.

There are ample oceanographic reasons to assume that the signal present in the $\overline{C}_{lm,\varsigma}$ and $\overline{S}_{lm,\varsigma}$ coefficients differs with respect to the signal in the $\overline{C}_{lm}$ and $\overline{S}_{lm}$ coefficients. This follows from the degree variance functions, compare Heiskanen & Moritz (1979), both for gravitation and PST. These functions take the form of:

$$\sigma^2_{l(\text{gravitation})} = \sum_{m=0}^{l} \overline{C}^2_{lm} + \overline{S}^2_{lm}$$

$$\sigma^2_{l(\text{PST})} = \sum_{m=0}^{l} \overline{C}^2_{lm,\varsigma} + \overline{S}^2_{lm,\varsigma}$$

The nature of the degree variance functions of the gravitational field is described in e.g. (Tscherning & Rapp,1974). For a description of the degree variance function of the PST field, that is based on the Levitus model, compare (Engelis,1983,1985) and (Wagner,1986). However the main difference is that uncertainties in $\overline{C}_{lm}$ and $\overline{S}_{lm}$ affect as well the sea surface as the orbit, whereas uncertainties in $\overline{C}_{lm,\varsigma}$ and $\overline{S}_{lm,\varsigma}$ only influence the sea surface.

8.2.4 Parameter estimation

In §8.2.1 to §8.2.3 three models are discussed that may be used to describe respectively Δr, ΔN and $\Delta\varsigma^p$. In the sequel it is assumed that Δr is modeled by (8.2),

ΔN by (8.6) and (8.7) and $\Delta\varsigma^p$ by (8.18). Under these assumptions the unknowns become:

1. Improvements of the potential coefficients: $\Delta\overline{C}_{lm}$ and $\Delta\overline{S}_{lm}$.
2. Improvements of the initial state vector: Δu_0, $\Delta\dot{u}_0$, Δv_0 and $\Delta\dot{v}_0$ in Δr_h, compare equation (4.36).
3. Improvements of the PST coefficients: $\Delta\overline{C}_{lm,\varsigma}$ and $\Delta\overline{S}_{lm,\varsigma}$, compare (8.18).

In first instance observations are formed by so-called residual sea surface heights found on the LHS of (8.10). These residuals consist of the corrected sea surface heights measured by the altimeter radar minus an a-priori geoid model minus an a-priori PST model as is described in §8.2.2. The integrated approach is not restricted to residual heights, it is also allowed to employ crossover differences as is described by Engelis (1987).

The parameter estimation problem described by Engelis (ibid) consists of 984 residual sea surface heights, 1178 crossover differences and some 200 unknowns. Engelis (ibid) considers as unknowns potential and PST coefficients up to degree and order 10 and observations derived from simulated SEASAT data lasting over a period of 3 days. Considering the amount of observations and unknowns in this experiment one can in principle follow a single step formulation of a least squares minimization.

However a single step least squares formulation of the problem leads to a poorly conditioned or probably even a singular system of normal equations. The reason for this comes from the fact that columns of the design matrix A become linear or nearly linear dependent.

Singularities of this sort do *not* exist in the parameter estimation problems described by Wagner (ibid) and Engelis (ibid), because an *a-priori* regular positive definite covariance matrix of the unknowns (P_{xx}) is included in the problem. The corresponding hybrid norm minimization takes the form of:

$$\vec{\epsilon}^{\,t} Q_{yy}^{-1} \vec{\epsilon} + \vec{x}^{\,t} P_{xx}^{-1} \vec{x} = \min \tag{8.19}$$

where the a-priori covariance matrix P_{xx} for the unknowns is assembled from covariance matrices for $\overline{C}_{lm}$ and $\overline{S}_{lm}$ (e.g. the inverse of the normal matrix which was used to compute a certain potential coefficient model such as GEM-T1) and for $\overline{C}_{lm,\varsigma}$ and $\overline{S}_{lm,\varsigma}$. For more details compare (Engelis,ibid) and (Wagner,1988).

A single step formulation of the parameter estimation problem of the integrated approach gives hardly any insight in the nature of the problem. For this purpose the single step approach is reformulated to a dual step approach. In a first step observations in the form of residual sea surface heights Δh are used to estimate the lumped coefficients $A_{km}^{\Delta h}$ and $B_{km}^{\Delta h}$ including additional unknowns required for modeling Δr_h and Δr_{pr} of (8.2):

$$\begin{aligned} \Delta h &= h^* - \rho - N - \varsigma^p - \varsigma^v = \Delta N - \Delta r + \Delta\varsigma^p \Rightarrow \\ \Delta h &= \sum_{k=-lmax}^{lmax} \sum_{m=0}^{lmax} \left[A_{km}^{\Delta h} \cos\psi_{km} + B_{km}^{\Delta h} \sin\psi_{km} \right] \\ &\quad - \left[(a_0 + a_1 t)\cos nt + (b_0 + b_1 t)\sin nt + (c_0 + c_1 t) \right]. \end{aligned} \tag{8.20}$$

The summations in (8.20) over k and m are carried out such that $\dot{\psi}_{km} = 0$ and $\dot{\psi}_{km} = \pm\dot{\omega}_o$ are avoided. Instead the coefficients a_0, a_1, b_0, b_1, c_0 and c_1 are employed for modeling the combined effect of Δr_h and Δr_{pr} in (8.2).

Essentially the unknowns $A^{\Delta h}_{km}$ and $B^{\Delta h}_{km}$ in (8.20) are recovered by frequency analysis. Unfortunately fast Fourier techniques are not directly applicable to this problem because the Δh time series is interrupted by gaps where the altimeter passes over land. A remedy to this problem is to apply a straightforward least squares minimization in which (8.20) forms the basis of the observation equations. The number of unknowns in this first step is determined by 1) the type of low pass filtering that is applied to Δh, compare also §8.2.2, and 2) the length of the Δh data record. An observation set spanning a short duration causes resolution problems for adjacent $A^{\Delta h}_{km}$ and $B^{\Delta h}_{km}$ coefficients in the frequency spectrum. Other problems that might affect the quality of the estimates come from the fact that Δh is given only over sea, compare also the results published by Wagner (1986).

In a second step the lumped coefficients $A^{\Delta h}_{km}$ and $B^{\Delta h}_{km}$ are linearly related to the original unknowns in the integrated approach:

$$(A^{\Delta h}_{km}, B^{\Delta h}_{km}) = \sum_{l=m}^{lmax} H^1_{lmk} \left[\begin{array}{cc} \Delta\overline{C}_{lm} & \Delta\overline{S}_{lm} \\ -\Delta\overline{S}_{lm} & \Delta\overline{C}_{lm} \end{array} \right] + H^2_{lmk} \left[\begin{array}{cc} \Delta\overline{C}_{lm,\varsigma} & \Delta\overline{S}_{lm,\varsigma} \\ -\Delta\overline{S}_{lm,\varsigma} & \Delta\overline{C}_{lm,\varsigma} \end{array} \right]^{l-m\ even}_{l-m\ odd} \tag{8.21}$$

where the summation is carried out for equal parity of k and l only and where

$$H^1_{lmk} = \left[a_e - r \left(\frac{a_e}{r} \right)^l \left\{ \frac{\beta(l+1) - 2k}{\beta(\beta^2 - 1)} \right\} \right] \overline{F}_{lm(l-k)/2} \tag{8.22}$$

and

$$H^2_{lmk} = a_e \overline{F}_{lm(l-k)/2} \tag{8.23}$$

which is found by an evaluation of $\Delta N - \Delta r + \Delta\varsigma^p$ using eqns. (8.2), (8.6), (8.7) and (8.18).

In the derivation of (8.21) it is assumed that the maximal degree and order $lmax$ is equal for the PST and the potential coefficients. It shows that there are maximally $4(lmax - m + 1)$ potential and PST coefficients connected in a linear combination (a cluster) to two lumped coefficients $A^{\Delta h}_{km}$ and $B^{\Delta h}_{km}$. Each (k, m) cluster maps on one unique frequency ($k + m(\dot{\omega}_e/\dot{\omega}_o)$ in c.p.r.) in the spectrum of Δh. However for the orbit of e.g. SEASAT some (k, m) clusters show an overlap as is discussed in §4.3. It is obvious that this effect depends on the resolution obtained in the first step while estimating $A^{\Delta h}_{km}$ and $B^{\Delta h}_{km}$ from the residual sea surface heights. An important property of the second step is, that most of the (k, m) clusters can be treated ***individually*** since there are no linear combinations of potential – and PST coefficients of different orders m. An exception is formed for those cases where overlapping of $A^{\Delta h}_{km}$ and $B^{\Delta h}_{km}$ coefficients occurs in the Δh frequency spectrum.

This means that it is possible to form a block diagonal system of observation equations which can be treated block by block as is described in Schrama (1986b). With this in view Engelis' statement, which is quoted on page 136, is probably exaggerated. *Most* of the work in an integrated approach sketched here comes from the first step, namely the spectral analysis of Δh.

Whether or not it is possible to solve the unknowns from the lumped coefficients $A^{\Delta h}_{km}$ and $B^{\Delta h}_{km}$ depends fully on: 1) the type of low pass filtering applied to Δh determining directly the amount of frequencies in the residual height spectrum and 2) the maximal degree and order $lmax$ in equation (8.21). A trivial condition concerns the amount of unknowns which should not exceed the number of $A^{\Delta h}_{km}$ and $B^{\Delta h}_{km}$ coefficients for all possible values of k of the corresponding order m. It was mentioned before that the maximal number of unknowns equals to $4(lmax - m + 1)$ whereas the maximal number of observations equals to $4 \times lmax$.

Eventually there remain a number of peculiar (k, m) combinations for $A^{\Delta h}_{km}$ and $B^{\Delta h}_{km}$ in (8.21) which may require special attention, compare also Wagner (1988):

- The term $A^{\Delta h}_{00}$ in (8.21) coincides with c_0 in (8.20). This means that the even zonal coefficients of the PST field coincide with the initial state vector disturbances Δu_0 and $\Delta \dot{v}_0$ in (4.36).
- The terms $A^{\Delta h}_{km}$ and $B^{\Delta h}_{km}$ in (8.21) for $k = \pm 1$ and $m = 0$ coincide with the terms a_0 and b_0 in (8.20). In this case there are a number of effects that cannot be separated: 1) initial state vector disturbances Δu_0, $\Delta \dot{u}_0$, Δv_0 and $\Delta \dot{v}_0$ in (4.36) 2) odd zonal coefficients of the gravitational field starting at $l = 3$ and 3) odd zonal coefficients in the PST field starting at $l = 1$.

An alternative for a secondary step in the dual approach is to combine constraint equations of lumped coefficients of other satellite tracking observations as is described by Tapley et al. (1988). Presumably this results in a more realistic improvement of the gravitational field than just employing the constraints for lumped coefficients coming from the integrated altimetric approach.

8.2.5 Some remarks on PST improvement

Restrictions of the current approach

Noteworthy are the problems that may arise when modeling PST in an integrated approach as is mentioned by Wagner (1988). An example is the modeling of the $\overline{C}_{10,\varsigma}$ term which is coinciding with a number of effects simultaneously. Presumably this results in a high correlation between $\overline{C}_{10,\varsigma}$ and initial state vector effects including the odd zonal perturbations of the gravitational field. It is the author's opinion that some of these high correlations are due to the inadequate modeling of PST in its current form.

It can, for instance, not be guaranteed that geostrophic currents (recovered by the integrated approach in question) do not show an unrealistic flow over the continents. Even the best a-priori covariance matrix for $\Delta\varsigma^p$ cannot prevent this peculiar behavior of the currents. The question arises whether or not it is possible to improve the modeling of $\Delta\varsigma^p$, e.g. by prohibiting geostrophic currents perpendicular to a shoreline.

Another important shortcoming of the current approach is that PST coefficients are limited to $l < lmax \approx 10$ implying that the short periodic western boundary currents cannot be modeled adequately. An obvious remedy for this effect is to extend the summation limit of the PST field. Presumably this will result in a problem of separating ς^p and N in the higher range of the frequency spectrum due to the damping behavior of Δr.

Instrumental limitations

First of all the actual sea surface topography is more complex than just its permanent part. Wunsch et al. (1980) describe a number of oceanographic phenomena in the context of combining hydrography with marine geodesy and satellite altimetry. The objective is to determine the general circulation pattern of the oceans, defining the eddy field and improving the marine geoid.

Some of the oceanographic effects known in physical oceanography are simply not relevant for an inclusion in an integrated approach due to the limited accuracy of the altimeter measurements and the length in time of the existing altimeter database, compare also Wunsch et al. (1980). For instance annual effects in ς are hard to recover from a 3 month's period of SEASAT data. In this context GEOSAT altimeter data would be more suitable for studying long periodic variations in the sea surface.

Another example of an effect that may not be recovered easily are the very longest internal waves (wavelengths of the order of 100 km) which generate surface elevations that may reach 1 or 2 cm. (cf. Wunsch et al. (1980) p. 258.) These effects are a factor 5 to 10 smaller than the noise level of the altimeter radars both of SEASAT and GEOSAT.

The remaining terms in ς suitable for an inclusion in the integrated approach appear currently 1) permanent and long periodic effects and 2) large scale features in the oceans due to circulation. Both are symbolized by the term ς^p in the fundamental altimetric equation. Oceanographic phenomena which are short periodic and acting on a small scale can be studied more effectively by monitoring the variations in the sea surface by either collinear – or crossover analysis. In this study these effects are gathered in the term ς^v.

Recommendations for an improved PST estimation

In order to model ς^p more accurately one could distinguish between two approaches, namely one in which an independent model for ς^p set up similar to the way tidal influences are treated or a simultaneous approach where ς^p remains in an integrated scheme but in a form different from now.

A typical independent approach might consist of a finite element or finite differences approach for modeling the oceanographic circulation. For a discussion of the underlying differential equations we refer to Wunsch et al. (1980) and Rummel (1985). Additionally this model should include suitable boundary conditions preventing unrealistic geostrophic currents. Possibly one might design a more realistic model by including other forcing terms such as the dominating effect of the wind field on ς^p. In this context it is worthwhile to mention that wind speed and direction may be provided by the scatterometer (e.g. on board SEASAT and in the future on ERS-1).

A second possibility is to keep the model of ς^p in its current version. However, in order to yield more realistic solutions, it is advisable to include additional constraints for the $\overline{C}_{lm,\varsigma}$ and $\overline{S}_{lm,\varsigma}$ coefficients in the integrated approach. (e.g. the earlier mentioned constraints prohibiting a geostrophic flow perpendicular to the shore) A disquieting effect will probably remain the omission effect of the gravity field which leaks in the $\overline{C}_{lm,\zeta}$ and $\overline{S}_{lm,\zeta}$ coefficients in the current integrated approach.

In which way both models have to be formulated and included in the processing of satellite altimeter data is a topic recommended for further research.

8.3 Some remarks on global crossover analysis

In this study several chapters describe aspects of crossover minimization in satellite altimetry. A description of the results obtained by global continuous crossover minimization is avoided here since it would be a repetition. Instead we conclude with a discussion of the possible dangers of over-constraining the crossover minimization schemes and secondly our comparison with Rosborough's (1986) definition of geographically correlated orbit errors.

8.3.1 Alternative crossover minimization schemes

Over-constrained crossover solutions

An alternative, which is a direct extension of the least squares minimization schemes discussed in chapter 3 for the local case and chapters 6 and 7 for the global case, is to include more constraints in the system of observation equations than strictly required for finding a particular solution.

The principle danger with this approach is as follows: Whenever too few constraints are introduced, the system of normal equations remains singular and cannot be solved. Hence for this case one has a clear indicator that "something is wrong". In the case of too many constraints (over-constraints) the solution may be deformed. However this undesirable deformation may be small so that it cannot easily be detected.

The typical structure of the eigenvalue spectra of the normal matrices of crossover problems are, according to the author's opinion, the main reason for the fact that several researchers prefer to include additional constraints, and possibly over-constraints, in the crossover minimization problem.

In fact the author himself is also to blame for this since, all crossover problems discussed in this work possess only one real singularity (namely the bias coefficient of the observation equations). Other small eigenvalues (the criteria are discussed in chapter 3 and 6) exist due to the fact that crossover time tags deviate from the linear congruent behavior in the local case, antisymmetry in the segmented global cases, or the nominal orbit in the continuous crossover minimization. In all cases the real crossover problem, based on the actual time tags, is conveyed in a problem closely resembling it. The technique applied for this purpose is called: time tag regularization.

The discussion so far indicates that there is no clear answer to the question: "what is the rank defect of your normal equations?". The problems discussed in this work are the ones encountered in literature. However it is very likely that there may exist other formulations of the crossover minimization problem which may result in other rank defects of the normal equations. It is the author's hope that this study may be a motivation for researchers to investigate these defects and their consequences on the results obtained by 'crossover altimetry'.

Inclusion of alternative observation equations

Technical developments in the near future can provide additional information which could allow an inclusion of other observation equations together with crossover differences. Implicitly this means that the crossover minimization problem is altered. Instead it should be called a crossover, "another observation type" minimization problem. In this work no attempt was made to study these minimization problems, therefore the topic is recommended for further research in satellite altimetry.

In the local adjustment one could imagine to include more than 2 master arc segments which are supported by accurate tracking. Unfortunately, at the moment for GEOS-3, SEASAT and GEOSAT such information is not available. However the configuration of ERS-1 is planned with a PRARE system whereas TOPEX is expected to fly with DORIS and GPS. These (experimental) developments can provide an accurate real time position determination of the spacecraft.

For local adjustments it means that one could derive, at least a number of, altimeter profiles which are known in some reference coordinate system. The advantage for 'crossover altimetry' is obvious: the eventual sea surface can be positioned absolutely in a known coordinate system.

This information is highly valuable since it allows to observe a number of effects which are obscured by the homogeneous solutions of the systems of normal equations in the conventional crossover minimization schemes. An application with great benefits to physical geodesy and – oceanography could be the monitoring of e.g. tides, currents and other phenomena which are currently so problematic to model in shallow waters close to the coast (e.g. the North sea and the Hudson bay).

Also in global crossover minimization schemes additional information, in the form of absolutely positioned altimeter profiles, would be useful. An absolutely positioned altimeter surface will probably allow to determine orbital perturbations free of unrealistic homogeneous effects currently present in the conventional crossover minimization schemes with benefits to the improvement of the Earth's gravitational field, permanent (or semi-permanent) sea surface topography and tides.

8.3.2 Some remarks on orbit errors and geographic correlation

Rosborough (1986) describes satellite orbit perturbations due to the geopotential. He follows, for the derivation of a first-order analytical perturbations theory, nearly the same approach as Wagner (1985,1987) and Engelis (1987). Rosborough's primary goal is to investigate the nature of the radial orbit errors for the TOPEX mission both temporally (i.e. in the form of perturbation spectra) but *also* spatially (i.e. in the form of a geographical presentation). Especially the latter approach is original.

The spectral analysis pursued by Rosborough (ibid) is based on geopotential coefficients, differences of geopotential coefficients and a variance propagation of potential coefficients into radial orbit errors. The former two require an analysis by means of linear perturbations theory, the latter requires propagation of variances of potential coefficients into variances of the radial orbit error. Variance propagation can be performed easily since there exists a linear relation of $\overline{C}_{lm}$ and $\overline{S}_{lm}$ with e.g. A_{km} and B_{km}, the lumped coefficients in the spectrum of Δr. Consider for instance (4.26) where A_{km} and B_{km} coefficients are gathered in a vector $\vec{r}$, H_{lmk} sensitivity coefficients in a matrix H and $\overline{C}_{lm}$, $\overline{S}_{lm}$ potential coefficients in a vector $\vec{c}$:

$$\begin{bmatrix} \vdots \\ A_{km} \\ B_{km} \\ \vdots \end{bmatrix} = \begin{bmatrix} & \vdots & \\ \cdots & H_{lmk} & \cdots \\ & \vdots & \end{bmatrix} \begin{bmatrix} \vdots \\ \overline{C}_{lm} \\ \overline{S}_{lm} \\ \vdots \end{bmatrix} \quad \Rightarrow \quad \vec{r} = H\vec{c}. \tag{8.24}$$

The covariance matrix Q_{rr} of the A_{km} and B_{km} coefficients may be formulated as:

$$Q_{rr} = HQ_{cc}H^T \tag{8.25}$$

where Q_{cc} is representing some a-priori covariance matrix of a geopotential model. Critical is the choice of a well calibrated Q_{cc} matrix in (8.25). For this purpose Rosborough (ibid) applies a GEM-L2 covariance matrix. (The GEM-L2 field is described by Lerch et al. (1982b)). For a discussion of the results we refer to Rosborough (ibid) as well as Wagner (1985,1987) whom pursued a covariance analysis similar to described above.

For spatial analysis the radial orbit error is transformed into an alternative representation. Rosborough (ibid) shows that the radial (including other) orbit errors per degree l and order m at a given location (ϕ, λ) on the sphere may be formulated as:

$$\begin{aligned} \Delta r_{lm}(t) = \sum_k & \Phi^M_{lmk}(\phi) H_{lmk} \left[\Delta\overline{C}_{lm}\cos m\lambda + \Delta\overline{S}_{lm}\sin m\lambda\right] \\ & \pm\Phi^V_{lmk}(\phi) H_{lmk} \left[-\Delta\overline{S}_{lm}\cos m\lambda + \Delta\overline{C}_{lm}\sin m\lambda\right] \end{aligned}$$

where Φ^M_{lmk} and Φ^V_{lmk} represent the so-called mean and variable component of Δr_{lm}. The choice of the sign in front of the term Φ^V_{lmk} is determined by whether the satellite moves over an ascending or a descending arc segment. An important fact is that both terms are a function of the latitude ϕ. Rosborough (ibid) shows that Δr_{lm} is separated into a function $\Delta\gamma_{lm}$ and $\Delta\nu_{lm}$:

$$\begin{aligned} \Delta\gamma_{lm}(\phi, \lambda) &= \sum_k \Phi^M_{lmk}(\phi) H_{lmk} \left[\Delta\overline{C}_{lm}\cos m\lambda + \Delta\overline{S}_{lm}\sin m\lambda\right] \\ \Delta\nu_{lm}(\phi, \lambda) &= \pm\sum_k \Phi^V_{lmk}(\phi) H_{lmk} \left[-\Delta\overline{S}_{lm}\cos m\lambda + \Delta\overline{C}_{lm}\sin m\lambda\right] \end{aligned}$$

where $\Delta\gamma_{lm}$ describes the so-called geographical mean and $\Delta\nu_{lm}$ the – variable contribution to the radial orbit error. The *reason* for calling $\Delta\gamma_{lm}$ a 'mean' radial orbit error is that it represents the result after *averaging* the individual contributions of Δr_{lm} on a crossover point at the corresponding geographical location. In contrary $\Delta\nu_{lm}$ is called a variable radial orbit error since it describes the deviations with respect to the 'mean' required for reconstructing Δr_{lm}.

The next step is to assume that $\Delta\gamma_{lm}$ represents an 'unobservable' and $\Delta\nu_{lm}$ an 'observable' signal at the crossover point in question. It is the author's opinion that this *intuitive* step is not reflecting the real nature of unobservability in the process of minimizing crossover differences. Nowhere in this work it was found that an average value of a crossover difference shows up as the only possible homogeneous solution of the system of normal equations in a global continuous crossover minimization problem.

The author has the following opinion concerning observability or not of Δr from crossover differences: Unobservable at crossover differences are, by definition as they are introduced in chapter 2, a manifold of stationary surface functions projected along a satellite ground track. The consequences of this statement are *very* drastic because it would prohibit the recovery of any surface function from crossover altimetry. It would simply not be possible to recover *any* highly detailed geoid from crossover minimization. A simple counter example shows the physical limitation of this reasoning: of all possible surface functions only *those* remain which map on frequencies in the lower range of the radial orbit error spectrum where most of the signal is concentrated.

A comparison of the a-priori mean and variable geographically correlated orbit errors of a SEASAT arc based on simulated potential coefficient differences using Rosborough's theory can be found in e.g. (Engelis,1987), figures 48 and 52. These figures reveal detailed surface structures which, projected along the SEASAT trajectory, most certainly result in quite some signal in the high frequency range of an orbit error spectrum. It is the author's opinion that the well known strong damping behavior of orbit errors is in direct contradiction with this hypothesis. However a separation in $\Delta\gamma_{lm}$ and $\Delta\nu_{lm}$ is considered useful for explaining the consequences of 'straightforward' averaging methods, e.g. as described by Marsh et al. (1982b).

Chapter 9

Conclusions and recommendations

The process of orbit determination is an important stage in the processing of satellite altimeter data. Uncertainties in the gravitational model, required for the computation of altimetric orbits, leave a considerable error signal in the radial position of the altimeter satellite. Other error effects in the altimetric configuration come from the a-priori geoid, Earth and ocean tides, atmospheric drag, radiation pressure, instrumental effects and other phenomena which are described in chapter 2. In this study most attention is focussed on the influence of radial orbit errors due to gravitational modeling in satellite altimetry.

In the past various researchers have developed selective filters for the purpose of removing radial orbit errors along short arc segments. These filters take the form of local crossover minimization schemes and were applied by e.g. Rummel et al. (1977), Marsh et al. (1984) and Vermeer (1983). In general it is envisaged to construct a mean sea surface model by removing empirical error functions over short arc segments. In this study the technique is applied on a test area in the North-east Atlantic for the purpose of demonstrating the method of local crossover minimization.

For local crossover minimization problems it is shown that the normal equations may be formulated in the form of a compatible self adjoint system as is described by Lanczos (1964). Self adjoint systems may be separated in two parts consisting of a particular solution and a homogeneous solution. Particular solutions are found by fixing a minimum number of master arc segments. Homogeneous solutions allow to transform the crossover solution without changing the original crossover observations.

In order to find a numerically stable particular solution it is necessary to regularize crossover time tags: a procedure where the actual time tags are replaced by model timings closely resembling the original pattern. For linear congruent crossover time tags it is shown that 2 non-intersecting, non-overlapping master arc segments are required for a numerically stable particular solution of the normal equations. It is found that the homogeneous solution corresponds with a polynomial deformation surface containing 4 degrees of freedom.

Variance analyses of the parameters involved in the local crossover adjustment revealed that inaccurate error functions pertain to short or poorly connected arc segments. The conclusion appears to be indifferent for either the inverse of the normal matrix required for finding a particular solution or a minimum trace covariance matrix derived from this inverse.

A topic recommended for further research is to combine several independent local solutions while solving optimally the shift vectors of the singularity transformation belonging to each solution. This technique might prevent the burden of computing very large crossover adjustments as in the case of many years of altimeter data coming from several altimeter satellites. This might be useful for mesoscale variability computations with limited computer resources over a long period of altimeter data.

In chapter 4 analytical perturbation theories are employed for describing radial orbit errors caused by the geopotential. These analytical theories are required for a better understanding of the interaction between the gravitational field and the radial orbit errors. In contrast to analytical theories are the numerical techniques of orbit determination. These techniques are considered to be more suitable for the production work in the processing of altimeter data.

The analytical theories in question are based on either the Lagrange planetary equations or, as an alternative, the Hill equations. Here we constrain ourselves to radial perturbations in near circular orbits which are not longer than 10 days. Currently this is approximately the longest period that is applied for orbit determination of altimetric satellites.

In order to convey the Lagrange planetary equations into a suitable description of the radial orbit error two approximations are made. The first assumption is the basis for the linear perturbations theory of Kaula (1966) where a nominal orbit is used to derive disturbances in the Keplerian elements. The second assumption concerns the transformation of the perturbations in the elements into a radial expression such that 'second-order' eccentricity effects are ignored.

An alternative for the Lagrange planetary equations consists of the Hill equations, as described by Kaplan (1976) and Colombo (1984a), holding for an idealized circular orbit. In contrary to the conventional Lagrange planetary equations there exists an exact general solution of the Hill equations consisting of a homogeneous and a particular case. A discussion of both solutions is given in §4.2.2 where it is shown that the non-resonant particular radial solution of the Hill equations coincides with the radial expression derived by Wagner (1985).

A verification of both analytical theories is made with a synthetically generated numerical orbit error. The numerical error signal is derived by differencing two trajectories computed by means of numerical integration of the equations of motions with the gravitational models GEM-10B and PGS-S4. It results in a so-called simulation dataset which is used throughout this study.

An impression of the limitations due to linearization inherent to both analytical theories is given in appendix A where long periodic effects in the eccentricity and the argument of perigee are described as a result of the odd zonal coefficients of the gravitational field.

In chapter 5 spectral characteristics of crossover – and repeat arc differences are discussed. For crossover differences computed from the nominal orbit it is found that 1) the relative time tags (the difference in time from the equator transit point to the crossover location) of ascending and descending arc segments possess an opposite sign and 2) that the magnitude of the time tags is determined only by the longitude separation of the equator transit points of both arc segments. Both properties are convenient in the derivation of the rank defect of global segmented crossover minimization schemes as discussed in chapter 6.

The spectral characteristics of crossover differences are investigated by examining the time tag pattern as it shows up in the simulation dataset. On basis of this information it is argued that it is not possible to recover completely a radial error effect from crossover differences. It has been verified that singular frequencies in the inverse transformation of crossovers to orbit errors exist in the spectral band where most of the signal is concentrated.

Another observation type described and analyzed in chapter 5 is the repeated measurement of sea surface heights over the same ground track. It is shown that 'collinear or repeat arc differences' behave as an almost perfect filter for all short periodic perturbations caused by the gravitational field. This implies that gravitational radial orbit errors – full or impart – cannot be recovered from repeat arc differences except for the long periodic modulation caused by the precession of the argument of perigee. The latter effect is investigated in more detail in chapter 6 where it is shown that repeat arc differences may be modeled by a 'bow tie' function. The nature of repeat arc differences cannot be explained by the resonant particular solution of the Hill equations, it requires an alternative treatment by means of Cook's theory as is described in appendix A.

In chapter 6 three global crossover minimization schemes have been worked out in detail for the purpose of reconstructing the simulated radial orbit error. The former two models are called chronologically segmented and are, mathematically seen, equivalent to local minimization schemes except that alternative error functions are defined per arc segment. Investigations concerning an optimal fitting accuracy and a minimal amount of parameters revealed that a 3 parameter Fourier function in the form of eq. (6.11) is eligible above others.

The normal equations based on these error functions show a rank defect of 3 provided that the crossover time tags are regularized in an antisymmetric way. The homogeneous solution of the problem is described in §6.3 and allows a strict zonal deformation of the altimetric surface. An artifact of the corresponding singularity transformation is the discontinuity effect of the radial velocity components of successive error functions which cannot be interpreted as a radial orbit error phenomenon. This was the motivation for the development of an alternative formulation of the minimization problem where additional smoothness conditions are employed to suppress the discontinuity effect.

Unfortunately it turns out that both segmented models are inadequate for recovering the simulated error signal. The differences between the stepwise radial orbit error signal recovered by the global crossover adjustment and the originally simulated signal show a consistent radial power spectrum. It consists of a number of peaks which cannot be explained by a singularity transformation. Moreover it has been found that the persisting systematic differences could be interpreted as the projection of a surface function expressed in spherical harmonics on the nominal orbit.

The problems encountered with the global segmented approaches lead to the investigation of a continuous minimization model. This approach avoids in a convenient way a number of problems inherent to segmented models. Shortly summarized, these problems are: 1) the mentioned velocity discontinuity effect; 2) overparameterization of short arc segments; and 3) poorly or even isolated arc segments with respect to the 'main' configuration.

Under suitable time tag regularization one can show that the rank defect of the normal equations of the continuous minimization model equals to 9. The homogeneous solution of this problem allows to deform the altimetric surface as a spherical harmonic expansion up to degree and order 2. This presumes a cutoff frequency of 2.3 c.p.r. in the Fourier series employed in the observation equations of the continuous crossover minimization model. The implementation of this minimization scheme and the abilities of its general solution to reconstruct the simulated radial orbit error signal are discussed in §6.4.

In chapter 7 the continuous crossover minimization scheme is applied on the adjustment of SEASAT derived crossover differences. An additional complication encountered in its application is caused by the fact that SEASAT orbits are computed in time windows up to 6 days. The method itself is applied on crossover data in 5 orbital periods in the first 2 months of the SEASAT mission. In the 5 cases considered in this study it was found that the r.m.s. of the crossover differences tends to decrease from ±1.65 m before to ≈ 30 cm after LSA. Additionally it was found that 1) the internal solutions appear to show a concentration of signal around the expected 1 c.p.r. and that 2) high correlations occur for orbit error functions individually solved in independent periods. As a result it is feasible to solve a number of adjacent orbital periods simultaneously by means of a combined approach.

The external evaluation of the independent internal consistent crossover solutions is performed by means of an optimal adjustment to the GEM-T1 reference geoid. Characteristic appear to be the consistent values of the C_{00} and C_{20} surface function coefficients which are the parameters of the singularity transformations. The nature of this effect is not well understood since there are a number of effects acting simultaneously. The mentioned components tend to absorb a combination of these effects meaning that the eventual transformed crossover solution is tailored to a specific reference geoid.

In chapter 8 a sketch of an integrated approach is discussed. For this purpose a recent technique introduced by Wagner (1985) is compared with the global crossover minimization schemes. The first part of chapter 8 describes the derivation and limitations of observation equations which may be applied for improvement of 1) potential coefficients of the gravitational field and 2) surface coefficients of a permanent sea surface topography model.

Observation equations derived from crossover minimization may be applied in the same context except that they do not contain geoid or PST information. Both classes of observation equations allow to estimate a certain linear combination of potential coefficients of the same order. However an independent treatment of observation equations of lumped coefficients derived by either 1) direct height measurements in the context of an integrated approach or 2) crossover difference observations is not pursued here. In chapter 8 it is argued that gravity model improvement should be performed by employing observation equations for potential coefficients derived from the perturbations of satellites at different inclinations and eccentricities.

There may be two more drawbacks in the current concept of an integrated approach. The first concerns the modeling of PST since the current version allows to estimate unrealistic solutions which do not necessarily fulfill the equation of continuity of currents. The second concerns an omission error of the gravitational field in the geoid and the orbit. Both topics are discussed in §8.2 and are recommended for further research on satellite altimetry.

Another subject concerns the inclusion of other observation equations to crossover differences in a combined minimization problem. Technical developments in the near future, such as PRARE on ERS-1 and DORIS and GPS on TOPEX, could provide the required information. These observations might be highly valuable since they enable to observe a number of effects – such as tides, currents and other oceanographic phenomena – which are obscured by the homogeneous solution of the system of normal equations in the conventional crossover minimization schemes.

The last topic in chapter 8 concerns the interpretation of geographically correlated orbit errors according to the theory of Rosborough (1986). It is argued that a separation into a mean and a variable component of the radial orbit error cannot be translated in observability or unobservability of radial orbit errors from crossover differences. However Rosborough's theory is considered useful for explaining the consequences of 'straightforward' averaging methods which have been employed for the construction of mean sea surfaces by Marsh et al. (1982b).

Appendix A

Long periodic resonant effects in near circular trajectories

Linear perturbation theory, as described in chapter 4, shows a good agreement with numerically integrated trajectories. It is mentioned that periodic resonant effects have to be removed from the numerical results before a comparison can be made. For this purpose special attention is given to the particular solution of the Hill equations, especially where a constant or once per revolution force determines the perturbations. In the zonal part of the gravitational field two sort of perturbations can give rise to long periodic resonant effects.

- Even zonal coefficients of the gravitational field are causing secular effects. This situation is described in chapter 4, equations (4.18) ff. The resulting orbit is frequently used throughout this work as a 'linearization' (or nominal) trajectory.
- Perturbations proportional to a complete revolution of the argument of perigee are caused by the odd zonal coefficients of the gravitational field.

In the sequel the latter result is worked out in more detail similar to Cook (1966). A perturbations theory based on this special situation is useful for understanding the concept of so-called frozen orbits as applied in the missions of SEASAT and currently GEOSAT. Besides the theory is useful for explaining the 'butterfly' effect showing up in the simulated repeat arc differences.

Odd zonal perturbations

The disturbance potential of odd zonal coefficients of the gravitational field causing long periodic perturbations takes the form of (4.4) for odd l, $m = 0$ with $p = (l+1)/2$ and $q = +1$ or $p = (l-1)/2$ and $q = -1$:

$$V = \frac{\mu}{a}\sum_{l=3}^{\infty}\left(\frac{a_e}{a}\right)^l \left[F_{l,0,(l-1)/2}G_{l,(l-1)/2,-1} - F_{l,0,(l+1)/2}G_{l,(l+1)/2,+1}\right] C_{l0}\sin\omega. \quad \text{(A.1)}$$

In this expression the F_{lmp} functions for $p = (l-1)/2$ and $p = (l+1)/2$ are:

$$F_{l,0,(l-1)/2} = -F_{l,0,(l+1)/2}. \quad \text{(A.2)}$$

A similar symmetry exists for the eccentricity functions for small e, compare (4.9):

$$G_{l,(l+1)/2,+1} = G_{l,(l-1)/2,-1} = (l-1)\frac{e}{2} \tag{A.3}$$

As a result (A.1) becomes:

$$\begin{aligned} V_{odd} &= \frac{\mu}{a}\sum_{l=3}^{\infty}\left(\frac{a_e}{a}\right)^l F_{l,0,(l-1)/2}(l-1)C_{l0}e\sin\omega \\ V_{odd} &= \frac{\mu}{a}C'e\sin\omega \end{aligned} \tag{A.4}$$

This disturbing function can be used in the LPE, compare (4.1). Elements of particular interest are the eccentricity and argument of perigee in near circular trajectories. The LPE for e and ω become:

$$\begin{aligned} \dot{e} &= \frac{de}{dt} = \frac{\sqrt{1-e^2}}{na^2e}\left[-\frac{\partial V_{odd}}{\partial\omega} + \sqrt{1-e^2}\frac{\partial V_{odd}}{\partial M}\right] \\ \dot{\omega} &= \frac{d\omega}{dt} = \frac{\sqrt{1-e^2}}{na^2e}\left[+\frac{\partial V_{odd}}{\partial e} - \frac{e\cot I}{1-e^2}\frac{\partial V_{odd}}{\partial I}\right] \end{aligned} \tag{A.5}$$

These expressions are used to transform to the so-called non-singular variables $u = e\cos\omega$ and $v = e\sin\omega$ which are differentiated with respect to the time:

$$\dot{u} = \dot{e}\cos\omega - e\dot{\omega}\sin\omega \tag{A.6}$$

$$\dot{v} = \dot{e}\sin\omega + e\dot{\omega}\cos\omega \tag{A.7}$$

We note that 1) all expressions in the form of e^2 and eC_{l0} are ignored due to the near circular situation and 2) the disturbing potential V_{odd} is independent of the mean anomaly M. As a result it follows that (A.6) becomes:

$$\begin{aligned} \dot{u} &= \frac{-1}{na^2e}\frac{\partial V_{odd}}{\partial\omega}\cos\omega - e\frac{1}{na^2e}\frac{\partial V_{odd}}{\partial e}\sin\omega \\ &= \frac{-1}{na^2e}[\frac{\mu}{a}C'e\cos\omega]\cos\omega - \frac{1}{na^2}[\frac{\mu}{a}C'\sin\omega]\sin\omega \\ &= -nC' = C \end{aligned} \tag{A.8}$$

For (A.7) it is found that

$$\dot{v} = \frac{-1}{na^2e}[\frac{\mu}{a}C'e\cos\omega]\sin\omega + e\frac{1}{na^2e}[\frac{\mu}{a}C'\sin\omega]\cos\omega = 0 \tag{A.9}$$

Expression (A.6) and (A.7) can be regarded as a system of differential equations describing a motion in the (u, v) plane caused by exact resonance of the even zonal coefficients. The even zonal coefficients explain that $\dot{e} = 0$ and $\dot{\omega} = k$ where k is determined by a, e and I. Hence from (A.6) and (A.7) it follows that $\dot{u} = -kv$ and $\dot{v} = +ku$. Equations (A.8) and (A.9) represent the contribution of the odd zonal coefficients of the gravitational field to this motion. Hence from (A.8) and (A.9) it follows that $\dot{u} = C$ and $\dot{v} = 0$. Therefore the combined differential equations take the form of:

$$\left.\begin{aligned} \dot{u} &= -kv + C, \\ \dot{v} &= +ku \end{aligned}\right\} \tag{A.10}$$

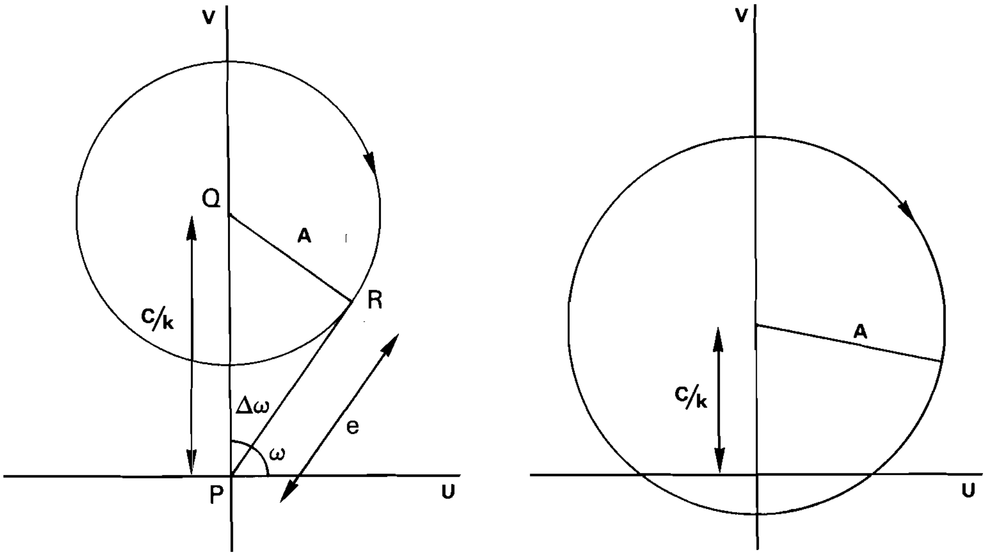

Figure A.1: Precession (right) and liberation (left) due to the zonal coefficients of the gravitational field.

with $k = \dot{\omega}$ due to the even zonal secular effect. This system of differential equations has the following solution, compare Cook (1966):

$$\left.\begin{aligned} u &= A\cos(kt+\alpha), \\ v &= A\sin(kt+\alpha)+C/k \end{aligned}\right\} \tag{A.11}$$

where A and α represent integration constants. The inverse relation to eccentricity and argument of perigee is found by:

$$\left.\begin{aligned} e &= \sqrt{u^2+v^2}, \\ \omega &= \tan^{-1}(v/u) \end{aligned}\right\} \tag{A.12}$$

The system of equations given in (A.11) represents a circular motion in the (u,v) plane about a center $(0, C/k)$ shifted over the v axis. This situation is demonstrated in figure A.1 for so-called precessing ($A > C/k$) and liberating ($A < C/k$) orbits where the argument of perigee is moving clockwise which suggests a negative value of k as in the simulated trajectory in chapter 4. In liberating orbits the argument of perigee stays in between the values of $90° - \Delta\omega$ and $90° + \Delta\omega$. The value of $\Delta\omega$ depends on the constants A and C/k and attains a maximum when segment PR is perpendicular to QR as is illustrated on the left figure of A.1. In this case $\Delta\omega = \tan^{-1}(A/\sqrt{(C/k)^2 - A^2})$. The value of $\Delta\omega$ is minimized when $A = 0$. In this case a so-called *frozen* orbit is obtained. In frozen orbits the argument of perigee is fixed to 90° whereas the eccentricity equals to C/k.

Precessing orbits occur when $A > C/k$; in this case the argument of perigee varies over the entire range of [0, 360°] as can be concluded from the right figure of A.1. For these orbits the eccentricity varies in between $A - C/k$ and $A + C/k$.

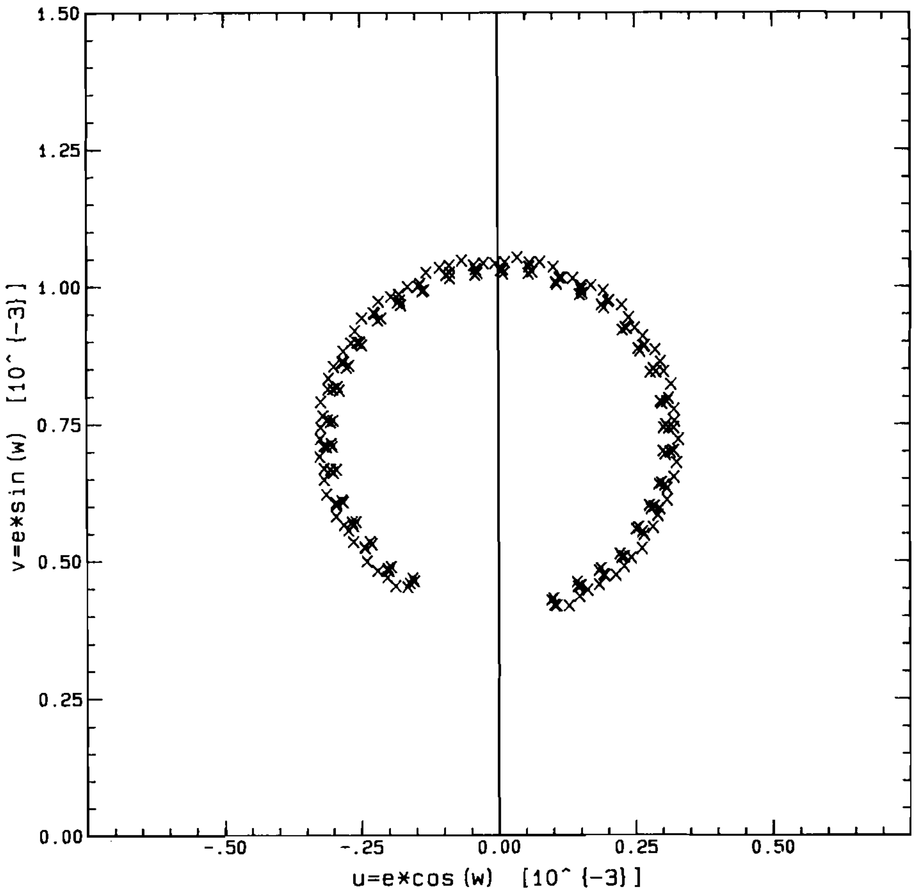

Figure A.2: Behavior of the long term non-singular variables u and v in a near circular numerically integrated trajectory. Only zonal coefficients have been used in the integration of the equations of motion.

The LPT of Kaula (1966) cannot explain this effect since it always results in oscillating solutions for the Keplerian elements, compare eqns. (4.22). Here we conclude that there exist other solutions than the oscillating ones. The motions of e and ω are not anymore harmonic oscillations.

In order to verify the theory discussed above a numerical experiment was conducted. In this experiment a trajectory is integrated numerically using the first 9 zonal coefficients of the GEM-T1 field, described by Marsh et al. (1986). For this purpose a 12^{th} order Adams/Moulton Adams/Bashforth multistep integrator was applied with a stepsize of 60 sec. It was used to integrate the equations of motion 180 days in advance. No perturbations other than the zonal gravitational effects were used to integrate the equations of motion. Other problem dependent constants were chosen according to GRS-80. The initial elements of the trajectory are $a = 7158$ km, $e = 0.75 \times 10^{-3}$, $I = 108°$, $\Omega = 0°$, $\omega = 90°$ and $f = 60°$.

In figure A.2 the results of this experiment are shown in the (u, v) plane. Each sample in this figure is derived by averaging the computed (u, v) values over 1 day of data. Averaging is required to filter out short periodic oscillations due to the dominant C_{20} effect. The results reveal the circular motion in the (u, v) plane centered around the $(0, C/k)$ point. The value of $\dot{\omega}$ according to (4.19) equals to -207 days (minus sign implies a clockwise motion). The theoretical value of C/k computed by (A.8) equals to 7.9×10^{-4} whereas the value of A equals to approximately 3.1×10^{-4}.

Appendix B

Optimal correlation of spectra

In this appendix it is briefly explained how optimal correlation is computed between two, so-called sequences $\{g\}$ and $\{h\}$. Here the $\{g\}$ and $\{h\}$ sequences denote a series of real numbers h_k and g_k with $k \in [0, N-1]$. Each sequence is considered to represent regular spaced samples of the radial orbit error function found by minimizing crossover differences. Both $\{g\}$ and $\{h\}$ are formed by an evaluation of equation (7.1) at regularly chosen epochs. In the computations it is assumed that the orbit error function is evaluated at 4096 samples regularly distributed over 43 revolutions. The reference time of each sequence coincides with the offset time used in the orbital period in which equation (7.1) is defined.

In Bracewell (1986) it is explained that the product-momentum correlation coefficient γ of the sequences $\{g\}$ and $\{h\}$ is defined as:

$$\gamma = \frac{\sum_{k=0}^{N-1}(g_k - M_g)(h_k - M_h)}{\left[\sum_{k=0}^{N-1}(g_k - M_g)^2 \sum_{k=0}^{N-1}(h_k - M_h)^2\right]^{1/2}} \tag{B.1}$$

where M_g and M_h symbolize averages of the $\{g\}$ and $\{h\}$ sequences:

$$M_g = \frac{1}{N}\sum_{k=0}^{N-1} g_k \quad \text{and} \quad M_h = \frac{1}{N}\sum_{k=0}^{N-1} h_k$$

A direct evaluation of (B.1) results in a correlation coefficient γ whose value varies from -1 to $+1$. If there is full correlation between the sequences then $\gamma = 1$, whenever there is no correlation $\gamma = 0$, if the sequences are anti-correlated then $\gamma = -1$.

In our case, where both sequences are defined with respect to independently chosen reference times, a direct evaluation of (B.1) is not possible since one may assume that there exists a phase shift between the sequences. As a result the problem is to find a specific phase shift resulting in an optimal correlation, defined as γ_{opt}, of the $\{g\}$ and $\{h\}$ sequence:

$$\gamma_{opt} = \frac{\sum_{k=0}^{N-1}(g_k - M_g)(h_{k+l} - M_h)}{\left[\sum_{k=0}^{N-1}(g_k - M_g)^2 \sum_{k=0}^{N-1}(h_k - M_h)^2\right]^{1/2}} \tag{B.2}$$

In this equation it is assumed that $\{g\}$ and $\{h\}$ behave as so-called cyclic sequences, i.e. $h_{N+k} = h_k$. A straightforward (expensive) algorithm for locating γ_{opt} in (B.2) is to compute all possible correlation coefficients for all $l \in [0, N-1]$. This algorithm takes at least N^2 floating point operations which is quite inefficient for large N. In an actual computation of the optimal correlation coefficient N would be 4096 resulting in 16×10^6 floating point operations.

Fortunately there is a less expensive alternative for computing the entire correlation function by means of fast Fourier techniques. The denominator of (B.2) is rapidly found according to Parceval's theorem, compare Bracewell (ibid). This theorem states that the sum of squares in the time domain equals to the sum of squares in the frequency domain:

$$\sum_{k=0}^{N-1} (g_k)^2 = \sum_{k=0}^{N/2-1} G_k G_k^* \tag{B.3}$$

Here G_k represents a complex number whereas G_k^* equals to its corresponding complex conjugate. The sequence $\{G\}$ represents the Fourier transform of the sequence $\{g\}$ (i.e. $G = \mathcal{F}(g)$). In the computation of γ_{opt} in (B.2) the averages M_g and M_h are easily eliminated by assuming the bias coefficient in the perturbation spectrum to be equal to zero. In fact this is already the case since the constraint equations in the LSA of crossover differences force this particular parameter to be equal to zero.

The numerator of (B.2) can be found by an evaluation of the correlation of the $\{g\}$ and the $\{h\}$ sequences. According to Bracewell (ibid) the correlation function $f(x) = g \star h$ is defined as:

$$f(x) = g \star h = \int_{-\infty}^{+\infty} g(u-x)h(u)\,du = \int_{-\infty}^{+\infty} g(u)h(u+x)\,du \tag{B.4}$$

which is identical with a convolution (indicated by $*$) of a reversed $\{g\}$ sequence $\{g_r\}$ and the $\{h\}$ sequence:

$$f = g \star h = g_r * h \tag{B.5}$$

Convolution of $g_r * h$ in time domain corresponds to a multiplication of the $\{G_r\}$ ($=\{G^*\}$) and $\{H\}$ sequences in frequency domain, compare (Bracewell,ibid). Summarizing: an inexpensive algorithm for finding an optimal correlation coefficient γ_{opt} of the $\{g\}$ and $\{h\}$ sequences is as follows:

- given as input data are the spectra G and H
- Parceval's theorem allows to evaluate the denominator of (B.2) by $\sum_k G_k G_k^*$ and $\sum_k H_k H_k^*$
- the Fourier transform of the correlation function $F = G \star H = G_r * H = G^* * H$,
- the optimal correlation coefficient γ_{opt} is found as:

$$\gamma_{opt} = \max \mathcal{F}^{-1}(\Lambda) \quad \text{where} \quad \Lambda = \frac{G \star H}{[\sum_k G_k G_k^* \sum_k H_k H_k^*]^{1/2}}.$$

Most of the computing time is caused by the FFT algorithm which takes, see (Bracewell,ibid), of the order of $2N \log_2 N$ floating point operations. This is a considerable improvement compared to the N^2 floating point operations required for a direct evaluation of equation (B.2).

Bibliography

[1] Allan R.R. (1967) *Satellite Resonance with Longitude Dependent Gravity, II, Effects Involving the Eccentricity*, Planetary and Space Sciences, 15, pp. 1829–1845.

[2] Anderle R.J. and Hoskin R.L. (1977) *Correlated Errors in Satellite Altimetry Geoids*, Geophysical Research Letters, Vol. 4, No. 10, pp. 421-423.

[3] Baarda W. (1973) *S-transformations and Criterion Matrices*, Netherlands Geodetic Commision, Publications on Geodesy, New Series, Vol. 5, No. 1, Delft.

[4] Bjerhammar A. (1971) *Estimation with singular inverses*, Tellus XXIII, 6.

[5] Bjerhammar A. (1973) *Theory of Errors and Generalized Matrix Inverses*, Elsevier, Amsterdam.

[6] Bracewell R.N. (1986) *The Fourier Transform and its Applications*, McGraw–Hill Book Co. ISBN 0-07-Y66454-4.

[7] Born G.H., Richards M.A. and Rosborough G.W. (1982) *An Empirical Determination of the Effects of Sea State Bias on SEASAT Altimetry*, Journal of Geophysical Research, Vol 87, No. C5, pp. 3221–3226.

[8] Cheney R.E., Marsh J.G. and Beckly B.D. (1983) *Global Mesoscale Variability from Collinear Tracks of SEASAT Altimeter Data*, Journal of Geophysical Research, Vol. 88, No. C7, pp. 4343-4354.

[9] Colombo O.L. (1981) *Numerical Methods for Harmonic Analysis on the Sphere* Report No. 310, Department of Geodetic Science, The Ohio State University.

[10] Colombo O.L. (1984a) *The Global Mapping of Gravity with two Satellites*, Netherlands Geodetic Commission, Publications on Geodesy, New Series, Vol. 7, No. 3, Delft.

[11] Colombo O.L. (1984b) *Altimetry, Orbits and Tides*, Report EG&G Washington Analytical Services Inc., NASA Technical Memorandum 86180.

[12] Colombo O.L. (1986) *Notes on the Mapping of the Gravity Field Using Satellite Data*, Paper presented on the summer school in the mountains, Admont, Austria, 1986. Bundled lecture notes are available in the Springer Verlag series on Earth sciences ISBN 3-540-16809-5 or ISBN 0-387-16809-5.

[13] Colquitt E.S., Malyevac C.W. and Anderle R.J. (1980) *Doppler Computed SEASAT Orbits*, The Journal of Astronautical Sciences, Vol. XXVIII, No. 4, pp. 391–403, Oct-Dec 1980.

[14] Conte S.D. and de Boor C. (1986) *Elementary Numerical Analysis, An Algorithmic Approach*, Third Edition, McGraw–Hill Book Co., ISBN 0-07-Y66228-2.

[15] Cook G.E. (1966) *Perturbations of Near Circular Orbits by the Earth's Gravitational Potential*, Planetary and Space Sciences, Vol. 14, pp. 433–444.

[16] Cooley J.W. and Tukey J.W. (1965) *An Algorithm for the Machine Calculation of Complex Fourier Series*, Math. Comp., Vol. 19, pp. 297–301.

[17] Douglas B.C., Agreen R.W. and Sandwell D.T. (1984) *Observing Global Ocean Circulation with SEASAT Altimeter Data*, Marine Geodesy, Vol. 8, No. 1–4, pp. 67–83.

[18] Engelis T. (1983) *Analysis of Sea Surface Topography Using Altimeter Data*, Report 343, Department of Geodetic Science, The Ohio State University.

[19] Engelis T. (1985) *Global Circulation from SEASAT Altimeter Data*, Marine Geodesy, Vol. 9, pp. 45-69.

[20] Engelis T. (1987) *Radial Orbit Error Reduction and Sea Surface Topography Determination Using Satellite Altimetry*, Report 377, Department of Geodetic Science and Surveying, The Ohio State University.

[21] Goad C.C., Douglas B.C. and Agreen R.W. (1980) *On the Use of Satellite Altimeter Data for Radial Ephemeris Improvement*, The Journal of Astronautical Sciences, Vol. XXVII, No. 4, pp. 419–428, Oct–Dec 1980.

[22] Goad C.C. (1987) *An Efficient Algorithm for the Evaluation of Inclination and Eccentricity Functions*, Manuscripta Geodaetica, Vol. 12, pp. 11-15.

[23] Gooding R.H. (1971) *A Recurrence Relation for Inclination Functions*, Celestial Mechanics, 4, pp. 91–98.

[24] Hearn A.C. (1985) *Reduce User's Manual*, Version 3.2, publ. no. CP78, Rev. 4/85, The Rand corporation, Santa Monica, CA 90406.

[25] Heiskanen W.A. and Moritz H. (1979) *Physical Geodesy*, Original edition published in 1967 by W.H. Freeman and Company San Francisco. Now available from: Institute of Physical Geodesy Steyergasse 17, A-8010 Graz, Austria.

[26] Hobson E.W. (1965) *The theory of spherical and ellipsoidal harmonics*, Chelsea publishing company, New York.

[27] Kaplan M.H. (1976) *Modern Spacecraft Dynamics and Control*, John Wiley and Sons, New York ISBN 0-471-45703-5.

[28] Kaula W.M. (1966) *Theory of Satellite Geodesy*, Blaisdell Publishing Co.

[29] Kaula W.M. (1983) *Inference of Variations in the Gravity Field From Satellite-to-Satellite Range Rate*, Journal of Geophysical Research, Vol. 88, No. B10, pp. 8345–8349.

[30] Knudsen P. (1987) *Determination of Mean Sea Surface and Free-air Gravity Anomalies Using Satellite Altimeter Data in The Faeroe Islands Region*, Paper presented at the XVI. NOFTIG meeting in Trondheim NTH, Norway, January 13-15, 1987.

[31] Kolenkiewicz R. and Martin C.F. (1982) *SEASAT Altimeter Height Calibration*, Journal of Geophysical Research, Vol. 87, No. C5, pp. 3189–3197.

[32] Kostelecký J., Klokočník and Kalina Z. (1986) *Computation of Normalized Inclination Function to High Degree – Comparative Analysis, Example of Application.* Preprint 24 Published by the center for scientific information of the astronomical institute of the Czechoslovak academy of science. Also published in Manuscripta Geodaetica, Vol. 11, No. 4, 1986.

[33] Kovalevsky J. (1988) *Lectures in Celestial Mechanics*, Presented on the summer school of theoretical geodesy on "Theory of satellite geodesy and gravity field determination", Assisi, Italy, May–June 1988.

[34] Kozai Y. (1961) *Note on the Motion of a Close Earth Satellite with a Small Eccentricity*, Astron. Journ. 66, 132–134.

[35] Kozai Y. (1962) *Second Order Solution of Artificial Satellite Theory without Air Drag*, Astron. Journal 67, 446–461.

[36] Lame D.B. and Born G.H. (1982) *SEASAT Measurement System Evaluation: Achievements and Limitations*, Journal of Geophysical Research, Vol. 87, No. C5, pp. 3175–3178.

[37] Lanczos C. (1964) *Linear Differential Operators*, D. van Nostrand Co., Library of Congress Catalog Card No. 61–13473.

[38] Lerch F.J., Wagner C.A. and Klosko S.M. (1981) *Goddard Earth Model for Oceanographic Applications (GEM 10B and 10C)*, Marine Geodesy, Vol. 5, pp. 145–187.

[39] Lerch F.J., Marsh J.G., Klosko S.M. and Williamson R.G. (1982a) *Gravity Model Improvement for SEASAT*, Journal of Geophysical Research, Vol. 87, No. C5, pp. 3281–3296.

[40] Lerch F.J., Klosko S.M., Wagner C.A. and Patel G.B. (1982b) *On the Accuracy of Recent Goddard Gravity Models*, Journal of Geophysical Research, Vol. 90, No. B11, pp. 9312–9334.

[41] Levitus S. (1982) *Climatologic Atlas of the World Ocean*, NOAA Geophysical fluid dynamics laboratory professional paper No. 13, Rockville, Maryland.

[42] Lorell J., Parke M.E. and Scott J.F. (1980) *Geophysical Data Record (GDR) User Handbook*, 622–97, Revision A, NASA JPL California Institute of Technology.

[43] Lorell J., Colquitt E. and Anderle R.J. (1982) *Ionospheric Correction for SEASAT Altimeter Height Measurements*, Journal of Geophysical Research, Vol. 87, No. C5, pp. 3207–3212.

[44] Marsh J.G. and Williamson R.G. (1982a) *SEASAT Altimeter Timing Bias Estimation*, Journal of Geophysical Research, Vol. 87, No. C5, pp. 3232–3238.

[45] Marsh J.G. and Martin T.V. (1982b) *The SEASAT Altimeter Mean Sea Surface Model*, Journal of Geophysical Research, Vol. 87, No. C5, pp. 3269–3280.

[46] Marsh J.G., Cheney R.E., McCarthy J.J. and Martin T.V. (1984) *Regional Mean Sea Surface Based on GEOS-3 and SEASAT Altimeter Data*, Marine Geodesy, Vol. 8, No. 1–4.

[47] Marsh J.G., Lerch F.J., Putney B.H., Christodoulidis D.C., Felsentreger T.L., Sanchez B.V., Smith D.E., Klosko S.M., Martin T.V., Pavlis E.C., Robbins J.W., Williamson R.G., Colombo O.L., Chandler N.L., Rachlin K.E., Patel G.B., Bhati S. and Chinn D.S. (1986) *An Improved Model of the Earth's Gravitational Field GEM-T1*, Goddard Space Flight Center, NASA.

[48] Martin T.V., Oh I.H., Eddy W.F. and Kogut J.A. (1976) *Geodyn System Description*, Vol. 1, Report NASA Goddard Space Flight Center.

[49] Martin T.V., Zwally H.J., Brenner A.C. and Bindschadler R.A. (1983) *Analysis and Retracking of Continental Ice Sheet Radar Altimeter Waveforms*, Journal of Geophysical Research, Vol. 88, No. C3, pp. 1608–1616.

[50] Melchior P. (1978) *The Tides of the Planet Earth*, Pergamon Press Ltd.

[51] Mittermayer E. (1971) *Eine Verallgemeinerung der Methode der kleinste Quadrate zur Ausgleichung freier Netze*, Zeitschrift für Vermessungswesen.

[52] Mittermayer E. (1972) *Zur Ausgleichung freier Netze*, Zeitschrift für Vermessungswesen.

[53] Moritz H. (1980) *Advanced Physical Geodesy*, Herbert Wichmann Verlag, ISBN 3-87907-106-3, Abacus Press ISBN 0 85626 195 5

[54] Moritz H. (1984) *Geodetic Reference System 1980*, Published in the geodesist's handbook 1984 Bulletin Géodésique, Vol. 58, No. 3.

[55] Parke M.E. and Hendershott M.C. (1980) *M2, S2, K1 Models of the Global Ocean Tide on an Elastic Earth*, Marine Geodesy, Vol. 3, pp. 379–408.

[56] Rao C.R. (1973) *Linear Statistical Inference and Its Applications*, second edition, John Wiley & Sons, Inc. ISBN 0-471-70823-2.

[57] Rapp R.H. (1983) *The Determination of Geoid Undulations and Gravity Anomalies from SEASAT Altimeter Data*, Journal of Geophysical Research, Vol. 88, No. C3, pp. 1552–1562.

[58] Rapp R.H. and Cruz J. (1986a) *Development and Comparison of High Degree Spherical Harmonic Models of the Earth's Gravity Field*, paper presented at the Symposium "Definition of the Geoid", Florence, Italy, May 1986.

[59] Rapp R.H. (1986b) *Global Geopotential Solutions*, Lecture notes in Earth sciences, Vol. 7, Springer Verlag. ISBN 3-540-16809-5 or 0-387-16809-5.

[60] Rosborough G.W. (1986) *Satellite Orbit Perturbations Due to the Geopotential*, Report No. CSR-86-1, Center for Space Research, The University of Texas at Austin.

[61] Rowlands D. (1981) *The Adjustment of SEASAT Altimeter Data on a Global Basis for Geoid and Sea Surface Height Determinations*, Report No. 325, Department of Geodetic Science and Surveying, The Ohio State University.

[62] Rummel R. and Rapp R.H. (1977) *Undulation and Anomaly Estimation using GEOS-3 Altimeter Data Without Precise Satellite Orbits*, Bulletin Géodésique, Vol. 51, pp. 73–88.

[63] Rummel R. (1985) *Satellite Altimetry as part of a Geodetic Model*, IAG proceeding, I Hotine–Marussi Symposium on Mathematical Geodesy, 3–6 june 1985, Rome.

[64] Sandwell D.T., Milbert D.G. and Douglas B.C. (1986) *Global Nondynamic Orbit Improvement for Altimetric Satellites*, Journal of Geophysical Research, Vol. 91 No. B9 pp. 9447–9451.

[65] Schrama E.J.O. (1986a) *Estimability of Potential Coefficients from Orbit Perturbations*, Report No. 86.1, Mathematical and Physical Geodesy, Department of Geodesy, Delft University of Technology.

[66] Schrama E.J.O. (1986b) *A study of a Satellite-to-Satellite Tracking Configuration by Application of Linear Perturbations Theory*, Report No. 86.3, Mathematical and Physical Geodesy, Department of Geodesy, Delft University of Technology. This work is also published in Quaterniones Geodaesiae, 7, 2, (101–142).

[67] Schwiderski E.W. (1978) *Global Ocean Tides, Part I, A Detailed Hydrodynamical Interpolation Model*, NSWC/DL TR–3866, Naval Surface Weapons Center, Dahlgren, Va.

[68] Singleton R.C. (1969) *An Algorithm for Computing the Mixed Radix Fast Fourier Transform*, IEEE trans. audio electroacoust., Vol. AU-17, pp. 93-103, June.

[69] Stoer J. and Bulirsch R. (1983) *Introduction to Numerical Analysis*, Springer–Verlag ISBN 0-387-90420-4 or 3-540-90420-4.

[70] Strang van Hees, G.L. (1982) *Variance-Covariance Transformations of Geodetic Networks*, Manuscripta Geodaetica, Vol. 7, pp. 1–20.

[71] Taff L.G. (1985) *Celestial Mechanics, a Computational Guide for the Practitioner*, John Wiley and Sons, ISBN 0-471-89316-1.

[72] Tapley B.D., Born G.H. and Parke M.E. (1982a) *The SEASAT Altimeter Data and its Accuracy Assessment*, Journal of Geophysical Research, Vol. 87, No. C5, pp. 3179–3188.

[73] Tapley B.D., Lundberg J.B. and Born G.H. (1982b) *The SEASAT Altimeter Wet Tropospheric Range Correction*, Journal of Geophysical Research, Vol. 87, No. C5, pp. 3213–3220.

[74] Tapley B.D. and Rosborough G.W. (1985) *Geographically Correlated Orbit Errors and Its Effect on Satellite Altimetry Missions*, Journal of Geophysical Research, Vol. 90, No. C6, pp. 11,817–11,831.

[75] Tapley B.D., Shum C.K., Yuan D.N., Ries J.C. and Schutz B.E. (1988) *An Improved Model for the Earth's Gravity Field, TEG-1*, paper presented at the Chapman conference on progress in the determination of the Earth's gravity field, Ft. Lauderdale Florida, Sep 13–16, 1988.

[76] Teunissen P.J.G. (1985) *The Geometry of Geodetic Inverse Linear Mapping and Non-linear Adjustment*, Netherlands Geodetic Commission, Vol. 8, No. 1, Delft.

[77] Tscherning C.C. and Rapp R.H. (1974) *Closed Covariance Expressions for Gravity Anomalies, and Deflections of the Vertical implied by Anomaly Degree Variance Models* Department of Geodetic Science, OSU, Report No. 208.

[78] Vermeer M. (1983) *A New SEASAT Altimetric Geoid for the Baltic*, Report No. 83:4, Reports of the Finnish Geodetic Institute, ISBN 951-711-091-X, Helsinki.

[79] Wagner C.A. and Klosko S.M. (1975) 15^{th} *Order Resonance Terms Using the Decaying Orbit of TETR-3*, Planetary and Space Sciences, 23, 541.

[80] Wagner C.A. and Klosko S.M. (1977) *Gravitational Harmonics from Shallow Resonant Orbits*, Celestial Mechanics, 16, 143.

[81] Wagner C.A. and Klosko S.M. (1981) *Spherical Harmonics Representation of the Gravity Field from Dynamic Satellite Data*, Planetary and Space Sciences, Vol. 30, No. 1, pp. 5–28.

[82] Wagner C.A. (1983) *Direct Determination of Gravitational Harmonics From Low-Low GRAVSAT data*, Journal of Geophysical Research, Vol. 88, No. B12, pp. 10,309–10,321.

[83] Wagner C.A. (1985) *Radial Variations of a Satellite Orbit Due to Gravitational Errors: Implications for Satellite Altimetry*, Journal of Geophysical Research, Vol. 90, No. B4, pp. 3027–3036.

[84] Wagner C.A. (1986) *Accuracy Estimate of Geoid and Ocean Topography Recovered Jointly From Satellite Altimetry*, Journal of Geophysical Research, Vol. 91, No. B1, pp. 453–461.

[85] Wagner C.A. (1987) *Geopotential Orbit Variations: Applications to Error Analysis*, Journal of Geophysical Research, Vol. 92, No. B8, pp. 8136–8146.

[86] Wagner C.A. (1988) *Summer School Lectures on Satellite Altimetry*, Presented on the summer school of theoretical geodesy on "Theory of satellite geodesy and gravity field determination", Assisi, Italy, May–June 1988.

[87] Wakker K.F., Ambrosius B.A.C. and Aardoom L. (1983) *Precise orbit determination for ERS-1*, Delft University of Technology, Faculty of Aerospace Engineering, ESOC contract report 5227/82/D/IM(SC).

[88] Wakker K.F., Ambrosius B.A.C., Zandbergen R.C.A. and Geldrop G.H.M. van (1987) *Precise orbit computation, gravity model adjustment and altimeter data processing for the ERS-1 altimetry mission*, Delft University of Technology, Faculty of Aerospace Engineering, ESA contract report 6140/84/D/IM.

[89] Wunsch C. and Gaposchkin E.M. (1980) *On Using Satellite Altimetry to Determine the General Circulation of the Oceans With Application to Geoid Improvement*, Reviews of Geophysics and Space Physics, Vol. 18, No. 4, pp. 725–745.

[90] Zandbergen R.C.A., Wakker K.F. and Ambrosius B.A.C. *Application of Satellite Altimeter Data to Orbit Error Correction and Gravity Model Adjustment*, Paper presented at the 27th COSPAR meeting, Espoo, July 1988, Technical Panel on Satellite Dynamics.

Errata

1. p.20 §3.3.1 paragraph 2, last line: "$p > 2\alpha$" should be "$p > 4\alpha$"
2. p.59 last two lines of eq.(4.47), p.59 last formula, p.60 second formula, eq.(4.49) last line: include $\overline{F}_{lmp}(I)$ as a multiplying factor
3. p.63 eq.(4.50) line 2: replace $\frac{d\overline{f}_i}{dt}$ by $\overline{f}_j$
4. p.69 line 9, word 5: replace "is" by "this"
5. p.103 line 3: read as "... the column vectors of the design matrix are linear dependent. The experiments ..."
6. p.128 item 6, last line: replace 'the "land" case' by 'the "sea" case'
7. p.144 section "Recommendations ...", line 2: insert "is" after ς^p